Process-microstructure-tensile properties relationships in the 316L austenitic stainless steel produced by additive manufacturing

Léo Monier

THÈSE

Pour obtenir le grade de

DOCTEUR DE L'UNIVERSITÉ GRENOBLE ALPES

École doctorale : I-MEP2 - Ingénierie - Matériaux, Mécanique, Environnement, Energétique, Procédés Production
Spécialité :
Unité de recherche : SIMaP

Liens procédé-microstructures-propriétés en traction de l'acier inoxydable austénitique 316L élaboré par fabrication additive

Process-microstructure-tensile properties relationships in the 316L austenitic stainless steel produced by additive manufacturing

Présentée par :
Léo Monier

Direction de thèse :

Muriel VERON PROFESSEURE DES UNIVERSITES, Grenoble-INP UGA	Directrice de thèse
Guilhem MARTIN MAITRE DE CONFERENCES, Grenoble-INP UGA	Co-encadrant de thèse
Arthur DESPRES MAITRE DE CONFERENCES, Grenoble-INP UGA	Co-encadrant de thèse
Jean-Jacques BLANDIN DIRECTEUR DE RECHERCHE, CNRS	Co-encadrant de thèse

Rapporteurs :

Stephane GODET
PROFESSEUR DES UNIVERSITES, Université libre de Bruxelles
Julien ZOLLINGER
PROFESSEUR DES UNIVERSITES, Université de Lorraine

Thèse soutenue publiquement le **14 décembre 2023** devant le jury composé de :

Remy DENDIEVEL PROFESSEUR DES UNIVERSITES, Grenoble-INP UGA	Président
Stephane GODET PROFESSEUR DES UNIVERSITES, Université libre de Bruxelles	Rapporteur
Julien ZOLLINGER PROFESSEUR DES UNIVERSITES, Université de Lorraine	Rapporteur
Sophie CAZOTTES MAITRESSE DE CONFERENCES, INSA Lyon	Examinatrice
Benoit MALARD MAITRE DE CONFERENCES, Toulouse-INP	Examinateur
Muriel VERON PROFESSEURE DES UNIVERSITES, Grenoble-INP UGA	Directrice de thèse

Invités :

Flore Villaret
INGENIEURE DOCTEURE, EDF
Arthur Despres
MAITRE DE CONFERENCES, Grenoble-INP UGA

Remerciements

Je tiens tout d'abord à remercier les membres de mon jury, Julien ZOLLINGER et Stéphane GODET pour avoir rapporté mon travail, Sophie CAZOTTES et Benoit MALLARD pour l'avoir examiné et Remy DENDIEVEL pour avoir examiné ce travail mais aussi présidé mon jury.

Je remercie aussi beaucoup mes encadrants de thèse. Arthur, je suis fière d'avoir été ton premier doctorant, où j'ai pu apprendre de ton côté philosophe et littéraire, que je possède peu, mais aussi de surprenantes anecdotes sur le chevalier Bayard, Stendhal, ou encore sur l'origine de la quenelle de brochet. Guilhem, j'ai eu de la chance d'être encadré par quelqu'un d'aussi investit que toi. De toi, j'ai pu apprendre à rédiger, présente et répondre aux éditeurs quand ils font n'importe quoi. Jean-Jacques, j'espère que j'ai réussi à faire passer mon message dans cette thèse puisque je sais que c'est important pour toi. Et enfin je te remercie Muriel pour savoir prendre le temps en cas de problème et d'avoir à cœur la réussite de tes étudiants.

Je remercie aussi EDF, qui m'a fait confiance pour réaliser ces travaux, Flore VILLARET, Yang SHEN et Bernard YRIEIX, avec qui la collaboration a toujours été simple et efficace.
Je remercie l'équipe du CEA Saclay, Hicham MASKROT, Pierre-francois GIROUD, Olivier HERCHER pour avoir permis de fabriquer la matière. Je remercie Edouard DE SONIS pour avoir fabriqué les matériaux mais aussi de toutes les discussions que l'on peut avoir eu, ainsi que Anne-francoise GOURGUES et Sylvain DEPINOY.

Je remercie aussi tout l'écosystème SIMaP. Il m'a été particulièrement précieux pour réussir ma thèse, du personnel technique aux chercheurs en passant par le CMTC. Je tiens notamment à remercier Gilles pour le temps consacré avec moi au TEM et les belles discussions qu'on a pu avoir autour et Florence pour le temps passé avec moi à l'EBSD et les discussions d'à côté. Je remercie aussi Sylvain Trouve en tant que stagiaire, qui m'a bien aidé et qui a réalisé quelques belles images présentes dans ce manuscrit.

Je remercie aussi tous les doctorants et post doctorants que j'ai pu côtoyer durant ma thèse, que ce soit du côté PM ou GPM2. D'abord les plus vieux comme Mohamed, Morgan, Mathis ou Camille puis après les plus jeunes, Pierre, Thomas, Déborah, Marion, Amanie, Lucile, Hélène, Thomas, Guillaume, Lucas. C'est grâce à vous que j'ai pu passer des bons moments au labo et je suis sûr que les pauses café au second étage me manqueront. Je remercie aussi un doctorant en particulier, Maxence tu as su beaucoup m'aider et même si ce que l'on a fait c'est révélé être globalement une fausse piste, j'ai vraiment apprécié collaborer avec toi.

Je remercie aussi ceux qui m'ont accompagné durant ces 3 ans sans faire partie du labo. Les amis avec qui j'ai vraiment pu profiter de Grenoble et surtout de ces environs, et aussi la famille.

Pour finir, j'aimerai remercier une des personnes les plus importantes de cette thèse. Cheyenne, tu as su totalement me soutenir. Accepter mes horaires de travail un peu lourd, et ma faible disponibilité pendant la rédaction, après tout on n'est même pas parti en vacances ! Je suis extrêmement fière de m'être marié avec toi.

Table of content

Introduction

Why the energy sector is interested in metal additive manufacturing?

Metal additive manufacturing (AM) is a family of processes that consists of building a metallic component layer-by-layer from a computer-aided design file. These processes allow the fabrication of sophisticated geometries and a large degree of freedom in the design of optimized components. AM presents additional advantages such as fast prototyping, shortening of the time between design and fabrication, and raw material savings compared to traditional fabrication processes. In this context, companies operating power plants like EDF are interested in AM for three main reasons:

(1) Fabrication of spare parts for power plants. The obsolescence of parts is a critical issue for companies operating power plants, due to their longevity. Throughout their lifecycle, some parts must be changed regularly, but the durability of the plant is frequently longer than that of the part supplier. To overcome this problem, EDF must have in stock many spare parts, which automatically means additional costs. AM turns out to be a solution to solve this problem by having a more local supply chain based on AM machines.

(2) Redesign and fabrication of parts with optimized geometries. Some parts show sophisticated geometries and require several successive processing and assembly steps to obtain the final part. This makes the component expensive with a long lead time. AM can help to shorten the production time since parts can be fabricated in a single step and with a potentially optimized design to achieve better performances.

(3) Repair of components on-site. Some AM processes allow repairing parts on-site. This can be useful to further increase the equipment lifetime.

However, the microstructure and properties of materials produced by additive manufacturing tend to differ from those obtained by traditional processes such as casting and forging. These microstructures and properties are also much less well understood. Before being used in real applications, these materials must be carefully evaluated. New specifications in terms of composition, processing and microstructures may arise from these evaluations.

Two additive manufacturing techniques are of highest interest for the energy sector. The first one is the laser powder bed fusion (LPBF). It consists in locally melting a powder bed, which after solidification of the melted part becomes dense. A new layer of powder is then deposited and the process is repeated until the desired dense part is obtained. This process is well suited to produce complex geometries with a high surface quality, but as a rather low production rate. A schematic of this process is shown in Figure 1(a). The second process is wire and arc additive manufacturing (WAAM). This process consists of laying weld beads by electric arc on top of each other to obtain the dense component. This process is well suited to produce large components, but at the cost of a cruder surface state. A schematic of the WAAM process is shown in Figure 1(b). These processes will be presented in more details in Chapter I and in Chapter VI.

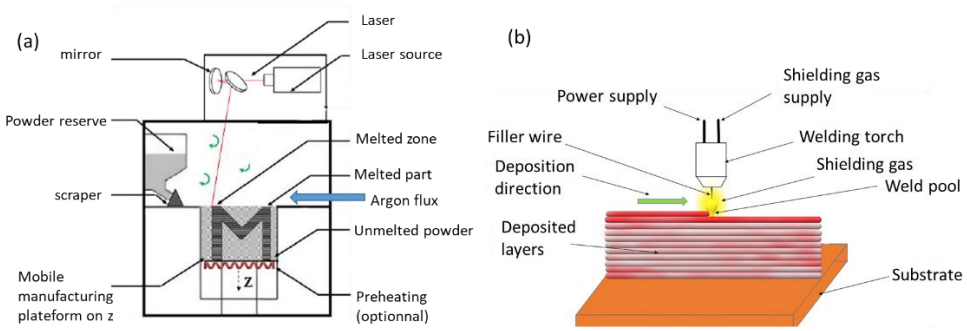

Figure 1: (a) Schematic of laser powder bed fusion (LPBF), from [1]. (b) Schematic of wire and arc additive manufacturing (WAAM), from [2].

As these processes are currently being evaluated, EDF only use them for producing non-critical parts. However, the objective is to be able to use AM to produce critical parts for nuclear power plants in 2024. For example, the NUCOBAM (NUclear Components Based On Additive Manufacturing) project [3] aims to establish a qualification process and evaluating in service behaviour for AM components in the nuclear industry. Two specific components have been selected for demonstration purposes. The first component is a valve body, shown in Figure 2(a). This valve body illustrates the challenges associated with the management of obsolescence because each valve body is unique in each nuclear plant to prevent chain failures. Consequently, stockpiling enough examples of each valve is difficult. AM offers a good solution to address such an issue.

The second component is a debris filter, see Figure 2(b). This component illustrates the complex geometry achievable in LPBF. Both components are considered critical and require extensive testing for qualification. These two components shown in Figure 2 are made of austenitic stainless steel (316L grade).

AM could also be used to produce larger components. EDF Hydro recently bought a sealing ring of one meter in diameter and 100 kg produced by Wire Arc Additive Manufacturing (WAAM), see Figure 2(c) [4]. This sealing ring is made of a 13-4 martensitic stainless steel.

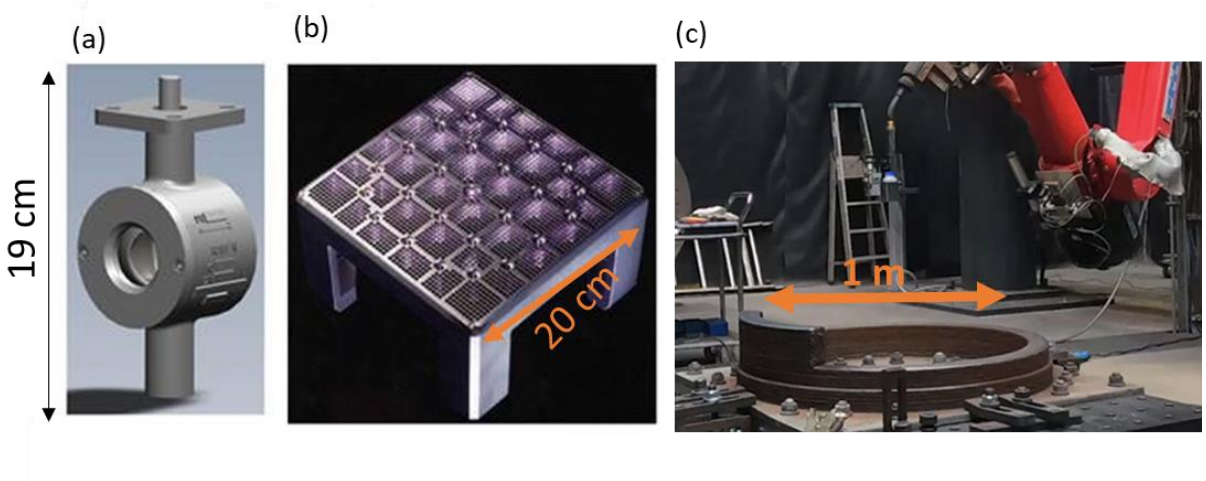

Figure 2: (a) A valve body studied in the NUCOBAM project which should be fabricated by Ramen Valves. (b) A debris filter studied in the NUCOBAM project which should be fabricated by Framatome. These two components are made of 316L and are/would be built by laser powder bed fusion (LPBF). (c) The sealing ring bought by EDF Hydro produced by WAAM [4].

The two first components shown in Figure 2 are made of 316L austenitic stainless steel (ASS). This material, as produced by conventional techniques, is already widely used in the energy field, particularly in the nuclear industry. It is used in many parts of the power generating system of a nuclear power plant, e.g. pipes, valves. Austenitic stainless steels exhibit [5]: an excellent resistance to corrosion, and a good balance between strength, ductility, and fracture toughness. Their good weldability also makes them good candidates for on-site assembly. Good weldability is considered desirable for processing materials by AM because these processes show strong similarities with welding. It is this alloy that will be studied in this thesis.

Some metallurgical challenges to be tackled

When processed by AM, the 316L alloy exhibits a different microstructure in comparison with more conventional processing routes such as forging. Figure 3 illustrates the differences at the intergranular and intra-granular scale of 316L processed by LPBF and traditional processes. When processed by LPBF, the 316L alloy shows a fully austenitic microstructure with three main characteristics: columnar grains and a relatively strong crystallographic texture (Figure 3(a)); a dislocation network, see Figure 3(c); and oxides in the range of 10-100 nm.

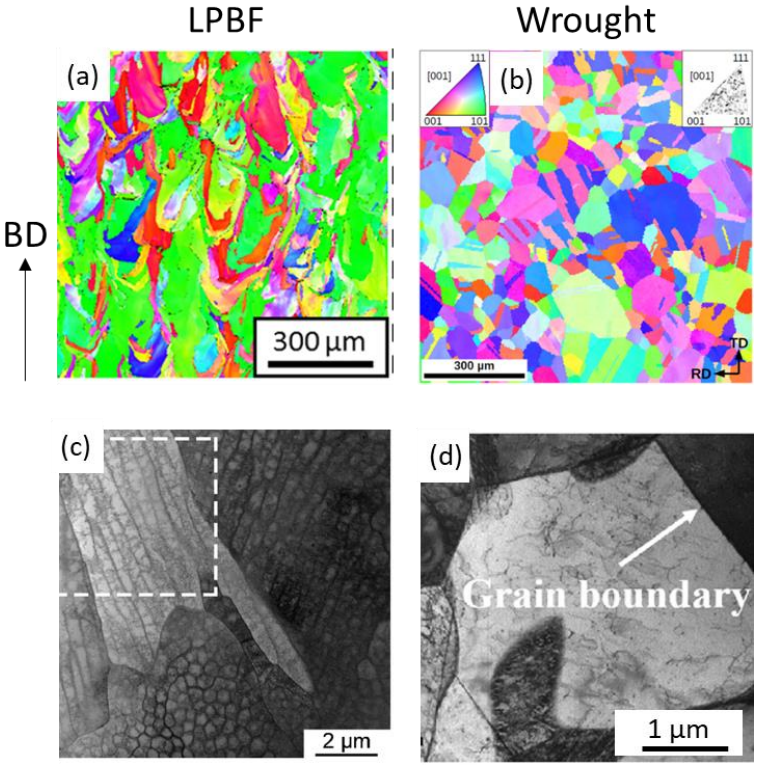

Figure 3: (a)-(b) IPF-EBSD map showing at the granular scale of a 316L stainless steel processed respectively by LPBF, and wrought. LPBF from [6], and wrought from [7]. (c)&(d) TEM images showing the intra-granular scale of the 316L stainless steel respectively processed by LPBF [8] and wrought [9] .

In addition to the significant differences between the LPBF products and the wrought ones, it was shown in the Ph.D. thesis of Chniouel [9], that there is a significant variability in microstructures as a function of the powder batch of 316L employed to build the samples. This is illustrated in Figure 4. This unexpected

variability in microstructure with composition may be a barrier to make AM a suitable and robust processing route for the nuclear industry.

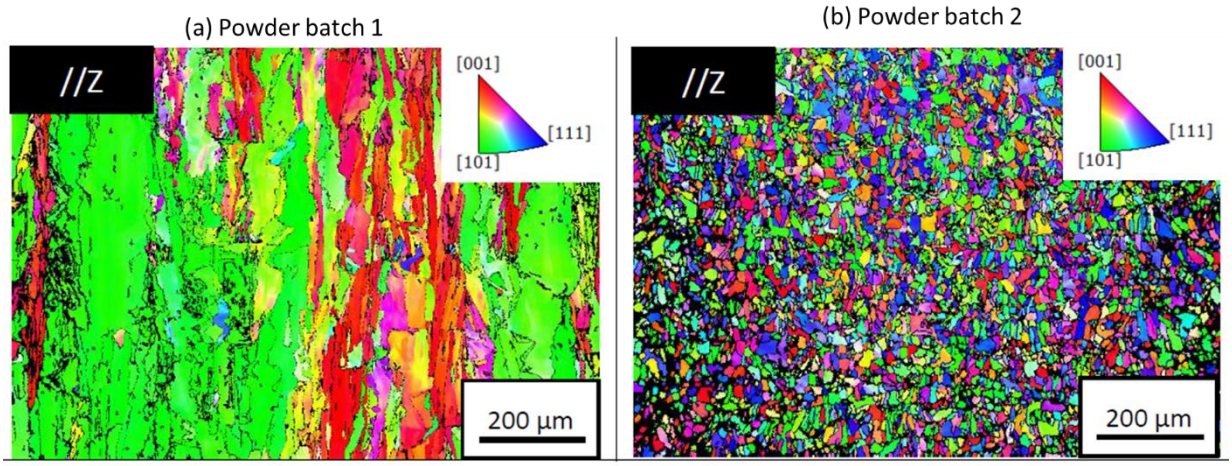

Figure 4: IPF-EBSD map for two 316L built with the same process parameters using two different powder batches, results from the Ph.D. of Chniouel [9]. (a) Powder batch 1. (b) Powder batch 2.

The microstructure and properties may also vary as a function of the processing technique employed. When processed by WAAM, the microstructure shows a two-phase mixture of austenite and residual ferrite (Figure 5 (c)), with large columnar grains of austenite (Figure 5 (a)), and a pronounced crystallographic texture.

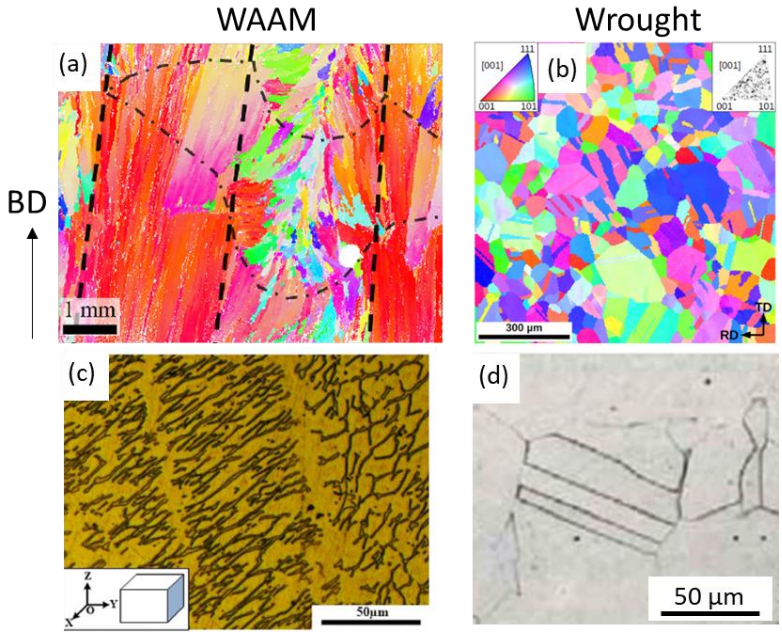

Figure 5: (a)-(b) IPF-EBSD map showing at the granular scale the microstructure of a 316L stainless steel processed respectively by WAAM, and wrought. WAAM from [10], and wrought from [7]. (c)&(d) Optical images showing the intra-granular scale of the 316L stainless steel respectively processed by WAAM [11] and wrought [9].

The microstructural specificities from LPBF or WAAM can impact the mechanical or corrosion properties of the material. Moreover, 316L stainless steels are often, if not always, used in the as-heat-treated state. It is likely that the specific microstructures obtained after fabrication lead to the definition of heat

treatment that are different from the usual ones. The evaluation of the effect of the process on the microstructure, and of the microstructure on the properties have to be evaluated for two main reasons. First, the material must meet strict requirements of mechanical properties to be suitable for nuclear energy application, the so-called RCC-M standard. As these properties depend on the state of the microstructure, it is necessary to identify a range of microstructures that meet these standards and the processing window to obtain them. Second, simulation codes need reliable constitutive laws as inputs to be able to predict the degradation of the material in use. For example, constitutive laws must be defined and adapted for AM products because they strongly differ in comparison with the constitutive laws for cast and wrought products.

A collaborative research program driven by EDF

These metallurgical challenges concern different companies. To reduce investment costs, EDF is part of several consortiums. The objective of consortiums is to mutualize the knowledge and part of the investments between different companies and academic partners. Between the different members of the consortium, results are shared and tasks are distributed. This Ph.D. is part of two consortiums. The first one is called “Additive Factory Hub” (AFH). AFH is a group of several French companies (EDF, Air liquide, Add Up, Vallourec) and academic partners (CETIM, ONERA, ENSAM…) with the main objective of developing a French industry for AM. AFH has several objectives and one of them is the control of the metallurgy inherited from AM. In this consortium, EDF launched and financially supported two Ph.D. theses on the additive manufacturing of 316L but with different scopes. A schematic of the organization of the two Ph.D. theses is presented in Figure 6. The first Ph.D. thesis corresponds to this work. It was conducted at the SIMaP laboratory in Grenoble with the aim of **investigating the relationships between processing, microstructure, and room temperature tensile mechanical properties of the 316L processed by LPBF and WAAM.** The second Ph.D. thesis conducted between the CEA Saclay and the Mines Paristech aimed to investigate the fracture behavior of the same materials. Between the two theses, results were shared and meetings were regularly planned (once every 3 months). To ensure optimal comparability and synergistic outcomes between these two theses, the materials used and the heat treatments are kept identical across both studies. The second consortium to which this thesis is part is the Material Aging Institute (MAI). This consortium, founded by EDF, gathers some international operators of nuclear plants (KEPCO Japan, CGNPC China…) and some actors of the nuclear industry (CEA, Framatome, Mitsubishi…). The main purpose of this consortium is to bring scientific skills and research facilities to address the aging of material used in electric power plants, particularly in nuclear power plants.

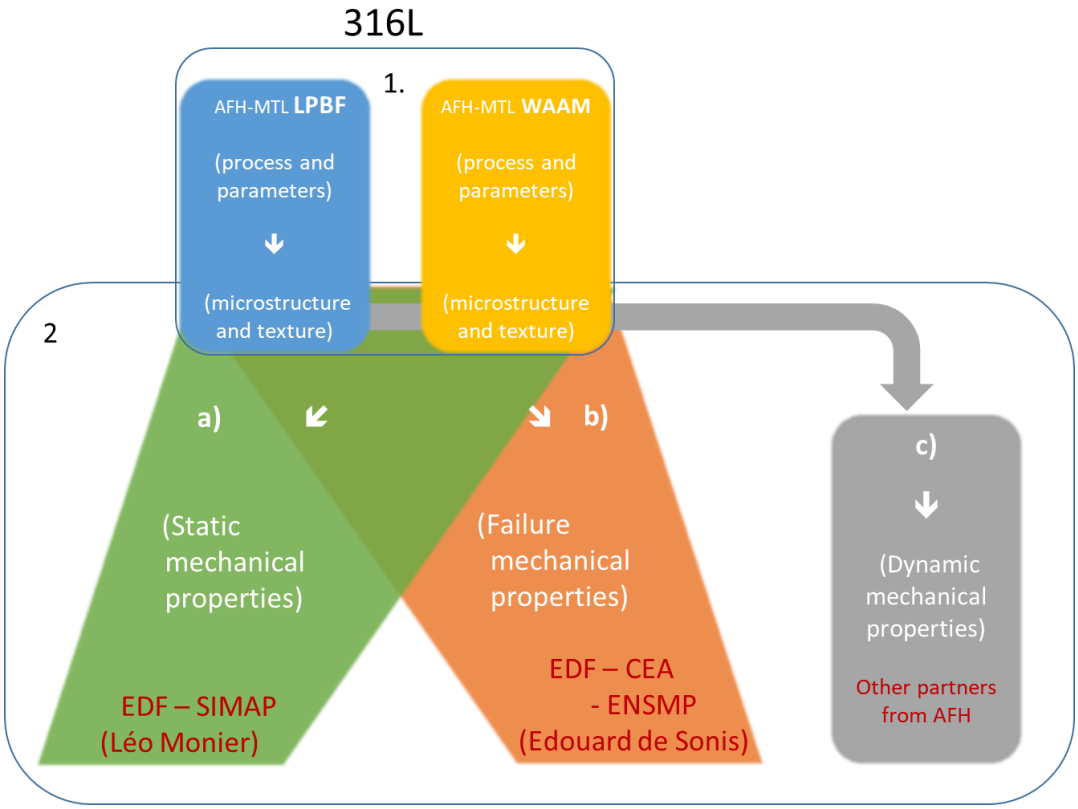

Figure 6: Schematic of the organization of the two Ph.D. theses supported by EDF within the AFH and MAI consortiums.

The scientific questions of the Ph.D. thesis

This Ph.D. thesis will focus on the link between processing, microstructure and tensile properties. The tensile properties of the as-built material are known to be strongly different from a wrought 316L, see Figure 7. This raises a number of scientific questions. For the 316L processed by LPBF, there is a lack of estimations in the literature for the various strengthening contributions to the yield stress, and the true contribution of each of these elements still needs to be clarified. There is also a lack of information regarding the role of the specific arrangement of dislocations in cells on strain-hardening. For the 316L processed by WAAM, there is a lack of information regarding the evolution of the microstructure with heat treatment, and the impact of the ferrite on the mechanical properties.

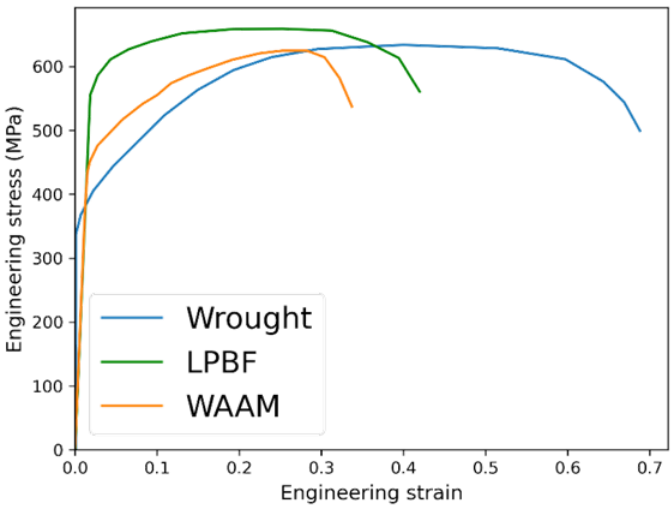

Figure 7: Tensile properties of a 316L. Wrought sample from [12], inherited from LPBF from [13] and inherited from WAAM from [10].

This Ph.D. work was intended to provide some insights into the issues raised and described above. The objectives of this Ph.D. thesis are fourfold:

- Understand the origin of the microstructural variability induced by slight variations in powder composition. Two as-built microstructures obtained using two different powder batches were supplied by the CEA Saclay. Extensive characterization of these two as-built microstructures is done and different hypotheses to explain the origin of this microstructural variability are successively examined.

- Identify appropriate heat treatments to control the tensile properties of the material produced by LPBF. The microstructure and mechanical properties as a function of heat treatment are carefully evaluated.

- Relate the evolution of the tensile properties with the development or disappearance of microstructural features during heat treatments. The impact of the microstructure on the yield stress and the strain hardening is investigated.

- Characterize the microstructure of 316L processed by WAAM and compare it with the microstructure inherited from LPBF.

On the basis of the results of this Ph.D. thesis, industrial recommendations to control the microstructure and the associated mechanical properties via a tight monitoring of the nominal composition and the optimization of the post-fabrication heat treatments is proposed.

Structure of the manuscript

The present work is organized in seven chapters:

Chapter I is a literature review focused on the 316L processed by LPBF. First, an overview of the standard microstructure and properties of the 316L alloy inherited from forging is given. To better understand how the microstructure can impact the tensile properties, the main mechanisms of strengthening and strain hardening are recalled. Then, the laser powder bed fusion (LPBF) process is briefly described. The typical microstructural characteristics of the 316L processed by LPBF and their evolutions with heat treatments are highlighted. Finally, the mechanical properties of this material are summarized, focusing on the aspects that make consensus in the AM community. The technical and scientific challenges that remain to be addressed will also be emphasized.

Chapter II presents the materials and methods used to investigate the 316L processed by LPBF. It provides information on the two different powder batches used as well as on the processing conditions employed to produce the samples studied in this work. The different microstructural and mechanical characterization methods are described. Limits, repeatability, and representativeness of tests are briefly discussed.

Chapter III compares the as-built microstructures inherited from LPBF from the two different powder batches. Differences are highlighted, and different hypotheses regarding the mechanism at the origin of these differences are successively discussed.

Chapter IV starts with a characterization of the evolution of the microstructure with heat treatments. The aim of these heat treatments is to alter different microstructural features, such as microsegregation, residual stresses, dislocation density, and grain size, to help discriminate the role of each microstructural characteristic on the tensile properties. Then, tensile properties are studied for the two steels and for two loading directions as a function of heat treatment. The plastic deformation mechanisms and the role of the different microstructural features on the tensile properties are finally discussed.

Chapter V proposes a model of the plastic tensile response. To do so, a modified Kocks-Mecking model is used. This chapter starts by presenting the model before applying it to the different cases investigated in this work. Based on the model, the different microstructural features contributing to the strain hardening are weighted.

Chapter VI is dedicated to the characterization of the 316L alloy processed by WAAM. It starts with a brief bibliographical review of the process, the microstructure, and the tensile properties of the 316L fabricated by WAAM. The as-built microstructure is characterized and its evolution upon heat treatments is briefly discussed. The tensile properties are measured only in the stress-relieved conditions. A comparison of the microstructure and mechanical properties inherited respectively from LPBF and WAAM is established.

Chapter VII gives the general conclusions followed by scientific perspectives and industrial recommendations based on the present work.

Chapter I. Literature review

I.1 Introduction

The objective of this chapter is to summarize the main characteristics of austenitic stainless steels fabricated by traditional forging while highlighting the differences when processed by laser powder bed fusion (LPBF). We will emphasize various aspects that still need to be clarified regarding the processing, the control of microstructures, and the microstructure-property relationships of the 316L alloy fabricated by LPBF. The first section is dedicated to the 316L austenitic stainless steel fabricated by forging in order to define a reference microstructure and its associated properties. Key aspects of the solidification of austenitic stainless steels are summarized. The second part introduces the typical characteristics of the tensile response of face-centered cubic (FCC) materials to better understand how the microstructure specificities of the 316L processed by LPBF could control it. The third part introduces the LPBF process studied in this work. The fourth part summarizes the unique microstructural characteristics of 316L produced by LPBF and their evolution with heat treatments. The last section gives an overview of the current state-of-the art regarding the microstructure-property relationships of the 316L austenitic stainless steel processed by LPBF. The objective is to distinguish aspects that are now well-established from questions that remain unclear and that would require further investigations.

I.2 Austenitic stainless steels (ASS)

Stainless steels are iron-based alloys containing more than 10.5% weight of chromium [14]. Stainless steels are classified into four classes depending on compositions: austenitic stainless steels, ferritic stainless steels, martensitic stainless steels, and duplex stainless steels.

Austenitic stainless steels (ASS) exhibit an FCC phase. They are widely used (>65% of the overall production of stainless steels [15]) because they are easy to shape, resistant to fracture, and show good corrosion resistance. The AISI 304L and AISI 316L grades represent the majority of the ASS market. The 304L grade contains 18% chromium and 8-10% nickel, while the 316L grade also contains 18% chromium and 10-14% nickel with the addition of around 2% molybdenum. The L of 316L stands for low carbon.

I.2.1 Microstructure and standard of rolled sheets of 316L

Depending on the application, there are different standards for the steel's nominal composition and the required properties. In the rest of this thesis, we will refer to a standard used in the French nuclear industry, the RCC-M 2020 REP ("Règles de conception et de construction des matériels mécaniques des ilots nucléaires pour réacteur à eau préssurisé") and specifically the one applicable in the component from the Nucobam project, presented in the introduction (RCC-M 3300 section on Forged or stamped parts in austenitic stainless steels of level 1,2 and 3, with AFNOR designation Z2 CND 17-12 with no nitrogen control) [16]. This standard will be called latter only RCC-M. The standards corresponding to the RCC-M requirements regarding the nominal composition and the tensile properties are respectively given in Table I-1 and Table I-2. Regarding the composition, the carbon is controlled to a low content as well as P and S (for corrosion consideration), while the standard allows large variations of Ni and Cr contents. Regarding the tensile properties, the standard imposes minimum values on the

yield stress (σ_y), ultimate tensile stress (UTS), and total elongation (A%). Compared to other stainless steels, the minimum yield stress is relatively low (175 MPa), but the minimal total elongation is high (45%).

Table I-1: Composition of a 316L respecting the RCC-Ms standard for forged ASS.

	Weight %							Weight ppm		
Element	Fe	Cr	Ni	Mn	Mo	Si	Cu	C	P	S
RCC-M standard	Bal.	16-19	10-14	<2	2-2.5	<1	<1	<300	<300	<150

Table I-2: Standards for the minimum tensile properties of the 316L at room temperature.

Grade	σ_y (MPa)	UTS (MPa)	A%
316L	>175	>490	>45

Sheets of austenitic stainless steels are often cold or hot rolled and heat treated at more than 1050°C followed by water quenching. A nearly fully austenitic microstructure is obtained with a low dislocation density, equiaxed grains with a typical size ranging between 10 and 100 µm, and a weak crystallographic texture. An industrially 316L rolled sheet will be taken as a reference in this manuscript. It is derived from a cold rolled sheet tempered at 1100°C for 90 minutes followed by water quenching [7]. Figure I-1 shows its typical microstructure. One will note the presence of Σ3 twins boundaries formed during recrystallization. It exhibits an equiaxed microstructure and a grain size of about 40 µm taking into account twin boundaries. This typical microstructure will be considered as our reference throughout this Ph.D. thesis and the terminology 'wrought product' will be sometimes employed to describe a material with this typical microstructure. Some residual ferrite, usually less than 1% appearing as bands is often observed in rolled products. A typical stress-strain curve of an industrial recrystallized cold-rolled sheet of 316L is given in Figure I-1(b).

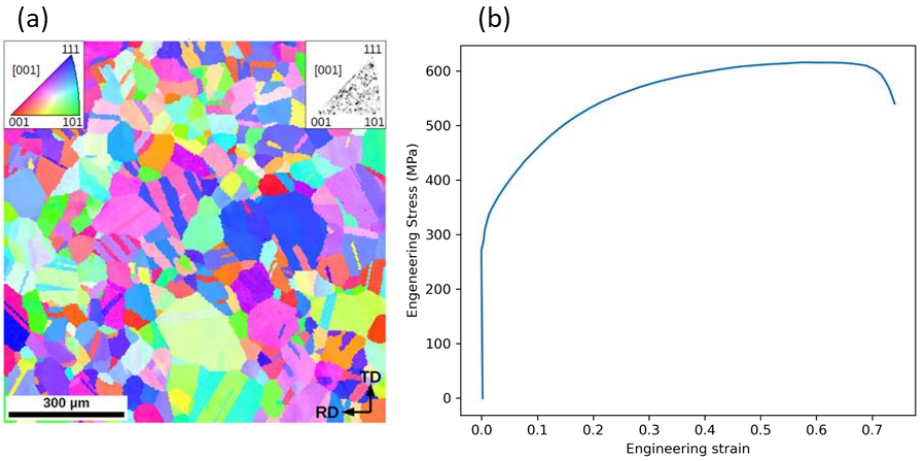

Figure I-1(a): (a) Typical IPF-EBSD map of the wrought 316L austenitic stainless steel after heat treatment at 1100°C/30min. It shows no preferential texture. (b) Typical tensile mechanical response of a wrought 316L steel, from [17].

I.2.2 Solidification of austenitic stainless steels

The laser powder bed fusion process melts the alloy so the microstructure results from solidification. To understand this microstructure, it is important to introduce key concepts of the solidification of austenitic stainless steels. This solidification microstructure of ASS is generally a mixture of ferrite (α) and austenite (γ). The fraction of each phase in the mixture is partially controlled by the chemical composition, especially the Ni and Cr content. The addition of Ni allows the stabilization of the γ phase, see Figure I-2(a). Thus, Ni is a γ-stabilizer. On the contrary, the addition of Cr stabilizes the ferrite and is considered an α-stabilizer. Other elements such as Mo or C are also identified as either α-stabilizer or γ-stabilizer, their power of stabilization being expressed relatively to that of Cr or Ni. This enables the possibility to calculate the chromium equivalent (Cr_{eq}) or nickel equivalent (Ni_{eq}). Several formulas can be used to calculate this Cr_{eq} or Ni_{eq}. All those formulas have been derived from empirical considerations. One of the most employed formulas is the one used in the WRC92 diagram [18], widely employed by the welding community, and given below with the composition given in weight percent (%wt.):

$$Cr_{eq} = Cr + Mo + 0.7Nb$$

$$Ni_{eq} = Ni + 35C + 20N + 0.25Cu\,.$$

As shown in Figure I-2(b), the Cr_{eq} and Ni_{eq} can be used on pseudo-binary phase diagram to determine the domain of the stability of the different phases. The pseudo phase diagram exhibits a three-phase domain (coexistence of $L+\alpha+\gamma$) located between the solidus and liquidus equilibrium lines. On the right of this domain, the alloy solidifies first as ferrite (primary ferrite), while on the left of the domain it solidifies first as austenite (primary austenite). As a result, four distinct solidification modes exist depending on the steel composition: pure ferrite (F), ferrite at the onset of solidification with austenite forming during the last stages of solidification (FA), austenite followed by ferrite (AF), and pure austenite (A). The domains of those four different solidification modes are indicated at the top of the figure. The solidification mode is mainly governed by the ratio Cr_{eq}/ Ni_{eq}.

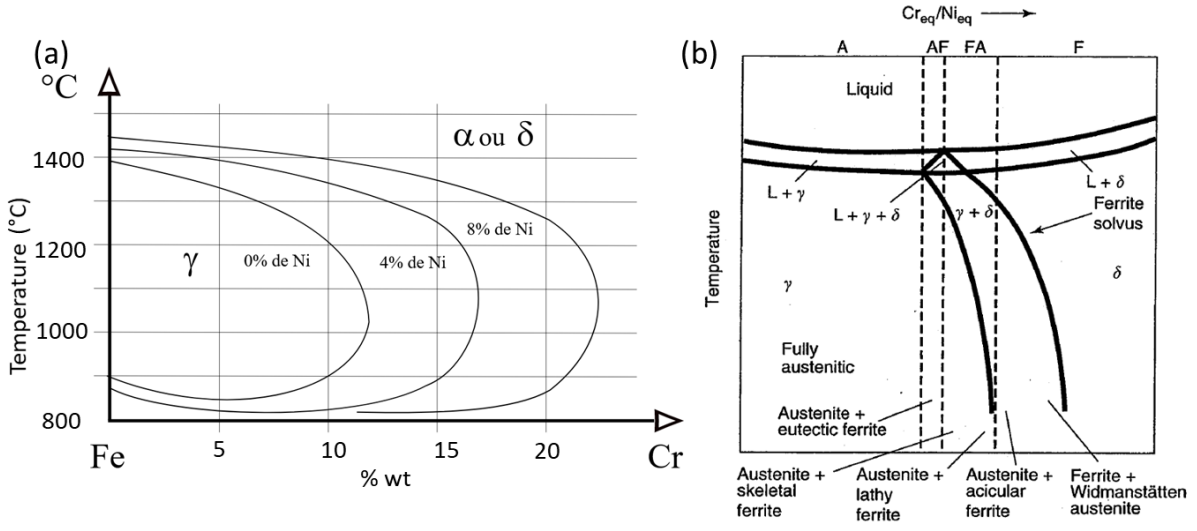

Figure I-2 : (a) Evolution of the austenite stability in the phase diagram Fe-Cr in relation with the Ni content. (b) Definition of the four solidification modes based on the pseudo-binary phase diagram. Both images from [19].

The solidification of austenitic stainless steels has been deeply investigated in the welding literature [19], [20]. In welding processes, the solidification mode plays a key role, and solidification in the F or FA mode is deemed desirable to prevent hot cracking [19]. This is attributed to the superior solubility of impurity elements such as S and P in ferrite [19]. In the nuclear industry, the WRC92 diagram [18] is employed to predict the solidification mode based on the steel nominal composition as shown in Figure I-3(a). This diagram relies on the calculation of both the Cr_{eq} and Ni_{eq}. It is worth noting that this diagram was initially built to predict welding microstructures, therefore for solidification rates typical of arc fusion-based welding (0.1-10 mm/s [21], [22]). The influence of the solidification rate becomes significant above 10 mm/s. We will see later in this chapter that the solidification rate of the 316L processed by LPBF can be much higher than this value.

Based on a dendrite tip model, Bobadilla [23] calculates the dendrite tip temperature as a function of the solidification rate, depending on the primary phase in austenitic stainless steels, see Figure I-3 (c). The dendrite tip undercooling is mainly induced by the chemical segregation at the dendrite tip. The difference in undercooling with solidification rate is mainly affected by the partition coefficient in elements in the primary phase. The phase that shows the higher dendrite tip temperature has a growth advantage, and is then the primary phase. One can see that the primary phase depends on the growth rate, the austenite is promoted at high growth rate.

As a result, Lippold proposed a modification of the WRC92 diagram to account for the solidification rate as illustrated in Figure I-3(b) [21]. At higher growth rates, AF and FA modes are suppressed. At a high growth rate and with a ratio Cr_{eq}/Ni_{eq} between 1.6 and 1.9, a full ferrite solidification (mode F) is predicted followed by a massive transformation of ferrite into austenite. The resulting microstructure is qualified for F/MA. A massive transformation is a phase transformation where the daughter phase has the same composition as that of the mother phase [24]. This phase transformation is a transition by interface migration [25], it does not induce shear as in a displacive phase transformation, but does not involve a long-range diffusion mechanism either. The interface of the phase transformation can cross grain boundaries of the mother phase, and is thus different from a martensitic transformation. In binary or multiconstituted alloys, this phase transformation appears only if the cooling rate is sufficiently high to prevent diffusion in the two-phase domain [26]. This phase transformation was observed in the solidification of ASS at high growth rate by Singh [27] and Elmer [28]. The occurrence of a massive transformation was deduced based on the presence of residual ferrite having the same composition as austenite. This results in a microstructure different from that of primary austenite solidification (mode A). Figure I-3 (d) presents the resulting microstructure after the A mode at a high solidification rate, while Figure I-3 (e) presents the resulting microstructure after the F/MA mode. One can see that the A mode shows a cellular microstructure, while the F/MA microstructure shows a more homogeneous microstructure.

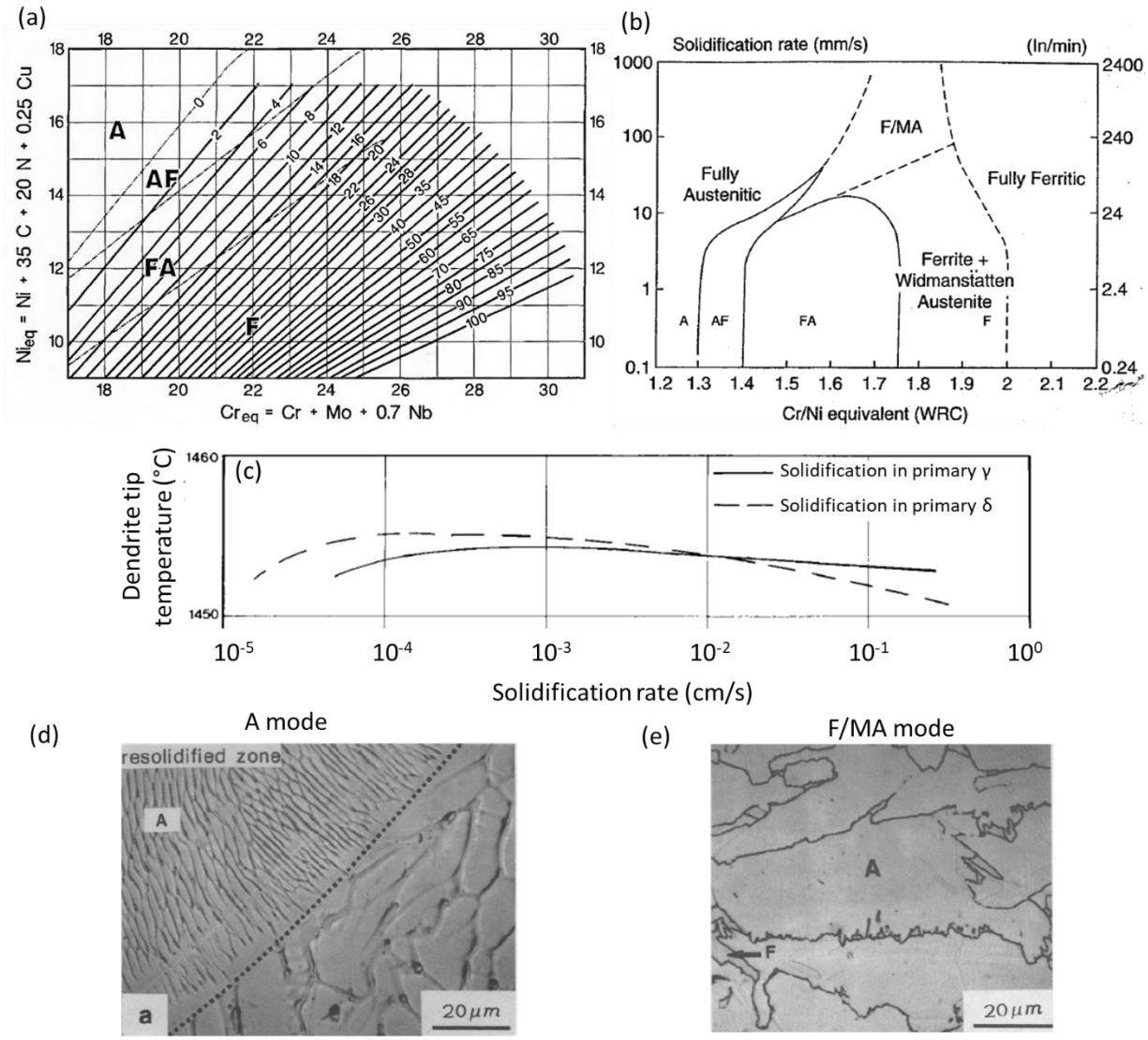

Figure I-3 : (a) WRC92 diagram [18]. The numbers given on each line represent the ferrite fraction found at the end of solidification in the welds. (b) The modified version of this diagram takes into account the solidification rate from [21]. (c) Dendrite tip temperature as a function of growth rate for an austenitic stainless steel, from [23] (d)-(e) Microstructures obtained after electron beam welding from [29]: (d) In an alloy that solidified in A mode; and (e) In an alloy that solidified in F/MA mode.

I.3 Tensile response of FCC crystals

The microstructure of the 316L grade processed by L-PBF exhibits distinct characteristics when compared to its wrought counterpart. To understand how these specific features might influence the mechanical properties at room temperature, it is essential to consider the strengthening and plastic deformation mechanisms of FCC (Face-Centered Cubic) crystals and how they can be tailored through the control of their microstructure or nominal composition.

I.3.1 Strengthening mechanisms

I.3.1.1 Relationship between the shear and the macroscopic stress

A. Single crystals

The yield stress σ_y is the initiation of plastic deformation, indicating the onset of significant dislocation motion. Dislocations start moving when they are subjected to a force component parallel to the slip plane along the slip direction. The stress experienced by the dislocation is, therefore, not the macroscopic stress but rather the resolved shear stress (τ) along the slip system of the dislocation. The relationship between the resolved shear stress and the macroscopic stress is defined by the Schmid factor (m), where $\tau = m\sigma$. For tensile loading, the Schmid factor falls within the range of 0 to 0.5. In a single crystal, the first slip system that becomes active during plastic deformation is the one with the highest Schmid factor, provided the resolved shear stress surpasses the critical resolved shear stress required to initiate dislocation glide. The stereographic projection with contour lines of equal highest Schmid factor is shown in Figure I-4. One can see that <100> and <110> directions have relatively high Schmid factor, but is lower for the <111> directions. Consequently <111> directions will be harder than <100> directions.

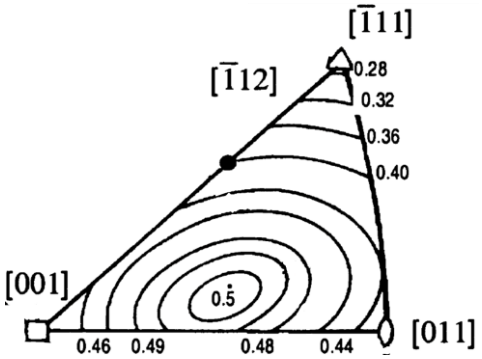

Figure I-4: Stereographic projection with contour lines of equal highest Schmid factor. From [30].

B. Polycrystals

In polycrystals, the yield point is reached only when a large majority of the grains in the polycrystal plastically deform. In polycrystals, grain boundaries are kept cohesive. If only one slip system was active per grain, plastic strain incompatibilities between different grains could not be accommodated. This means that several slip systems are active per grain. Consequently, the straightforward application of the Schmid law, which applies to single crystals, is no longer directly applicable to polycrystals.

To rely on the increase in shear stress to increase in macroscopic stress, one uses the Taylor factor, noted M. In this case, $M\tau = \sigma$. This factor is dependent on the texture of the material and can be estimated with different models. The most common one is the Taylor model. This model hypothesizes that all grains in the material undergo the same deformation (the macroscopic one). With this model, the Taylor factor for a FCC structure with a random texture is estimated to 3.06 and is considered as an upper bound. This model needs at least five different slip systems to be activated to ensure the cohesion of grains by plastic deformation, but does not satisfy the stress equilibrium through a grain boundary [31]. Another model is the Sachs model. This model hypothesizes that all grains undergo the

same stress (macroscopic stress), and only one slip system is active per grain. With this model, the Taylor factor is the inverse of the average Schmid factor, which is for a FCC structure with a random texture 2.22, and is considered as a lower bound. This model ensures the continuity of stresses through a grain boundary, but does not respect the cohesion of grains. Another way to estimate this factor is by using a homogenization model with a crystal plasticity code. An example of such crystal plasticity code is VPSC [32]. With this code, the Taylor factor of random FCC structure is 2.65, between the Sachs and Taylor values.

I.3.1.2 Strengthening mechanisms in ASS

There are five mechanisms that can contribute to strengthening an alloy: solid solution strengthening, forest hardening (dislocations), grain size strengthening (Hall-Petch effect), dispersion strengthening, and precipitation strengthening [30]. The addition of those mechanisms gives an estimate of the yield strength.

1. Solid solution strengthening

Solid solution strengthening is caused by the interaction of alloying elements with the dislocations, which results in an increased glide resistance [30]. For ASS, some empirical formulas have been established to relate the strengthening of the solid solution to the composition. The one from the textbook 'Stainless steel' [33], published in 1991, is given below and is a function of the content of alloying elements introduced in the material (composition is given in %wt.):

$$\sigma_{ss} = 68 + 354(\%C) + 493(\%N) + 20(\%Si) + 3.7(\%Cr) + 14.5(\%Mo). \quad \text{(I-1)}$$

From this formula, the value of the solid solution of the 316L varies between 150 and 250 MPa. One can see the great impact of interstitial elements such as C and N on the strengthening of the austenite, around 50 MPa for the addition of 0.1% of N.

2. Grain Size strengthening: the Hall-Petch effect

Grain size hardening is based on the concept that a material consisting of smaller grains is generally stronger and harder than one with larger grains. When the grain size is reduced, the interfaces between the grains act as barriers to dislocation motion, impeding their movement and resulting in improved strength. The hardening obtained by the grain size effect can be estimated using the phenomenological Hall-Petch law [30]:

$$\sigma_{GB} = \frac{K_{HP}}{\sqrt{D}} \quad \text{(I-2)}$$

In this equation, σ_{GB} is the increase in yield stress induced by the grain size, K_{HP} is the Hall-Petch coefficient, and D is the mean grain size. The value of the Hall-Petch coefficient in ASS was measured in different studies. It was estimated at 225 MPa.$\mu m^{-0.5}$ by Pickering [33], at 300 MPa.$\mu m^{-0.5}$ by Schwartz in [34], at 310 MPa.$\mu m^{-0.5}$ by Kashyap [35], and at 1200 MPa.$\mu m^{-0.5}$ for Feaugas et al. [36].

3. Forest hardening: dislocation strengthening

Gliding dislocations interact with other immobile dislocations (called dislocation forest), which hinders their movement. The shear stress due to dislocation hardening can be estimated by the equation below [30]:

$$\tau_d = \alpha \mu b \sqrt{\rho} \tag{I-3}$$

In this equation, τ_d is the increase in shear stress induced by dislocation hardening, α is a coefficient which represents the mean interaction strength between dislocation (typically around 0.3 for FCC crystals [37]), μ is the shear modulus, b the Burger vector and ρ is the dislocation density. The increase in tensile yield stress resulting from dislocation is simply estimated by multiplying τ_d by the Taylor factor M.

4. Dispersion strengthening

When a material contains non-metallic particles such as oxides or carbides, these particles can contribute to strengthening the material. The reason for this hardening is the interaction between dislocations and particles. Dislocations cannot shear or penetrate hard particles (incoherent interfaces), so they have to circumvent the particles by bowing[30]. This mechanism is described as the Orowan mechanism. The additional increase of shear stress can be estimated by the Orowan law as follows:

$$\tau_p = \frac{\mu b}{l} \, . \tag{I-4}$$

In this equation, τ_p is the increase in shear stress caused by particles and l is the mean distance between particles. The associated increase in tensile yield strength is simply estimated by multiplying τ_p by the Taylor factor M.

5. Precipitation strengthening

Precipitates that form from the decomposition of a supersaturated solid solution can contribute to the strength of a material. If the phase boundary between precipitates and the matrix is incoherent, precipitates act as dispersion particles as described previously [30]. However, it is possible to form metastable precipitates with coherent or partially coherent phase boundaries. Dislocations can shear these precipitates. The increase in shear stress can be described by the equation below [30]:

$$\tau_p = \frac{\gamma}{b} \sqrt{f} . \sqrt{\frac{r \, \gamma}{3 \mu b^2}} \tag{I-5}$$

Where γ is an effective interface energy, f is the volume fraction of precipitates and r the radius of the precipitates. This shear stress evolves with $\sqrt{r}$ but cannot be more than the shear of Orowan law. If the precipitates reach a radius Ro, dislocations will bow out precipitates, and precipitates will act as dispersion hardening. Once again, the tensile yield stress is then estimated by multiplying τ_p by the Taylor factor M.

It is important to note that the different hardening modes can often interact with each other, leading to combined strengthening effects in materials. The addition law depends on the dimensions of the obstacles [38], [39]. If it differs by one order of magnitude or more, the addition can be done linearly. It is typically the case for hardening resulting from grain size and the solid solution, where the structural dimensions of grain boundaries are about several micrometers while it is only a few atomic distances for the solid solution. However, when the structural scales of the set of obstacles are not widely different, linear superposition does not generally hold. If one adds two sets of obstacles of identical strength and with similar spacing of obstacles, a quadratic addition is assumed more appropriate. When considering the contributions from dislocations and particles, the space between obstacles is close (~ 100 nm). In this case, the cumulative effect can be described by a quadratic addition [38], [39]. With this model, the yield stress can be written:

$$\sigma_y = \sigma_{ss} + \sigma_{GB} + M\sqrt{\tau_p^2 + \tau_d^2} \quad \text{(I-6)}$$

However, the quadratic addition is an over simplification and the cumulative effect is between a linear addition and a quadratic addition [40].

I.3.2 Plastic deformation mechanisms

In this section, the basics of austenite plastic deformation are introduced in order to better understand how the microstructure of 316L stainless steel can have an impact on its plastic deformation.

I.3.2.1 Dislocation glide

The main deformation mechanism of austenite is dislocation glide. In austenite, the burger vector is a/2<110>, with *a* the lattice vector. For edge and mix dislocations, the slip plane is {111}. For these dislocations, the burger vector must lie in the slip plane, and there are thus 12 slip systems in austenite. Screw dislocations do not have a defined slip plane and can then change their slip plane (cross slip) [30].

To understand the strain hardening of a FCC polycrystalline material, we can first refer to the strain hardening of a FCC single crystal. The shear stress-shear strain curves of a single crystal of copper for different orientations are shown in Figure I-5. In a single crystal, there are three stages of strain hardening, which can be observed on the plot of the strain hardening rate and can be described as follows:

- Stage I is called easy glide. In this stage, dislocations slip partially through the crystal and exit through the surface. There is no dislocation accumulation.

- Stage II is characterized by a linear increase in stress. This can be explained by a model based on dislocations. The appearance of internal stress is due to primary dislocations remaining inside the crystal. These stresses can trigger dislocation glide in a second slip system. Interactions between the primary and secondary systems are strong, and dislocations are blocked after they have traveled a mean free path L. When dislocations are blocked after a

distance L, then the dislocation density increases by dρ and causes a shear strain written as follows: $d\gamma = bLd\rho$. Dislocations interact with each other and can block their motion. If we assume that they are blocked by a fraction of the dislocation density, the mean free path can be written as $L = 1/(k_1\sqrt{\rho})$. One can write $\frac{d\rho}{d\gamma} = \frac{k1}{b}\sqrt{\rho}$. If we derive equation (I-3) with respect to the shear strain, then $\frac{d\tau}{d\gamma} = \alpha\mu\frac{k_1}{2}$. This model explains the linear increase in stress observed in Stage II.

- Stage III shows a decrease in strain-hardening compared to stage II. This is mainly caused by screw dislocations that can cross-slip and annihilates with another dislocation of the opposite sign [30]. This mechanism contributes to decreasing the dislocation density and increasing the mean free path of mobile dislocations. This is called dynamic recovery. In this case, the probability of annihilation is proportional to the dislocation density with a coefficient k_2. In this stage, there is still the hardening induced by the multiplication of dislocations described in stage II. During stage III, the strain hardening can thus be written: $\frac{d\rho}{d\gamma} = \frac{k_1}{b}\sqrt{\rho} - k_2\rho$.

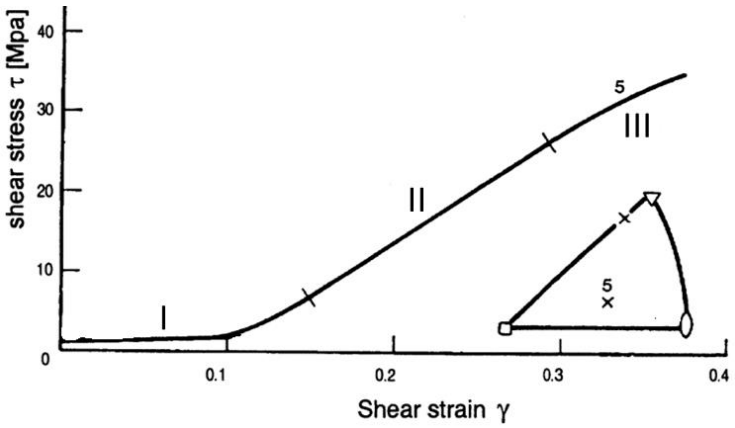

Figure I-5: Shear stress-strain curves of a single crystal of pure copper at room temperature. Adapted from [37]. The three strain hardening stages are indicated on the curve.

In polycrystals, stage I and stage II of single crystal does not exist as such. The work hardening rate of a copper polycrystal is given in Figure I-6 (a). Stage I does not exist. One can see that stage II of polycrystal is characterized by a large decrease of the work hardening rate. Stage III is the same for mono or polycrystal and is characterized by a linear decrease in work hardening rate. The corresponding flow curve is given in Figure I-6 (b) along with the different stages. One can see that Stage III represents the main stage of the flow curve.

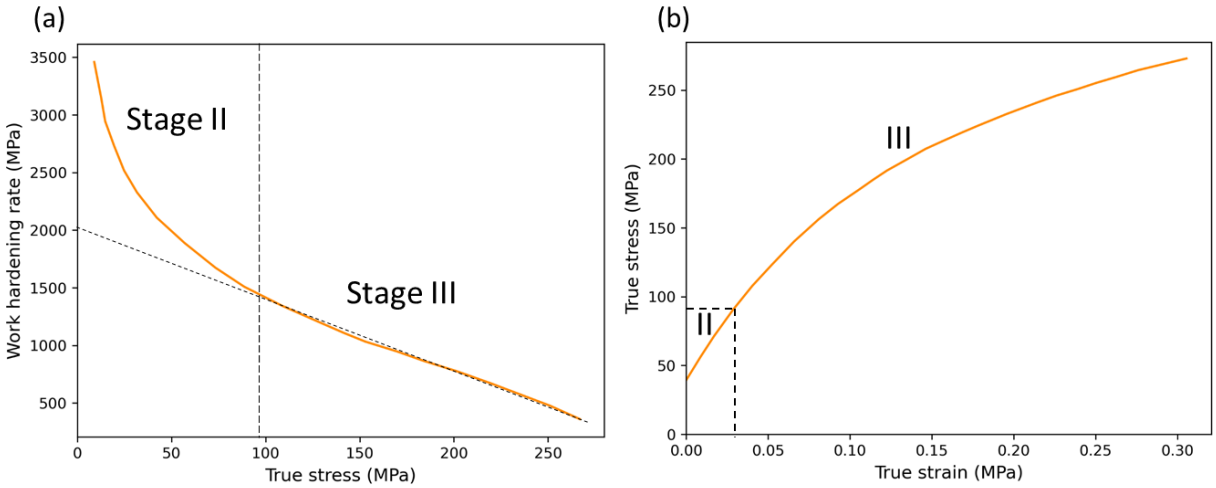

Figure I-6: Tensile behavior of a copper polycrystal. (a) Work hardening rate as a function of the true stress. (b) Flow curve. From [41].

It has been shown that the coefficient k_2, which controls the linear decrease in work hardening rate during Stage III, is highly material-dependent. This is explained by the dissociation of perfect dislocations into partial Shockley dislocations [30]. A Shockley partial dislocation occurs when a perfect dislocation with a (a/2)<110> Burgers vector splits into two partial dislocations with a (a/6)<112> Burgers vector type. These two partial dislocations are confined to the {111} plane. Two dislocations of the same sign tend to repel each other. However, as they are not perfect, there is a stacking fault between them, on a {111} plane. The distance at which the two partial dislocations are apart is inversely proportional to the stacking fault energy. The lower this energy, the further apart the partial dislocations will be. If a dissociated screw dislocation wants to cross slip, it must first recombine its two partial dislocations. The further apart they are, the more energy this requires. So, the lower the stacking fault energy, the more limited the dynamic restoration. An example of TEM images of extended stacking fault is shown in Figure I-7. One can see the special contrast of the stacking fault with stripes.

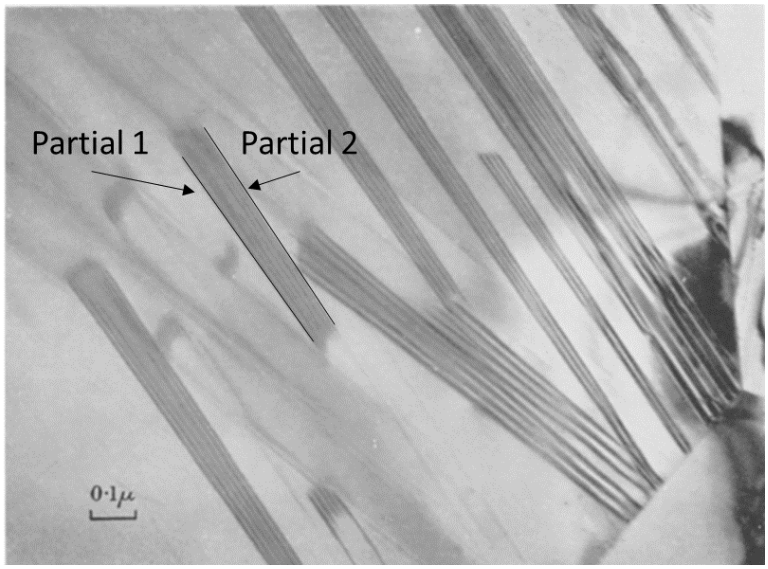

Figure I-7: TEM image of an austenitic stainless steel after a thickness reduction of 2.5% during rolling. Adapted from [42].

Another mechanism that can impact the strain hardening during a tensile test is the rotation of grains. When grains rotate, it can change the Taylor factor of the material, inducing a potential hardening. The

final orientation of the grain depends on the initial orientation of the grain prior to deformation [43]. The grain rotation has been studied in FCC pure crystals which only exhibit dislocation glide as a plastic deformation mechanism, such as copper or aluminum. It is generally admitted that grain rotation follows the sketch shown in Figure I-8. One can see that both <100> and <111> directions are stable directions while other directions rotate toward these two directions, even if it is not by a direct path. It is not expected to have a grain with one of its <110> directions close to the loading direction at the end of the deformation.

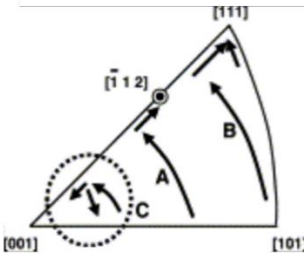

Figure I-8: Sketch of grain rotation during a tensile test in pure aluminum. <110> directions will strongly rotate, while <111> and <100> direction will not rotate. From [30].

I.3.2.2 Twinning induced plasticity (TWIP)

During a sufficiently large plastic deformation at room temperature of ASS, other deformation mechanisms can be activated in addition to dislocation glides such as Twinning Induced Plasticity (TWIP) or Transformation Induced Plasticity (TRIP). Twinning is a shear deformation in which a crystalline volume is transformed into an orientation with mirror symmetry relative to the parent material, see Figure I-9 (a). The mirror plane is common to both twin and matrix and is referred to as the (coherent) twinning plane. Deformation twins show a lenticular shape. Because of its mirror symmetry to the matrix, the twin has the same crystal structure. A deformation twin can be described by the gliding of one portion of a partial Shockley dislocation on each successive {111} atomic plane. This can be described by the stacking of different {111} planes such as ABCAB/ACBACB as described by the schematic in Figure I-9 (b). The reason that induces the movement of one end of the partial dislocation to induce twin is still debated [43].

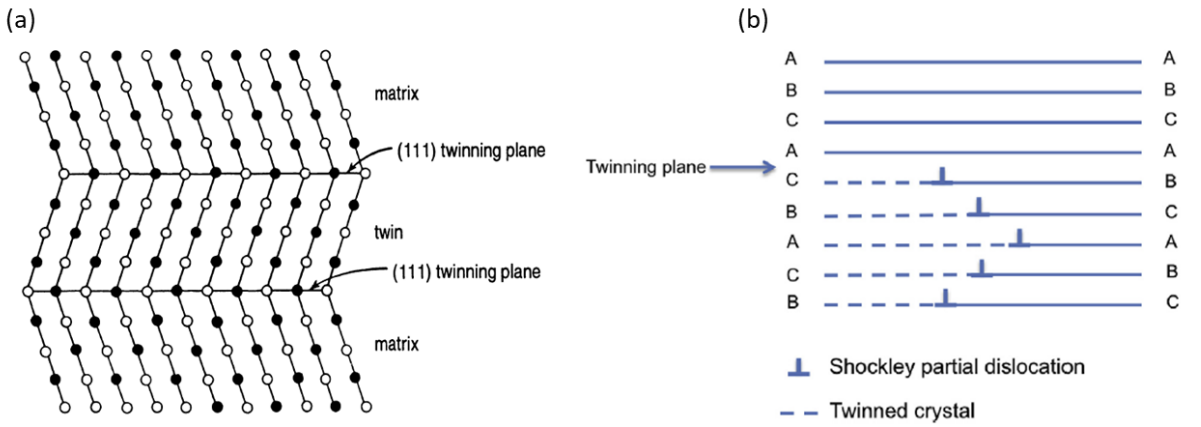

Figure I-9: Schematic illustrating the case of twinning in a FCC matrix. (a) Illustration of the twinning from [30]. (b) Stacking of Shockley partial dislocation From [43].

TRIP is also a shear deformation, but where the crystal structure is not conserved, and it goes from a FCC crystal structure to a hexagonal martensite crystal structure. What governs the activation of different mechanisms is the stacking fault energy (SFE). For low SFE, the predominant deformation mechanisms will be TRIP and dislocation slip. For intermediate SFE, TWIP and dislocation slip will be the main deformation mechanisms while only dislocation slip will be activated for high SFE materials [43]. This is summarized in Table I-3. The SFE of the material depends on the chemical composition of the austenitic phase.

Table I-3: Deformation mechanism as a function of stacking fault energy [44].

SFE (mJ/m²)	SFE<15	15<SFE<50	50<SFE
Deformation mechanism	Slip and TRIP	Slip and TWIP	Slip

Some empirical formula can be used to estimate the SFE at room temperature from the nominal composition of the steel given in %wt. The one from Pickering [45] is given in equation (I-7).

$$SFE\ (mJ/m^2) = 25.7 + 2Ni + 410C - 0.9Cr - 77N - 13Si - 1.2Mn \qquad \text{(I-7)}$$

Using equation (I-7), the SFE of 316L ranges from 20 to 35 mJ/m² [44] depending on the variations of the nominal composition. Within this range of SFE, the 316L steel often exhibits a TWIP effect [44], but can for some compositions show a TRIP effect [46]. Figure I-10 (a) shows deformation twins in a 316L deformed at room temperature. As shown in Figure I-10(b), the density of twins in the 316L steel increases with plastic deformation. It is believed that twinning in the 316L does not contribute significantly to the macroscopic strain. Thus dislocation glide remains the most important deformation mechanism [33]. However, it is believed that twinning contributes to the strain hardening. During plastic deformation, twin boundaries are created. The latter act as obstacles to dislocation motion and hence enhance the strain hardening. This contributes to delaying necking and thus increases the ductility. Based on modeling of the strain hardening taking into account the TWIP effect, Pommier quantified the impact of twinning on the flow curve of the 316L steel [7]. This is shown in Figure I-11. One can see that twinning is expected to have a negligible impact below 10% of plastic strain but have a large impact at larger plastic deformation.

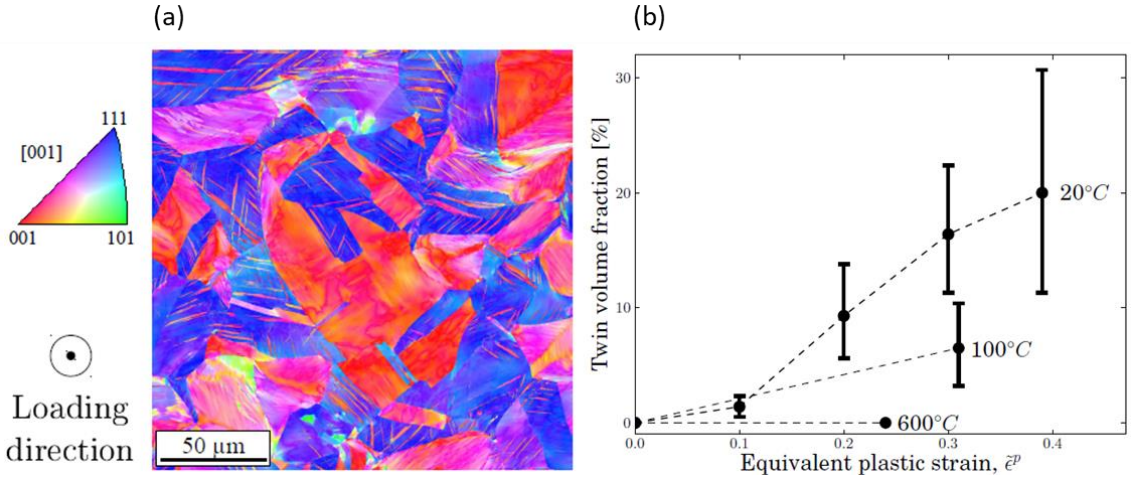

Figure I-10: (a) IPF-EBSD map of a recrystallized rolled sheet of 316L steel after 30% of plastic strain. (b) Twin volume fraction as a function of plastic strain at different temperatures. From [7].

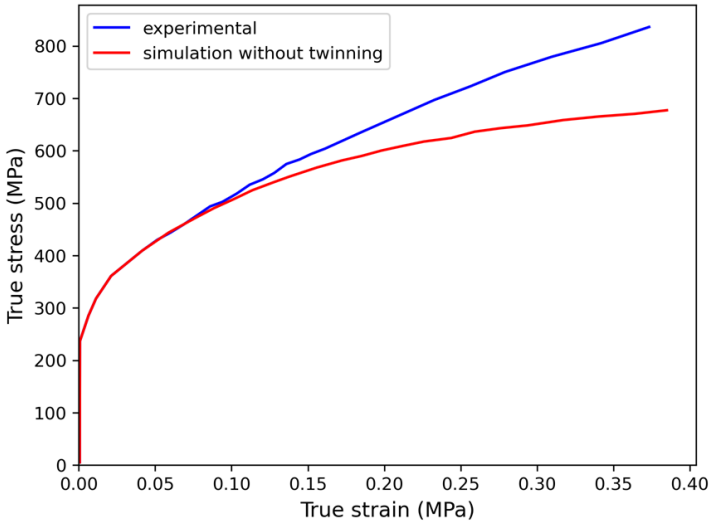

Figure I-11: Experimental and simulated flow curves of a 316L loaded in tension. The simulated curve ignores twinning. From [7].

It has been shown that the occurrence of twinning depends on the grain orientation with respect to the loading direction [47]. This can be explained by texture effects: grains are favorably oriented for twinning while others are not. Twinning has a slip plane {111} and a slip direction <112>, thus a Schmid factor can be defined for twinning. Directions for which the Schmid factor for dislocation slip is lower than that of twin will TWIP more easily. Orientations that meet this criterion are shown in Figure I-12. It can be seen that directions <111> and <110> are favorably oriented for twinning, but directions <100> are not. This orientation space gives the trend and is valid at low plastic strains, but is expected to widen at larger plastic strains.

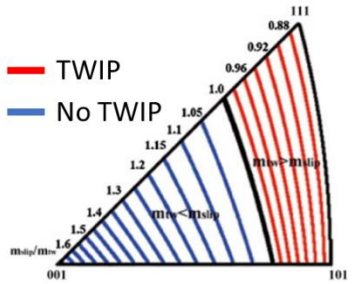

Figure I-12: Inverse pole figure along the tensile axis direction showing the grain orientations which are favorably (area with red lines) and unfavorably oriented (area with blue lines) for twinning. From [47].

I.4 Laser powder bed fusion (LPBF)

This section focuses on fusion-based additive manufacturing processes describing briefly the fundamental principles. Additive manufacturing (AM) starts with the creation of a model of the component using Computer-Aided Design. This model is subsequently fed into a slicer program that partitions the model into discrete layers. AM processes can differ with regard to their primary material (wire or powder) and heat sources employed. Figure I-13 provides a schematic representation of the various techniques classified based on the material and heat source used. The raw material can be a powder bed or deposited during the process. The powder bed can be melted by a laser beam (LPBF) or

by an electron beam (EPBF). For the direct metal deposition, two heat sources can be employed. It can be a laser beam that melts powder or wire or an electric arc that melts the wire.

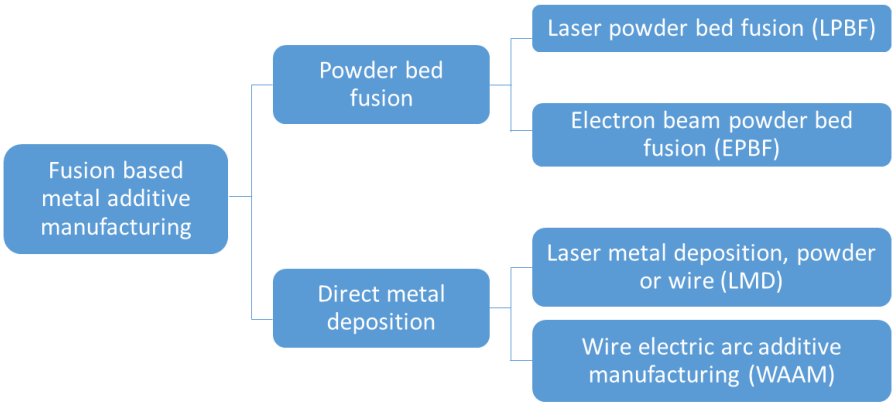

Figure I-13 : Additive manufacturing processes based on fusion. Adapted from [1].

Figure I-14 provides a schematic illustration of the LPBF technique. Among the various AM techniques, Laser Powder Bed Fusion (LPBF) is the process with the best spatial resolution and that can produce very complex shapes. This method uses a laser beam, to selectively melt a specific area of a thin layer (20-50 µm) of powder bed that has been uniformly spread onto a build plate. Once the laser has melted the desired region of the layer, the build plate goes down by an increment corresponding to the layer thickness, and a new layer of powder is spread on top of the previous layer. This process is iterated until the entire component is fabricated. The atmosphere of printing is generally an inert gas (nitrogen or argon). During the process, a constant flux of the inert gas is imposed in order to remove spatters from the melting regions.

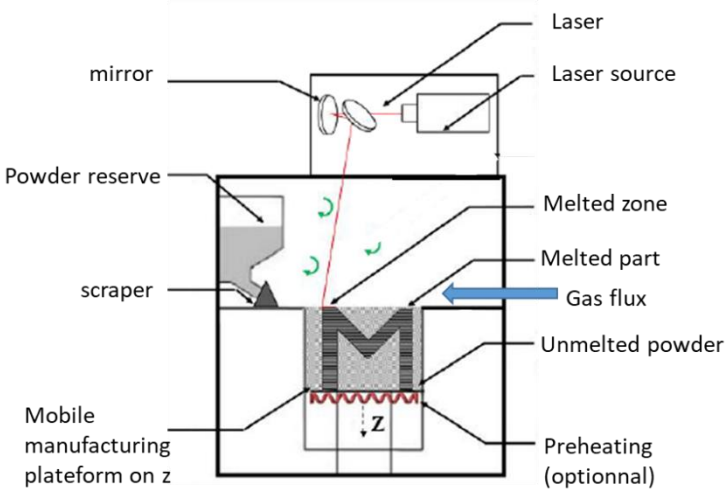

Figure I-14 : Schematic of the LPBF process, adapted from [1].

During the LPBF process, several processing parameters must be adjusted to ensure an optimal fabrication. These can be classified into two groups. The first group is the melt parameters. It corresponds to the laser speed (typically between 200 and 1500 mm/s), laser power (50 < P< 500 W), and beam diameter (20 < D <100 µm). The second group is the scanning parameter. It corresponds to the hatching distance (H~100 µm) - the distance between two adjacent tracks, the layer thickness

(e~30 µm), and the scanning strategy, which describes the laser trajectories at each layer. Figure I-15(a) illustrates some of the processing parameters, and Figure I-15(b) is an example of a 67° scanning strategy. The primary objective of adjusting these six processing parameters is often to produce a dense component (minimization of the porosity).

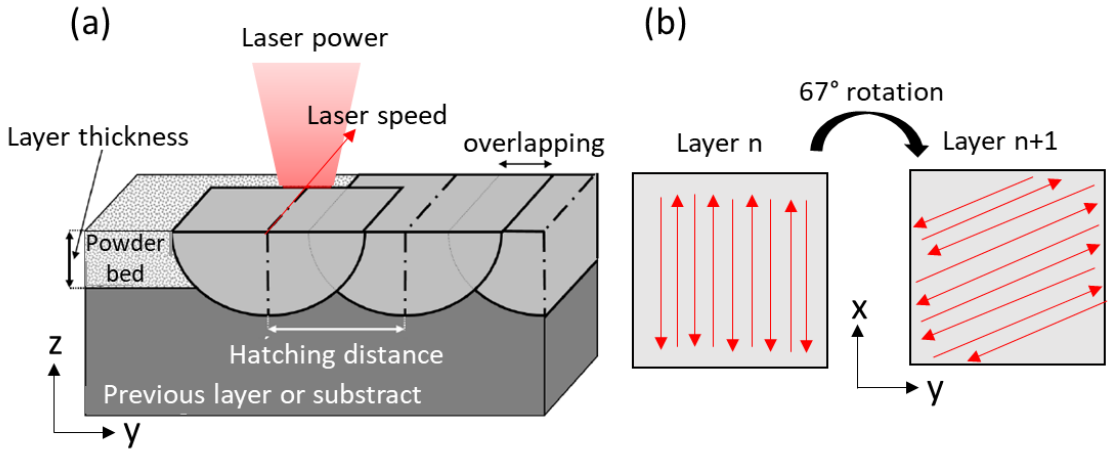

Figure I-15: (a) LPBF melting beads and definition of the main processing parameters, adapted from [1]. (b) Example of a laser scanning strategy with a scan rotation of 67°.

I.5 Microstructure of the 316L processed by LPBF

I.5.1 Main characteristics of the as-built microstructure

The objective of this section is to summarize the main characteristics of the microstructure of the 316L steel inherited from LPBF. High cooling rates, of the order of 10^6 °C/s [48] are found during LPBF. This leads to an out-of-equilibrium as-built microstructure. This, added to the layer-by-layer nature of the fabrication, results in various microstructural specificities. Figure I-16 illustrates these microstructural specificities. Figure I-16(a) and (b) show the peculiar grain morphology, with large columnar grains growing epitaxially along the building direction with a grain width in the order of 20-200 µm depending on the process parameters. Figure I-16 (d) and (e) show the cellular structure inherited from solidification. It is composed of solidification cells, and a high density of dislocations is found in the intercellular regions. The size of these cells is in the range 100-1000 nm. Figure I-16(f) shows particles identified as oxides in the range of 10-100 nm which are mainly located in the intercellular regions.

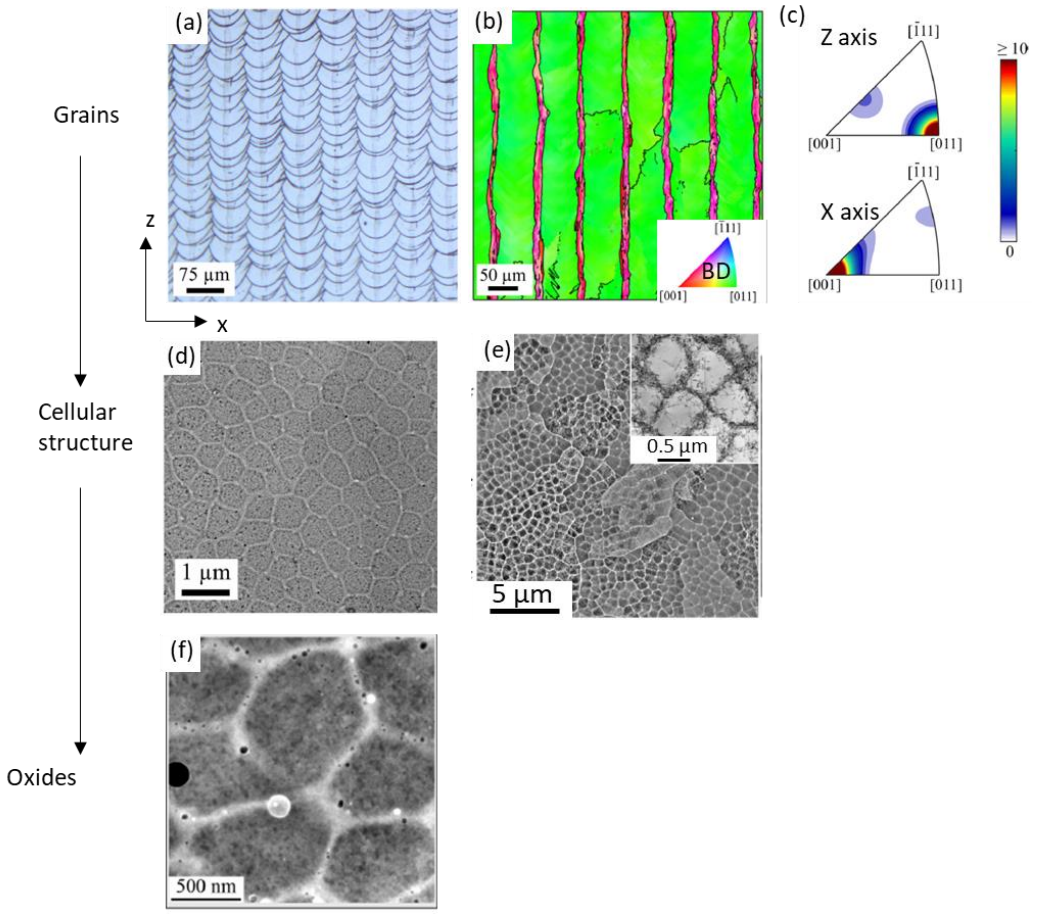

Figure I-16: (a) Optical micrograph after chemical etching showing the melt pool boundaries, (b) IPF-EBSD map corresponding to the region of interest shown in (a). (c) IPF-EBSD map. (d) BSE-SEM micrograph of the solidification cellular structures. (a)-(b)-(c) from [49]. (e) BF- STEM micrograph of the dislocation cellular substructure, (f) STEM-HAADF micrograph taken at the intra cellular scale. (e) and (f) from [50].

I.5.1.1 Grains

The 316L processed by LPBF produces a microstructure that is always 100% austenitic due to the solidification conditions (relatively high solidification rate). The grain size varies between studies, and ranges from 9 µm in Voisin et al. [50] to 100 µm for Chniouel [51] and Lemarquis [6]. The grain morphology is generally columnar along the building direction, with an aspect ratio from 1.6 for Pham et al. [52] to 3.5 for Chao et al. [53]. The shape of the melt pool can vary significantly depending on the processing parameters (conduction vs. keyhole regime), which has a direct impact on the grain morphology and texture. Dendrites grow preferentially in the <100> directions and their growth is the easiest in the direction of the thermal gradient [54]. Grains tend to preferentially grow with one of their <100> directions aligned with the thermal gradient, which is oriented normally to the solid-liquid interface. This is illustrated in Figure I-17 (a) with grains preferentially aligned with one of their <100> directions parallel to the building direction in the center of the melt pool boundary. There are more misaligned when it is at the borders of the melt pool. This explains the microstructure provided as an example in Figure I-17 (b), with grains oriented <100> toward the building direction in the center of the melt pool, while it is their <110> directions aligned with the building direction when approaching the sides of the melt pool. This is induced by a unidirectional scanning strategy (i.e. no rotation between layers), with the center of the melt pool always located in the same position. This strategy leads to large

columnar grains growing along the building direction. In order to alter the texture, a common strategy is to rotate the scanning axis by 67° at each layer. An example of microstructures obtained with this strategy is shown in Figure I-17 (c). With 67° rotation between layers, a fibrous <110>//BD texture is generally obtained [1], [6], [13], [50].

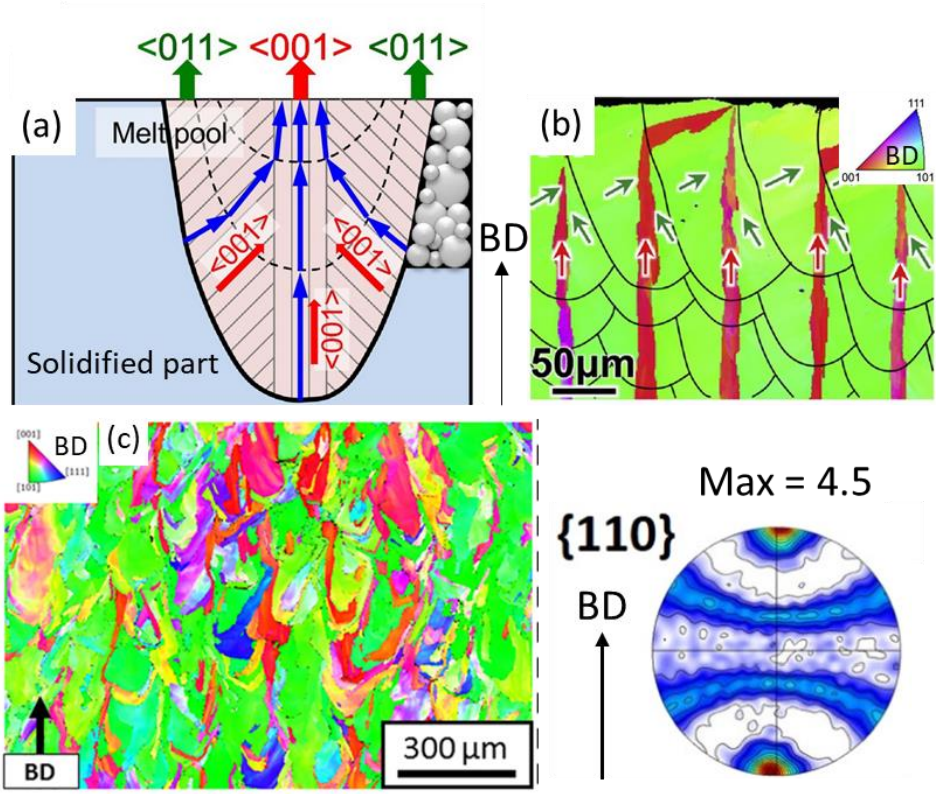

Figure I-17: (a) Schematic of growth direction in a melt pool. (b) Microstructure obtained after a unidirectional scanning strategy. From [55]. (c) Microstructure obtained after a 67° scanning strategy. From [51]. Pole figure was obtained after a scanning strategy of 67°. From [56].

Another characteristic of the as-built microstructure is the significant proportion of low-angle grain boundaries (LAGBs) over the total fraction of interfaces [12], [50], [57], [58]. A LAGB can be defined as a boundary with a misorientation angle between 2° and 10° [57]. This can be seen in Figure I-18, where in this example taken from the literature, LAGBs account for approximately 41% of the total boundaries. The origin of these LAGBs is still debated and could come from the solidification [50] or during the deformation post cooling [1].

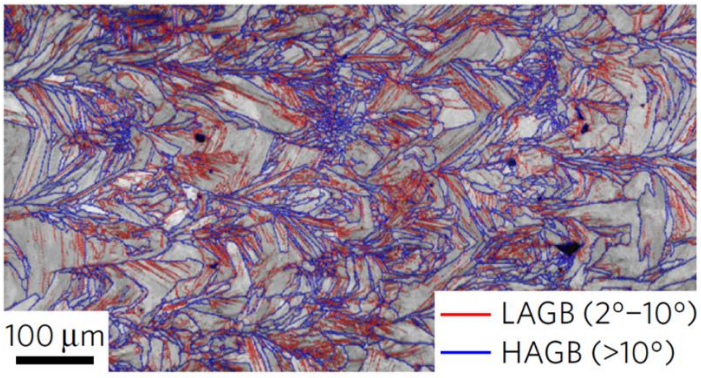

Figure I-18: EBSD Image quality map of an as-built microstructure of 316L processed by LPBF and where HAGB and LAGB have been highlighted respectively in red and blue. From [57].

I.5.1.2 Cellular structure (solidification)

In a primary austenitic solidification mode (A), the solidification structure depends on the temperature gradient and on the solidification rate, as depicted in Figure I-19 (a). The ratio G/R governs the morphology of the structure, while the cooling rate (product G*R) governs the characteristic size of the solidified microstructure [59]. The temperature gradient and solidification rate vary inside the melt pool. Finite element simulation from Pham et al. [60], shown in Figure I-19 (b), presents the relation between the thermal gradient, solidification velocity and the distance from the melt pool. It shows that the temperature gradient is expected to be around 10^7 K/m at the bottom of the melt pool and around 10^6 K/m at the top of the melt pool, while the solidification rate varies between 0 m/s at the bottom of the melt pool to the laser speed at the top of the melt pool. These results are confirmed by other studies [59], [61]. This induced a planar solidification front at the melt pool boundary that quickly destabilized to a cellular morphology in the melt pool interior, see Figure I-19 (c). The cooling rate is of the order of 10^6 to 10^7 °C/s [59], [62], [61], [63].

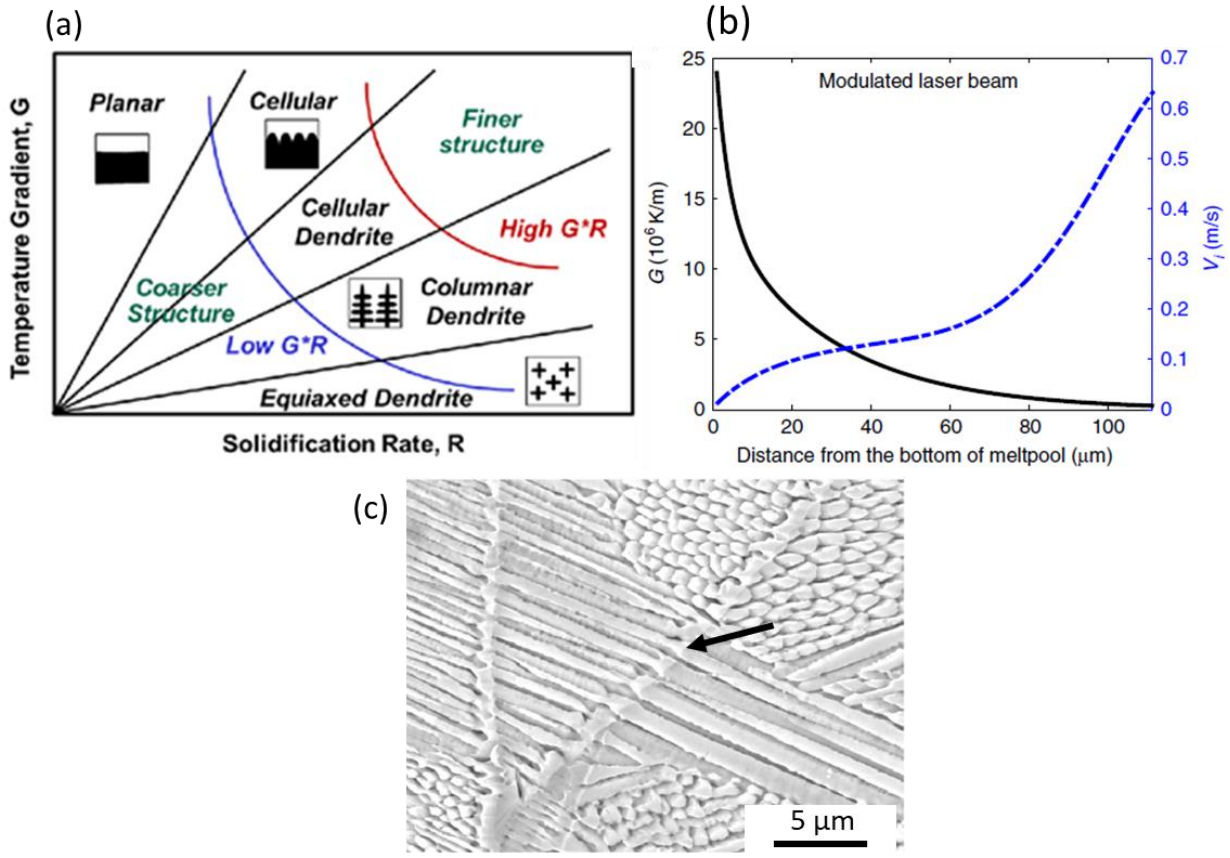

Figure I-19: (a) Schematic dependence of the solidification structure as a function of the thermal gradient and solidification rate. Adapted from [64]. (b) Thermal gradient and solidification velocity simulated as a function of the distance from the melt pool boundary, simulated for a 316L elaborated by LPBF. From [60]. Example of planar growth along the melt pool (indicated by a black arrow), rapidly destabilized in cells. From [60].

A representative illustration of a solidification cell along the longitudinal axis is depicted in Figure I-20(e). These cells adopt a tubular shape, corresponding to the primary dendrite trunk. This primary dendrite trunk is growing along the <100> direction. The size of the primary dendrite trunk depends directly on the cooling rate and so on the processing parameters but is in the range of 100 nm-1000 nm. These

cellular structures, induced by solute partitioning during solidification, exhibit microsegregation in Cr and Mo. This leads to a local variation in the composition of approximately 1-2%wt for each of these elements [49] [50].

In addition to the microsegregation, walls of dislocations are also present in the intercellular regions, as depicted in Figure I-20(e). The density of dislocations inside the walls is estimated to be extremely high, reaching around 10^{15} m^{-2} [65]. This leads to an average dislocation density ranging from 10^{14} m^{-2} to 10^{15} m^{-2} in the as-built state, without any external plastic deformation applied.

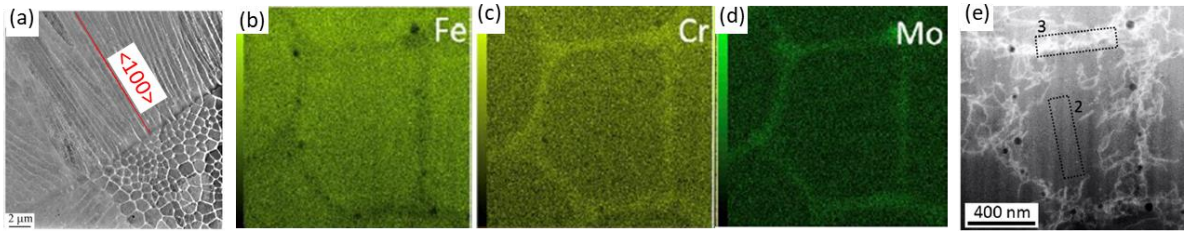

Figure I-20: (a) STEM-HAADF image of the dislocation cell structure showing some of the cells on their longitudinal plane. Adapted from [50]. (b)-(d) STEM- maps EDS of a solidification cell. (e) STEM-HAADF micrograph of the dislocation cell structure. From [12].

Voisin [50] demonstrated that the dislocation walls are misoriented by packets of cells that do not show misorientation higher than 1° between them as illustrated in Figure I-21(a). This result was confirmed in other studies [57], [66]. This suggests that the dislocations can predominantly be classified as statistically stored dislocations (SSD) and not geometrically necessary dislocations (GND). Moreover, it has been showed that a large number of dislocations are dissociated, see Figure I-21(b).

There are two notable distinctions between the dislocation cells in the as-built microstructure and those found in plastically deformed materials: the former are not equiaxed but rather columnar. The origin of this dislocation network remains unclear. Bertsch [67] demonstrated the high dislocation density appears to be a consequence of thermal stresses. Furthermore, the recent work by Gaudez et al. [68] has revealed that the dislocation structure evolves with the rapid reheating cycles induced by the deposition of new layers, suggesting that the dislocation structure is not solely dependent on the solidification conditions.

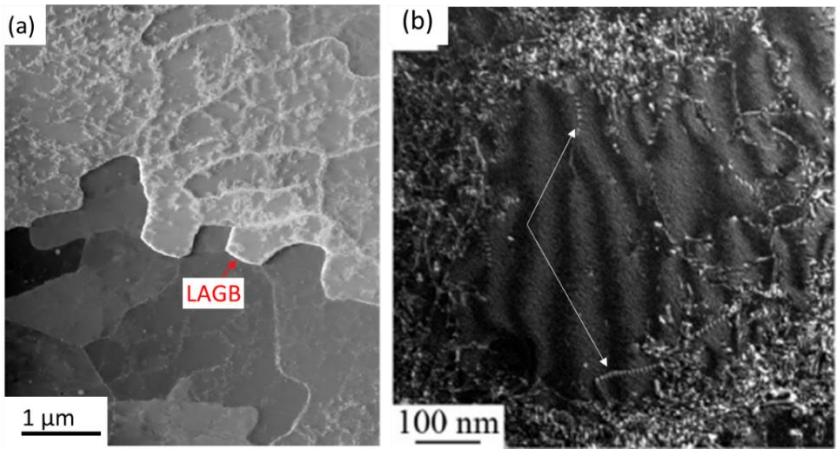

Figure I-21: (a) Dark field image of the cellular structure showing packets of cell misoriented. (b) $\vec{g}/3\,\vec{g}$ weak beam dark field of the cellular structure. Examples of dissociated dislocations are shown in white arrows and can be recognized by the stripe contrast. Both images are adapted from [50].

I.5.1.3 Oxides

The majority of studies focused on the characterization of microstructure of the 316L steel inherited from LPBF reported the presence of second-phase particles within the as-built material. Voisin [50] found that these particles are spherical and relatively small, measuring approximately 15 nm in size, and are primarily located within the cell walls. An illustration of the particle distribution within cell walls is provided in Figure I-22. Other authors determined the distribution of these particles inside cell walls, [12], [69]–[71]. However, some authors found a uniform spatial distribution [72], [73], with no preferentially oxides location. These particles are identified as Mn-Si-rich oxides and are found to be mainly amorphous [51], [53], [69], [73]. Deng demonstrated that these particles primarily originate from oxides present within the powder used during atomization [69]. The mean size of oxides varies between studies, it is 15 nm for Voisin [50] or Yan [74], 36 nm in Chao [53], 42 nm for Riabov [73], and 50 nm for Deng [69]. The area fraction is estimated to be about 0.25% for Deng [69] and 0.37% for Chao [53].

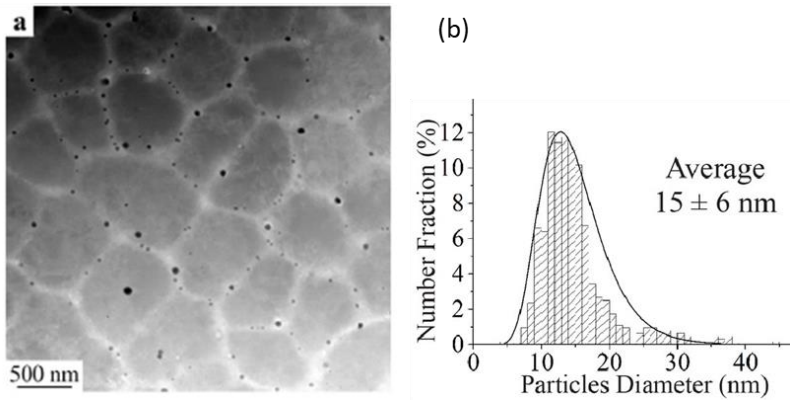

Figure I-22: (a) STEM/HAADF picture of the cellular structure showing the precipitates (black particles) in intercellular regions. (b) Distribution obtained. From [50].

I.5.2 Variability of microstructures: the role of powder composition

In the Ph.D. of Chniouel [9], two powder batches satisfying the 316L RCC-M standard processed in a given LPBF machine using the same parameters led to very different microstructures. The composition of the two steels is given in Table I-4. The IPF-EBSD map and the resulting {110} pole figure are given in Figure I-23. In both steels, no residual ferrite was detected. Both microstructures are different. Steel 1 presents elongated grains along the building direction with a strong {110} fiber texture, while Steel 2 exhibits equiaxed grains with a weaker texture. Both materials show a cellular solidification microstructure of roughly the same size, see Figure I-23(e)-(f), in agreement with the literature. Other studies observed the same difference in microstructure with minor differences in powder composition, see e.g the Ph.D. of Relave [75] or the one of Ziri [63].

Table I-4: Nominal composition given in %wt of the RCC-M standard 316L and the two steels studied in the Ph.D. of Chniouel [9].

	Weight %						Weight ppm	
Element	Fe	Cr	Ni	Mn	Mo	Si	C	N
RCC-M	Bal.	16-19	10-14	<2	2-2.5	<1	<300	-
Steel 1	Bal.	16.85	12.35	1.05	1.98	0.61	150	1230
Steel 2	Bal.	17.7	12.25	0.55	2.17	0.65	130	100

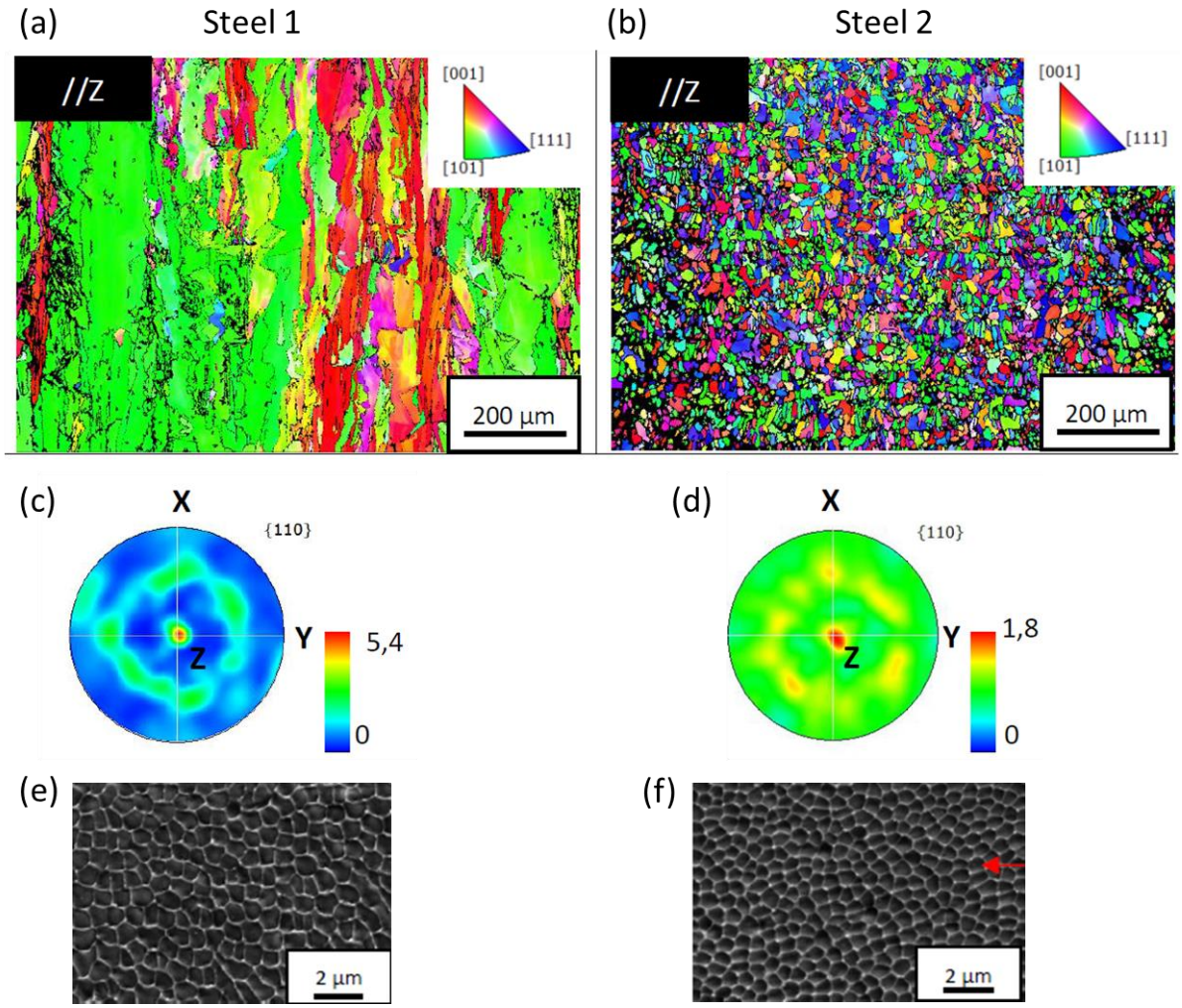

Figure I-23: (a)-(b) IPF-EBSD map of respectively Steel 1 and Steel 2. (c)-(d) {110} Pole figure of respectively Steel 1 and Steel 2. From [9]. (e)-(f) SEM images after chemical etching for respectively Steel 1 and Steel 2.

A strong difference in microstructure with only a slight difference in nominal composition was not necessarily expected. From an industrial point of view, if the microstructure is sensitive to the composition, it can be an issue for the qualification process of components and thus new standards for AM products need to be established. Additionally, a microstructure with a weak texture can be interesting because this is expected to show a reduced anisotropy of the mechanical properties. We will see that this is specifically interesting for the total elongation, where the material can show a bad total

elongation (<45% RCC-M standard) on a specific loading direction because of the texture. Finally, a random texture makes non-destructive testing easier to perform. In the present Ph.D. thesis, the same type of microstructure difference is observed, and we attempted to clarify the reason behind such a change in microstructure.

I.5.3 Effect of post-fabrication heat treatments on the microstructure inherited from LPBF

Different studies investigated different post-fabrication heat treatments. This section summarized the effect of different heat treatments on the microstructure.

I.5.3.1 Effect at the scale of the grain structure

At high temperatures of heat treatment (typically >1050°C), the grain structure can be modified. Recrystallization can be triggered. The temperature at which the recrystallization starts is different between studies and depends on the processing parameters [76] [77]. However, no recrystallization was reported in a temperature below 1000°C [50], [78], [79]. This is a high recrystallization temperature considering the high density of dislocations in the as-built material. As an example, the recrystallization starts at 550°C for a cold rolled 316L [80]. This is supposed to be induced by two mechanisms. First, there is no gradient of deformation in the microstructure, which does not promote the energy required to recrystallize [77]. Second, it seems that oxides are efficiently pinning the grain boundaries [77], [81]. After complete recrystallization, an equiaxed grain size is observed [9], [50], [82] but with a residual texture which is still <110> along the building direction [50] [74].

I.5.3.2 Microsegregation and dislocations walls

Heat treatments can also affect the solidification of cellular structure, in particular microsegregation. Dryepondt does not see microsegregation after a heat treatment at 800°C for 5h [83], Hong [78] after 900°C for 1h and the same conclusion was drawn by Voisin [50] and Roirand [72]. Traces of microsegregation are still partially visible after 1h at 800°C [66] [72]. However, microsegregation does not seem to be strongly affected after 600°C/1h [83] or 650°C/2h [53] [72]. Voisin [50] rationalized these observations by simulating the diffusion of microsegregated elements. The cell size was reported to be equal to 450 nm, which is a commonly observed cell size. Their results are shown in Figure I-24. One can see that diffusion starts at 650°C, but higher temperatures are needed to suppress the microsegregation (typically 850°C/1h).

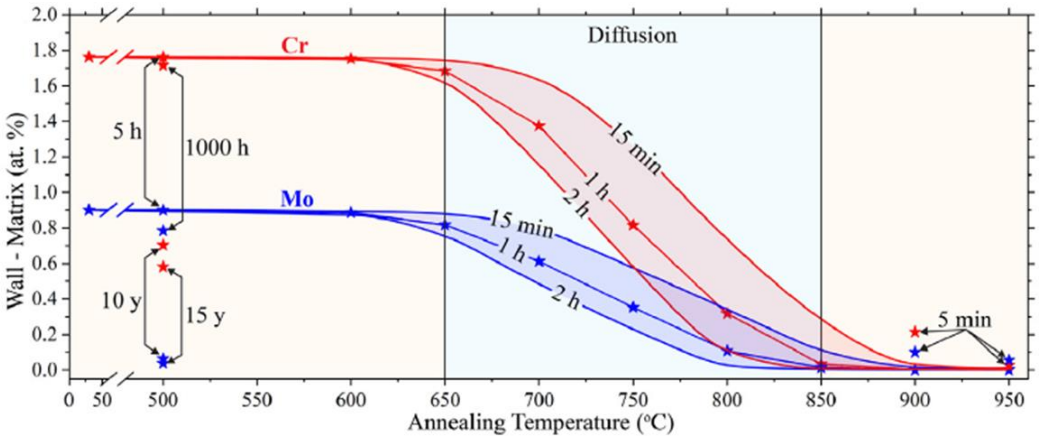

Figure I-24: Estimations of the variations in Cr and Mo content between cell walls and cell interior as a function of annealing temperature for different annealing times. Calculations performed using CALPHAD, assuming a cell size of 450 nm and with initial solute partitioning measured experimentally. From [50].

Another effect of heat treatment on as-built microstructure is the progressive disappearance of dislocation walls. Dislocation walls are still visible after a heat treatment at 600°C for 1h [50] or at 650°C for 2h [72].

Dislocation walls can still be hardly visible after a heat treatment at 800°C for 1h [50] [66] but only traces of dislocation walls are observed after 900°C/2h [72]. Dislocation walls are suppressed after 1050°C/1h [84] and after complete recrystallization after 1200°C/1h [50]. The modification of dislocation walls is associated with a decrease in dislocation density [50], [72].

I.5.3.3 Oxides

Heat treatments can also have an impact on oxides. No significant impact was detected below 650°C (coarsening or change in composition) in [81]. Voisin found similar results after 800°C/1h [50]. Riabov found a coarsening of particles after 900°C/1h with a decrease in the number density of 30% [73]. Deng et al. also reported oxide coarsening after 950°C/2h [81]. Deng found that the area fraction did not change upon heat treatment suggesting that no oxides are forming during the heat treatment [81]. This result was confirmed by Riabov [73]. There is a significant coarsening at a temperature higher than 1000°C, with a particle diameter that is three times larger for a heat treatment at 1100°C for 1h (150 nm) [81]. After recrystallization at high temperature (>1100°C), the majority of the oxides are found at grain boundaries showing that the oxides are efficient to pin the grain boundaries [50], [53], [81].

The chemistry of oxides can also evolve upon heat treatment. After 900°C/1h, Roirand found a transformation of the amorphous oxides in Al_2MnO_4. After 1050°C/1h, Byun found oxides to be Mn-Cr rich oxides [84]. Yan identified these oxides in $MnCr_2O_4$ spinel oxides [74] which are the stable oxides. After 1100°C 1h Deng et al. [81] obtained a microstructure partially recrystallized. They found that the chemistry of oxides depends on the grain where oxides are, with oxides in the form Mn-Si-Al rich oxides in recrystallized grains, and $MnCr_2O_4$ spinel in non-recrystallized grains. As a result, the transformation of oxides at high temperatures depends greatly on the recrystallization.

I.6 Mechanical properties of the 316L processed by LPBF

I.6.1 As-built condition

It has been shown in section I.5 that the microstructure of the 316L inherited from LPBF is different from that obtained after traditional processing routes. Typical mechanical properties of 316L LPBF are shown in Figure I-25. Samples tested with the loading direction perpendicular to the building direction (the horizontal) are harder but less ductile than the samples tested with the loading direction aligned with the building direction [1], [9], [13], [57], [85]. In addition, the horizontal orientation does not necessarily meet the minimum elongation required by the RCC-M standard (indicated by the black line) [12], [56], [66], [70], [82], [86], [87]. However, the yield stress is much higher than the one measured in a rolled and recrystallized material and is well above the minimum yield stress imposed in the RCC-M standard, see the blue dashed line in Figure I-25.

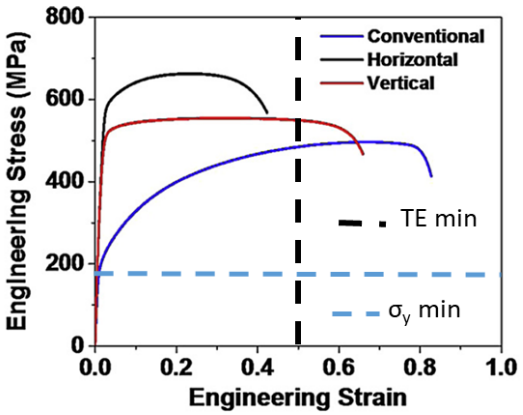

Figure I-25: Typical engineering tensile stress-strain curves of a 316L processed by LPBF for two different orientations: horizontal (in black) and vertical (in red). The blue curve corresponds to a 316L shaped by the traditional rolled and recrystallized heat treatment. The vertical line represents the minimum total elongation required by the RCC-M standard. The horizontal line represents the minimum $Rp_{0.2}$ imposed in the RCC-M standard. Adapted from [13].

I.6.1.1 Main sources of strengthening

In all the studies dedicated to the 316L steel fabricated using LPBF, it has been shown that the yield stress is higher than its wrought counterparts [12], [50], [57], [86], [88], with a yield stress ranging from 430 MPa [84] to 710 MPa [89].

Authors agree that the main reason is the high density of dislocations organized into walls [50], [57], [78], [90]. Two methods were proposed to take them into account. Wang [57] proposed to consider the cell boundaries as effective interfaces and therefore applied the Hall-Petch law using the mean cellular distance instead of the grain size. This was used to estimate the strengthening of the dislocation cellular structure in Wang's work. A strengthening contribution of around 330 MPa was reported, which corresponds to half the yield stress. This approach was used in [78], [91]. This approach, which has the advantage of being simple, has been questioned in the recent work of Dépinoy [49], which did not evidence a correlation between the cell size and the yield stress. Moreover, Bean [92] showed that the

slip lines crossed the cells but were stopped at the grain boundaries, suggesting that cells act more as forest dislocation than as an impenetrable interface such as a grain boundary. Some other work attempted to consider dislocations observed in the intercellular regions as forest dislocations. This approach was proposed by Shamsujjoha [88], who measured the dislocation density using XRD. Following this approach, the forest dislocations are found to account for 450 MPa, which corresponds to 75% of the yield stress. However, measuring the dislocation density is a challenging task in AM samples, because dislocation density can be locally very high (10^{15} m^{-2}), which makes it difficult to measure by TEM, and different sources can induce a pic broadening other than dislocations in XRD (chemical segregations, texture, oxides) which makes XRD line analysis difficult as well. In both cases, the grain size is not explicitly taken into account.

In some studies, authors estimated the strengthening induced by the nanoscale oxides and found that it was negligible [57], [69], while Voisin [50] and Deng [69] evaluated it using the Orowan law and found that it can contribute to respectively about 150 MPa and 100 MPa (nearly 20% of the yield stress). It is not clear if the reason for such discrepancies between different publications results from differences in chemical composition or from the method employed to estimate the strengthening contribution of oxides.

Chen et al [93] showed that the yield stress was higher in compression than in tension by approximately 60 MPa in the as-built conditions. However, after a stress-relief treatment at 500°C for 4h, the anisotropy was found to vanish. Therefore, based on in situ XRD tensile tests, they concluded that micron scale residual stresses were at the origin of such differences in yield stress between tension and compression in the as-built conditions.

In the literature, there is a lack of estimations for the global contributions to yield stress. For example, the contribution of the solid solution is often based on an average value of 316L and not on the composition of the steel studied, even though there may be significant differences in the composition of the 316L steels investigated in the literature. Similarly, hardening induced by grain size is not always taken into account without justification.

I.6.1.2 Microstructural features contributing to the strain hardening

The uniform elongation of the 316L processed by LPBF is found to vary a lot between studies from 15% to 80% [89], even for materials with low porosity (density >99%). This range of uniform elongation frames the one from a wrought product (~45%-70% [7], [17]). Reasons for this variability can be multiple: texture, grain size, solidification cell size, composition... It is known that uniform elongation and strain hardening are closely linked by the Considere criterion. The potential role of dislocation walls and texture on the work hardening, as highlighted in the literature, will be discussed in this section.

A. The role of the dislocation walls

It has been claimed that the 316L processed by LPBF showed superior strength and ductility than its wrought counterpart [57], [58], [94], [95], [96]. Wang and Liu [57], [94] attributed this specific behavior to the cellular structure that would induce a hierarchical strain hardening by the interaction between twin and dislocation cells. However, this assertion was not rationalized with physically based arguments or models.

In order to understand the behavior of the cellular structure during plastic deformation, the deformation of the material was deeply investigated [57], [66], [94], [95]. It has been shown that the dislocations arranged in walls were still visible after plastic deformation [57], [66], up to 30% [41]. This suggests that this arrangement of dislocations is relatively stable with plastic deformation. Riabov [66] shows that microsegregation is not the main reason for the stability of cellular dislocation structure upon deformation. According to Voisin [50], a reason for the stability of this cellular structure is the pinning of dislocations by the numerous oxides located in the cell walls. He showed by dislocation dynamic simulations that a cellular structure without oxides will show no arrangement during plastic straining, while this was the case for a cellular structure with oxides. Voisin [98] demonstrated that even with the high dislocation density in the cell walls, there is still a multiplication of dislocations and that new dislocations are trapped in the cell walls. However, at large plastic strains, He et al. [97] showed that new dislocation walls can be created within the solidification cells.

However, there is a lack of physical argument or quantification for the role of this specific arrangement of dislocations in cells on the strain-hardening.

B. The role of texture

It was shown that texture plays an important role in the plasticity of 316L processed by LPBF. To study the impact of texture, Wang et al. [89] built strongly textured samples of 316L by LPBF and compared their mechanical properties as a function of the loading direction. A summary of this work is shown in Figure I-26. He showed that a strong texture has a huge impact on the ductility, from 30% to 100% in elongation to failure. In Figure I-26, one can see that the sample with the <110> direction oriented close to the loading direction shows a high elongation to failure (nearly 100%), while the <100> has a limited elongation to failure (about 35%). Recently, these curves have been rationalized using crystal plasticity calculations [99]. They concluded that the difference was not solely induced by variations of the Taylor factor, but that specific interactions between the different slip systems activated must be taken into account. The very low strain hardening in the <110> samples was induced by the low interactions between the active slip systems, while there is a strong interaction between slip systems for the <100> sample. However, at larger plastic strains, the <100> samples show lower strain hardening compared to the <111> or <110> sample. This is believed to be the reason for the difference in twinning activity, the <100> samples showed no twin after fracture, while the <111> and <110> samples show a large twinning activity. It is also believed that the continuous rotation of the grains in the <110> samples plays a key role into the large elongation measured experimentally.

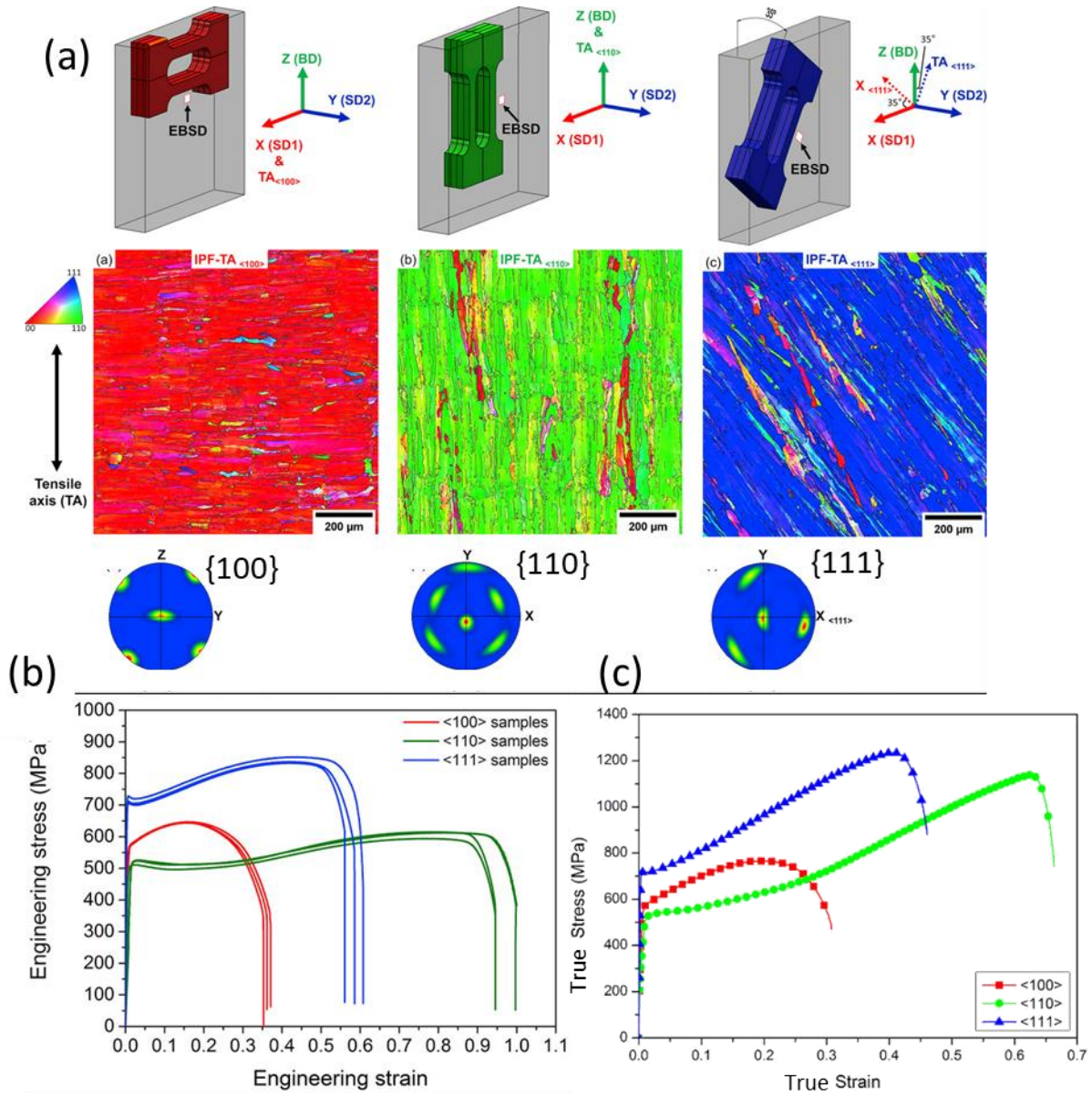

Figure I-26: (a) Schematic of the tensile specimens and the different orientations investigated along with their resulting IPF map and pole figure. (b) Engineering stress-strain tensile curve of the different orientations. Adapted from [89]. (c) True stress-strain tensile curves of the different orientations. From [99].

I.6.2 Effect of post-fabrication heat treatments on the mechanical properties

It has been shown that heat treatments can strongly impact the microstructure of the 316 produced by LPBF. Those modifications of the microstructure are expected to alter the resulting mechanical response. The yield stress is found to decrease [50], [53], [66], [78], [83], [84], [96], the higher the temperature of heat treatment from 600°C to 1200°C, the lower the yield stress. After 600°C/6h, Salman reported a decrease in yield stress of 110 MPa (from 550 MPa in the as-built conditions to 440 MPa MPa after heat treatment), and Byun reported a decrease of 50 MPa after 650°C/1h. This is thought to be induced by the decrease in dislocation density with heat treatment. After a total

recrystallization (>1100°C 1h), the yield stress is found to be 174 MPa [96] to 300 MPa [50], in the same range as the one found in the rolled and recrystallized 316L alloy.

It is found that the total elongation increases with heat treatment, the higher temperature of heat treatment, the higher the total elongation [50], [53], [66], [78], [83], [84], [96]. The increase in total elongation with heat treatment is supposed to be induced by the decrease in dislocation density, which will increase the work hardening capacity and delay strain localization [72]. The only discrepancy in this result is when the heat treatment is performed at temperatures <700°C. In this case, the total elongation can be reduced. This is observed in the study of Voisin after 600°C/1h, and in the study of Hong after 500°C/1h, while other studies found no significant modification of the total elongation [83], [84]. This is supposed to be induced by the decrease in residual stresses [50]. A summary of the typical evolution of mechanical properties with heat treatment is shown in Figure I-27.

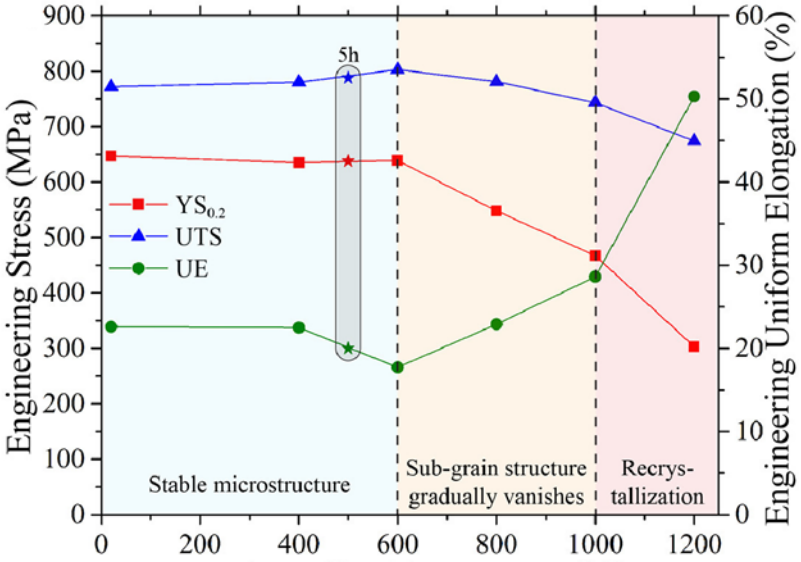

Figure I-27: Summary of the evolution of tensile properties with 1h heat treatment. From [50].

I.7 Conclusion

As a result of rapid and directional solidification, the microstructure of 316L produced by LPBF shows some specificities that are not found in wrought products. The main microstructure features inherited from LPBF can be summarized as follows:

- a strong texture (generally fibrous <110>//BD);
- columnar grains elongated along the building direction (width~50 µm);
- microsegregation inherited from solute partitioning during solidification, especially in Cr and Mo;
- a high density of dislocations (~10^{14}-10^{15} m^{-2}) organized in cells and superimposed with microsegregation;
- the presence of Si, Mn rich oxides which are preferentially located in the intercellular spacing.

However, the literature review has shown that there are variations of the as-built microstructure with the nominal composition. Slight variations in nominal composition sometimes lead to different microstructure, especially at the grain scale and the main causes for such a variability are not properly understood yet. Regarding the mechanical properties, the 316L produced by LPBF exhibits:

- a high yield stress
- a significant anisotropy in strain hardening, which induces high variation in total elongation depending on the loading direction.

The microstructure and the mechanical properties can be efficiently altered using post-fabrication heat treatment, with a decrease in the yield stress and an increase in the total elongation. It is admitted that the reason for the higher yield stress of the 316L LPBF in comparison to its wrought counterpart is the high density of dislocations organized into walls. However, the strengthening mechanisms induced by such dislocations are still debated (Hall-Petch or forest dislocations). The presence of fine oxide particles of the order of several dozens of nanometers is also likely to contribute to increasing the yield strength while decreasing the ductility. The significance of each individual contribution remains is still under debate.

It is widely recognized that material texture has a major influence on plasticity, with a well-established understanding of the mechanisms involved. However, the specific impact of the dislocation arrangement, the presence of oxides, and grain size on the strain hardening remains ambiguous. Does the arrangement of dislocations in walls in the as-built microstructure affect the elongation or contribute to enhancing the strain hardening? If so, what are the underlying mechanisms? Additionally, does this organization of the dislocations into walls affect the twinning activity? These questions warrant further investigations and clarifications to get a detailed understanding of the mechanical properties of the 316 ASS fabricated by LPBF.

Chapter II. Materials and methods

II.1 Powder batches

In this thesis, two powder batches of 316L having slight differences in composition have been used. The composition of the two powder batches, i.e. before fabricating the part, is given in Table II-1. These compositions are given as provided on the datasheets from the suppliers. The powder batch 1 was supplied by SLM Solution, while the powder batch 2 from Praxair. The former was atomized using nitrogen, while the latter was with argon. The difference in the gas used for the atomization atmosphere likely explains the difference in nitrogen content between the two powder batches. Size information is also given in Table II-1. These two powder batches have been selected following the Ph.D. thesis of Chniouel [9], where variability in microstructure after processing has been reported between the two powders. Before laser processing, powders were sieved using a 50 µm-sieve and heated up to 60°C to remove humidity. Recycled powders have been used but they were mixed with new powders before being loaded into the LPBF machine.

Table II-1: Compositions and size information given by the suppliers for the two compositions.

	Weight %						**Weight ppm**					**Size information (µm)**		
	Fe	Cr	Ni	Mn	Mo	Si	C	N	O	S	P	D10	D50	D90
Powder batch 1	Bal.	17.9	12.7	0.68	2.36	0.68	200	1000	300	50	80	19	31	53
Powder batch 2	Bal.	17.0	12.7	1.29	2.48	0.59	50	100	300	50	50	20	31	42

II.2 Processing

II.2.1 Laser powder bed fusion

Fabrication has been done by partners in CEA Saclay, especially Edouard De Sonis and Olivier Hercher. Both powders have been used to fabricate 56 × 56 × 56 mm^3 cube samples using an SLM Solutions 280HL LPBF machine. The samples were built under an argon atmosphere using a laser power of 200 W, a laser speed of 800 mm/s, a hatch distance of 120 µm, and a layer thickness of 30 µm. A raster scanning strategy with 7-mm-wide strips and a 67° rotation between layers was used. The last layer was melt twice. A single batch of powder was used for each fabrication. A scheme for the scanning strategy is shown in Figure II-1 (a) and (b). The coordinate system XYZ is relative to the coordinate system of the cube. The X axis of Steel 1 is aligned with the argon flux, while the argon flux is at 45° of the X axis of Steel 2. Five cubes were manufactured in one fabrication, and all the analyzed cubes come from the same fabrication. A picture of the cubes positioned on the building substrate along with the coordinates system used is shown in Figure II-1 (c).

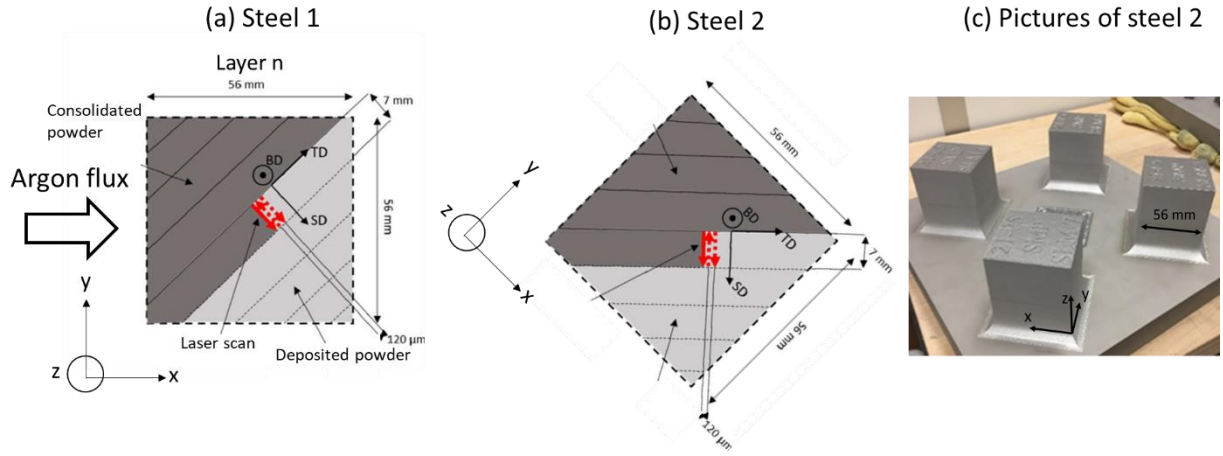

Figure II-1: (a)-(b) Schematic representation of the cube samples fabricated by LPBF for respectively Steel 1 and Steel 2. (c) Picture of the fabricated samples made of Steel 2.

It must be noted that, to avoid an alignment of the laser scanning direction with the argon flux, the laser was not allowed to scan at less than + or – 33° of the argon flow direction. A schematic of the limitation window parameter is shown in Figure II-2. This strategy is common when fabricating parts by LPBF, although it is rarely mentioned in reports. This strategy was implemented to prevent undesirable interactions between the laser and the argon flux that are known to cause defects [1]. When the scanning direction would be in this limitation window, the scanning angle is incremented by 67°, to avoid the scanning in this window. The gas flux helps to remove smoke (vaporization of alloying elements) and prevents spatters from being redeposited onto the powder bed during localized melting. The optimal angle for smoke removal was determined to be 90° (from SLM solution). Inadequate smoke removal can lead to the formation of porosity within the material [1]. Nevertheless, adopting a scan strategy with only one scanning direction results in a pronounced anisotropy. It also increases the probability of leaving pores in the samples. An effective approach to decrease the epitaxial growth involves the use of a scan angle of 67°. Consequently, the limitation window parameter is a compromise between these considerations.

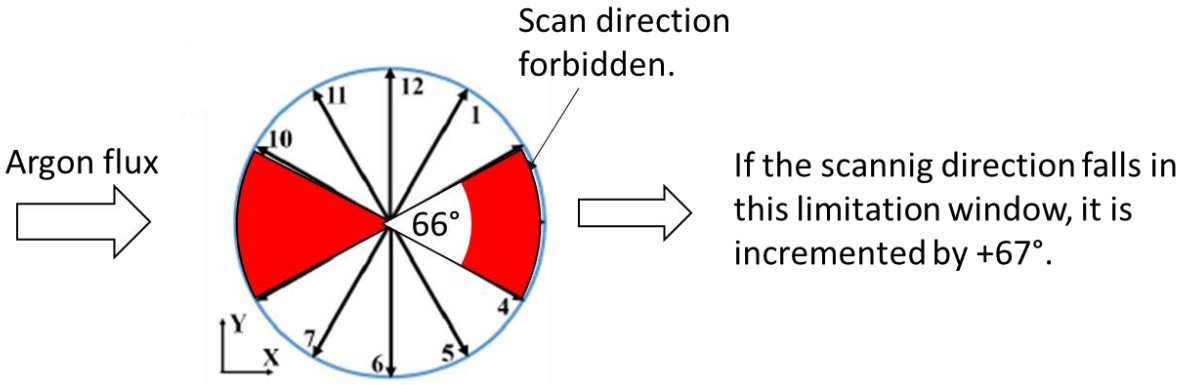

Figure II-2: Schematic of the limitation window parameter for the scanning direction. Adapted from [1].

II.2.2 Composition after processing

After being fabricated, part compositions have been measured by inductively coupled plasma atomic emission spectroscopy (ICP-AES) for major and minor elements and by combustion analysis for trace elements (O, N, C…). The composition after fabrication is given Table II-2. Compared with the powder composition (i.e. before processing, see Table II-1), there is no significant difference, except that the oxygen content varies between the two steels, which is higher than the one measured by the supplier (300 ppm vs. 700 ppm). This O enrichment in the samples was attributed to the use of recycled powders. Both compositions are in line with the 316L RCC-M standard, except the Mo content in Steel 2.

Table II-2: Chemical compositions for the two fabricated steels.

	Weight %						Weight ppm							
Element	Fe	Cr	Ni	Mn	Mo	Si	O	N	C	P	S	Cu	Ti	Al
Steel 1	Bal.	17.6	12.4	0.90	2.36	0.68	340	900	210	160	20	430	50	10
Steel 2	Bal.	16.9	12.2	1.21	2.69	0.50	710	130	60	100	20	80	310	40
RCC-M	Bal.	16-19	10-14	<2	2-2.5	<1	-	-	<300	<300	<150	<1000	-	-

II.3 Heat treatments

Three heat treatments have been chosen and applied to each steel. They were carried out in a muffle furnace under air, and the samples were hot-baked. The samples for heat treatment were prepared as cubes of 10mm x 56 mm x 56 mm, taken from the manufactured cubes.

The first heat treatment is a stress relief heat treatment at 600°C for 1h followed by air cooling. The role of this heat treatment is to reduce the residual stresses coming from fabrication. It is a common practice, in welding and additive manufacturing to reduce these stresses as they can negatively impact the mechanical properties.

The second heat treatment consists of a first stress relief treatment, followed by homogenization at 900°C for 1h, followed by water quenching. The role of this heat treatment is to make the chemical segregations disappear.

The third heat treatment consists of a first stress relief treatment, then a recrystallization heat treatment at 1200°C followed by water quenching. Steel 1 will be exposed for 1h, while Steel 2 will be exposed for 2h. The role of this heat treatment is to recrystallize the material, inducing the formation of new equiaxed grains free from dislocations. The time of heat treatment has been designed to obtain the recrystallization. The heat treatments are schematized in Figure II-3.

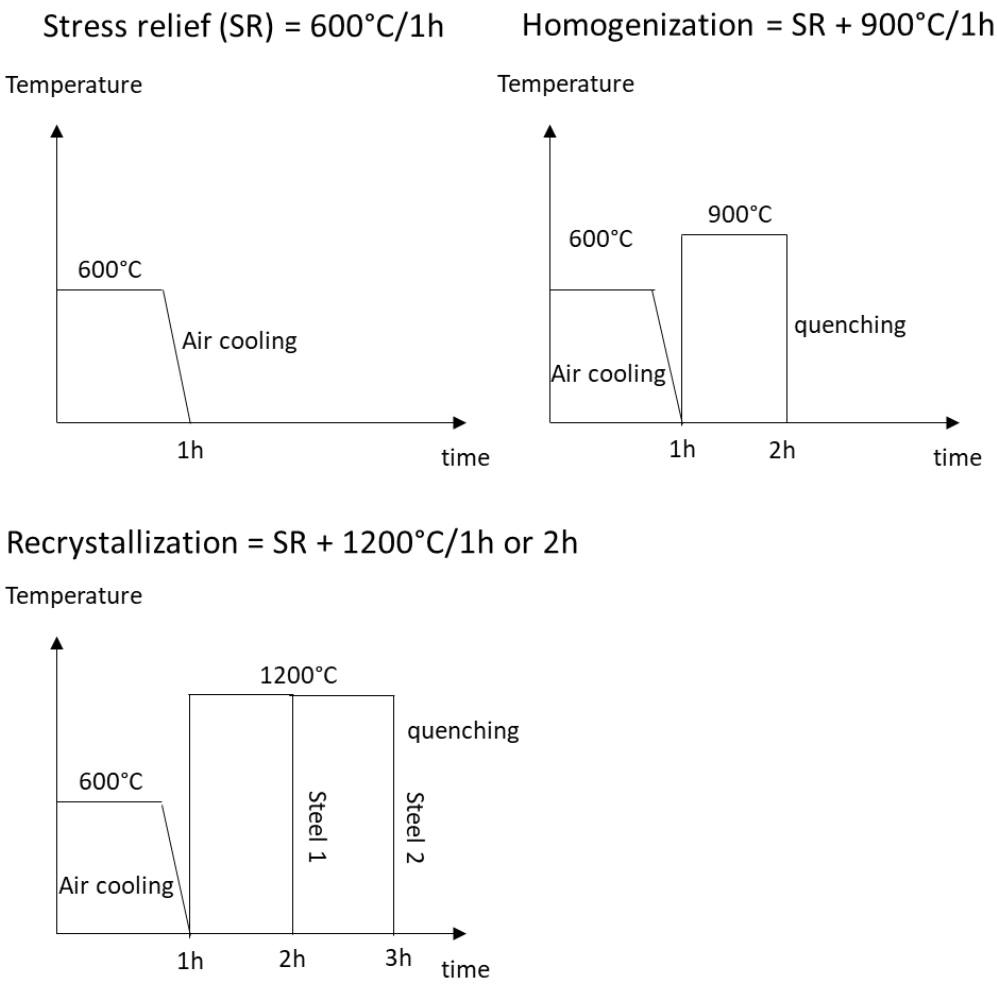

Figure II-3: Schematic temperature evolution during the heat treatments.

II.4 Microstructural characterization

II.4.1 Samples preparation

In order to image the microstructure, samples were hot mounted in an epoxy resin and mechanically ground using SiC abrasive papers followed by a polishing step with a 3µm-diamond suspension. Finally, a polishing using a 0.04 µm colloidal silica solution diluted in water (1:24 in proportion) has been carried out for 5 min. To remove the residual colloidal silica, samples were polished under a water flow for 5 min.

For microstructure observation by optical microscopy or in the scanning electron microscope (SEM), the samples were then etched using the V2a etchant (100 mL water, 10 mL HNO_3, 100 mL HCl) for 5 min at room temperature. For some observations, samples were electrochemically etched in a 10% acid oxalic solution diluted with water under 5 V at room temperature for 2 min. To analyze porosity, samples were not etched.

For Transmission Electronic Microscope (TEM) observations, samples were mechanically polished down to ~100 µm thickness. The finishing surface of both faces were obtained with an abrasive paper of mesh size of 3 µm. Then samples were punched to obtain disk of 3 mm in diameter. Finally, samples were electro polished using a Tenupol 5 from Struers using a solution consisting of 8 % perchloric acid 92 % methanol at -30 °C and 15 V.

II.4.2 Optical microscopy

Observations of the melt pool structure were carried out with an opto-numerical Olympus DSX500 microscope. An optical micrograph of Steel 2 prior to etching is shown in Figure II-4 (a). An example of the microstructure of Steel 1 after chemical etching with the V2a solution is shown in Figure II-4 (b). One can see the melt pool boundaries after chemical etching. In both steels, no pores larger than 10 µm were detected, and the density of samples was estimated at 99.4%.

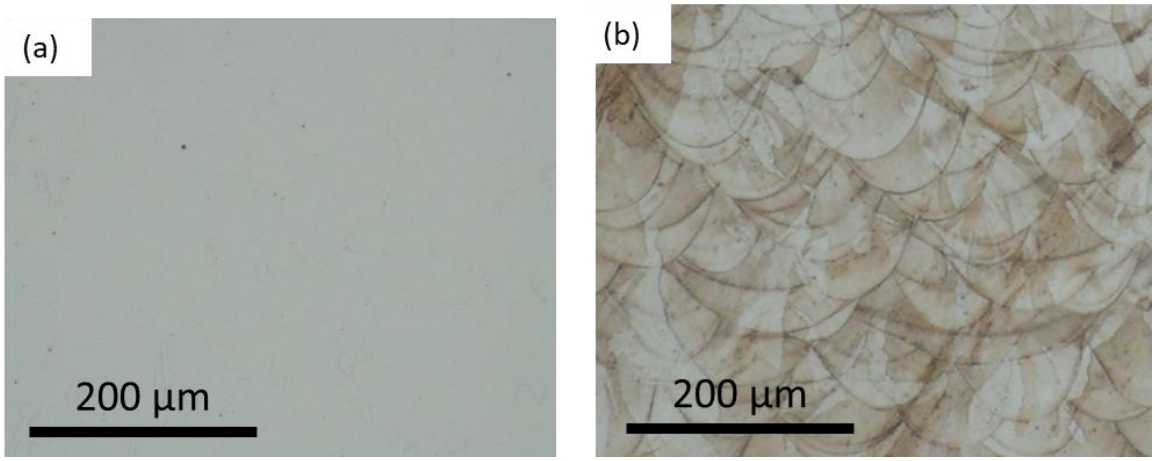

Figure II-4: Optical images. (a) Steel 2 prior to etching. (b) Steel 1 after chemical etching with the V2a solution.

II.4.3 Imaging in the scanning electron microscope (SEM)

A Zeiss Gemini SEM 500 FEG was used to characterize the microstructure (grains, solidification structure, oxides). The solidification cell size of the material was estimated by taking 3 images of different areas with the Inlens detector on a chemically etched sample. The cell size was then estimated for each picture by the manual intercept method (five vertical and horizontal lines). Then, the image that gives the lower cell size is retained, the other images are discarded because they are considered to contain misaligned cells.

Scanning Electron Microscopy (SEM) was employed as a characterization tool to assess the average distance between oxide particles, as well as their mean diameter. Observations were carried out with the Backscattered Electron Detector (BSD), which provides an image contrast influenced by the difference in electron density. The objective of such measurements was to estimate the contribution of oxides to the yield strength using the Orowan equation. This approach has the advantage of providing a direct value for the mean distance between particles, which is not the case for other methods which estimates this value from volume fraction and mean diameter, which often assumes a uniform

distribution of particles. The Orowan equation suggests that the distance between particles is related to the mean distance between particles within the plane of dislocations. To obtain the most accurate measurements of this mean distance from a slip plane, it is important to approach the measurement from the surface. Images were captured with an energy of 5 KeV and with a pixel size of 2.3 nm. Figure II-5 gives an illustrative example of a micrograph obtained from Steel 2 sample. Observations reveal that particles of approximately 10 nm in size are discernible. 8 images were acquired from various regions. Subsequently, the image processing and analysis procedure was carried out using the Fiji software [100]. First, background subtraction was performed using a rolling ball algorithm, with a radius of 50 pixels. This was followed by automated thresholding and particle closing operations. Finally, the dimensions of these particles were determined, along with their average separation distance, utilizing the Delaunay triangulation method.

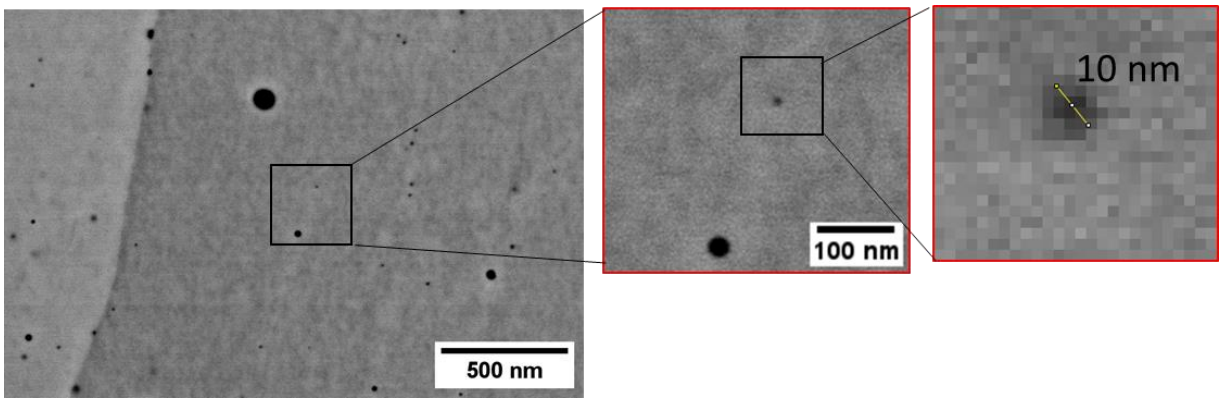

Figure II-5: An example of a SEM-BSE image of Steel 2 used to estimate mean distance between oxide particles.

II.4.4 Orientation mapping with electron backscattered diffraction (EBSD)

SEM was equipped with an Electron Back Scattered Diffraction (EBSD) detector. EBSD was performed to study the crystallographic orientation of the FCC-Fe matrix with an accelerating voltage of 20 KeV. Data acquisition was done using the APEX EBSD software. The data underwent processing using the OIM analysis software. The data cleaning procedure involved grain dilatation, wherein a grain was defined by a misorientation exceeding 5° and comprising a minimum size of 4 pixels. Grains failing to meet these criteria were excluded for further consideration, rendering them in black within the resulting plots.

To assess grain size and orientation distribution (texture), large EBSD maps were acquired, covering different areas: 2x2 mm² for the as-built Steel 1, 1.5x1.5 mm² for the as-built Steel 2, and 2.3x2.3 mm² for both steels after recrystallization. Each cartographic dataset used for data extraction contained more than 8000 individual grains. The grain size was determined using the intercept method using a threshold angle set to 15°. It is worth noting that due to the elongation of grains along the building direction, the intercept length in the building direction may not be the same as in the horizontal direction. To obtain a single representative grain size value, the grain size was defined as the average intercept length between the x, y, and z directions, assuming that the size is consistent in the x and y directions. The equivalent diameter of grain gives the same number.

The coincidence site lattice boundaries were also detected from the EBSD maps. In particular, the Σ3 (twin boundaries) and Σ9 boundaries were detected, using the Brandon criterion [101]. In this criterion, the tolerance angle is defined by $15/\sqrt{\Sigma i}$, with i the degree of coincidence of the boundary. It is the most common definition used in grain boundary engineering studies [102]. Moreover, it corresponds to only 1.48% of grain boundaries resulting from a random process (calculated using equation (3) in [103]). While these boundaries were identified as specific boundaries, they were still considered as normal boundaries for grain size calculation.

The orientation distribution (texture) was computed with the ATEX-software [104]. Orientation of grains were averaged in OIM with a threshold of 5° and extracted with their surface. Triclinic sample symmetry was assumed. The calculation was done with boxing + C coefficient, the development even and odd were respectively at 22 and 21, and Gaussian width was set to 5°.

HR-EBSD has been performed in the framework of a collaboration with a research group of the LEM3 laboratory in Metz (Clement Ernould). A FEG-SEM Jeol F100 equipped with an Oxford Symmetry camera was used to acquire the EBSD-HR maps. The sample to detector distance was 14 mm and accelerating voltage, current and aperture size were at 15 kV, 6 nA and 50 µm, respectively. Kikuchi patterns of resolution 1244 × 1024 pixels (~19.3 µm/pixel) were recorded with an exposure time of 20 ms. The step size was 50 nm.

II.4.5 Transmission electron microscope (TEM)

Observations in the TEM were conducted on a JEOL 2100, equipped with a FEG-tip and operating at 200 kV. Most images were acquired in bright-field mode, in Scanning Transmission Electron Microscopy (STEM). Mapping of the chemistry was performed by energy-Dispersive X-ray Spectroscopy (EDS). EDS maps were treated in order to decrease the impact of the local thickness. To do this, the intensity of each point for each element was normalized by the signal which came from the total spectrum.

To characterize orientations at the 1-100nm scale, Automated Crystallography Orientation Mapping (ACOM) was employed. ACOM was conducted using the hardware and software toolset ASTAR™ from Nanomegas, enabling the retrieval of local phase and orientation information. While a more detailed description of this technique can be found in reference [105], a brief overview is provided below.

The underlying philosophy of ACOM is analogous to that of EBSD, but it is adapted for TEM. An area of interest is scanned and the local diffraction patterns are recorded. Then the recorded diffraction patterns are compared to theoretical diffraction patterns of the candidate phases and orientations via a template matching approach. While EBSD relies on Kikuchi lines for orientation or phase determination, ACOM utilizes Bragg spots. To reduce the influence of dynamical diffraction conditions on the diffraction pattern, which are not accounted for in the template, precession is applied. Precession consists in rotating the beam above the sample, and de-rotating it below, to better approach kinematic diffraction conditions, which are those simulated by the templates.

The primary objective of ACOM in this study was to achieve the highest resolution for the orientation of the FCC matrix. To accomplish this, ACOM requires Bragg spots that are positioned farthest away from the transmitted beam, as their positions are more sensitive to orientation variations. To achieve this

goal, the camera length was set to its minimum available distance: 8 cm. The precession angle was set at 1.2° with a frequency of 100 fps. Figure II-6 illustrates the ACOM method, showing diffraction patterns obtained from observed 316L at two camera lengths, 15 and 8 cm respectively, for same the zone axis (<110>). The advantage of the 8 cm camera length becomes obvious: it enables to recording more Bragg diffraction spots.

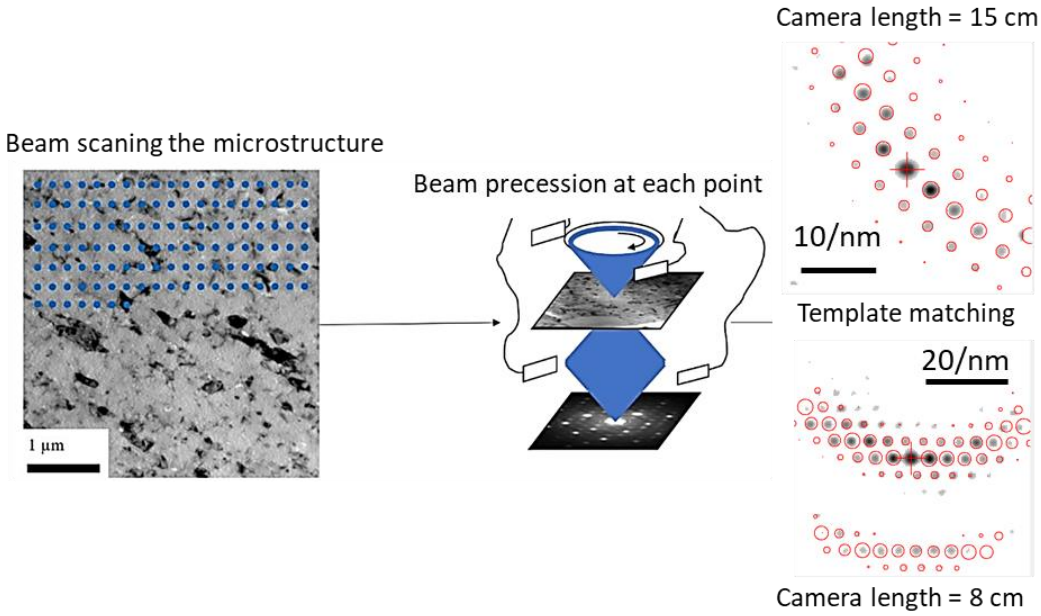

Figure II-6: Illustration of the ACOM method. Both diffraction patterns collected at two different camera lengths are shown close to a <110> zone axis.

II.5 Mechanical characterization

II.5.1 Hardness

Micro hardness was performed using a Tukon 1102 hardness machine with a load of 1 Kg, which gives an indent size around 90 µm, which is around the size of a melt pool, see Figure II-4. It was checked that hardness was homogeneous in the cube and independent on the height or the observation plane. To do so, 8 indents were performed at around 2 mm from the bottom and from the top of the cubes, and others were done in the middle of the cube in a plane perpendicular to the build direction (xy plane). Results are summarized in Figure II-7. One can see that no difference in hardness could be detected between the top and the bottom of the cube samples for the two steels. Steel 1 (HV1 = 240) was harder than Steel 2 (HV1 = 205). This difference will be commented in more detail in the chapter 4.

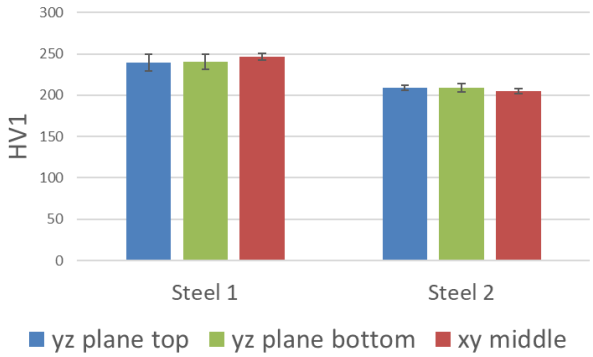

Figure II-7: Hardness measurements as a function of the plane of observation and position in the cube samples.

II.5.2 Tensile tests

II.5.2.1 Experimental

To characterize the yield strength and strain hardening behavior, tensile tests were conducted. Dog bone shaped specimens were machined using electro discharge machining. The geometry is shown in Figure II-8 (a). A first type of specimen was extracted at the top and at the bottom of cubes so as to put the loading direction perpendicular to the build direction. These samples will be later called horizontal). A second type of specimen was prepared with their loading direction parallel to the build direction. These specimens will be called vertical). A schematic illustrating the geometry of the specimens with regard to the cube axis is shown in Figure II-8 (b). Prior to tensile testing, the thickness and width of the specimens were measured using a digital caliper, with a precision of 10 µm. This induces an uncertainty of 2% on the stress.

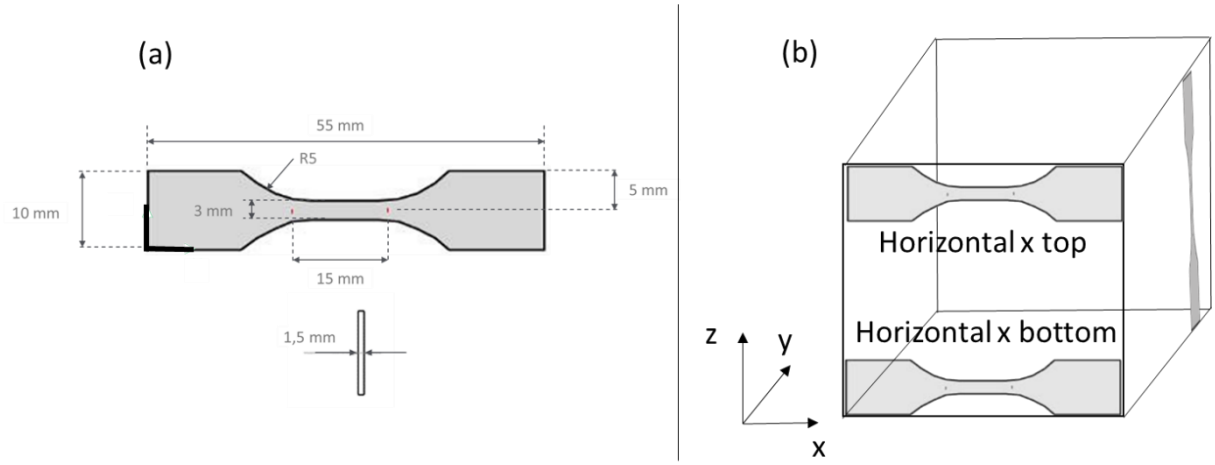

Figure II-8 : (a) Dimensions of the tensile specimens. (b) Schematic illustrating how the tensile specimens were extracted from the cube samples.

The tensile tests were conducted on a MTS4M testing machine equipped with a 20kN load cell. The strain rate was set constant to $\dot{\varepsilon}= 10^{-3}$ s^{-1}.The strain was measured using Digital Image Correlation (DIC). For this, 6 megapixel cameras with a 50 mm lens were used. The GOM Correlate software was employed to acquire and analyze the data. To track features the sample, a speckle pattern was painted on the specimen surface.

This was done by first painting the specimens in white and then using an IWATA Custom Micron series airbrush to project fine black India ink droplets onto them. This speckle makes easier the tracking and analysis of the local deformations during mechanical testing.

II.5.2.2 Data treatment

A constant virtual extensometer with an initial length of 15 mm was created at the surface of the gauge length of the tensile specimens. The deformation field was computed with a facet size of 15 pixels, with a pixel size of 45 µm. Images recorded during the test and showing the deformation field are shown in Figure II-9 (a-b). Before necking, the deformation field is uniform (Figure II-9 (a)) while it becomes heterogeneous due to strain localization after necking (Figure II-9 (b)).

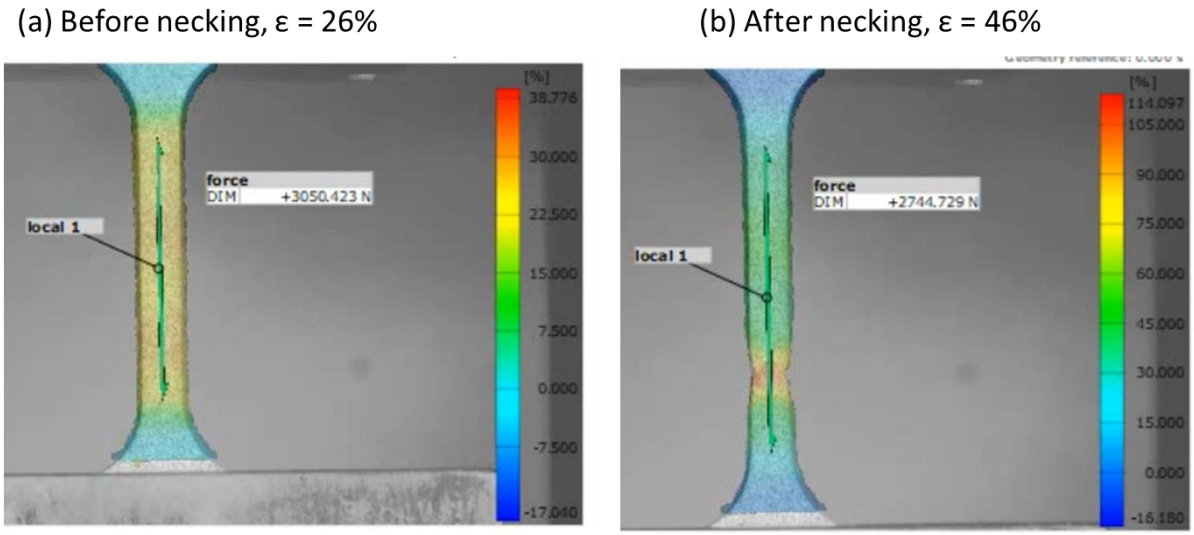

Figure II-9: Image showing the deformation field in Steel 1 (horizontal orientation). (a) Before necking, (b) after necking.

Three tensile tests were performed in each condition. The yield stress is taken at 0.2% of plastic deformation. The uncertainty on stress will be taken at ± 2% (uncertainty which comes from the measurement of the section). The total elongation is taken at the failure of the sample, and the uniform elongation is taken when the force is at the maximum. The uncertainty of elongation is determined by taking the minimum and maximum values of the three tensile tests. Figure II-10 shows the engineering stress-strain curve of the as built material for the two steels loaded perpendicularly to the build direction (horizontal orientation). One can see noise in the engineering stress-strain curve. This was attributed to the load cell sensibility. With a sensibility taken as $F_{max}/5$, curves are noisy, but noise disappears with a calibration taken as $F_{max}/2$. The yield stress of Steel 1 is 600 ± 12 MPa at the bottom of the cube sample, while and 601 ± 12 MPa at the top of the cube sample. The total elongation was measured to be about 0.53 ± 0.02 for specimens extracted at the bottom of the cube sample, while it was found to be about 0.50 ± 0.05 for specimens extracted at the top of the cube sample. For Steel 2, the yield stress at the bottom is equal to 474 ± 10 MPa and 485 ± 10 MPa at the top. The total elongation is about 0.57 ± 0.01 at the bottom and at 0.57 ± 0.02 at the top. Based on those values, no significant difference between specimens extracted at the top and bottom of the cube samples was found in both steels. As a result, in the next chapters, no difference will be made between specimens extracted at the top and bottom of the cube sample, and, for the sake of clarity, only one tensile response for each condition will be plotted.

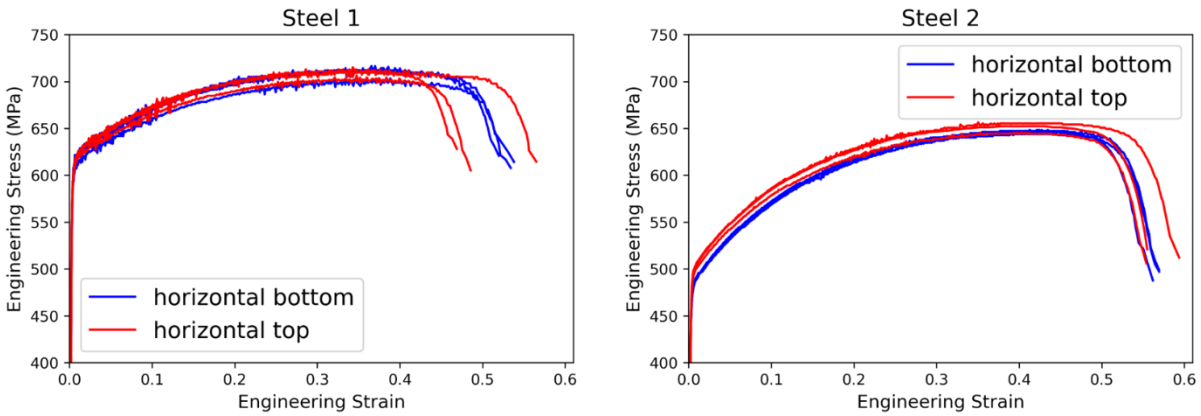

Figure II-10: Engineering stress strain curves for (a) Steel 1 and (b) Steel 2 respectively for samples extracted at the bottom and top of the cube samples (horizontal orientation).

II.6 Measurement of the twin fraction in plastically deformed samples

Electron Back Scattered Diffraction (EBSD) analysis was employed to quantify the twin fraction within deformed samples. This twin fraction is defined as the area of the portion of grains in which the orientation has been changed induced by twinning on the area of all grains analyzed. This is different from twin boundaries fraction, defined as the length of twin boundaries over the length of total boundaries.

To assess the twin fraction, maps of 400x400 µm² were acquired with a step size of 250 nm. It is worth noting that the majority of the twins are thinner than this step size. The area fraction of twins can depend on the beam size, which is assumed to be of the order of 30 nm, and should not depend on the step size. Following the acquisition, the maps were not cleaned to avoid the disappearance of thin twins (less than 4 pixels) upon cleaning. To determine the twin area fraction, a specific algorithm was developed using the MTEX library [106]. Grains considered as twins were selected based on specific criteria, including their orientation relative to neighboring grains and their thickness. Orientation-wise, the criterion indicates a misorientation of 5° from the perfect twin relationship of 60° around the <111> direction.

After identification of the parts of the microstructure which are twinned, the twin fraction was computed by dividing the total area of grains identified as twins by the total area of the map. The thickness was measured by fitting an ellipse around each grain, and taking the minor axis of the ellipse as the twin grain thickness. For deformation twins, a maximum thickness threshold of 1 µm was applied, except for samples deformed at levels exceeding 40% engineering strain. In this case, the threshold was set to 1.5 µm (twins are larger for highly deformed samples). For non-deformed microstructures, these conditions yielded low twin fractions, of the order of 0.6% for the as-built condition and 0.23% for the recrystallized condition. These baseline values were subtracted from the results obtained from deformed samples. Figure II-11 provides an illustrative example of the segmentation process.

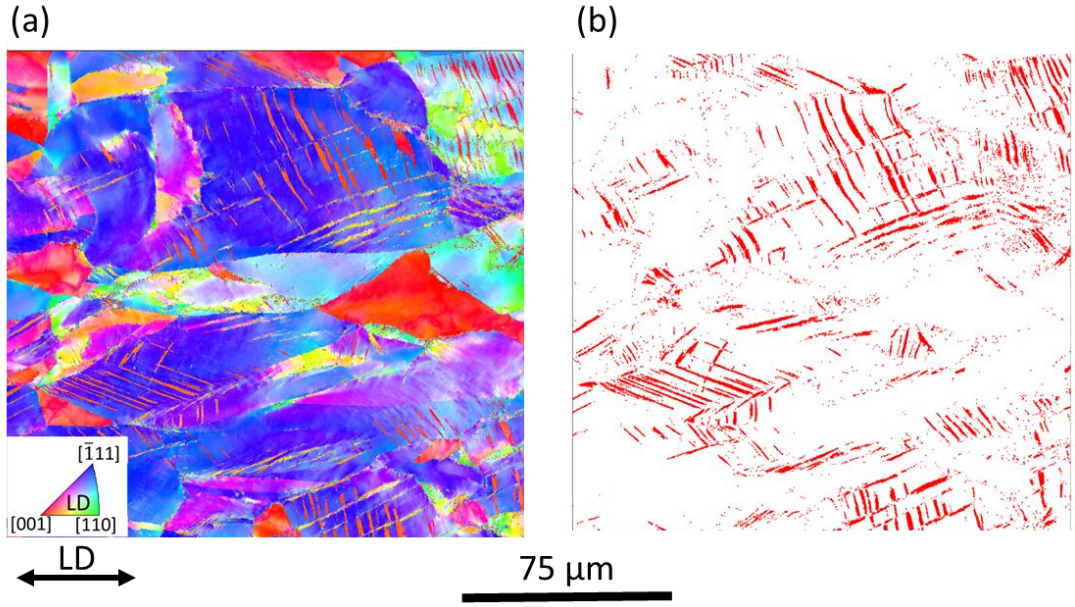

Figure II-11: Recrystallized Steel 2 after 32% deformation. (a) IPF EBSD map and (b) Result of the segmentation to identify twins, grains segmented as deformation twins are plotted in red.

Chapter III. Origin of the as-built microstructure variations

III.1 Introduction

Laser power bed fusion (L-PBF) has many advantages in comparison with traditional processing routes (casting, forging, sintering) such as greater design freedom in addition to a possible reduction of the manufacturing times (fabrication, shaping, and heat treatments). Austenitic stainless steels are widely used in the energy industry such as nuclear energy [107] for their high mechanical properties over a wide temperature range combined with a high corrosion resistance [33] [108]. Austenitic stainless steels inherited from L-PBF possess typical microstructural characteristics that can be summarized as follows: (i) columnar grains with their <110> direction parallel to the building direction where the texture index is more or less pronounced depending on the applied processing parameters [109] [85] [51] ; (ii) a cellular/dendritic growth (no development of secondary arms) where the inter-dendritic regions are enriched in Cr and Mo due to microsegregation [12], [50], [110] ; (iii) a high density of dislocations arranged in cells superimposed to the microsegregated interdendritic regions [57] [94]; (iv) the presence of nanoscale oxides enriched in Si and Mn [50] [82] [110]; and (v) a low density of Σ3 boundaries [57] [12] [52] [82].

More recently, it has been shown that peculiar microstructures can be obtained by loading 316L powder from Praxair Surface Technology in L-PBF machines, see e.g.[9] [6] [83] [84]. The peculiarity of this microstructure is its finer grain size and weak crystallographic texture. In the PhD of Chniouel [9], heterogeneous nucleation on particles such as carbides was invoked to explain such microstructural characteristics. This peculiar microstructure obtained using powders from Praxair was found regardless of the processing parameters applied and powder batch used [6]. A very similar microstructure has been found in the Ph.D. theses of Relave [75], Ziri [63], and Roirand [72] with a powder batch of 316L from Höganäs. The hypothesis invoked in these works is a change in solidification path but very few observations were provided to support this assumption.

It has to be emphasized that microstructural variability has been reported in 316L [111] and 304L austenitic stainless steel processed by L-PBF [112],[113]. The distinctive features of these microstructures in comparison with the common features summarized previously are their finer grain size and their surprisingly high density of Σ3 twin boundaries. In these previous works [111] [113], the authors account for such microstructures by suggesting that the thermomechanical hysteresis that the material experiences during L-PBF is a situation favorable for grain boundary engineering (GBE). Laleh et al. [111] relied on an EBSD map of the topmost layer, where no Σ3 boundaries are detected suggesting that the presence of Σ3 boundaries results from in-situ GBE during L-PBF due to the combination of dislocation accumulation and thermal cycling. Zhu et al. [113] attributed the high density of twin boundaries and low density of low angle grain boundaries (LAGB) in comparison with other 316L microstructures reported in the literature to grain boundary migration and possible dynamic recrystallization that may occur upon L-PBF, due to the combination of residual stresses which activates local plastic deformation and intrinsic heat treatment. Both authors agreed that the Σ3 boundaries cannot be the result of deformation twinning because of the morphology of those twins (wide and large twins).

Microstructures with a high density of Σ3 twin boundaries and fine grains have also been recently reported in other FCC alloys as-built made by additive manufacturing such as in an Inconel 718

fabricated by a coaxial laser wire process [114], [115], in aluminum alloys made by L-PBF [116], [117] and in a commercially pure Nickel made by L-PBF [118]. However, in these studies, the hypothesis which has been put forward to account for the fine grains and high density of Σ3 boundaries is the impact of local liquid ordering. A recent viewpoint by Rappaz et al. [119] summarizes how the liquid ordering can impact the microstructures during solidification. To date, the impact of local liquid ordering on the microstructure has not been yet reported in additively manufactured austenitic stainless steels.

In this chapter, parts made of 316L stainless steel have been fabricated using two different powder batches while keeping the exact same processing conditions. The first powder batch from SLM Solutions leads to the classic as-built microstructure of austenitic stainless steels where the various typical features described above have been evidenced. The second powder batch from Praxair leads to the non-classical microstructure with smaller grains and a high density of Σ3 boundaries. The high density of Σ3 boundaries in the printed parts using the second powder batch from Praxair was not reported yet. This new element can potentially question the hypothesis of heterogeneous nucleation made by Chniouel [9] to explain grain refinement. Different hypotheses are then reviewed and discussed to account for the differences in microstructures between the two different powder batches and identify the underlying mechanisms.

III.2 Characterization of two different microstructures

III.2.1 Microstructure at the grain scale

Figure III-1 (a-b) shows an optical image after chemical etching of the topmost layer of the two printed steels, namely Steel 1 (SLM) and Steel 2 (Praxair). To evaluate the melt pool geometry, a 2D cross-section taken such as the molten track can be observed in the plane containing the building direction (BD) and the transverse direction (TD). The laser direction (LD) is out of the plane. The size of the melt pool is very similar for both steels, with nearly 200 µm in width and about 100 µm in depth. They exhibit a hemispherical morphology with the aspect ratio, defined as the ratio of depth to width, equal to 0.5 suggesting that the samples were produced in a conduction regime rather than in a regime governed by the keyhole [120]. Grains appear mostly columnar, which will be further verified by EBSD. The fact that the melt pool geometry and dimensions are the same for both steels also indicates that the density of energy received by the powder is identical for both steels.

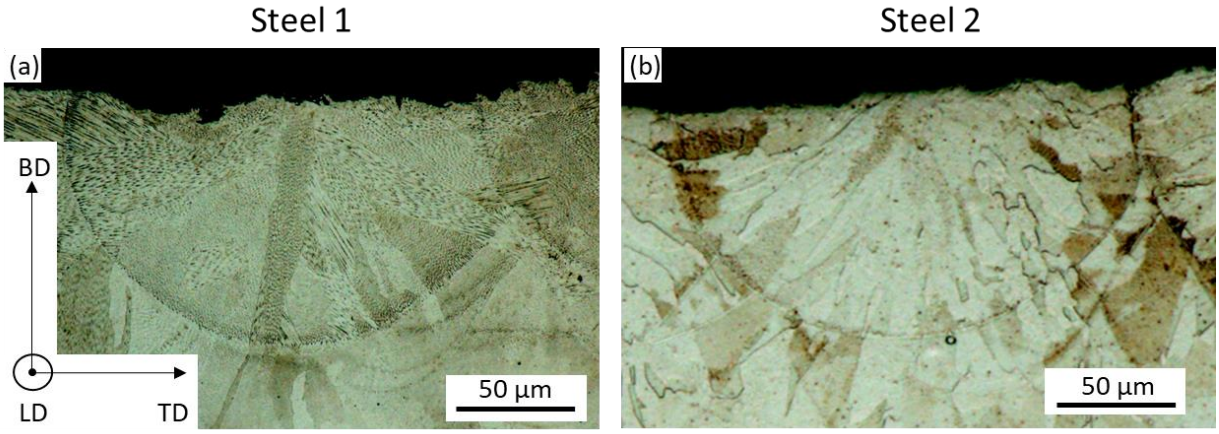

Figure III-1: Optical micrographs of the topmost layer taken in the (BD-TD)-cross section where molten pools were revealed by chemical etching with V2a. Sample fabricated using (a) powder batch 1 from SLM solutions, and (b) powder batch 2 from Praxair.

Figure III-2 (a) and (b) show IPF EBSD maps of samples produced using respectively powder batch 1 and powder batch 2. In both steels, the grains are columnar, but they are finer in Steel 2. To quantify the grain size, equivalent grain size was calculated using the definition of the Feret number. The average largest dimension of the Feret diameter is 28 µm in Steel 1 and 14 µm in Steel 2. Figure III-2 (c) shows that the microstructure of Steel 1 is textured, with grains preferentially oriented with one of their <110> directions parallel to the building direction, in agreement with other studies, see e.g. [93] [85]. By contrast, Figure III-2 (d) shows that Steel 2 has a more random texture. Figure III-2 (e) and (f) are the grain boundaries map corresponding to the regions of interest highlighting using the white boxes in the two EBSD maps shown respectively in Figure III-2 (a) and (b). In these Figures, grain boundaries with a misorientation > 5° are plotted in black, Σ3 boundaries in red and Σ9 boundaries in blue.

The fraction of Σ3 boundaries is very different in the two steels: 1.5% in Steel 1 and reaches 30% in Steel 2. As a result, Steel 1 is seen as the typical microstructure of austenitic stainless steels inherited from L-PBF [57] [12] [52], while Steel 2 has the unconventional microstructure observed by Laleh and others, see e.g. [113] [112]. Figure III-2 (g) shows histograms of grain boundaries misorientation in Steel 1. Superimposed in black is the Makenzie distribution which is the histogram of grains with a random orientation. In orange is the histogram of the misorientation of grain boundaries uncorrelated, i.e. taking into account that the microstructure shows a <110> texture. Figure III-2 (h) is the equivalent of Figure III-2 (g) but for Steel 2. One can observe that there is no peak at 60° misorientation in Steel 1, in agreement with the uncorrelated and random distributions. However, there is a peak at 60° misorientation in Steel 2, which is not consistent with the uncorrelated and random distributions. This peak is associated with the high fraction of Σ3 boundaries and confirms that the fraction of Σ3 boundaries is above the expected one from an uncorrelated distribution, while the fraction of Σ3 boundaries in Steel 1 is close to the expected one. A summary of the different characteristics of the microstructures for both steels is given in Table III-1. Finally, it is also interesting to emphasize that nearly all the twins are incoherent twins and do not show a flat morphology as opposed to coherent twins. This morphology is incompatible with deformation twins, which are coherent and have lenticular morphology.

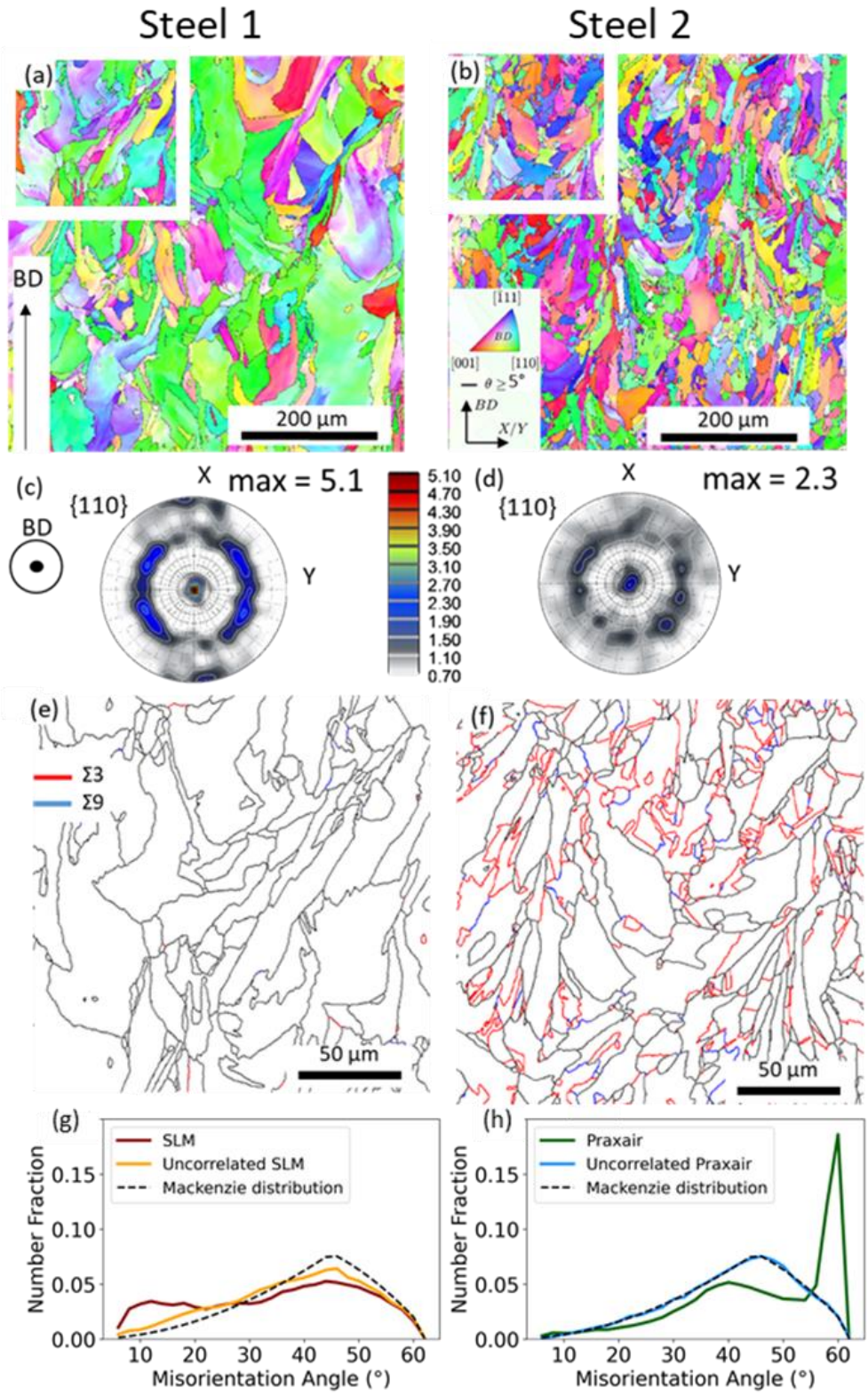

Figure III-2: EBSD-IPF maps in the middle of the cubes representing the grain orientations normal to the building direction for (a) the sample fabricated using the SLM solutions powder (Steel 1), and (b) the Praxair powder (Steel 2). (110) Pole figures for respectively (c) Steel 1 (maximum texture index of 5.1 Multiple of Random (MRD)), and (d) Steel 2 (maximum texture index of 2.3 MRD). Grain boundary maps of (e) Steel 1 from the white frame in (a), and (f) Steel 2 from the white frame in (b), Σ3, and Σ9 boundaries are highlighted respectively in red and blue. Number fraction of grain boundaries as a function of misorientation angle for (g) Steel 1 along with the uncorrelated distribution and the Mackenzie distributions, and (h) for Steel2 along with the uncorrelated distribution and the Mackenzie distribution (statistical analysis conducted on more than 2000 grains in each case). In Steel 2, the Mackenzie distribution is almost superimposed with the uncorrelated distribution.

Table III-1 : Summary of the differences between the two steels.

	Average max. ferret diameter (µm)	Aspect ratio	Maximum intensity index (MRD)	Σ3 boundaries fraction (%)	Σ9 boundaries fraction (%)
Steel 1	28	3	5.1	1.5	0.7
Steel 2	14	2.3	2.3	30	4.5

III.2.2 Microstructure at the intragranular scale

Figure III-3 (a) and (b) show the inner grain structure after chemical etching in Steel 1 and 2 respectively. It is composed of cells of a diameter around 450 nm in both cases. These cells correspond to columnar dendrites formed during solidification [60], and result from an austenitic solidification. The cooling rate can be estimated from the empirical formula proposed in [121] and used by Elmer [28] to 8.106 °C/s. Figure III-3 (c) and (d) show that dislocations are superimposed on the dendritic structure, which is consistent with the literature, see e.g. [67] [78]. In these micrographs, black dots can be observed, which are mainly identified as oxides in the literature [7] [28] [29]. Figure III-3 (e) and (f) show HR-EBSD maps of the two steels and give an estimation of the local geometry necessary dislocation (GND) density. Those maps reveal a high dislocation density in the cells walls and lower inside the cell. The GND density is of the same order of magnitude in both steels (~1014 m-2), in agreement with other studies [122], [76]. Based on these observations, no significant differences between the two steels were detected at the intragranular scale.

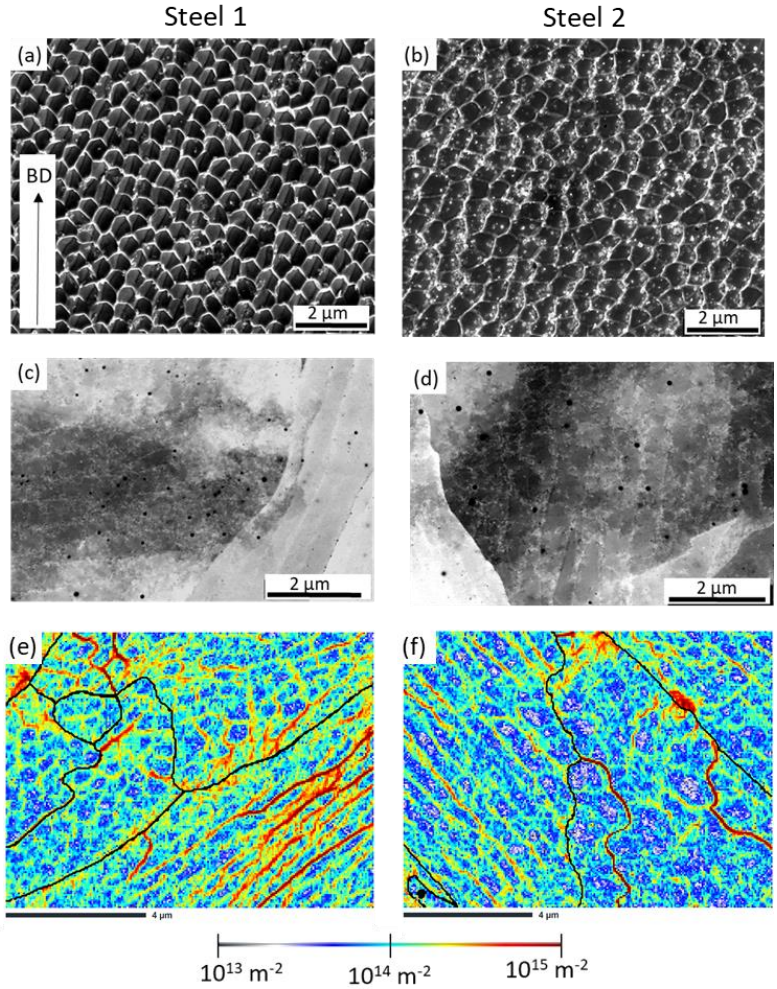

Figure III-3: SEM-SE micrographs of the solidification cells after etching with V2a for respectively (a) Steel 1, and (b) Steel 2. SEM-BSE micrographs for respectively (c) Steel 1, and (d) Steel 2. GND density maps were determined using HR-EBSD for respectively (e) stee1, and (f) Steel 2.

Microsegregation inherited from solidification have been characterized with EDX in TEM in both steels, see Figure III-4. It reveals Cr and Mo partitioning, and shows that particles in both steels have the same chemistry, i.e. Mn-Si rich oxides as reported in the literature [12], [50], [69], [73]. No partitioning in Ni is observed. Other elements were examined (Al, C, P, S, Ti, V, Co, Cu, Nb), but they were not found to be partitioned.

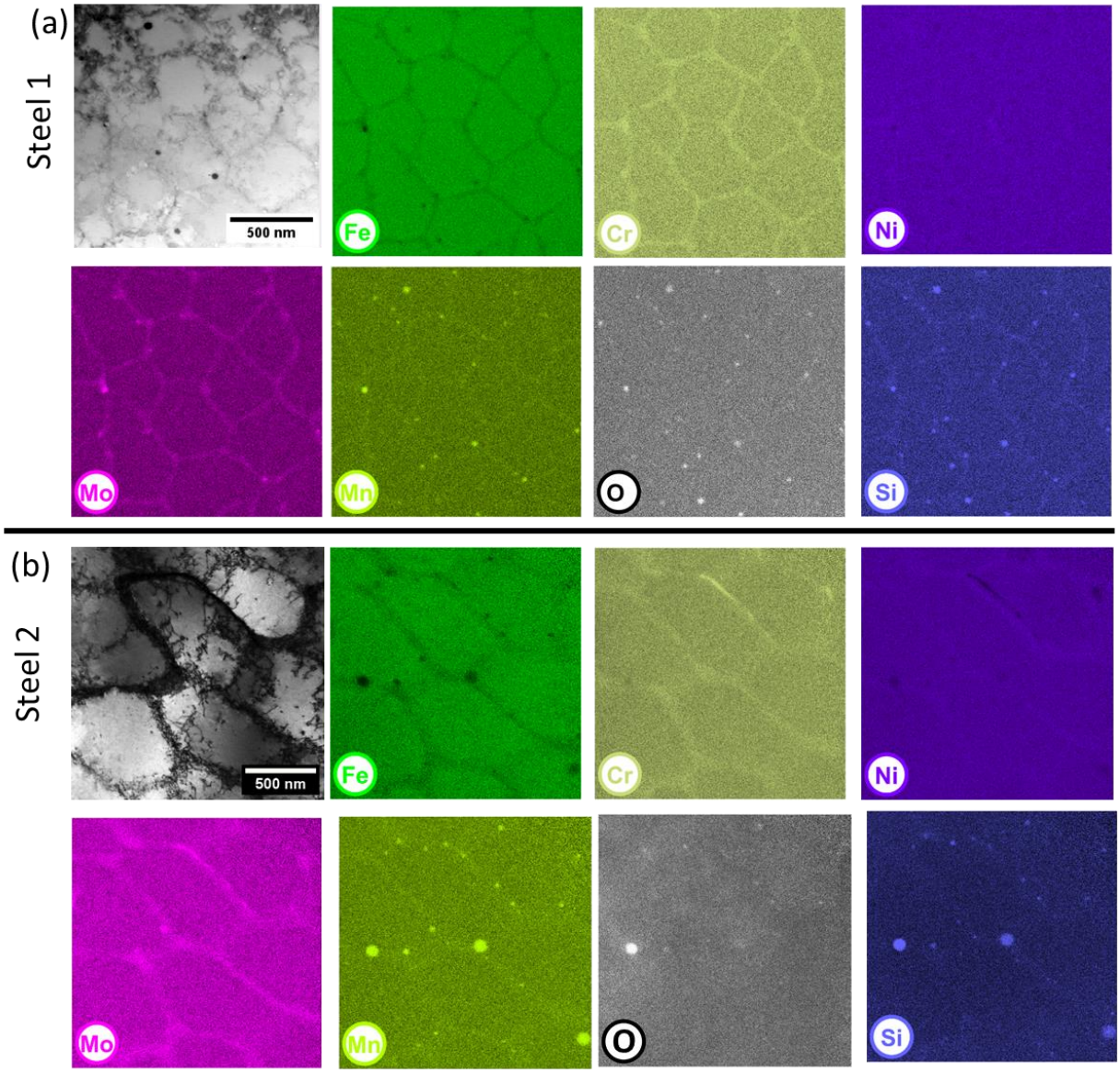

Figure III-4 : STEM bright field image and X-ray count maps for (a) Steel 1 and (b) Steel 2 measured by EDX in the TEM. The color contrast is proportional to the number of X-rays counted for each element.

III.3 Review of the hypotheses

Several hypotheses will be successively examined to rationalize the differences in microstructures between Steel 1 and Steel 2 that have been evidenced in III.2. All the characterizations shown below have been conducted in Steel 2.

III.3.1 The hypothesis of heterogeneous nucleation on inoculating particles

One of the differences between Steel 1 and Steel 2 is the grain size. The hypothesis of a grain refinement caused by the heterogeneous nucleation of grains on particles will first be examined, the latter being primary phases or exogenous nucleating agents intentionally added to the powder. It was the hypothesis retained to account for the formation of fine grains in a modified 316L austenitic stainless steel with the addition of 3% wt. TiC particles [123]. It has also been shown in austenitic stainless steel that with the addition of 300 ppm of Ce, Ce_2O_3 or Ce_2O_2S particles form and act as heterogeneous nucleation sites for austenitic grains [124]. A similar mechanism was reported in ferritic steel processed by L-PBF with the addition of 5% wt of Ti [125]. In this case, they observed that particles of TiO play the role of a nucleating agent.

Let us consider that heterogeneous nucleation occurs on a particle in Steel 2 but not in Steel 1. It was the hypothesis proposed by Chniouel in his PhD to explain similar microstructural differences as the ones shown in III.2 of the present work [9]. However, we do not think that this is a reasonable hypothesis for different reasons. First, it has to be highlighted that inoculating particles were not intentionally introduced in the pre-alloyed powder contrary to what was done in other studies, see [125] [126] [123]. In both steels, several particles can be observed in each austenitic grain and such particles are also found in columnar grains suggesting that such particles do not act as a nucleating agent, see Figure III-3 (c) and (d). These particles are very similar between both steels and correspond to the Si, Mn-rich oxides well-documented in the literature [50], [82], [110], see TEM images in Figure III-4. In addition, such a mechanism does not account for the presence of the high density of Σ3 boundaries in Steel 2. TiC sometimes reported promoting the heterogeneous nucleation of austenitic grains [123] is unlikely to form due to the very low content of C in Steel 2 (the one having the finer grains) and was not observed.

III.3.2 The hypothesis of annealing twins

It is well known that austenitic stainless steels form twin boundaries when subjected to thermomechanical treatments. This phenomenon is often exploited in grain boundary engineering approaches as increasing the density of Σ3 twin boundaries is interesting to mitigate undesirable interfacial phenomena (oxidation, corrosion, grain boundary embrittlement or fracture). According to reviews on the subject [102], these twins are obtained by applying one or several cycles of deformation followed by annealing. The micro-mechanisms at the origin of twin formation during annealing are still debated, but all seem to be related to grain boundary migration (recrystallization, grain growth).

Hereafter, they will be referred to as annealing twins. In the literature, it is described that annealing twins can be either coherent or incoherent twin boundaries [102].

During L-PBF, the material experiences complex thermomechanical cycles due the thermal stresses and the high temperatures induced by cycles of cooling and reheating when building new layers. This could be seen as an in situ thermomechanical treatment, potentially leading to the formation of annealing twins. It is then possible to hypothesize that the microstructure of Steel 2 would be modified during L-PBF, while microstructure of Steel 1 would have not. This could explain the difference of density of Σ3 boundaries between Steel 1 and Steel 2 as highlighted in III.2.1. It is the hypothesis developed by Laleh et al. [111] to account for the high density of Σ3 boundaries in the as-built microstructure of the 316L investigated in their study. The hypothesis suggesting that the high density of Σ3 twin boundaries in Steel 2 results from the in situ thermomechanical treatment experienced by the material during L-PBF is carefully examined.

The formation of Σ3 boundaries during thermomechanical treatments is known to be dependent on the stacking fault energy (SFE) [102]. For high SFE materials such as aluminum, no Σ3 boundaries are created via thermomechanical treatments. The ability to form twins in austenitic stainless steel is often related to their low stacking fault energy (SFE), see e.g. [127]. Thus, the SFE of Steel 1 and Steel 2 have been estimated using the empirical formula from Pickering [45]:

$$SFE\ (mJ.m^{-2}) = 25.7 + 2wt.\%Ni - 0.9wt.\%Cr - 13wt.\%Si - 1.2wt.\%Mn + 410wt.\%C - 77wt.\%N \quad \text{(III-1)}$$

Using this equation, the SFE of Steel 1 and Steel 2 is respectively equal to 26.4 and 28.3 mJ.m^{-2}. These values are very close, which means that the difference in SFE cannot be held responsible for the difference of microstructure between both steels.

To examine if the in situ thermomechanical treatment undergone by the material during L-PBF could be responsible for the presence of Σ3 boundaries, areas that did not experience a cycle of deformation and reheating have been examined in Steel 2. If the thermomechanical cycling induced by the layer-by-layer processing is responsible for the high density of Σ3 twin boundaries in Steel 2, there should be a visible effect on the microstructure of the topmost layer (since this later does not experience the thermomechanical cycling induced by adding new layers). Figure III-5 (a) is an IPF EBSD map taken in the topmost of Steel 2, and Figure III-5 (b) is the grain boundary map of a molten pool in the last layer. The Σ3 twin boundaries are highlighted in red. There are many Σ3 twin boundaries in the topmost layer, and the microstructure does not seem to be different in comparison with the underlying layers. This observation does not support the idea that twins originate from the in situ thermomechanical treatment experienced by the material during L-PBF. In addition, we would like to comment on the time scale because microstructural evolution during annealing requires some time. For instance, it was reported in [82] and [50] that a 316L fabricated by L-PBF requires 1h at 1100°C to achieve a fully recrystallized microstructure. The time spent by the material above 1100°C during the intrinsic heat treatment experienced by the material during L-PBF is believed to be of the order of the millisecond [128] [48]. Thus, the order of magnitude of the time of heat treatment during L-PBF might not be long enough to induce grain boundary migration over significant distances.

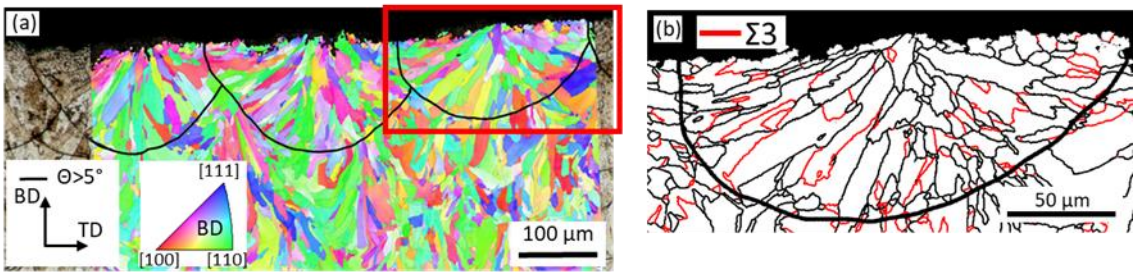

Figure III-5: (a) Superposition of an EBSD-IPF map with its optical micrograph after chemical etching to reveal the position of the molten pool boundaries. (b) Grain boundary map of the region highlighted in red in (a), Σ3 boundaries are displayed in red.

A second observation that questions the hypothesis of annealing twins was made. The initial powder particles of Steel 2 were examined using EBSD. Figure III-6 (a) shows the IPF map of powder particles and Figure III-6 (b) the associated grain boundary map. There is a high density of Σ3 twin boundaries in the powder particles (around 28%, measured on more than 600 particles). The similarity between the Σ3 twin boundary density in the powder and as-built sample of Steel 2 suggests that it could originate from similar mechanisms. The absence of thermomechanical cycling during powder atomization is an additional argument against the hypothesis of annealing twins. Finally, Figure III-6 (c) and (d) show optical micrographs of the powders after electrochemical etching. They reveal that the powder microstructure is dendritic with primary and secondary arms. This is a characteristic of a microstructure inherited from solidification. To explain the grain refinement and twin formation, one should rather look for solidification mechanisms instead of mechanisms related to annealing twins.

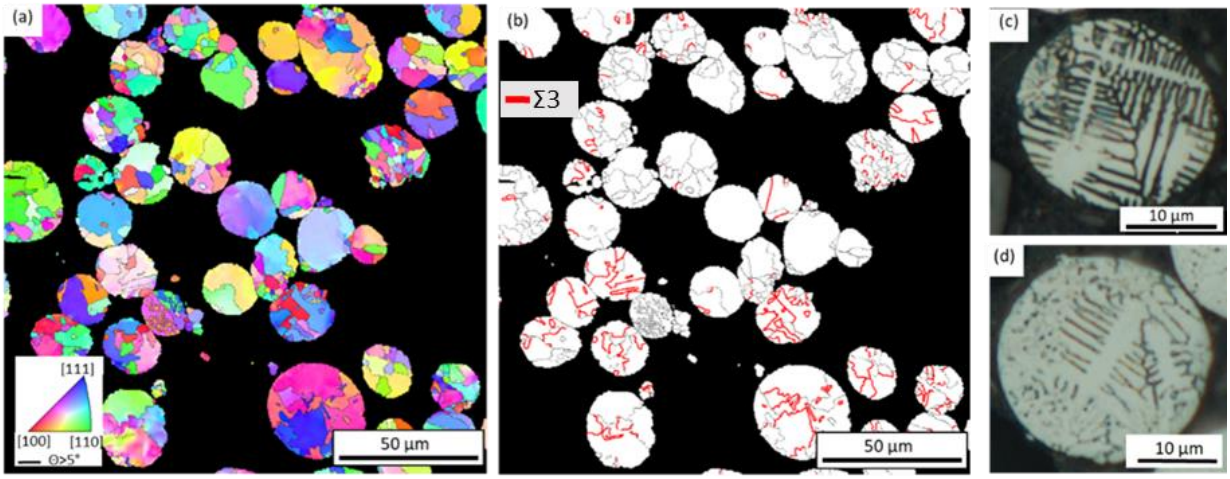

Figure III-6: (a) EBSD-IPF map and (b) grain boundary map of the powder batch 2 from Praxair (step size of 0.5 µm). Σ3 boundaries are highlighted in red. (c) and (d) Optical micrographs of powder particles from powder batch 2 after electrochemical etching oxalic acid.

III.3.3 The hypothesis of a local liquid ordering

III.3.3.1 Mechanism affecting grain nucleation: ISRO-mediated nucleation

Another mechanism that can generate Σ3 boundaries and fine grains during solidification is the local ordering of the liquid at a short/medium distance with an icosahedron topology. Frank suggested in

1952 that liquid could be organized in such topology to explain the large undercooling nucleation observed by Turnbull [129]. Since then, it has been demonstrated experimentally by conducting in situ diffraction in the liquid [130]. It has also been proven that liquid locally ordered can have a significant impact on the resulting microstructure, see the recent viewpoint paper from Rappaz et al. [119].

The impact of the structure of the liquid on solidified microstructures has been suggested for the first time to account for a modification of the microstructure of an Al-20Zn alloy with a minute addition of Cr (0.1%) [131]. With the addition of 0.1% Cr, the authors observed a grain refinement that goes along with an increase in the Σ3 boundaries density. They suggested that with the addition of Cr, the degree of local icosahedral ordering in the liquid becomes more important. This local liquid ordering is often described in the literature as Icosahedral Short Range Order (ISRO) [132] [133]. ISRO is thought to promote the nucleation of FCC grains via the ISRO-mediated nucleation mechanism [131], [134], [135]. In such a situation, FCC-grains nucleate from a hypothetical icosahedron template where each facet corresponds to different grain orientations and with a specific heteroepitaxy orientation relationship. Given the geometry of the icosahedron, the nucleated grains exhibit a Σ3 twin relationship as well as multiple fivefold symmetries axes <110>. A schematic representation of this mechanism adapted from [131] is shown in Figure III-7.

More recently, this mechanism has been observed in additively manufactured microstructures in different alloys: in a superalloy (Inconel 718) made by a coaxial laser wire process [114], in an aluminum alloy made by L-PBF [116], and in a commercially pure Nickel processed by L-PBF [118], but not yet in a Fe based alloy.

This mechanism is attractive to account for the specific features of the as-built microstructure of Steel 2 because it can be invoked to simultaneously rationalize the presence of finer grains and the high density of Σ3 boundaries. In the literature, such a mechanism is sometimes described as Icosahedral quasicrystal (iQC) [118] or ISRO-mediated nucleation [114]. In the present case, we prefer using the terminology ISRO because in the literature we did not find a quasicrystal or approximant phase, which could nucleate as a primary phase in the liquid of austenitic stainless steels. The only quasicrystalline phases to our knowledge in 316L can precipitate via a solid phase transformation after a long time of annealing: 100h at 550°C [136] or after 50h at 700°C [137].

This hypothesis could explain the twin boundaries but also the grain refinement. Indeed, considering an icosahedron as the nucleation site, 20 orientations of new austenitic grains are theoretically possible (the polyhedral describing the icosahedron can be constructed using 20 equilateral triangles). ISRO-mediated nucleation can be considered very powerful regarding nucleation efficiency because a given inoculating particle usually leads to the nucleation of a single orientation.

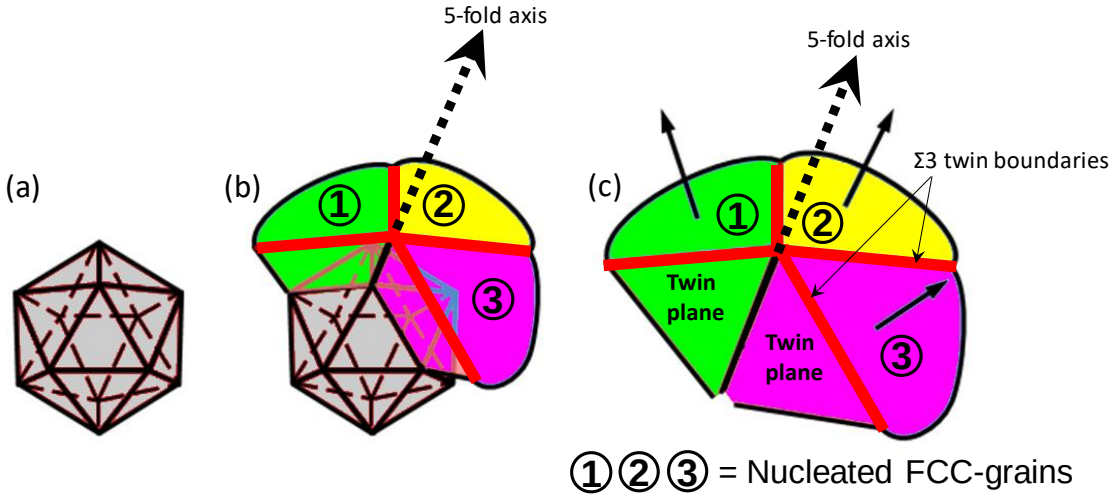

Figure III-7: Schematic representation of the ISRO-mediated nucleation. (a) Hypothetic icosahedron template (atoms are positioned on each vertex as well as in its center). (b) Nucleation with heteroepitaxy relationships of 3 FCC-grains on an icosahedron template considered as a trace of a local liquid ordering. Grains 1, 2 and 3 have been colored to show that they have a different crystallographic orientation. (c) Twin relationships between the nucleated FCC-grains with a common <110>-direction that corresponds to a 5-fold symmetry axis (black dotted arrow). Adapted from ref [131].

To evaluate if ISRO-mediated nucleation is responsible for the high Σ3 boundaries fraction observed in Steel 2, clusters of grains are identified where nearest neighbor grains were related by a Σ3 twin relationship while finding the typical <110> fivefold symmetries of the hypothetical icosahedron template as suggested in [131] [114] [118].

Several clusters of grains with multiple orientation relationships (OR) have been found in Steel 2. A cluster is defined here as a set of grains all related by a Σ3 or a Σ9 boundary using Brandon's criterion tolerance angle. Figure III-8 (a) and (b) show an example of a cluster of 44 grains with 13 different orientations. The grains with the 13 different orientations are numbered from 1 to 13 in Figure III-8 (c). For further analyses of the specific relationships between the grains belonging to the identified cluster, Mtex was employed [138]. Here, note that an average orientation was attributed to each grain.

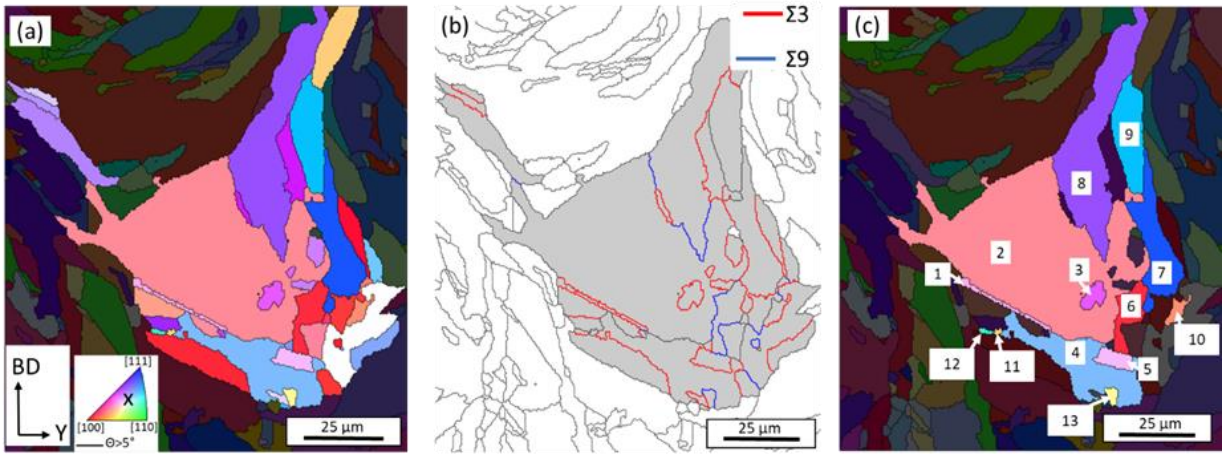

Figure III-8: (a) EBSD-IPF map where the color code corresponds to the average orientation per grain. Grains belonging to the identified cluster are highlighted. (b) Grain boundary map of this cluster of grains, with Σ3 in red and Σ9 in blue. (c) EBSD-IPF map of the 13 different grain orientations (labeled from 1 to 13) found in this cluster.

In this cluster of grains, orientation relationships (OR) of all grains are analyzed to investigate the existence of fivefold symmetries axes typical of the icosahedron. To do so, the <110> directions of several grains belonging to this cluster are reported in a pole figure to identify if some grains share a common <110> direction and if this cluster exhibits a multiple twin symmetry compatible with an icosahedron template.

In Figure III-8, 10 grains from the cluster can be positioned in an icosahedral template and six fivefold symmetries axes have been found, labeled (b) to (g) in Figure III-9. In these pole figures, common or nearly common {111} planes are represented as arcs of circles. To link these orientations with an icosahedron template, an icosahedron with 10 visible facets has been drawn in Figure III-9 (a). The triangular facets of the icosahedron are numbered and colored in a way corresponding to the fcc grains in Figure III-8(c).

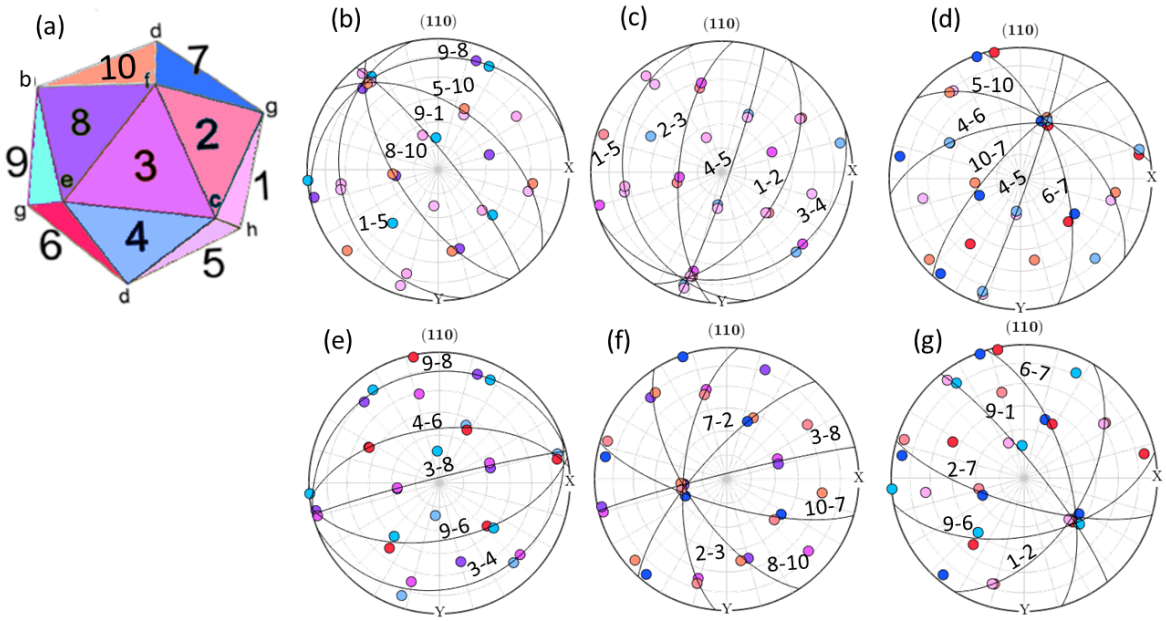

Figure III-9: The <110> pole figures of sets of multiple twin grains from Figure III-8 are shown in (b through g), with the indication of the {111} twin or near-twin planes by arcs of circles. The <110> common pole (fivefold symmetry) is found at the intersection of the twin planes. In (a), an icosahedron has been schematically drawn in a position such that the six 5-fold symmetry axes labeled (b through g) approximately correspond to the common <110> axes of the FCC grains, and with corresponding facets of the same color as grains in Figure III-8. Adapted from ref [134].

Other clusters were analyzed and similar orientation relationships between neighboring grains were evidenced, see Appendix A, with one where 9 grains can be placed in an icosahedron template and another were 7 grains can be placed.

But are these special orientation relationships between nearest-neighbor grains enough to demonstrate that this icosahedron template acts as a nucleating agent for FCC grains? In other words, would it be possible to generate these fivefold symmetries by a random twinning process?

To address this question, we suggest determining the probability that the special orientation relationships from Figure 8 and Figure 9 appear by chance. To calculate such a probability, a simple algorithm is built where the scheme is summarized in Figure III-10. The principle of this algorithm is to artificially construct several clusters of grains where grains are related by random twin relationships. The

idea is then to test these clusters to evaluate if they can be placed on an icosahedron template as done in Figure III-10. Finally, the number of times where this event happens is recorded.

To be more specific, in step 1, a random orientation (Orientation 1) is given to a grain. In Step 2, a second orientation is created by a rotation of 60° around one of the 4 planes {111} of the Orientation 1. In Step 3, a third orientation is generated via similar considerations but from orientation 2 and taking care that they are different from the previous orientations. In Step 4, after having repeated this operation, 13 different orientations are generated to artificially create a cluster. In Step 5, the cluster is analyzed by evaluating if 10 of the 13-grain orientations can be placed on an icosahedron template as shown in Figure III-9.

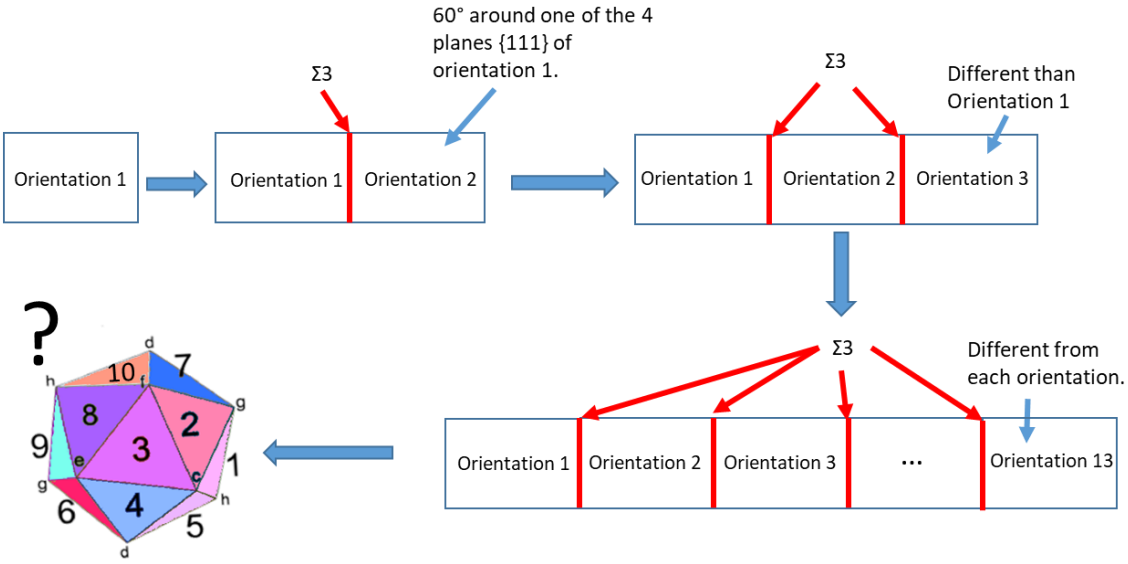

Figure III-10: Flow chart summarizing the algorithm developed to calculate the probability of forming a cluster of grains where near-neighbors are related with Σ3 relationships.

500 simulations of artificial clusters have been performed and none of them could be placed on an icosahedron template. For us, it is an additional argument that what is experimentally observed cannot be the result of a random twinning process but rather suggests that there is an icosahedron template that leads to the nucleation of such kind of cluster of austenitic grains where nearest neighbors are in a Σ3 twin relationship. However, one should keep in mind that this simulation is run in 1D, which means that one grain gives only one other grain with a twin relationship. Assuming now that each grain gives for example 2 or 3 other grains with a twin relationship, the probability increases to respectively at 3.4% and 15%. These orientations relationships are not common, but not impossible to get by a random process assuming that each grain can show a twin relationship with 3 other grains.

This hypothesis could explain the twin boundaries but also the grain refinement. Indeed, considering an icosahedron as the nucleation site, 20 orientations of new austenitic grains are theoretically possible (the polyhedral describing the icosahedron can be constructed using 20 equilateral triangles). ISRO-mediated nucleation can be considered very powerful regarding nucleation efficiency because a given inoculating particle usually leads to the nucleation of a single orientation.

III.3.3.2 Mechanism during grain growth: ISRO-induced stacking fault

The ISRO-mediated nucleation mechanism enables to explain the finer grains and the high density of Σ3 twin boundaries observed in Steel 2. However, this mechanism does not necessarily account for all the Σ3 twin boundaries observed in Steel 2. For example, some of the Σ3 boundaries shown in Figure III-11 (a-c) pass through successive stacked molten pools. The black arrow in Figure III-11(c) indicates the melt pool where the nucleation of the grain represented in pink likely took place. This pink grain has grown epitaxially and crossed three different melt pools. The orange arrows in Figure III-11 (c) points out Σ3 boundaries in the upper part of the grain, three melts pool above the melt pool where this grain has nucleated. Such Σ3 twin boundaries are rather believed to have formed during the growth of the cellular dendrites. Interestingly, ISRO was also found to have an effect on the dendrite growth, see e.g. [119] [139] [140]. In these references, it is suggested that icosahedral motifs present in the liquid can attach to the growing FCC-phase, most probably via a facet as illustrated in the schematic shown in Figure III-12. This mechanism has been described as ISRO-induced Stacking Fault in [139] because a stacking fault is created in the red plane shown in Figure III-12 which gives a schematic view of this mechanism. Once the icosahedron is attached via its red facet to the red facet of a tetrahedron of the FCC unit cell as illustrated in Figure III-12, then a new grain orientation (in yellow in Figure III-12) can nucleate from the icosahedron template as explained previously creating a Σ3 twin boundary. However, for now, this mechanism is only a conjecture. Absolute proofs of the occurrence of such a mechanism still need to be provided. This mechanism was also thought to be responsible for changes in dendrite growth direction in other FCC-alloys as reported in [139] [140]. However, in the present case, the dendrite growth directions do not seem to be altered (see Figure III-13).

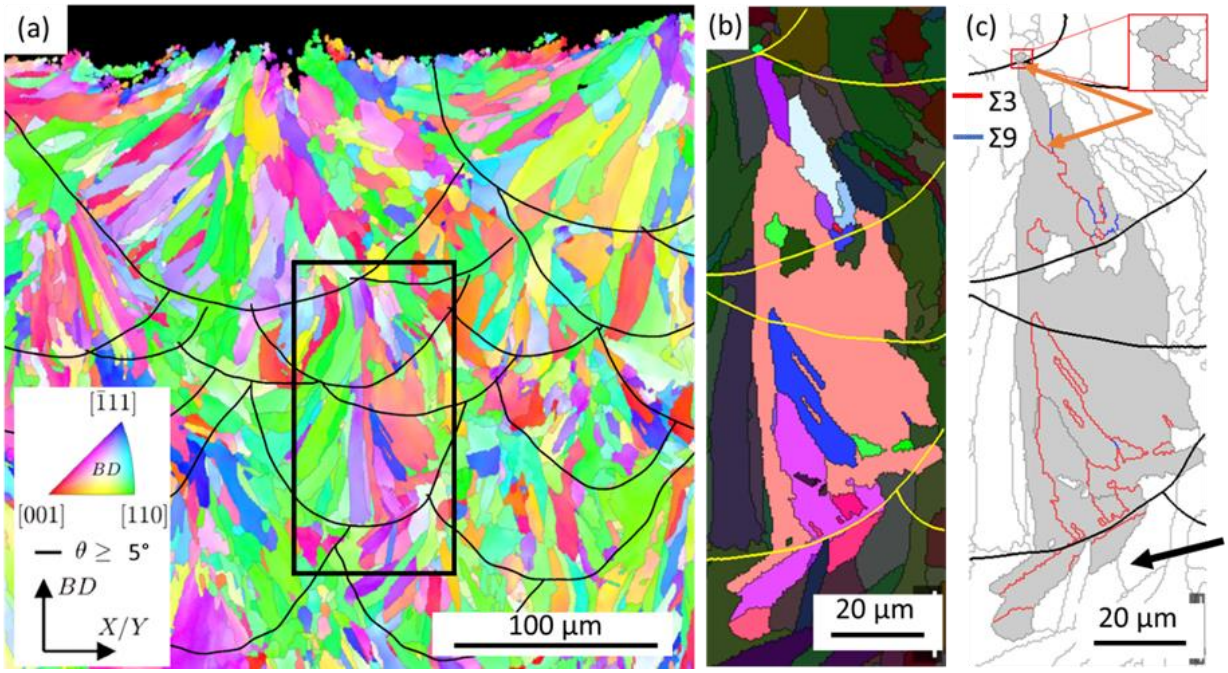

Figure III-11: (a) EBSD-IPF map acquired in the XZ-cross-section of Steel 2. Melt pool boundaries are drawn in black from a superposition with an optical micrograph taken in the same region of interest. (b) EBSD-IPF map of the black rectangle shown in (a). The grains from the cluster are highlighted and melt pool boundaries are in yellow. (c) Grain boundary map of (b). The cluster is highlighted in gray. The black arrow indicates the melt pool where nucleation occurred. The orange arrows indicate two Σ3 boundaries three melt pools above the initial melt pool.

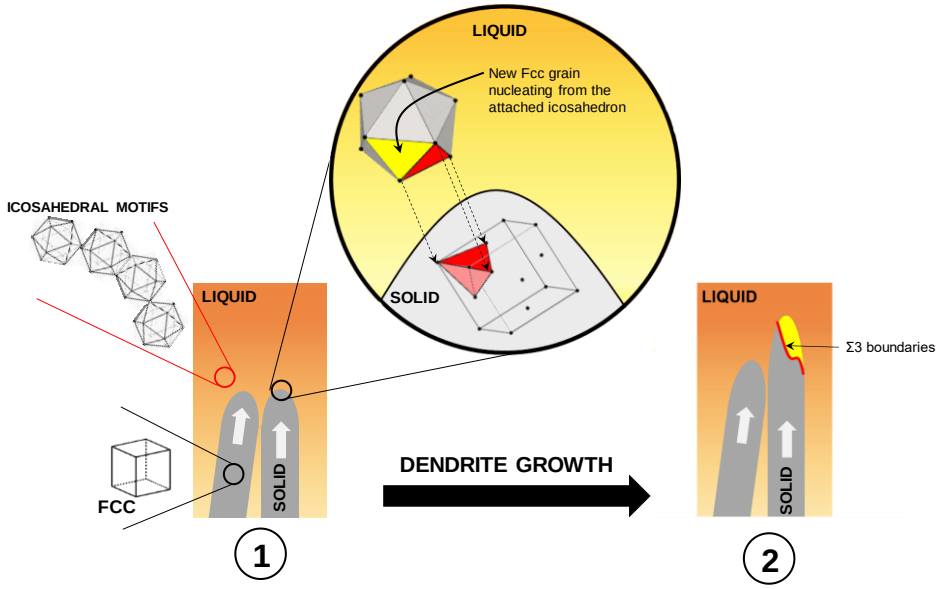

Figure III-12: Description of the ISRO-induced stacking fault inspired from [139]. The red tetrahedron represents the regular tetrahedron sites in the FCC unit cell. The red tetrahedron from the liquid with icosahedron attaches on the tetrahedron from the solid (FCC), inducing a stacking fault. This induces that dendrite grows in the liquid and a tetrahedron from the liquid order attaches on the growing dendrite inducing a stacking fault which creates a Σ3 boundary.

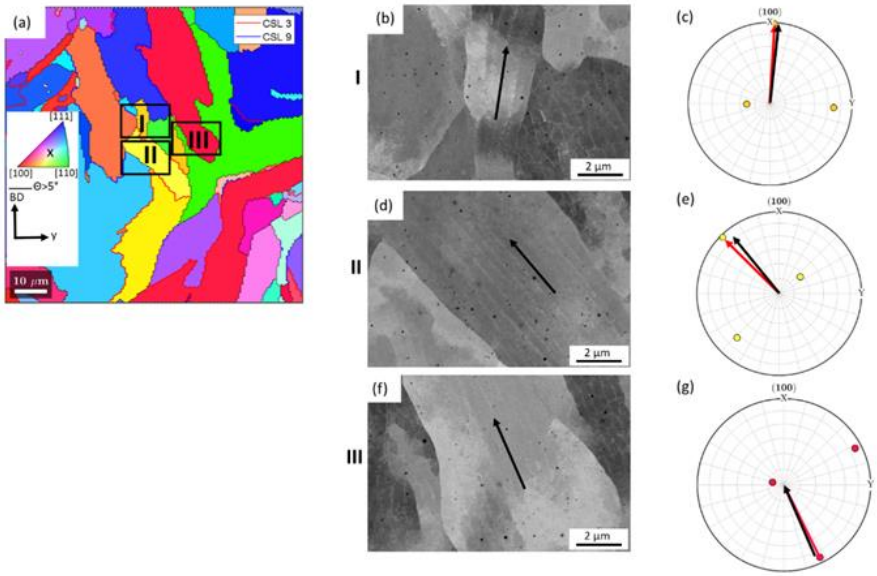

Figure III-13: Growth direction of dendrites of Steel 2. (a) IPF EBSD Map of Steel 2 showing grain average orientation. (b), (d) and (f) are SEM BSE image of respectively the magnified zone I, II and III from (a). Blacks arrows represent growth dendrites direction. (c), (e) and (g) are the <100> pole figures of grain shown in respectively (b) (d) and (f). Red arrows represent the <100> direction from the orientation of grains. Black arrows are growth dendrite direction of grains. One can see that red arrows and black arrows are very close, showing that the dendrite growth directions of these three grains are <100>.

In this part, we brought elements which might be in good agreement with ISRO-based mechanisms during solidification. However, the analyses reported are not an absolute proof of such mechanisms. That being said, we thought that those crystallographic analyses are worth being reported as a strong possible explanation.

III.3.4 The hypothesis of the solidification sequence

The last hypothesis that can be made to explain differences between microstructures would be to assume a difference in solidification mode. It is known that stainless steels have different solidification modes: Austenite (A), Austenite/Ferrite (AF), Ferrite/Austenite (FA) and Ferrite (F) [21]. This is the hypothesis retained by Relave [75] and Ziri [63] to explain their microstructure with fine and equiaxed grains inherited from LPBF.

The solidification mode at high solidification velocity can be estimated using the diagram proposed by Lippold [21]. This diagram was established based on data from the 300 series of stainless steels. In this diagram, the Cr_{eq} and Ni_{eq} are calculated by the formula of the WRC92 diagram, by assuming that Ti, Nb and Cu are not in quantities that would have a significant impact on the solidification mode:

$$Cr_{eq} = \%Cr + \%Mo \quad \text{(III-2)}$$

$$Ni_{eq} = \%Ni + 35\%C + 20\%N \quad \text{(III-3)}$$

This gives a ratio of Cr_{eq}/Ni_{eq} = 1.34 for Steel 1 and 1.55 for Steel 2. The solidification velocity is estimated as equal to the scan speed (800 mm/s in this study). This is an upper bound [21]. As can be seen in Figure III-14 (a), both steels are expected to have a full austenitic solidification, even if Steel 2 is closer to the mode where primary ferrite followed by massive transformation is expected. However, this diagram should be used carefully and would deserve more work to be considered as a predictive diagram in the context of additive manufacturing. This is why, we decided to investigate in more detail the F/MA solidification mode.

Elmer was one of the first researchers to clarify the F/MA solidification mode in austenitic stainless steels [28]. Within the scope of his Ph.D. work, Elmer studied the resultant microstructural attributes of austenitic stainless steels after the process of electron beam welding, varying parameters such as the steel compositions and electron beam velocities. For a given composition, he successfully produced an austenitic microstructure with traces of residual ferrite showing the same composition as the austenite. A remarkable observation was that the cellular structure induced by microsegregation was not revealed after chemical etching. Some years later, Lippold [21] found a similar microstructure after pulsed laser welding, but without residual ferrite. In addition, some regions showed the presence of solidification cells while other regions of interest did not show evidence of solidification cells. An optical micrograph of the resulting microstructure is shown in Figure III-14 (b).

Both authors assumed that areas of austenite that do not show cells solidified in F mode followed by a massive transformation of ferrite into austenite. A massive transformation usually appears in an alloy that is cooled down sufficiently fast to skip the ferrite+austenite stability domain in the phase diagram. This massive phase transformation does not need long-range distance diffusion. There is no elemental partitioning between ferrite and austenite in the presence of a massive transformation and all the ferrite can be transformed into austenite [19]. This solidification mode is often described as the F/MA mode and is different from FA or AF mode, because there is no second phase in the interdendritic regions just after the solidification.

The absence of microsegregation in the transformed austenite could result from the higher diffusion coefficient in ferrite than in austenite which gives more time to erase the microsegregation inherited from solidification [141], [142]. Variability in microstructure within a specific melt pool is believed to arise from disparities in solidification modes (F/MA or A). These distinctions can be attributed to variations in solidification velocities among the individual grains. It is anticipated that a greater solidification velocity would promote the formation of primary austenite [23]. Furthermore, it is well-established that grains aligning their <100> orientation with the thermal gradient exhibit a higher growth rate compared to grains aligned differently with respect to the thermal gradient [54]. Hence, the solidification mode may indeed be contingent upon the grain's orientation with respect to the thermal gradient.

Lippold [21] and Elmer [28] mentioned the presence of Σ3 twin boundaries in the microstructure when solidification occurs through a F/MA mode. However, no comment was made on their origin. We can assume that Σ3 interfaces are created during α/γ interface migration during the phase transformation. This mechanism could be analogous to that responsible for the formation of Σ3 twin boundaries during γ/γ interface migration during recrystallization (annealing twins). In recrystallized material, different mechanisms are suggested to explain the presence of annealing twins, namely the growth accident or the coalescence of stacking fault packets [102]. These mechanisms are still debated in the literature. However, in our case, the Σ3 twin boundaries would result from the α/γ interface migration, and not from γ/γ interface migration. Whether migration of this interface can create Σ3 twin boundaries remains to be clarified. Lippold and Elmer also do not comment on a possible grain refinement induced by this solidification mode, but we can also suppose that the phase transformation can induce a grain refinement by preventing epitaxial growth and introducing a higher density of interfaces (twin boundaries).

Change in solidification path has recently been identified as a possible source of microstructure variability in austenitic stainless steels fabricated by LPBF [143]. In this paper, the authors found a nearly fully austenitic microstructure but with different intragranular characteristics. They show that some regions showed elemental partitioning with Cr and Mo enrichments in the interdendritic regions (typical partitioning observed in an austenitic solidification), while other regions of interest were found to be more homogeneous or with Ni enrichments in the interdendritic regions. This Ni enrichment in the interdendritic spaces is the signature of a ferritic solidification. However, the authors did not establish some correlations between this solidification in ferrite, the presence of Σ3 twin boundaries, and fine grains, or intragranular regions free of microsegregation.

This hypothesis is interesting to rationalize our observations in Steel 2 because it can explain both the presence of Σ3 twin boundaries and grain refinement. We could then assume that Steel 1 is subjected to a solidification mode A, while Steel 2 shows, at least in some areas, regions subjected to a full ferritic solidification mode followed by a massive transformation into austenite. This hypothesis is thoroughly discussed hereafter. This hypothesis could also explain the Σ3 boundaries observed in powders, which could follow the same solidification path. Some powder grains could have been solidified in A mode and some others in F/MA mode.

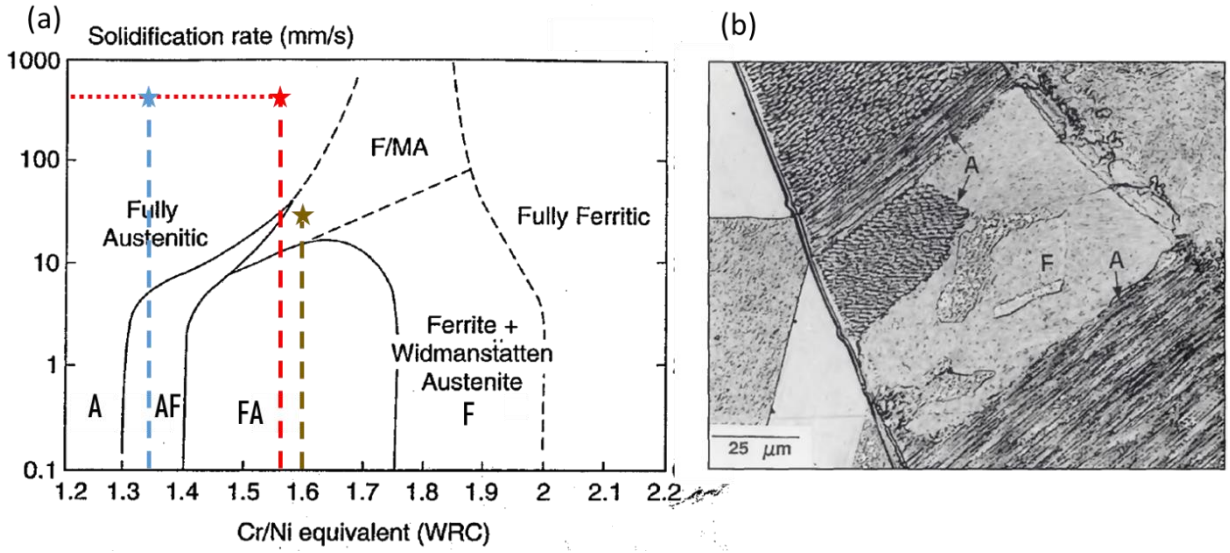

Figure III-14: (a) Solidification map for austenitic stainless steel as a function of solidification rate, from [21]. The blue star represents Steel 1 and the red star Steel 2. The maroon star represents the steel from the study of Lippold [21] shown in (b). (b) A 304L after pulsed laser welding at a welding speed of 1.6 mm/s and etched electrolytically with oxalic acid. The microstructure is fully austenitic. Areas noted with A are believed to come from primary austenite solidification while F area from primary ferritic mode followed by massive transformation of ferrite into austenite. From [21].

III.3.4.1 Regions without microsegregation (no evidence of elemental partitioning)

A microstructure with regions without traces of microsegregation in a 316L steel was observed by Birnbaum [144] in a single laser track. The authors did not mention the solidification mode in this study. To evidence regions with and without microsegregation, optical microscopy using a polarized contrast was employed after chemical etching. Under polarized contrast, areas with relief appear in bright, while flat areas appear in dark. The same analysis for the two steels investigated in this study is presented in Figure III-15 (a) and (b) after electrochemical etching using a solution of oxalic acid. On the optical micrographs, one can see a clear difference between both steels. In Steel 1, most of the surface appears with a relatively uniform contrast. On the opposite, bright and dark regions are observed in Steel 2. In the SEM images, Steel 1 shows a cellular structure on the whole region of interest. It is not the case for Steel 2, which shows distinct areas with areas where cells can be observed and others where cells are hardly distinguishable, see Figure III-15 (c) and (d). This observation would be in agreement with the hypothesis of a mixed solidification mode (FA), followed by a massive transformation of ferrite into austenite. We will show in the next section that this contrast is not related to the orientation of the grain. One can observe in optical or SEM images of Steel 2 that the solidification along the melt pool boundaries systematically starts with a planar mode that is rapidly destabilized in a cellular structure.

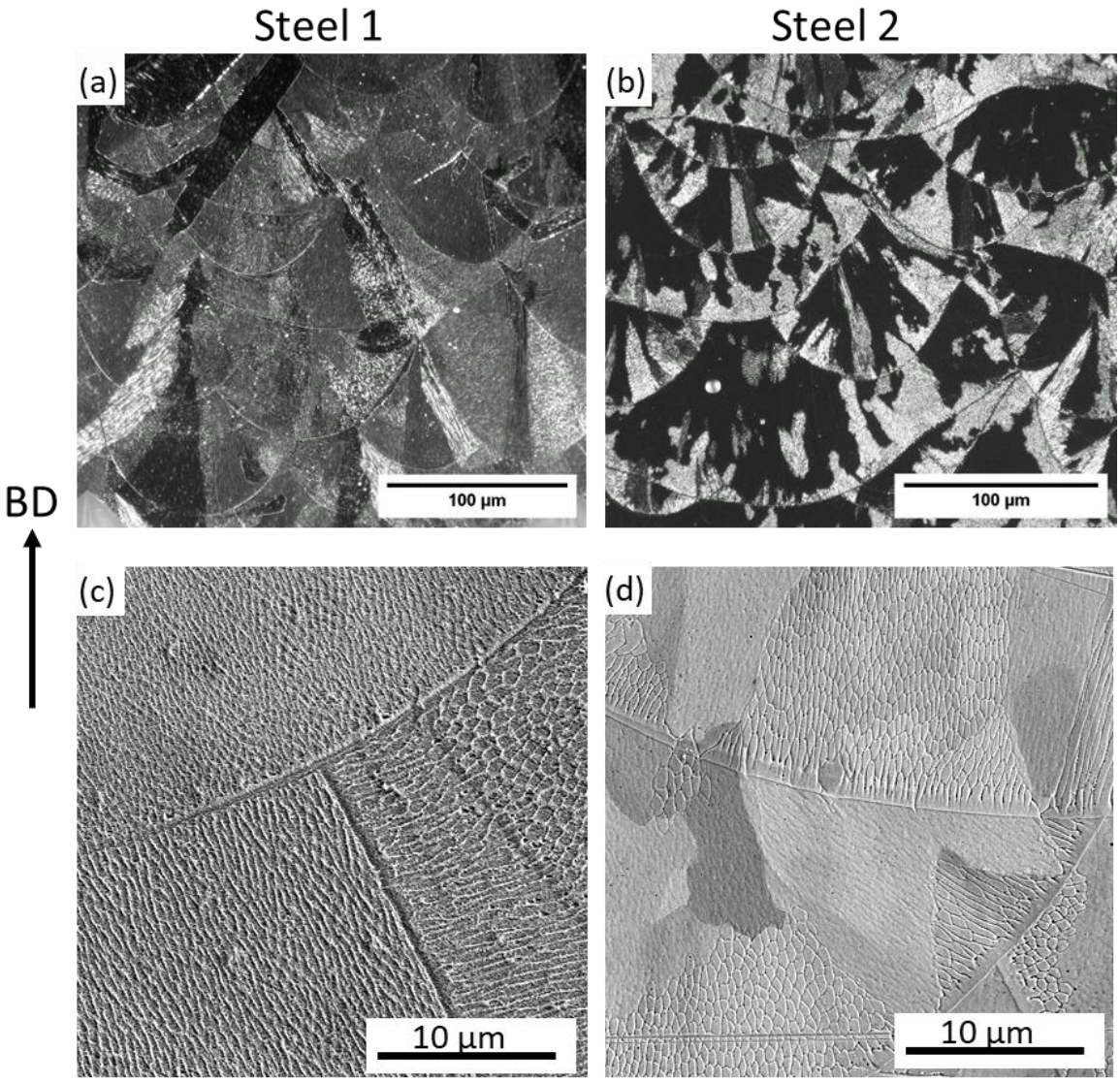

Figure III-15: (a)-(b) Optical images after electrochemical etching using oxalic acid for respectively Steel 1 and Steel 2. (c)-(d) SEM image of Steel 1 and Steel 2 respectively.

Bright areas visible in the optical micrographs using the polarized contrast correspond to regions where solidification cells are visible in the SEM, and the dark areas are associated with regions where solidification cells are difficult to observe, see Figure III-17 (a) and (b). We wanted to check if we could find areas with differences in elemental partitioning that might correspond to the one resulting from a solidification in primary ferrite. From a Scheil calculation with Thermocalc using the TCFE11 database, it is expected to find Ni partitioning in the interdendritic regions, see Figure III-16.

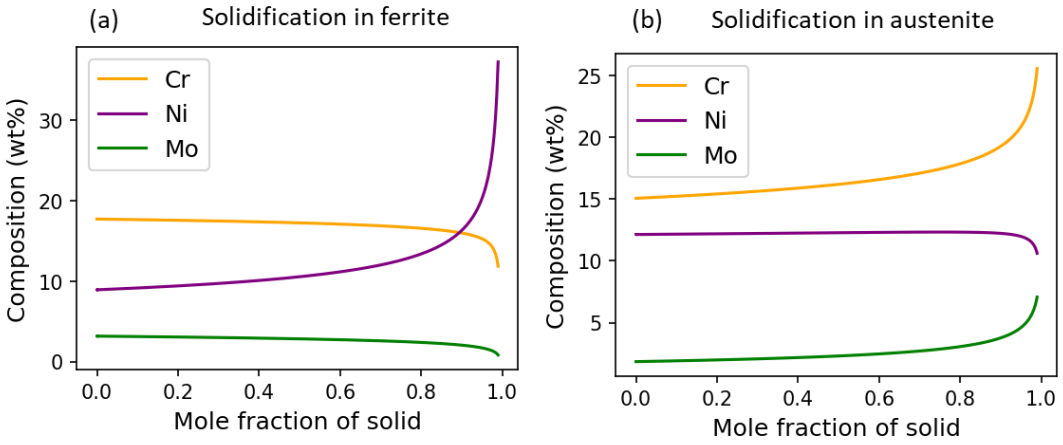

Figure III-16: Composition as a function of the mole fraction of solid, calculated with a Scheil model for Steel 2. (a) With a solidification in full ferrite (austenite excluded as potential phase), (b) With a solidification in full austenite (ferrite excluded as potential phase).

For this, EDX maps were collected in the TEM in different areas while keeping the count time constant. Results are presented in Figure III-17 (c) and (d). The first area shows microsegregation in Cr and Mo. These microsegregations are the same already reported in Figure III-4 for both steels and it corresponds to the expected segregations from a full austenitic solidification. No microsegregation was evidenced in the second area. It is then believed that the first area is located in a region where the cellular structure can be observed in the SEM image after etching, see the region highlighted using an orange rectangle in Figure III-17 (a). The second area is typical of an area where the cellular structure is difficult to observe after etching, see the blue rectangle in Figure III-17 (a). This observation suggests that there are some areas that do not show microsegregation. Our hypothesis is that those regions had enough time during cooling to homogenize at high temperatures when the microstructure was ferritic. In the rest of the text, we will refer to regions without microsegregation as regions without microsegregation in Cr and Mo. In fact, these regions can have microsegregations in Ni. No obvious differences in dislocation arrangement were observed between these two areas, see TEM images in Figure III-17 (c) and (d).

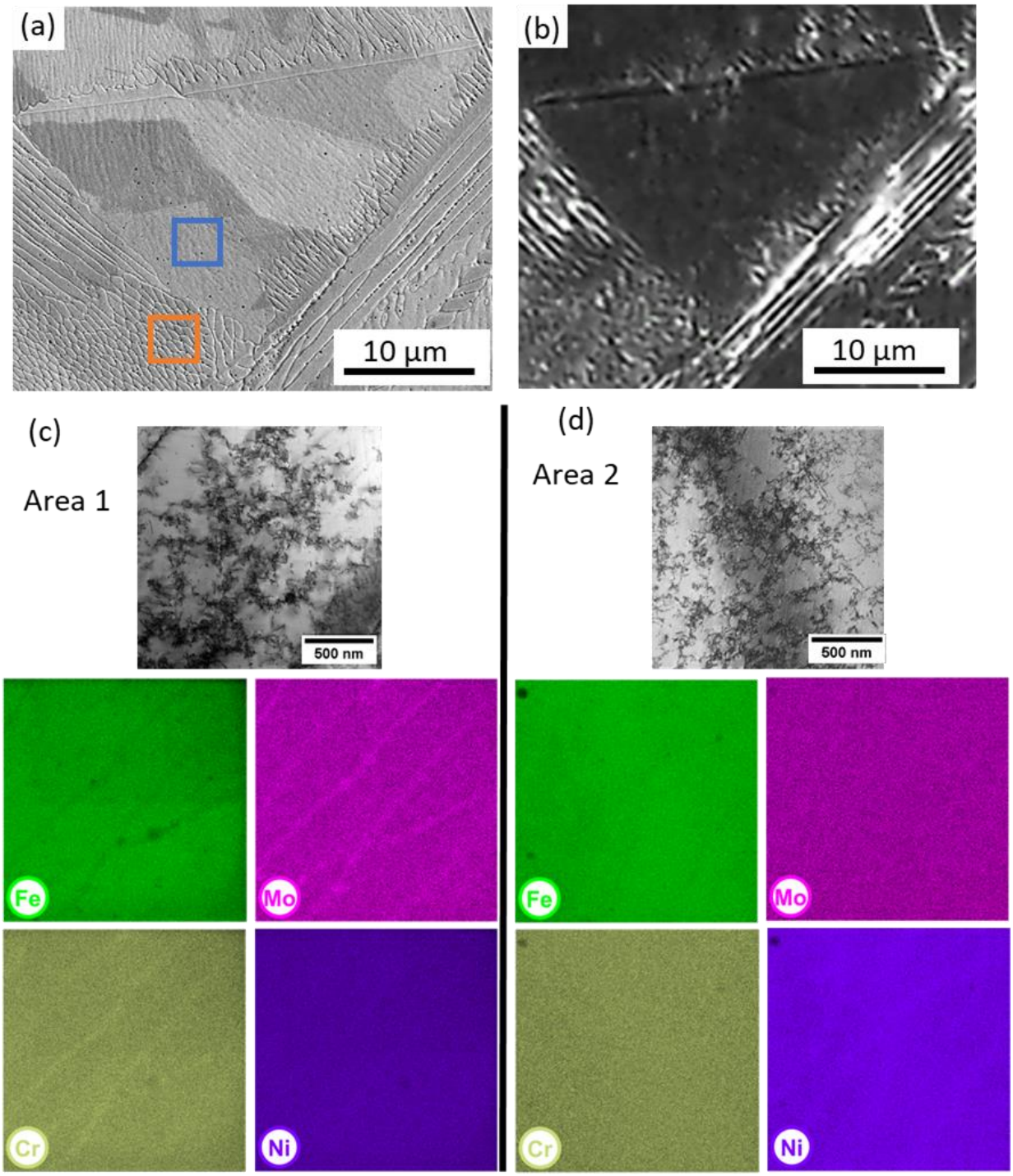

Figure III-17: (a) SEM image of Steel 2 after etching. (b) Optical image of the same area shown in (a). (c)-(d) STEM bright field image from an electropolished foil and associated X-ray count maps of two different areas. The EDX count time was kept constant (~1h).

Nonetheless, in regions where cell boundaries are poorly defined, see typically the blue squares in Figure III-17, one can still distinguish the presence of a cell network, as depicted in Figure III-18. These cells appear to have a diameter of approximately 600 nm. These cells are certainly the ghosts of previous microsegregation in Ni. Given the difficulty in precisely measuring such dimensions, it can be asserted that the size of these cells is roughly comparable to the size of well-defined cells.

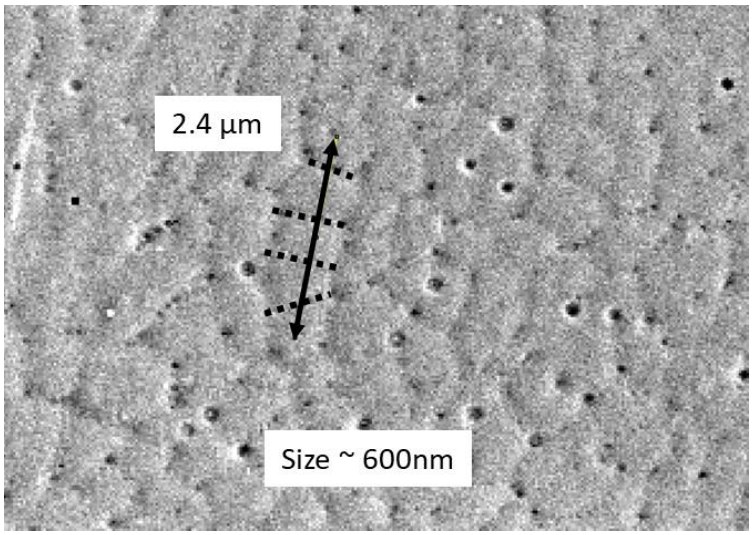

Figure III-18: SEM SE image of areas with badly defined cells (regions supposed to be solidified in primary ferrite).

III.3.4.2 Differences between segregated and non-segregated areas

Σ3 twin boundaries are also supposed to result from the massive transformation. One could expect that the density of Σ3 boundaries would be higher in areas that have been transformed massively (i.e. areas with no trace of microsegregation in Cr or Mo). This is what measured Birnbaum in [144]. To verify this hypothesis, we superimposed an SEM image taken after chemical etching and a EBSD grain map (Figure III-19(a)) as well as a EBSD IPF map (Figure III-19(b)). In Figure III-19(a), melt pool boundaries are highlighted in white, grain boundaries in black and Σ3 boundaries in red.

In Figure III-19, it can be seen that there are no grain boundaries in the melt pool boundary. This absence suggests the presence of epitaxial growth from the underlying layers. Additionally, different regions belonging to the same grain react differently to chemical etching, see the blue arrows. Such differences indicate that the contrast variation in a given grain cannot be attributed to differences in grain orientation. Σ3 twin boundaries are mostly found in non-segregated regions, i.e. in regions that are supposed to solidify in primary ferrite. However, twin boundaries are sometimes found to propagate through the melt pool boundaries through epitaxial growth, as indicated by the green arrow. Some Σ3 boundaries are also found at the interface between segregated and non-segregated areas, as depicted by the orange arrows. Notably, there is a much higher density of Σ3 boundaries in regions free of microsegregation. The orange triangle depicted in Figure III-19(a) highlights an area with a high density of Σ3 boundaries that is associated with a zone with nearly no microsegregation. These observations suggest a potential association between regions without microsegregation and the presence of a high density of Σ3 boundaries.

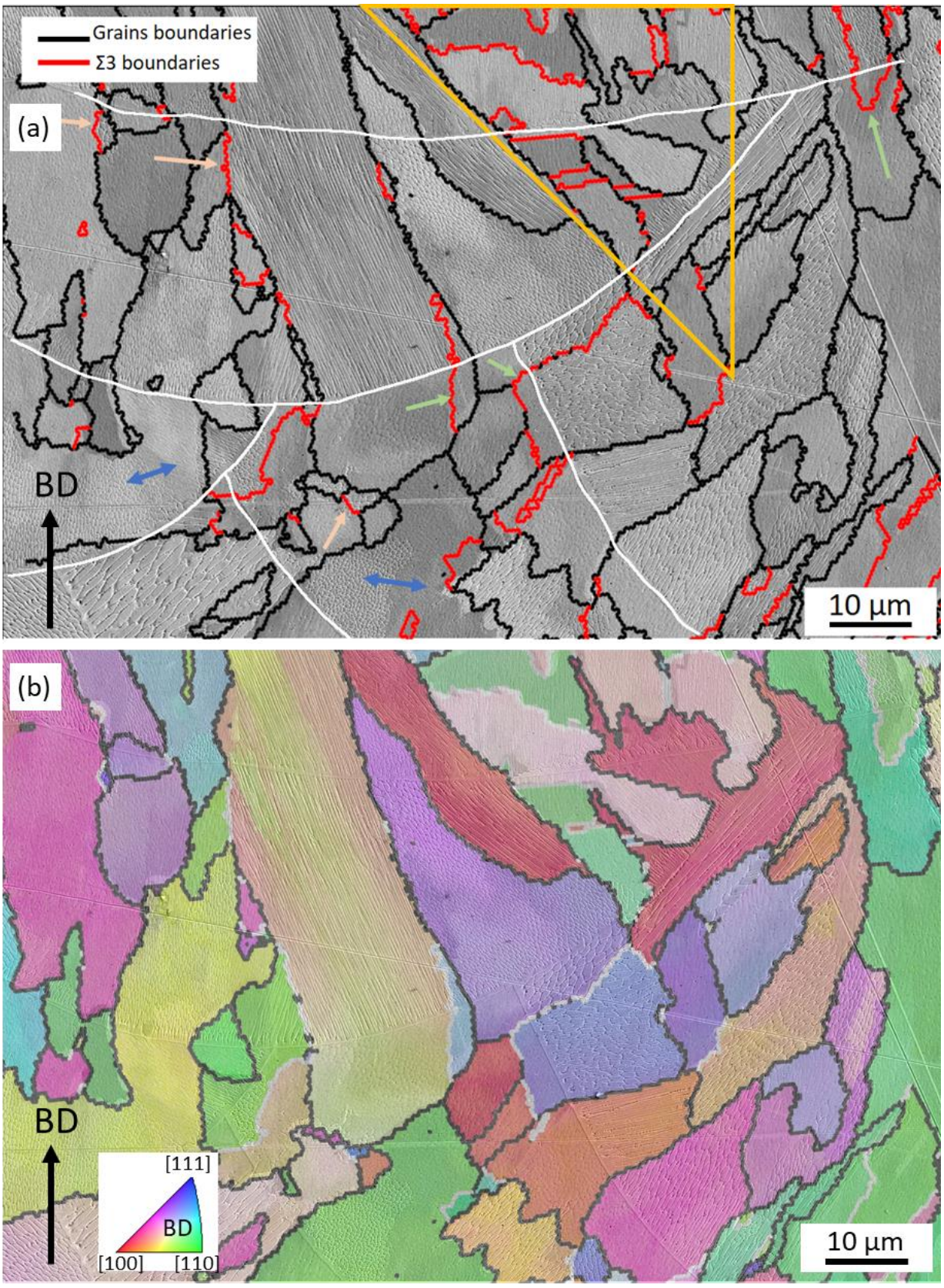

Figure III-19: (a) Superposition of an SEM image of the etched microstructure with an EBSD IPF map. Melt pool boundaries are highlighted in white. The orange triangle corresponds to an area with a high density of twin boundaries, which seems to be correlated to an area where solidification cells are hardly distinguishable. Blue arrows indicate a difference in etching response within the same grain. Green arrows indicate Σ3 twin boundaries which seem to nucleate in non-segregated areas. Orange arrows indicate Σ3 twin boundaries at the interface between segregated and non-segregated areas. (b) Superposition of SEM and IPF map.

The Vickers hardness (HV0.05) was measured in segregated and non-segregated areas (10 indents per zones), see Figure III-20 (a). The values are respectively 206 ± 6 and 207 ± 4. We can conclude that no difference in hardness is found between these zones. The local composition of the two areas (segregated and non-segregated) was also measured using EDX. Results are presented in Figure III-20 (b). No significant difference in composition between the two areas is observed.

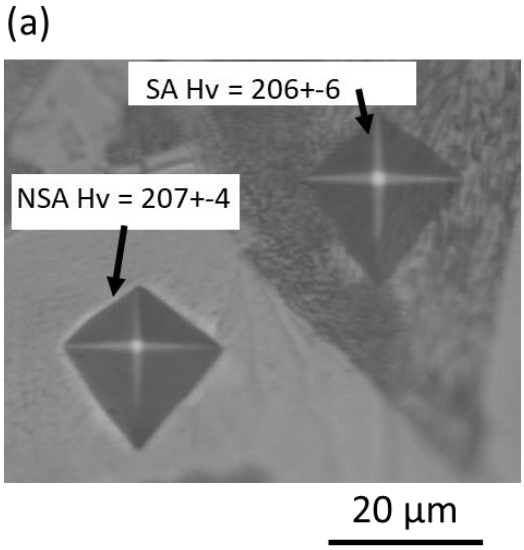

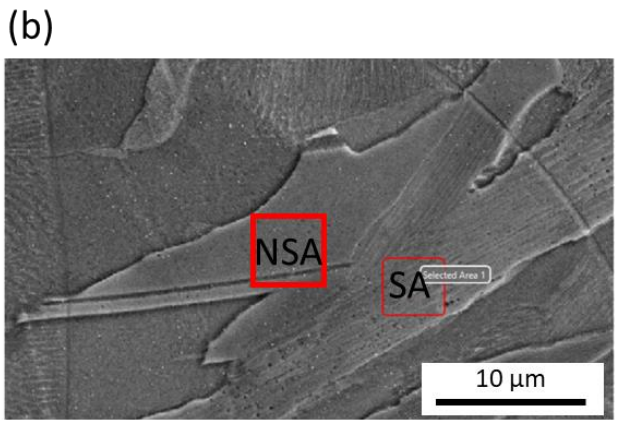

	Fe	Cr	Ni	Mn	Mo	Si
Nominal composition (wt%)	66.0	16.9	12.2	1.2	2.7	0.5
Segregated area (SA) (wt%)	66.6	16.8	12.7	1.4	2.1	0.4
Non segregated area (NSA) (wt%)	66.9	16.8	12.5	1.3	2.1	0.4

Figure III-20: (a) Images of the indents in segregated area (SA) and non-segregated area (NSA). (b) Local composition measured by EDX in the two zones.

III.3.4.3 Kinetics and thermodynamic considerations

Some experimental results support the hypothesis of a difference in solidification mode between Steel 1 and Steel 2, especially the absence of microsegregation in Cr and Mo in some regions of the microstructure of Steel 2. Steel 1 shows a fully austenitic solidification (A mode), while Steel 2 solidifies following a mixed solidification mode, with A and F/MA areas. Microsegregation induced by a ferritic solidification would have time to diffuse, and the massive transformation of ferrite into austenite would create Σ3 twin boundaries during interface migration.

However, this solidification mode has only been reported once in LPBF [143]. It has been observed for laser-cladding [21], but with a speed of 1.6 mm/s, far from the 800 mm/s used in this study, or in electron beam welding with a power 2000 W [28], which is far from the 200 W used in this study. We would like to evaluate if this solidification mode is consistent with the solidification conditions encountered in LPBF. Four different aspects will be discussed hereafter: (i) equilibrium considerations, (ii) the growth advantage of ferrite over austenite during solidification; (iii) the homogenization of the microsegregation by diffusion, and (iv) interface migration velocity during the phase transformation.

A. At the equilibrium

Equilibrium considerations can be useful to better understand solidification. Equilibrium calculations have been done using Thermocalc and the TCFE11 database. Only the liquid, ferrite and austenite were selected as candidate phases. Figure III-21 (a) shows the pseudo-binary diagram based on the composition of Steel 2 as a function of the N content. The N content is the principal variation in composition between Steel 1 and Steel 2. On this pseudo-binary diagram, one can see that both Steel 1 and Steel 2 should solidify as ferrite first. Both steels are far from a solidification starting with primary austenite. Figure III-21 (b) and (c) show the solidification equilibrium of Steel 1 and Steel 2 respectively. It confirms that both steels should solidify as ferrite first under equilibrium conditions. However, the difference in temperature between the onset of ferrite formation and the onset of the austenite formation is lower for Steel 1 compared to Steel 2 (8°C for Steel 1 while it is 15°C for Steel 2). Consequently, Steel 1 needs to be less destabilized than Steel 2 to solidify in austenite.

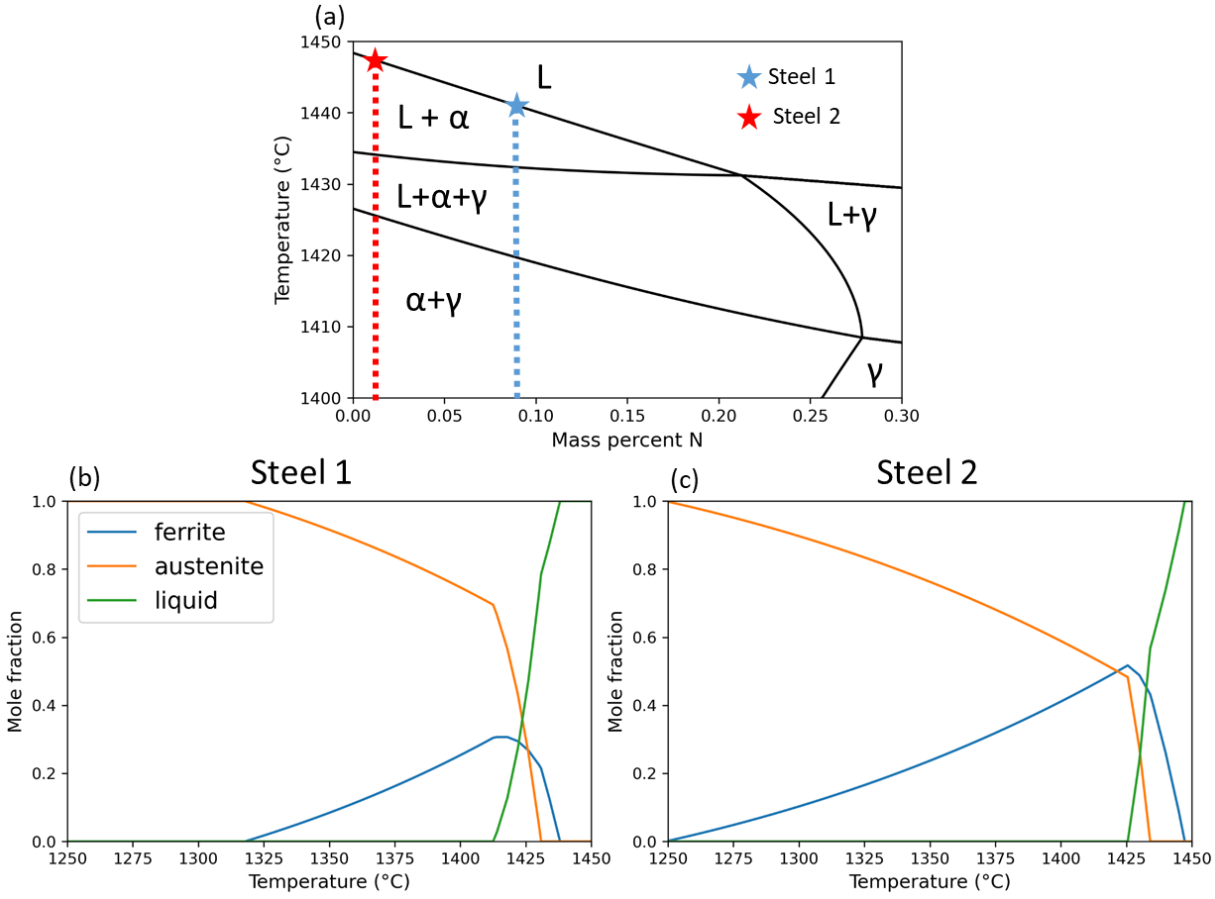

Figure III-21: Pseudo-binary diagram based on the composition of Steel 2 as a function of N content. (b)-(c) Solidification equilibrium for respectively Steel 1 and Steel 2. Only the liquid, ferrite and austenite were selected as candidate phases.

B. Growth advantage

Along the melt pool boundaries, a cellular microstructure (with elemental partitioning in Cr and Mo) is observed for both steels, see Figure III-15. This indicates that the solidification consistently starts in the A mode through epitaxy from the underlying melt pools. However, at a certain distance from the melt pool boundaries for Steel 2, an apparent shift to mode F takes place. This transition suggests that the

nucleation of ferrite occurs, and this initial ferrite seed must possess a growth advantage to expand at the expense of austenite. In Fukumoto's study [145], the growth advantage of austenite over ferrite has been quantitatively assessed through a dendrite tip model. The authors' model enables the computation of the dendrite tip temperature for both phases at varying solidification velocities, whereby the phase with the higher dendrite tip temperature exhibits a superior growth rate. In Fukumoto's research, a shift from primary ferrite to primary austenite during solidification occurred at a velocity of 30 mm/s for a Ni_{eq}/Cr_{eq} ratio of 1.47 (calculated using the WRC 92 formula), see Figure III-22. In the case of Steel 2, the Ni_{eq}/Cr_{eq} ratio is equal to 1.55, slightly higher than the Fukumoto's ratio. Therefore, it can be assumed that the transition will take place at a higher solidification velocity. In this study, the laser speed employed is 800 mm/s, corresponding to the maximum achievable solidification velocity. However, this value can vary from 0 to this maximum value.

Thus, it can be hypothesized that in regions characterized by relatively low solidification velocities, the growth advantage might promote a solidification mode with primary ferrite instead of primary austenite. This is consistent with the presence of regions supposedly solidifying in primary ferrite close to the melt pool boundaries, regions where the solidification velocity is expected to be the lowest in the melt pool. However, this hypothesis would require further validation through more advanced simulations, taking into consideration the composition of the alloy.

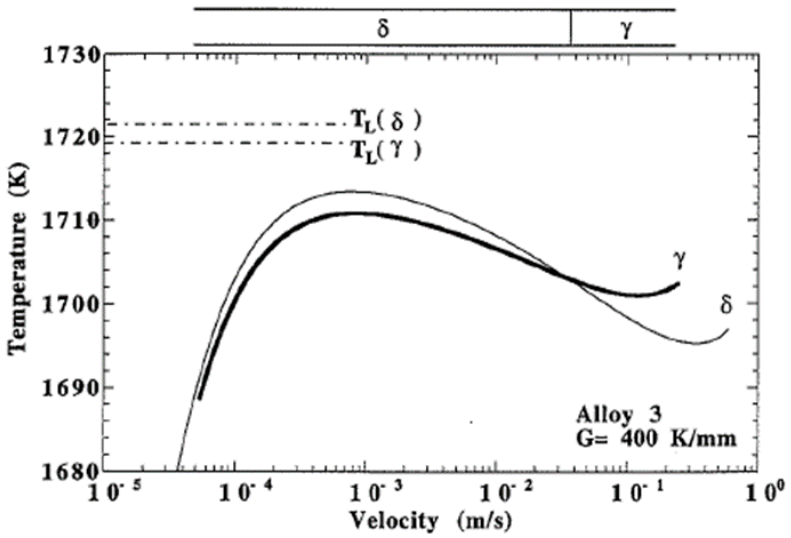

Figure III-22: Dendrite tip temperature for an alloy Fe-Cr-Ni-C with a Ni_{eq}/Cr_{eq} ratio of 1.47. From [145].

C. Homogenization: removal of microsegregation through diffusion in the regions solidifying in primary ferrite

To produce areas without microsegregation, diffusion is required over distances larger than the characteristic length of the microsegregation, i.e. half of the intercellular spacing (here ~200-300 nm). In other words, it means that microsegregation would have enough time to be suppressed through diffusion during cooling in the solid state. During isothermal heat treatment, a diffusion distance can be defined by the length where the ratio between the minimum and maximum value is e^{-1}~0.37 ($x=2*\sqrt{(Dt)}$), if the initial condition is a Dirac peak of the diffusive element [30]. This definition of the diffusion distance will be used considering a linear cooling rate, and the diffusion profile is simulated with Thermocalc

using Dictra and the Mob2 mobility database. The temperature step size is set at 10K, and the cooling rate at 10^5°C/s. When considering the equilibrium phase diagram with only the liquid and the austenite phase retained, the solidus temperature is computed to be 1420°C. However, if we select only the liquid and ferrite, the solidus temperature is determined to be 1400°C. These will be the initial temperatures considered in the subsequent calculations. Cumulative diffusion distance is then estimated for Ni in both phases (Ni is the element that partitions when the solidification is ferritic), see Figure III-23. One can see that the diffusion distance is 10 times higher in ferrite than in austenite and reaches 200 nm in the ferrite. Assuming an intercellular spacing of ferrite that is similar to that of the austenite (which is consistent with our observations), the diffusion length (200 nm) of Ni upon cooling is half the intercellular spacing. Thus, it can account for the suppression of microsegregation in the regions having solidified in primary ferrite.

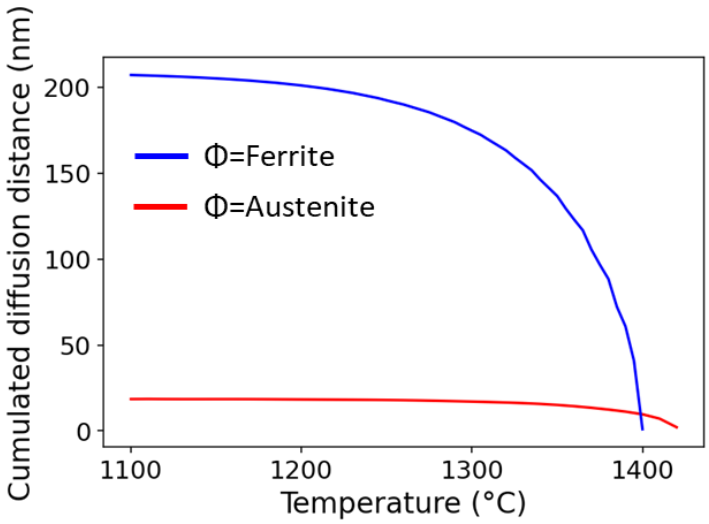

Figure III-23: Cumulated diffusion distance of Ni for two phases at a cooling rate of 10^5°C/s.

D. Velocity of the α/γ interface

To evaluate if a massive transformation could have time to fully transform the primary ferrite into austenite during LPBF, the distance to be traveled by the interface must be around 30 µm, the typical size of the ferrite grains at the end of solidification, see Figure III-15. The distance traveled by the interface α/γ will be estimated and compared to the typical ferritic domain size.

Results from the Ph.D. thesis of Chehab suggest that a massive transformation could occur only when the alloy is in a single-phase domain [26]. From Thermocalc, there is a single-phase domain in Steel 2 between 1250°C and 700°C. The interface velocity of the massive transformation is controlled by the interface mobility. This can be written as:

$$v_{inter} = M * \Delta G \quad \text{(III-4)}$$

With v the interface velocity, M the mobility of interface and ΔG the difference in Gibbs energy between the two phases (here ferrite and austenite). A review from Hillert [146] reports some data to estimate the mobility of the interface α/γ in Fe alloys during a massive transformation. From this review, the expression below is given:

$$M = C * \exp\left(-\frac{Q}{RT}\right) \quad \text{(III-5)}$$

With C the pre-exponential coefficient, which is between 0.058 to 2.4 m.mol/(J.s) and Q the energy of re organization of the interface, which is measured at 140 KJ/mol. The difference in Gibbs energy is calculated from Thermocalc (TCFE11 database). The cumulative distance of the interface L is calculated for a cooling rate (c_r) of 10^5°C/s for the two pre-exponential coefficients:

$$L = \int_{700}^{1250} v_{inter}(T) * \frac{dT}{c_r} \quad \text{(III-6)}$$

This calculation implicitly assumed that the temperature is uniform within the melt pool, a hypothesis that is reasonable[1]. Results are shown in Figure III-24 (a). There is a large variation in the results depending on the choice of the pre-exponential factor. For the higher coefficient (2.4 m.mol/(J.s)), the cumulated distance is ~14 µm, while it is only 0.3 µm for the lower coefficient (0.058 m.mol/(J.s)). The larger distance is half the size of the size of the ferrite grains inherited from solidification (~30 µm). With this result in mind, one could expect to observe residual ferrite in the as-built microstructure of Steel 2 but this was not the case. One could argue that ferrite could be transformed during the intrinsic heat treatment undergone by the sample during LPBF. However, there is no residual ferrite in the last layer neither: this was verified by collecting an EBSD map with a step size of 100 nm, see Figure III-24(b). This result does not seem consistent with the hypothesis of a massive transformation. However, one should note that this result is obtained by assuming a linear cooling rate. It is possible that the phase transformation α/γ is exothermic and this would modify the linear cooling rate. Moreover, the data used to calculate the velocity come from a Fe binary dilute alloy, with a lot of uncertainties as shown by the deviation between the two exponential pre-factors. This can lead to significant variations.

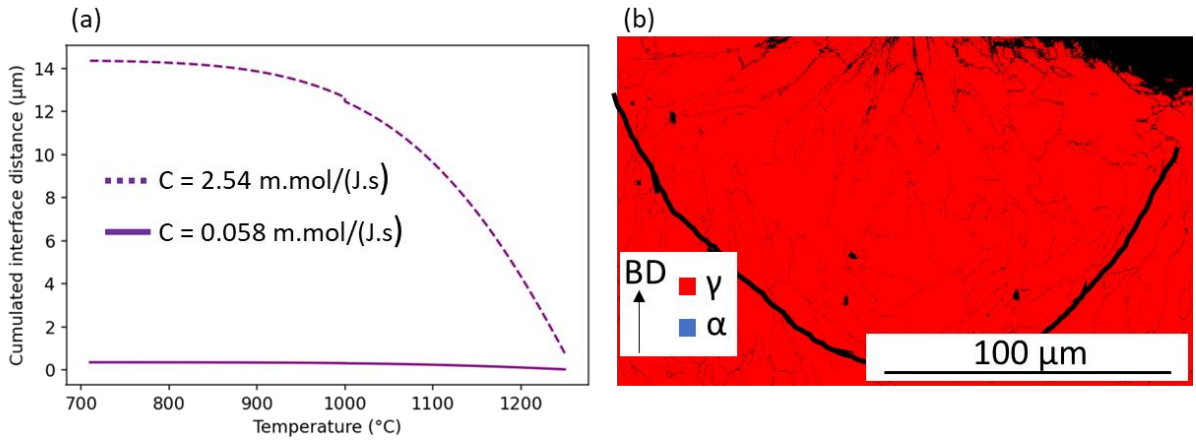

Figure III-24: (a) Cumulative interface distance traveled by the α/γ interface for a cooling rate of 10^5 °C/s. (b) EBSD phase map collected in the last layer of the as-built microstructure of Steel 2.

[1] The difference in temperature between the position of the interface and the initial starting point is given by ΔT = G*L. If one chooses G=10^6 K/m, typical gradient encountered in LPBF solidification [61], and L=15 µm, the value of the cumulative interface distance, ΔT=15K, which is not significant.

III.3.4.4 Summary

In this section, we demonstrate that the microstructure of Steel 2 is heterogeneous, encompassing a mixture of segregated and non-segregated areas. Σ3 twin boundaries are predominantly found in non-segregated areas. Additionally, we found no discernible differences between these regions in terms of hardness or local composition. We have established that the observation of segregated and non-segregated areas is in line with the old welding literature[21], [29], [147], indicating a shift in solidification mode from A mode to F mode, followed by a massive transformation of ferrite into austenite. In a recent study dedicated to 316L processed by LPBF, the authors showed the presence of areas with Ni-rich interdendritic regions [143], which is the signature of a ferritic solidification. We investigated whether this solidification mode is compatible with the high cooling rates in L-PBF. It appears that the growth of ferrite might have an advantage over austenite, particularly in regions with low solidification velocity near the melt pool boundaries. Microsegregation could be removed in the ferrite due to its higher diffusion coefficient compared to austenite, and potentially due to a smaller intercellular spacing in ferrite. Nevertheless, our calculations of the α/γ interface velocity suggest that the transformation interface during the massive transformation process is too slow to allow the complete transformation of ferrite into austenite. However, those calculations should be taken with caution because of the uncertainties.

A schematic of the hypothesized mechanism that could induce the finer grains and a higher density of twin boundaries in Steel 2 in comparison with Steel 1 is shown in Figure III-25.

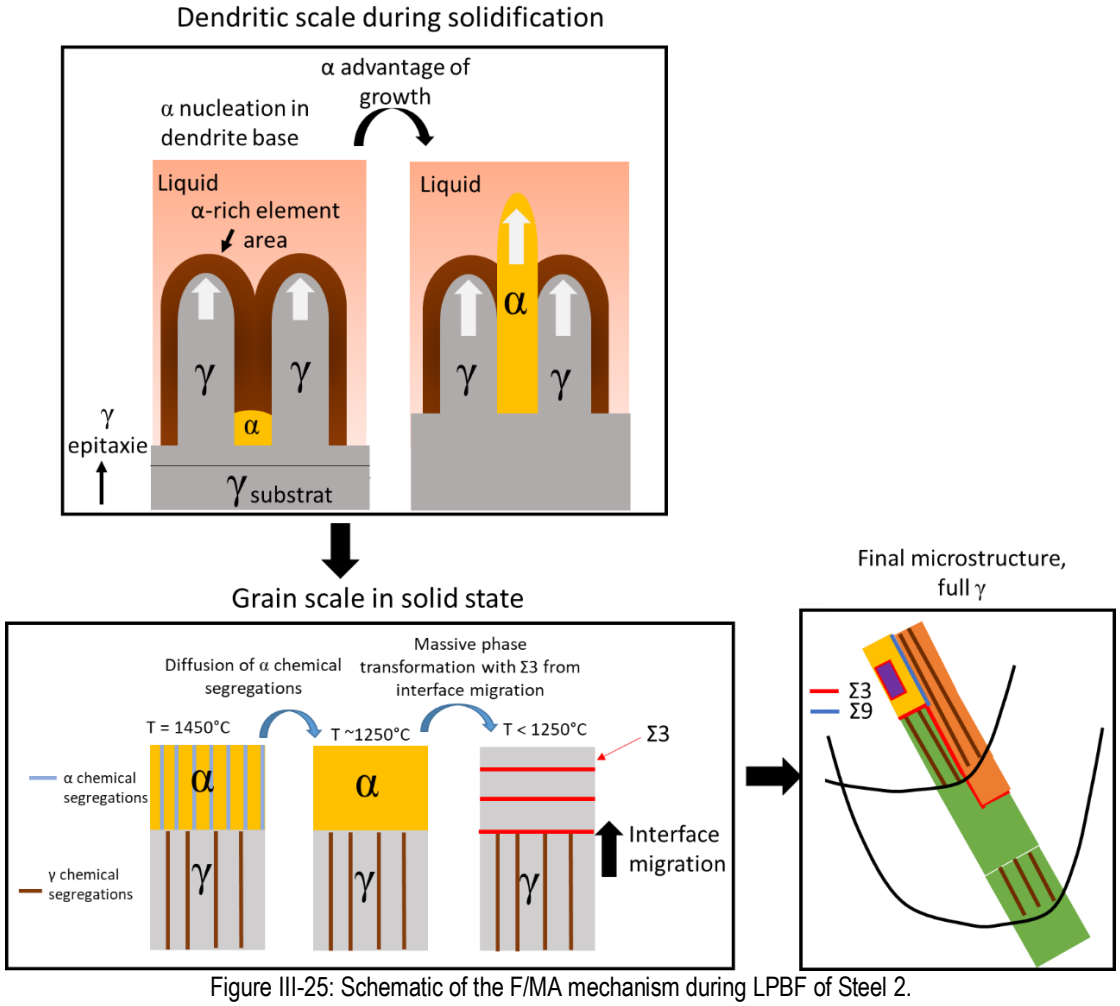

Figure III-25: Schematic of the F/MA mechanism during LPBF of Steel 2.

At this point, we have two possible hypotheses to account for the peculiar microstructure of Steel 2. On the one hand, the IRSO-based mechanisms could explain the twin boundaries, the grain refinement, and the high number of fivefold symmetries found between neighbor grains, but this does not explain the absence of microsegregation in Cr and Mo in some areas. On the other hand, the difference in solidification mode is a reasonable explanation of the absence of Cr-microsegregation in some areas, but does not explain the high density of the fivefold symmetry axes. Both hypotheses can explain the twin boundaries that propagate over several melt pools; the first with the mechanism of ISRO-induced stacking fault mechanism (conjecture), and the second with a mechanism of growth accident during migration of the α/γ interface.

To come to a decision on the most consistent hypothesis, we conducted a literature review by looking at the effect of the nominal chemical composition on the microstructure.

III.4 Links between the nominal composition and microstructure variations

A few studies reporting microstructures having similar microstructural characteristics as the ones highlighted in Steel 2 have been found in the AM-literature dedicated to austenitic stainless steels. In order to draw a correlation between composition and microstructure, we recorded 25 different compositions of austenitic stainless steels (316L or 304L) processed by LPBF. Then, we associated each of them with two different microstructures: a microstructure like that of Steel 1 with large columnar grains, and a microstructure like that of Steel 2, with fine grains and a high density of Σ3 twin boundaries. Based on such a classification, we attempted to correlate the microstructure of Steel 2 with the steel composition. We found 8 compositions showing similar characteristics to the microstructure of Steel 2, and 16 compositions having a microstructure as the one of Steel 1. The compositions with the references are given in Appendix B. Note that the compositions were measured on powders or printed parts depending on the study. However, if the composition reported was that of the powder, we verified that the samples were fabricated using an argon atmosphere to avoid possible nitrogen contamination during the LPBF process.

The only correlation with one element that was established is related to the nitrogen content, see Figure III-26 (a). Interestingly, all compositions that lead to a microstructure like the one of Steel 2 exhibit a low nitrogen content (<300 ppm). However, this correlation can be questionable, because it was reported in the Ph.D. thesis of Hugo Roirand [72] a steel with a composition with a low nitrogen content (100 ppm) that shows a microstructure close to that of Steel 2. This composition is circled in black in Figure III-26 (a).

On the one hand, the low content of N might be considered as a possible explanation for the activation of ISRO-based mechanisms. To further explore this idea, one could make use of ab-initio calculations to predict the amount of ISRO in the undercooled liquid, following approaches already implemented for other systems [148] [149]. While these simulations can only be carried out for binary or, at best, ternary systems, they could bring valuable information on the relation between the liquid structure and the content in C and N. For example, ab-initio calculations of undercooled liquid have shown that there is a

large fraction of ISRO in undercooled Fe and Ni liquid [150], [151], [130]. It has also been shown that the addition of carbon to iron tends to decrease the icosahedral local ordering of the undercooled liquid iron [152]. We think that it could be reasonable to assume that nitrogen plays the same role as carbon, both being small interstitial atoms that strongly stabilize the austenitic phase but this idea would certainly need to be consolidated. However, in [72] the nitrogen content in the steel is 100 ppm and the microstructure exhibits similar characteristics as the one of Steel 2. Thus, this exception shows the limits of our reasoning.

On the other hand, N is a strong austenitic stabilizer. The observed correlation could simply be due to this effect. We then calculated the Cr_{eq}/Ni_{eq} ratio for the different compositions found in the literature using the equations of the WRC 92 diagram [18], by supposing Cu and Nb are not in sufficient quantity in the steels to affect the solidification mode. The correlation is shown in Figure III-26 (b). One can see that all compositions having a ratio lower than 1.5 lead to a microstructure similar to that of Steel 1. On the opposite, all compositions with a ratio higher than 1.6 have a microstructure with the typical characteristics observed in Steel 2. However, in the range between a ratio of 1.5 and 1.6, no clear discrimination can be made.

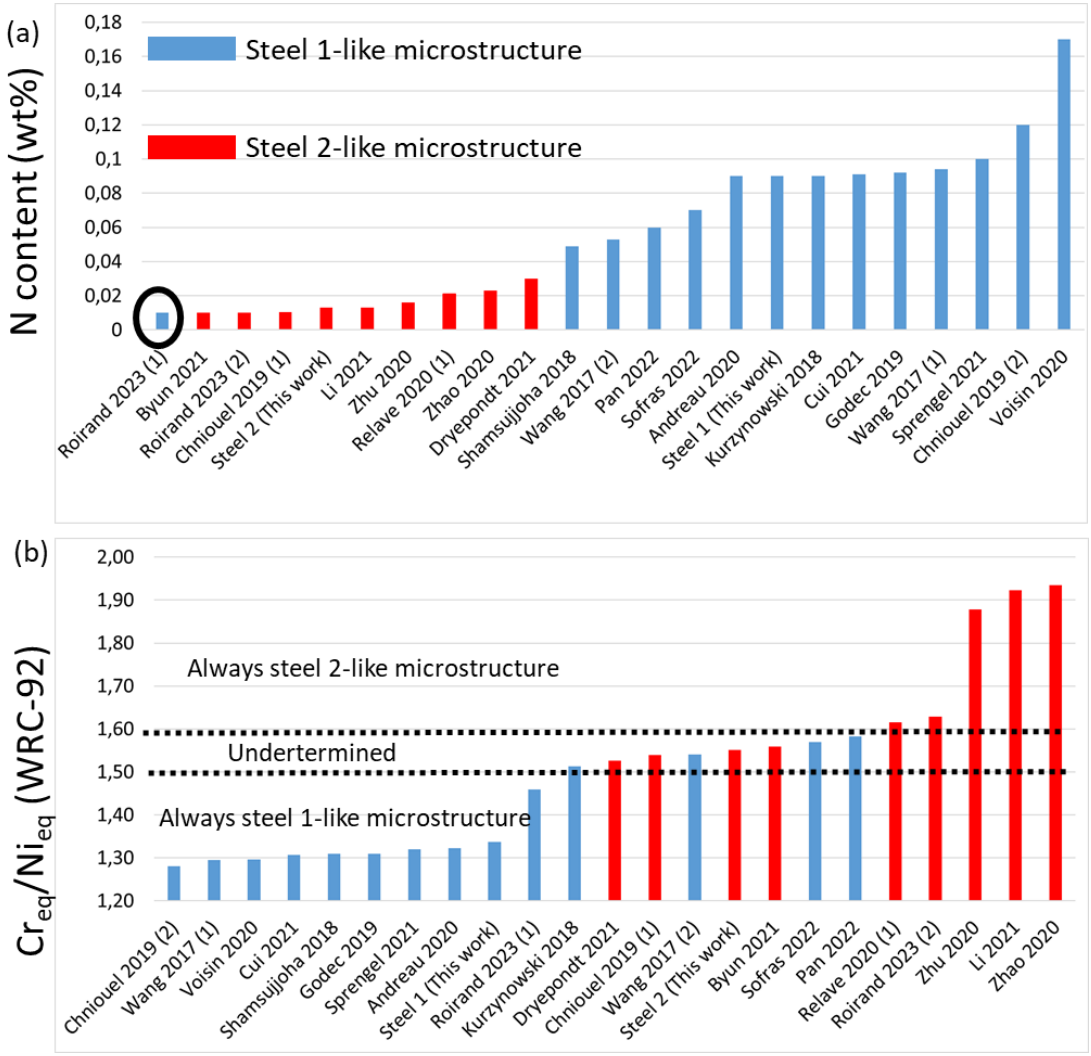

Figure III-26: Correlation between the steel composition and their microstructure. Blue bars represent the steel composition leading to a microstructure close to that of Steel 1, and red bars are associated with microstructure analogous to that of Steel 2: (a) Correlation with the nitrogen content in the steel composition. (b) Correlation with the Cr_{eq}/Ni_{eq} ratio.

The different steel compositions have also been positioned on the WRC-92 diagram [18], see Figure III-27. It becomes relatively obvious that a line can be drawn to discriminate compositions leading to a microstructure similar to that of Steel 1 from those showing a microstructure analogous to the one of Steel 2. This line closely aligns with the composition line which gives a ferrite number of 4 (FN4) and runs parallel to the boundary between the A mode and AF mode in arc-fusion based welding. With this criteria, the composition from Roirand [72] that gives a Steel 1-like microstructure with a low N content is well classified, see circle point in Figure III-27.

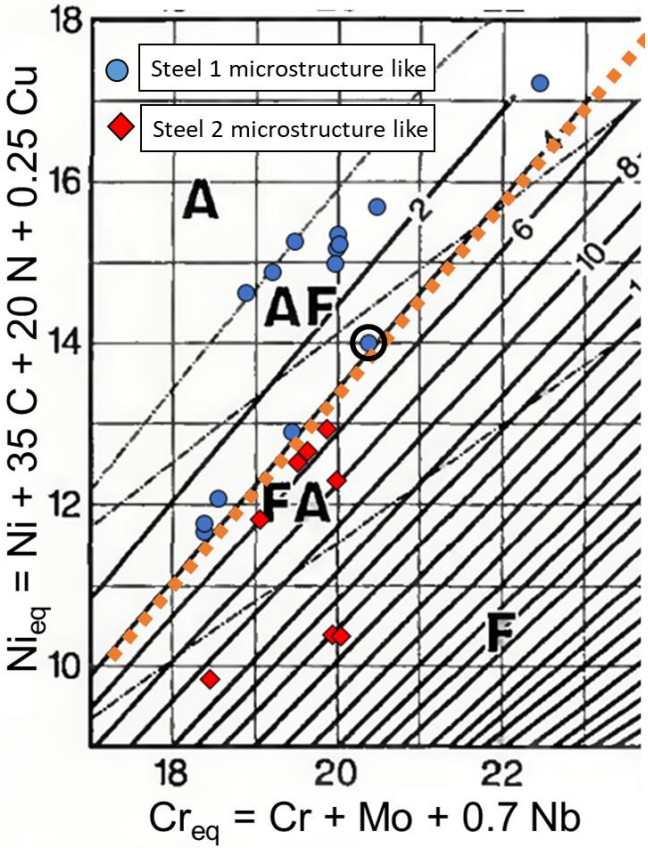

Figure III-27: Position of the different steel compositions in the WRC-92 diagram. The orange line is a hypothesized frontier between compositions showing a Steel 1-like microstructure and microstructures showing similar characteristics as those of Steel 2. The circle point corresponds to the one from ref [72] with a low N content but still gives Steel 1 microstructure-like.

Those complementary considerations based on multiple compositions from the literature show that no insights could be gained regarding the hypothesis of local liquid ordering, while a relatively good correlation can be found for the hypothesis of a difference in solidification mode. This tips the scale toward the hypothesis of a difference in solidification mode.

III.5 Conclusions

III.5.1 Conclusions

Two very different microstructures have been observed in two 316L stainless steels produced with the same set of processing parameters using the same L-PBF machine. Only minor variations of some alloying elements differ between the two steels investigated. One of these microstructures is different from what is usually reported in the literature: it shows finer grains with a more isotropic morphology, a less pronounced <110> texture, and an unexpectedly high fraction of Σ3 twin boundaries. This peculiar microstructure has already been observed in the AM literature dedicated to austenitic stainless steels such as the 316L or 304L grade but was not related to variations of the nominal composition and the authors did not pay attention to the density of twins in their as-built microstructure. Several assumptions have been examined and discussed to identify the mechanisms responsible for such microstructural variations between Steel 1 and Steel 2. Some of those hypotheses do not appear reasonable and have been excluded. Only two of them turned out to be interesting to account for our observations. On the one hand, the presence of fivefold symmetries between neighbors suggests a mechanism based on local liquid ordering. On the other hand, there are some regions, representing approximately 50% of the steel, that exhibit no clear microsegregation in Cr and Mo. This phenomenon is attributed to a shift in solidification mode. This hypothesis appears to be in agreement with the correlations established from multiple compositions from the literature. Interestingly, the hypothesis of a shift in solidification mode was further supported in a recent study from another research group reporting Ni-rich intercellular regions [143].

III.5.2 Main outcomes from Chapter 3

In this Ph.D., two 316L steels processed in the same conditions were studied. In this chapter, their as-built microstructures were characterized and differences have been highlighted. Their responses to different heat treatments and their mechanical properties will be studied in Chapter IV and V. It is then important to keep in mind the differences between the two steels.

Steel 1 presents the typical 316L microstructure observed in many studies, while Steel 2 shows a microstructure with different characteristics, that are summarized in Figure III-28. Steel 1 has large columnar grains oriented along the building directions (D~20 µm), while Steel 2 shows finer grain with a more equiaxed morphology (D~6 µm). Steel 1 has a {110} texture parallel to the building direction (maximum of texture intensity of 5 mrd), while Steel 2 has the same texture but with a different intensity (around 2 mrd). Steel 1 has all of its surface which presents microsegregation in Cr and Mo, while it is the case only for 50% of the surface of Steel 2. In segregated areas, the solidification cell size was found similar between both steels, with a cell size around 450 nm. Both steels have a high density of dislocations arranged in cells superimposed with microsegregation, and oxides enriched in Si and Mn. In Steel 2, no difference in the arrangement of dislocations was observed between segregated and non-segregated areas. The dislocation density between these two areas appears to be similar (no difference in hardness was measured).

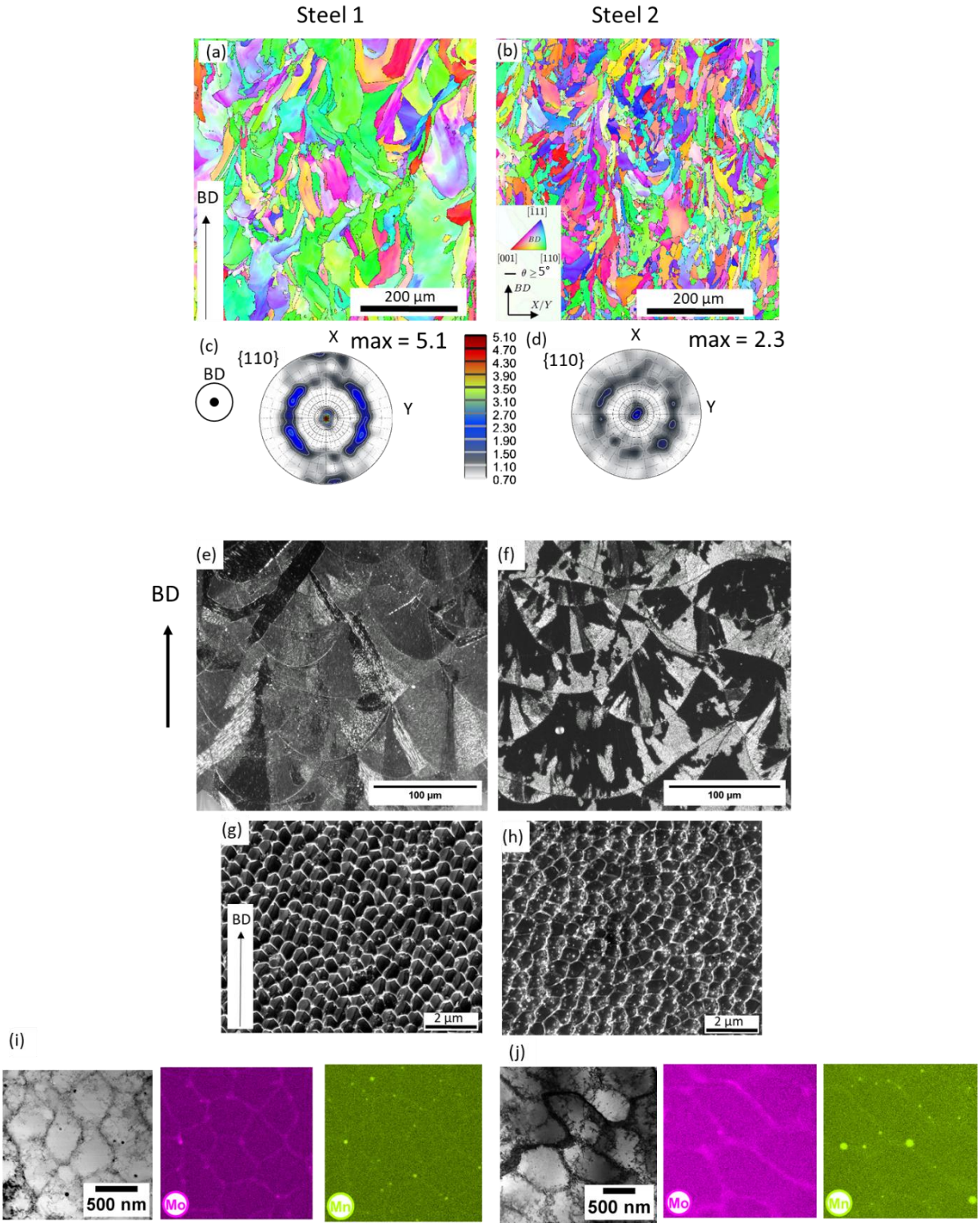

Figure III-28: Summary of the differences between the two steels investigated in this work. (a)-(b) EBSD IPF map of the two steels showing the difference in grain structure. (c)-(d) {110} pole figure of the two steels, showing the difference in texture intensity. (e)-(f) Optical images illustrating the difference in microsegregation between the two steels. Steel 2 has only 50% of its microstructure which shows evidence of microsegregation. (g)-(h) SEM-SE micrographs taken after chemical etching. Both steels have the same solidification cell size. (i)-(j) STEM/EDX images showing dislocations arranged in cells, and microsegregation superimposed to dislocations cells. Oxides have the same chemistry between two steels.

Chapter IV. Evolution of the microstructures and mechanical properties upon heat treatments

IV.1 Introduction

It has been shown in Chapter III that depending on the powder composition, different as-built microstructures can be obtained.

The literature review has shown that austenitic stainless steels are often heat treated to alter their mechanical properties. However, due to the particular characteristics of the as-built microstructures, conventional heat treatments may not be optimized for samples fabricated by L-PBF. The main objective of this chapter is to evaluate the evolution of the microstructures and mechanical properties during post-fabrication heat treatments. Several heat treatments are investigated. The influence of the different microstructural features on the mechanical properties is also discussed.

First, the selected heat treatments and the mechanical testing conditions are detailed. Then, the microstructural evolutions during heat treatments are described. The results of the tensile tests are given in the third section of this chapter. The characterization of plastically deformed specimens allows us to shed light on the mechanisms controlling the plastic tensile response of the materials investigated. The relationships between the microstructure and the mechanical properties are discussed. We estimate the different strengthening contributions to the yield stress and we identify the mechanisms responsible for the strain hardening.

IV.2 Methodology: design of heat treatments

Three heat treatments have been chosen and applied on both steels (Steel 1 and Steel 2). They were carried out under air, and the samples were introduced in the hot furnace. The heat treated samples were prepared from the 10 × 56 × 56 mm^3 additively manufactured cubes.

The first heat treatment is a **stress relief** performed at 600°C for 1h followed by air cooling. The role of this heat treatment is to reduce the residual stresses arising from the fabrication. It is a common practice in welding and additive manufacturing to reduce residual stresses because they can negatively impact the mechanical properties. 600°C is in the range of the stress relief heat treatments applied to austenitic stainless steels in welding [19]. All the microstructural characteristics (grains, microsegregation, dislocations, precipitates) are expected to be nearly unaffected by the stress relief. This heat treatment was systematically applied prior to any other heat treatment.

The second heat treatment consists of a stress relief treatment, followed by additional annealing at 900°C for 1h and followed by water quenching. The objective of this heat treatment is to remove the microsegregation (elemental partitioning during solidification) to homogenize the microstructure through diffusion [50], [66], [72], [83]. This heat treatment can thus be qualified as a **homogenization** treatment. The network of dislocations is also expected to vanish due to extended recovery [50], [66], [72], [83]. Oxides can possibly grow [66], [72]. However, no change in grain size or morphology is expected after 900°C/1h [50], [66], [72], [83].

The third heat treatment consists of first a stress relief, followed by an annealing at 1200°C and water quenching. Steel 1 was exposed for 1h, while Steel 2 was exposed for 2h at 1200°C. The aim of this

heat treatment was to fully recrystallize the material, inducing the formation of new equiaxed grains free of dislocations [50], [77], [81]. This can be qualified as a **recrystallization** heat treatment. Oxide coalescence is also a phenomenon typically observed at this temperature [77], [81]. The reason for selecting a different annealing time for the two steels is that they have different recrystallization kinetics [153]. This has been extensively investigated by Edouard De Sonis during in Ph.D. The differences in the time of heat treatment at 1200°C to achieve a fully recrystallized microstructure result from suggestions from Edouard De Sonis. The different heat treatments described above are schematically represented in Figure IV-1.

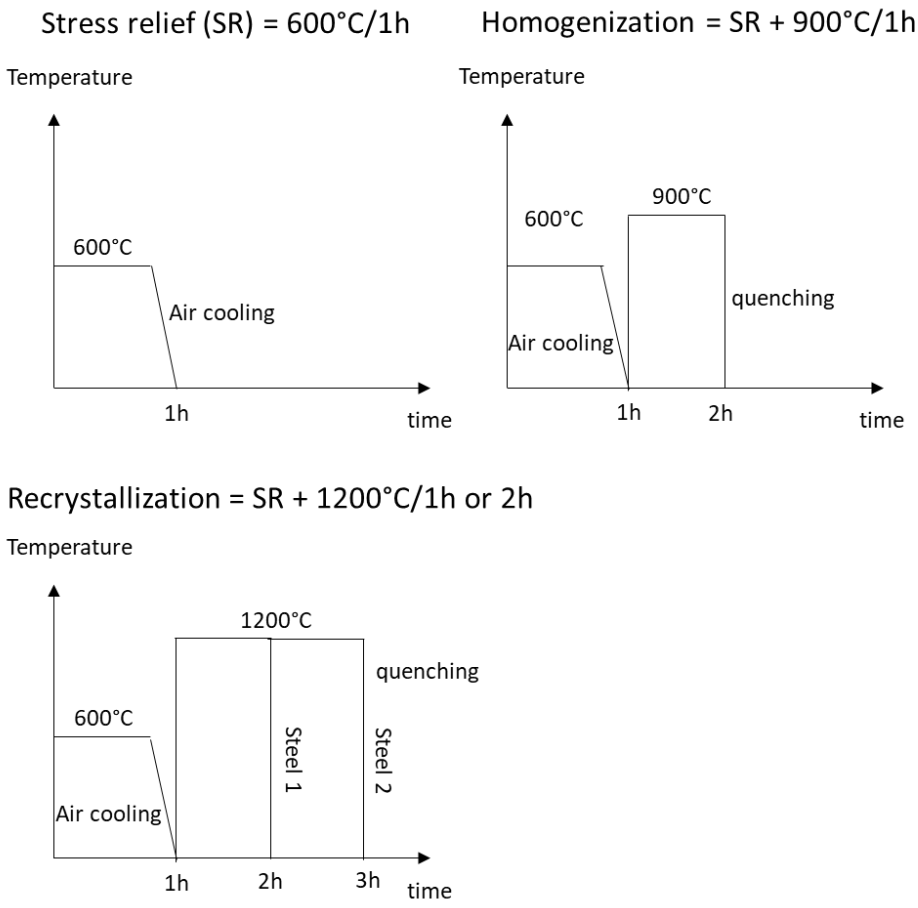

Figure IV-1: Schematic representation of the various heat treatments investigated in this work.

The samples were then all tested in tension, with a constant strain rate of 10^{-3} s^{-1}. The deformation was measured using digital image correlation (DIC). The mechanical tests were carried out along different loading directions, namely, in the X, Y, and Z axes for Steel 1 and only in the Y and Z directions for Steel 2. The X and Y directions of Steel 1 are tested because their orientation relative to the argon flux in the L-PBF machine is different. This can induce differences in mechanical properties. However, for Steel 2, the argon flux has the same angle relative to the X or Y axis (45°). Therefore, it is not expected to see any difference in mechanical properties between the X and Y directions in Steel 2. A summary of all the conditions tested is given in Figure IV-2.

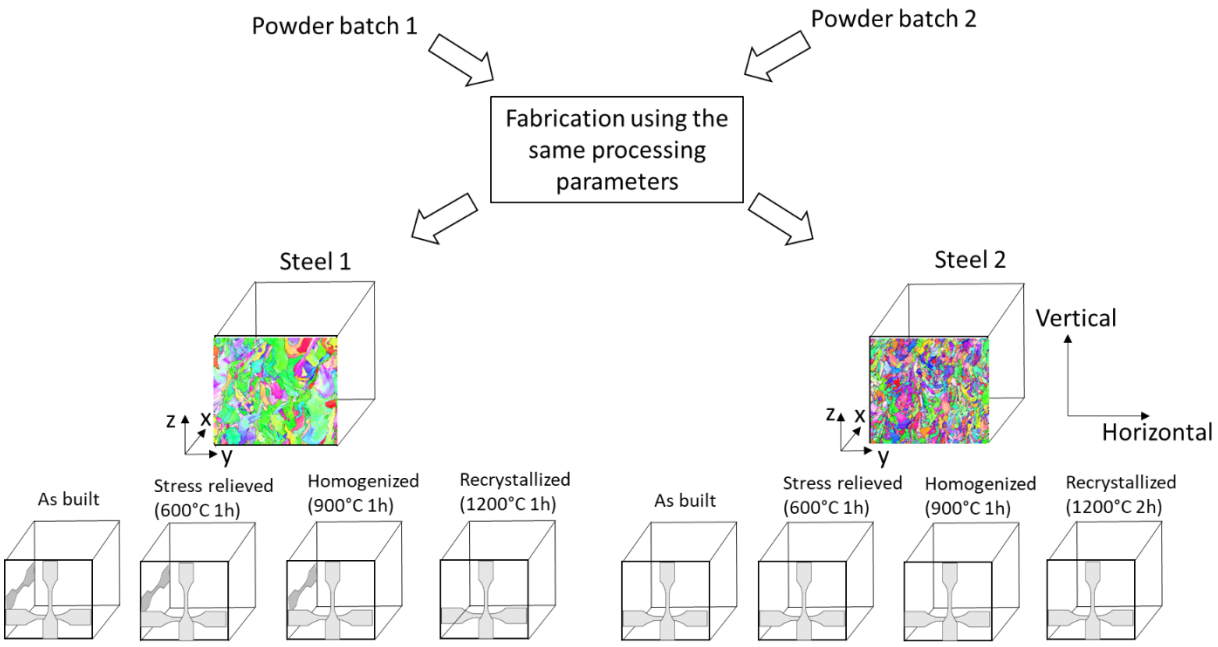

Figure IV-2: Summary of all the conditions tested to record the mechanical properties.

IV.3 Evolution of the microstructure with heat treatments

IV.3.1 Steel 2

In this section, the evolution of the microstructure with heat treatments is presented only for Steel 2. This steel is selected because it is the one that was the more deeply characterized and Steel 1 follows mostly the same evolutions upon heat treatments. Differences in microstructure evolution between Steel 1 and Steel 2 are highlighted.

IV.3.1.1 Evolutions of grains and texture

Figure IV-3 shows the evolution of the grain structure as a function of heat treatment. The grain structure (size, morphology, and density of twin boundaries) is unaffected after the heat treatment at 600°C/1h or at 900°C/1h, and the grain size is equal to 6 µm (average intercept method in X, Y and Z). This is consistent with the literature, where no recrystallization is reported at temperatures below 1000°C [50], [78], [79].

After the heat treatment at 1200°C/2h, the steel shows a recrystallized microstructure with grains showing an equiaxed morphology. A recrystallized grain is defined as a grain with its grain orientation spread lower than 1°. Based on such a definition, the fraction of recrystallized grains is estimated to be about 98%. The recrystallized grain size is measured to be 23 µm. There is a large increase in twin boundaries fraction with recrystallization, from 30% to 70% of the grain boundaries. In other words, 70% of the interfaces are twin boundaries after recrystallization.

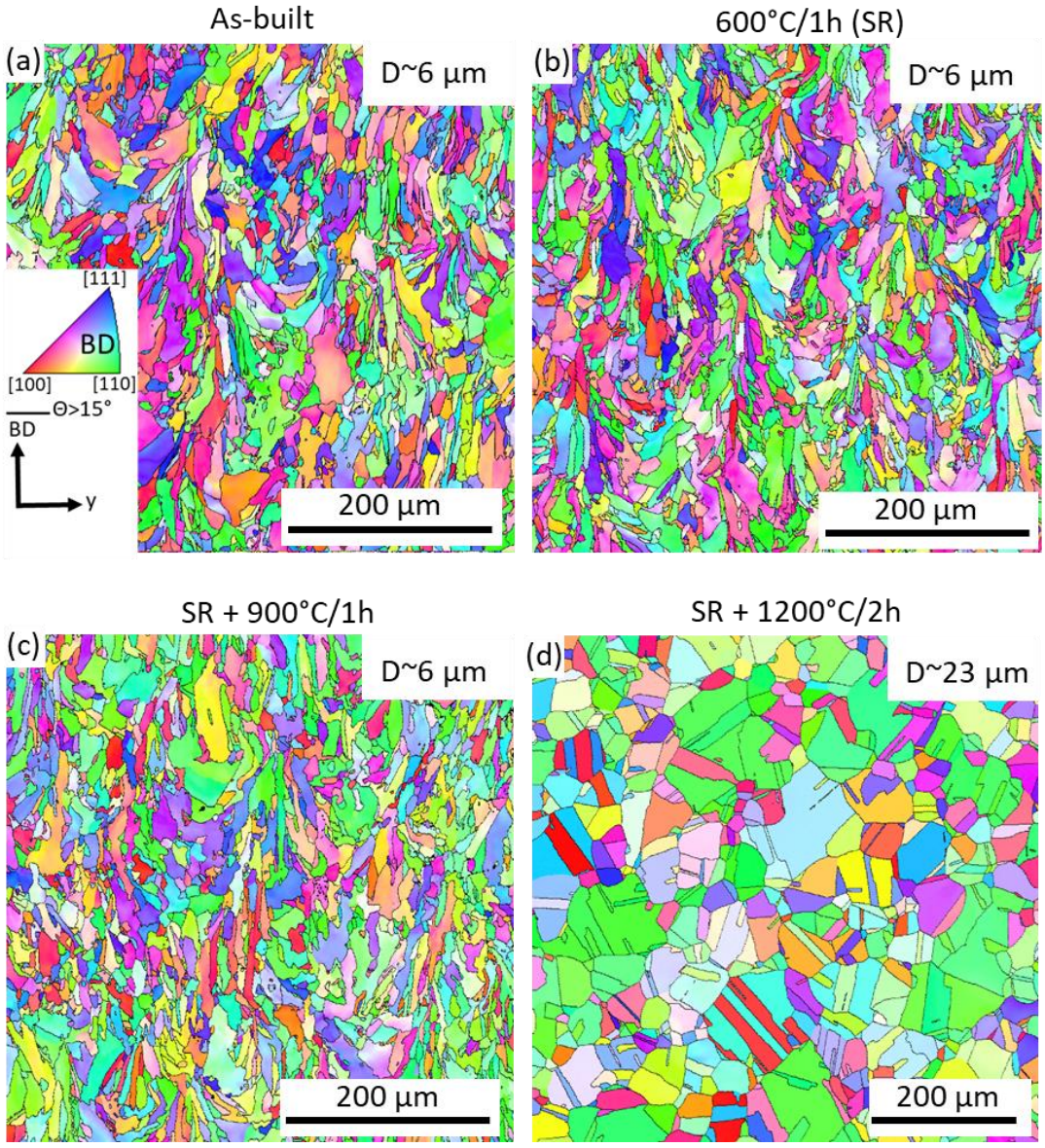

Figure IV-3: IPF EBSD maps for Steel 2 as a function of the heat treatment. (a) As-built, (b) After 600°C/1h (SR), (c) after SR + 900°C/1h, (d) after SR + 1200°C/2h.

Texture was measured only for the as-built and recrystallized conditions. Since there is no recrystallization after 600°C/1h and 900°C/1h, the texture is supposed to be unchanged in comparison with the as-built texture. The (100) and (110) pole figures are shown in Figure IV-4. There is no significant texture evolution during the heat treatments between the as-built and 1200°C conditions. Texture in the as-built sample was already relatively weak, with a maximum intensity of 2.3. Only a slight (110)//BD texture was present. After recrystallization, the maximum intensity evolves from 2.3 to 2.1 mrd, which can be considered a negligible variation.

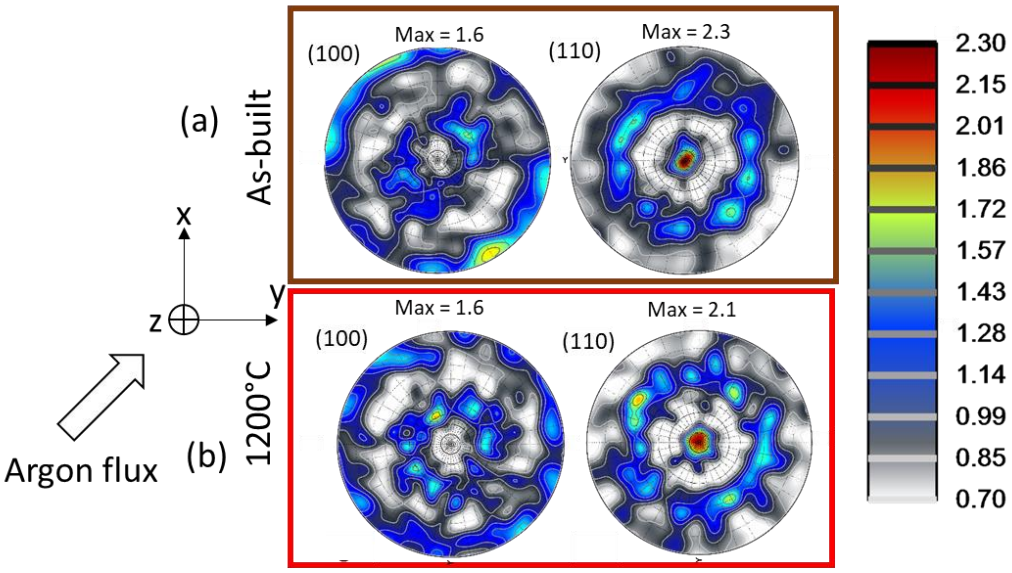

Figure IV-4: (100) and (110) pole figures determined using EBSD for Steel 2: (a) in the as-built conditions and (b) after recrystallization (SR+1200°C/2h).

IV.3.1.2 Evolution of the microsegregation

Figure IV-5 shows the modification of microsegregation in Cr and Mo with heat treatment. These two are the main segregated elements that are typical of an austenitic solidification. These remain after 600°C/1h, while they disappear after 900°C/1h as well as after the recrystallization treatment at 1200°C/2h. These observations are in agreement with the work of Voisin et al. [50], and the experiments reported in [50], [66], [72], [83]. This is also in agreement with the estimations of the diffusion lengths given in Table IV-1. After 600°C/1h, the diffusion length is too short compared to half the primary dendrite arm spacing (PDAS), while after SR+900°C/1h, the diffusion distance is larger than half the PDAS. Values for D_o and Q used for the calculations are reported in Table IV-2. It has to be noted that after SR+900°C/1h, a very small amount of σ phase (0.02%) is identified in Steel 2. This amount is not suspected to have any impact on the mechanical properties. The identification is presented in Appendix C.

Table IV-1: Diffusion distance for 600°C 1h and 900°C heat treatment. Calculated with [141], [154].

Diffusion distance ($2\sqrt{(Dt)}$)	Cr (nm)	Mo (nm)	PDAS/2 (nm)
600°C/1h (SR)	4	15	225
SR+900°C/1h	630	1030	225

Table IV-2: Do and Q for Cr and Mo.

	D_0 (m²/s)	Q(KJ)
Cr	1.54×10^{-4}	286
Mo	3.73×10^{-6}	240

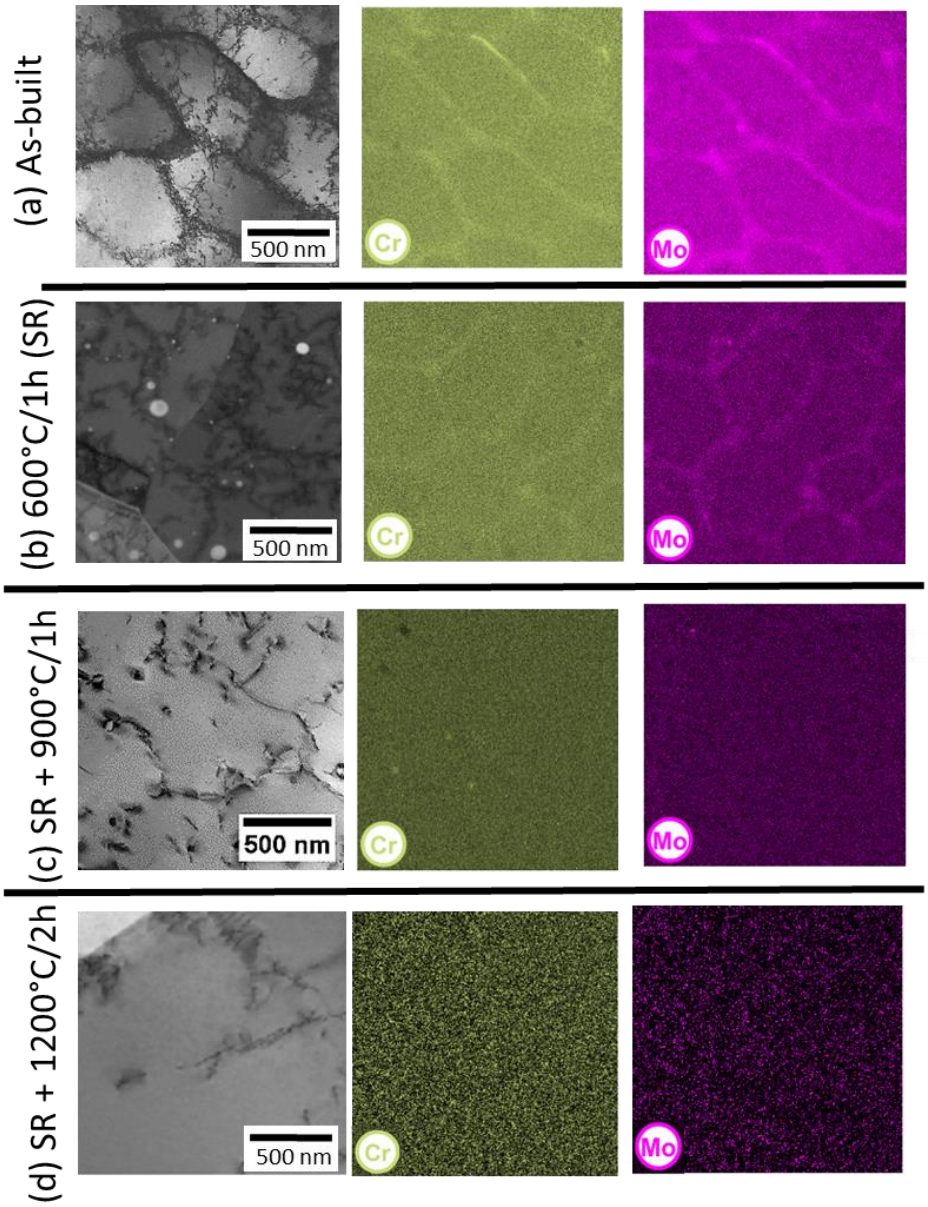

Figure IV-5: EDX count maps to evaluate the presence of microsegregation in Steel 2. (a) As-built, (b) after 600°C/1h (SR), (c) after SR+900°C/1h, and (d) after SR+1200°C/2h.

IV.3.1.3 Evolution of the dislocation arrangement

Examples of the dislocation structures found in the as-built and heat treated samples are shown in Figure IV-6. After 600°C/1h, the dislocation cells are still visible and of roughly the same size (~450 nm). The dislocation density between the as-built and stress relieved state is expected to slightly decrease. However, this is difficult to quantify from TEM images. This suggests that the dislocation density remains of the same order of magnitude (~10^{14} m^{-2} [53]). After 900°C/1h, the dislocation density has significantly decreased, but the average dislocation cell size does not seem to be altered (~450 nm). After 1200°C/2h, there are very few dislocations, and the cells have disappeared. The order of magnitude of the dislocation density for a recrystallized austenitic stainless steel is between 10^{10} m^{-2} and 10^{13} m^{-2} [155], [156].

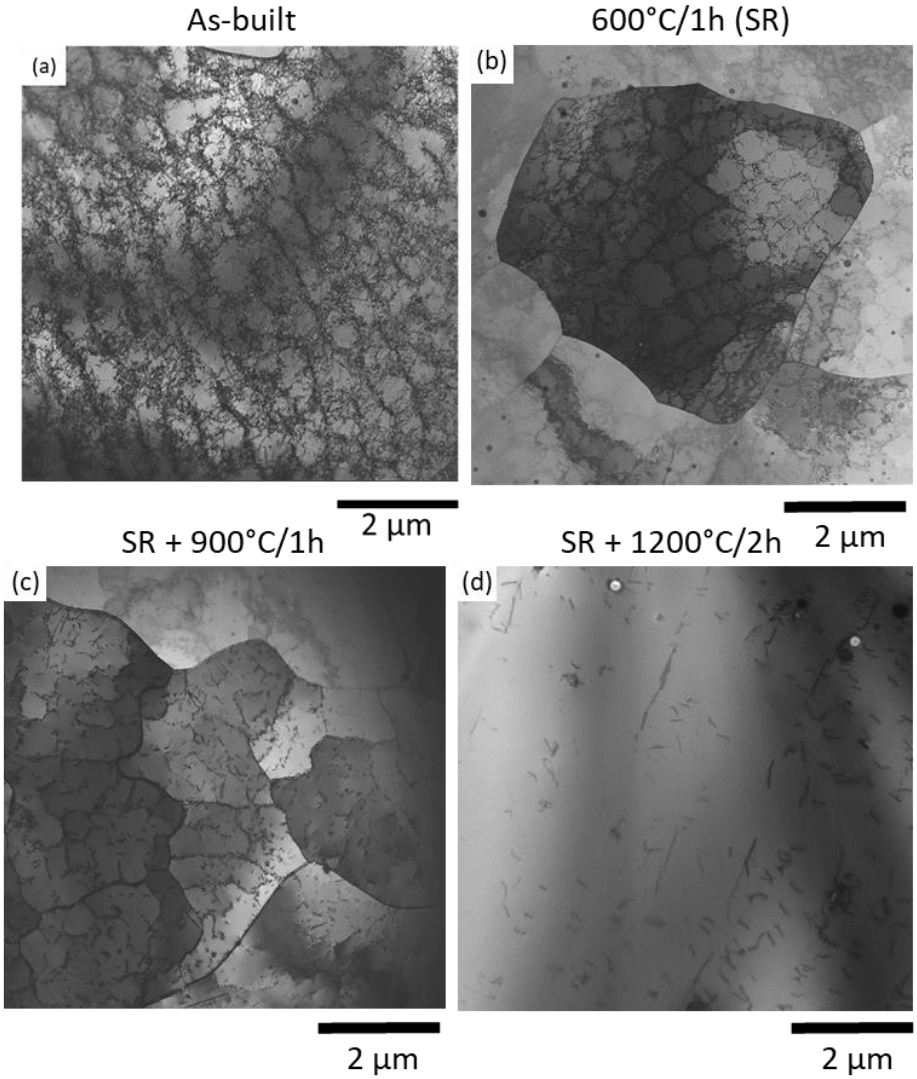

Figure IV-6: STEM bright field taken in <110> zone axis for the different heat treatments. (a) As-built, (b) after 600°C/1h (SR), (c) after SR+900°C/1h, and (d) after SR+1200°C/2h.

IV.3.1.4 Evolution of the oxide population

The evolution of the spatial distribution of oxides was characterized using SEM-BSE images. Images are shown in Figure IV-7. Oxides appear as black dots (since they are enriched in Si and O, their average atomic number is lower than the iron matrix, which makes it appear darker). Interdendritic areas are also visible in brighter contrast (as they are enriched in Mo which is a heavy element). In the as-built state, most of the oxides are preferentially located in the interdendritic regions and have a diameter of approximately 20 nm. This preferential location was also reported in other studies [12], [69]–[71]. The few oxides that are not located in interdendritic are bigger than those located in the interdendritic areas. There is no clear evolution of the oxides after 600°C (Figure IV-7 (b)), as well as after the homogenization treatment at 900°C/1h. After 1200°C/2h, the oxides have significantly coarsened and have a diameter of around 200 nm. It has been shown that they are mostly located at the grain boundaries [153].

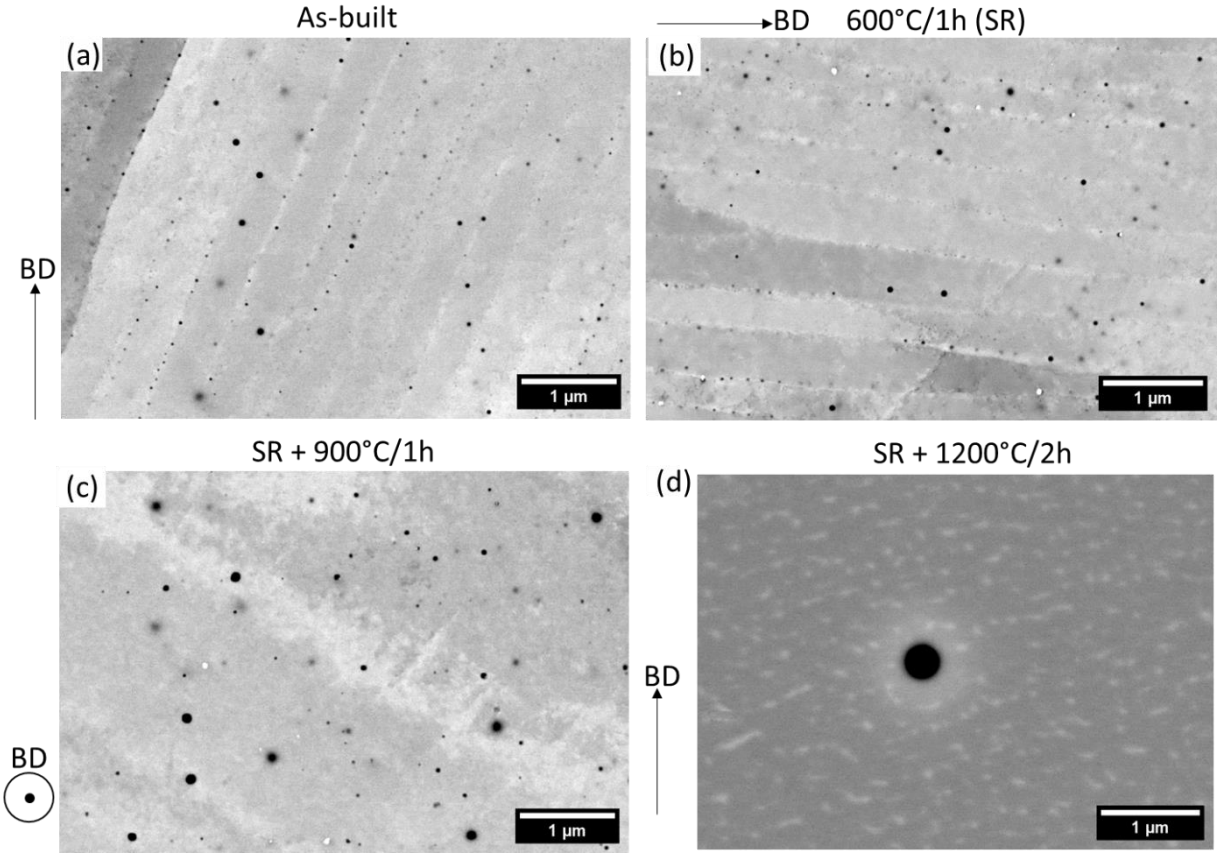

Figure IV-7: SEM-BSE images collected at 20 KeV for different heat treatments. (a) As-built, (b) after 600°C/1h (SR), (c) after SR+900°C/1h, and (d) after SR+1200°C/2h.

The method to estimate the mean oxide diameter, mean distance between the center of particles, and the number density is described in detail in section II.4.3 and is based on SEM images. These values are given in Figure IV-8. The diameter of around 20 nm in the as-built condition is in agreement with the literature, where Voisin [50] and Yan [74] found 15 nm while Riabov [73] found 42 nm. The surface density of 6×10^{12} nb/m² is also consistent with values from the literature. Roirand [72] found in the as-built condition a surface density of 4×10^{12} nb/m², and Riabov [73] found 13×10^{12} nb/m². A coarsening of oxides is observed after 900°C/1h, with an increase of 80% of the average diameter and a decrease of around 50% of the number density. After 1200°C/2h, there is a large coarsening of oxides, with an increase of around a factor 10 of the mean oxides size, and with a surface density decrease by a factor of nearly 100 compared to the as-built conditions. The presence of oxides with a size of 20 nm is a unique feature of the 316L process by LPBF. In a wrought product, the oxygen content is of the order of 10-40 ppm [17] (against 300 ppm in this Ph.D.) and the few oxides present have a diameter above 200 nm. When the 316L is processed by powder metallurgy, the oxygen content is similar to the one found in 316L LPBF, but the size of the oxides is of the order 200 nm [17].

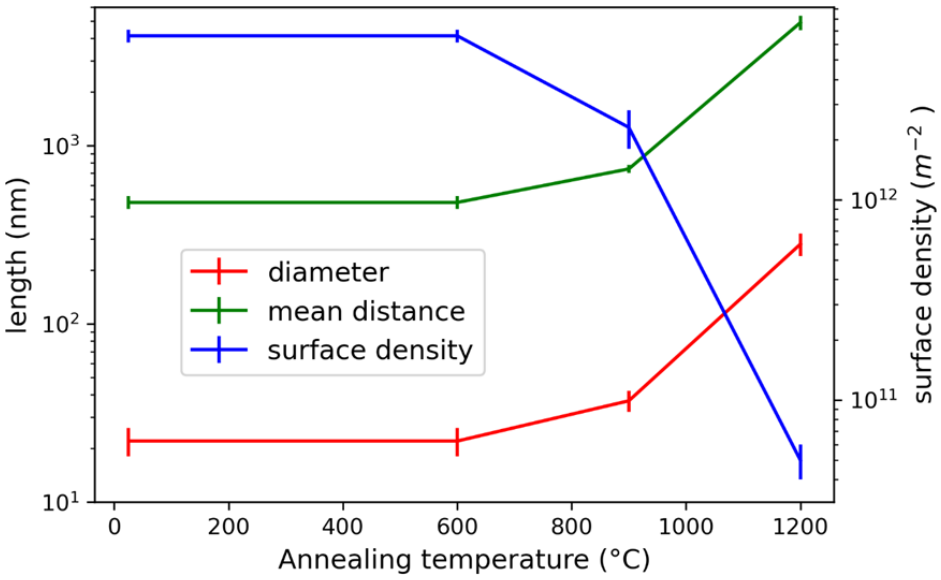

Figure IV-8: Evolution of the oxide population (size, density, and mean distance between particles) as a function of heat treatments.

The chemistry of the oxides was also investigated using EDX in the TEM, see Figure IV-9. No difference in chemistry between the as-built condition and after 600°C/1h is observed. In these conditions, particles are still Mn-Si rich oxides as reported in the literature [50], [72]. After 900°C/1h and 1200°C/2h, most particles are still Mn-Si rich oxides in agreement with the literature [77], [81]. The crystallography of oxides has been characterized and some results are shown in Appendix D.

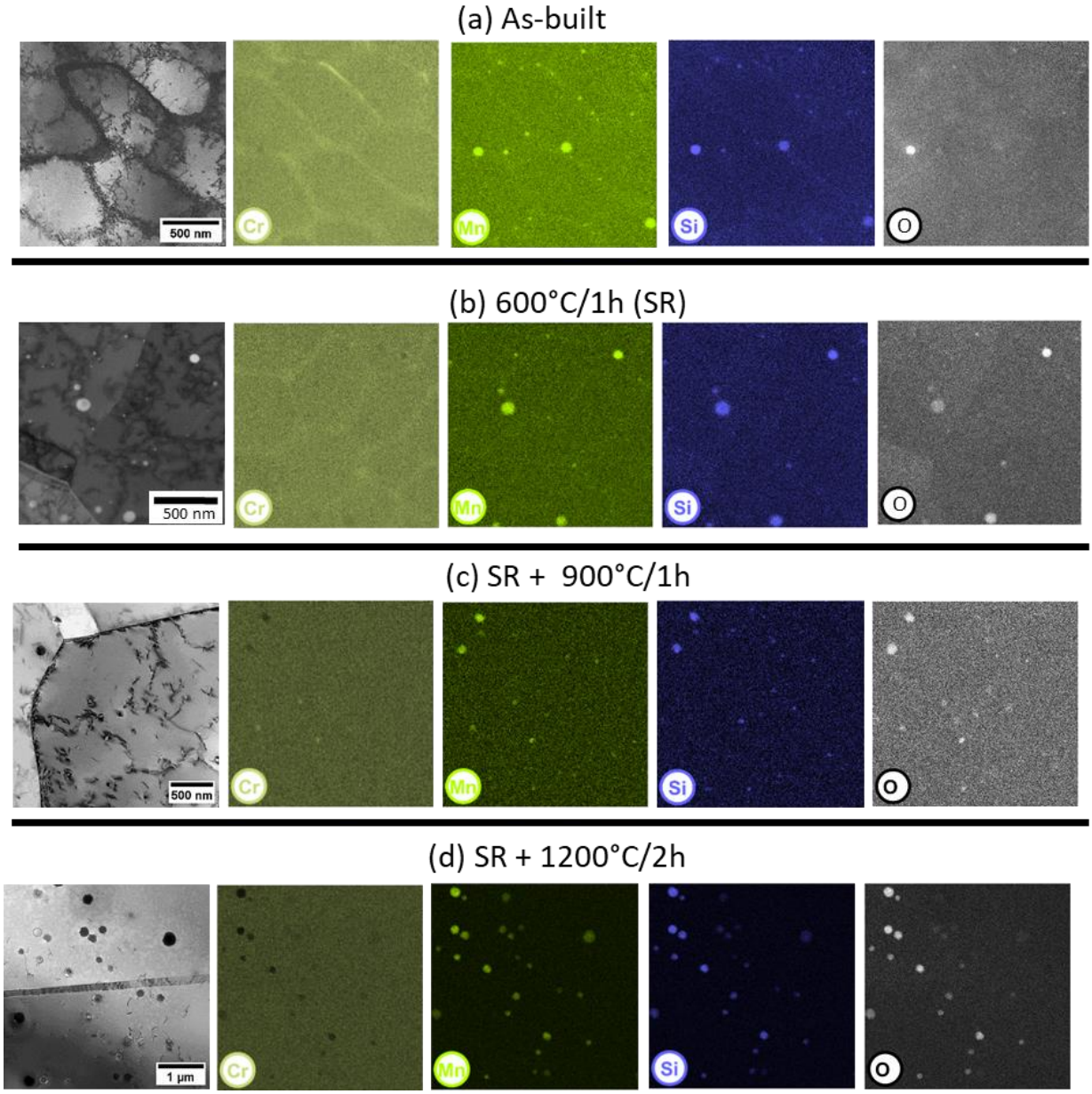

Figure IV-9: EDX count maps to identify the chemistry of oxides in the different materials studied. (a) As-built, (b) after 600°C/1h (SR), (c) after SR+900°C/1h, and (d) after SR+1200°C/2h.

IV.3.2 Comparison between Steel 1 and Steel 2

This section highlights the similarities and differences in microstructure between Steel 1 and Steel 2 after the different heat treatments investigated.

In Steel 1, after 600°C/1h and 900°C/1h, there is no evolution of the grain size, as was observed in Steel 2 (Figure IV-3). After 1200°C/1h, the microstructure is recrystallized, with a fraction of recrystallized grains of nearly 80%. The recrystallized microstructure exhibits equiaxed grains, with a grain size of 25 µm and the fraction of twin boundaries is estimated at about 50% (it was respectively 23 µm and 70% for Steel 2).

The (100) and (110) pole figures for Steel 1 in the as-built conditions and after 1200°C/1h are shown in Figure IV-10. The (100) pole figure does not show a cylindrical symmetry around the build direction. It has a more pronounced <100> intensity along the Y-axis. This non-cylindrical symmetry is likely induced by the process parameter limitation window (section II.2.1), which prevents the laser from scanning the powder bed parallel to the argon flux with a prohibited angle of ± 33° relative to the direction of argon flow. The relation between this parameter and the resulting texture was also observed by Andreau [1]. It has been shown that an unidirectional scan strategy induced a pronounced <100> direction along the scanning direction [49] [77], [109], [56]. It is then consistent to observe that a preferred scanning direction along the Y direction induced a preferred <100> direction along Y. After recrystallization, the texture intensity slightly decreases in Steel 1.

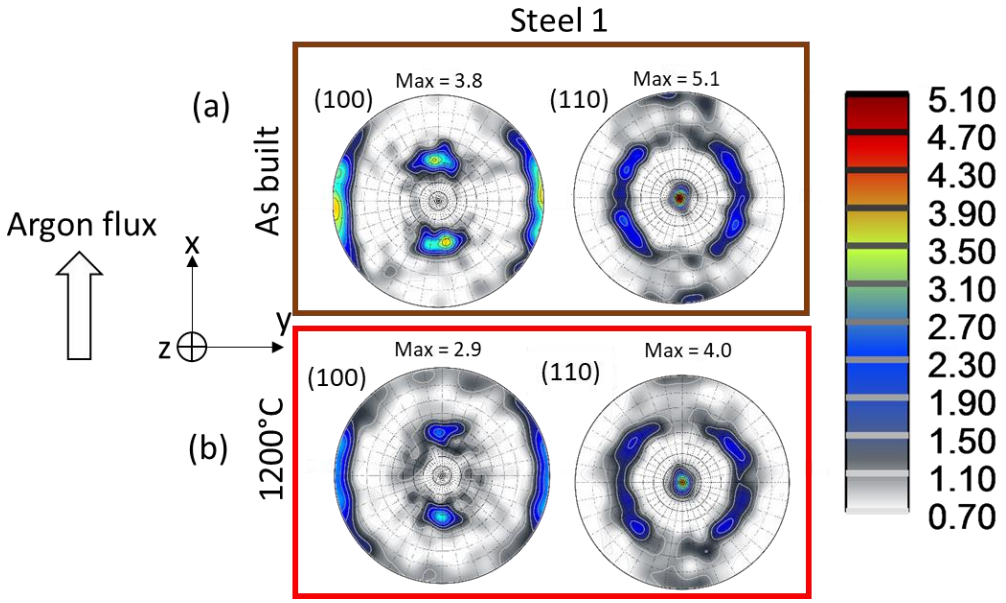

Figure IV-10: (100), (110) pole figures for Steel 1: (a) in the as-built conditions, and (b) after SR+1200°C/1h.

After the different heat treatments, the microsegregation and the dislocation network evolve in the same way in Steel 1 and Steel 2.

The oxide populations in the as-built Steel 1 and Steel 2 are compared in Figure IV-11. One can see that there is not a large difference between Steel 1 and Steel 2 for the diameter (20 ± 4 nm vs. 22 ± 4 nm), surface density (5.3 ± 0.5 10^{12} nb/m² vs. 6.6 ± 0.5 10^{12} nb/m²), and mean distance between particles (530 ± 40 nm vs. 480 ± 40 nm). These values evolve with heat treatments but are found to be similar for both steels. These values are shown in Appendix E.

Between the two steels, there is an important difference in oxygen content (300 vs. 700 ppm). However, this difference in oxygen content does not affect the surface density nor mean diameter of the oxides. One difference is that in Steel 2, there is a few large oxide particles, which do not affect the surface density but account for the higher oxygen content. The mean diameter and surface density are affected by the high number of small particles, which are similar in the two steels. This has been shown by Edouard De Sonis [153], and this was further confirmed using SAXS, see Appendix F.

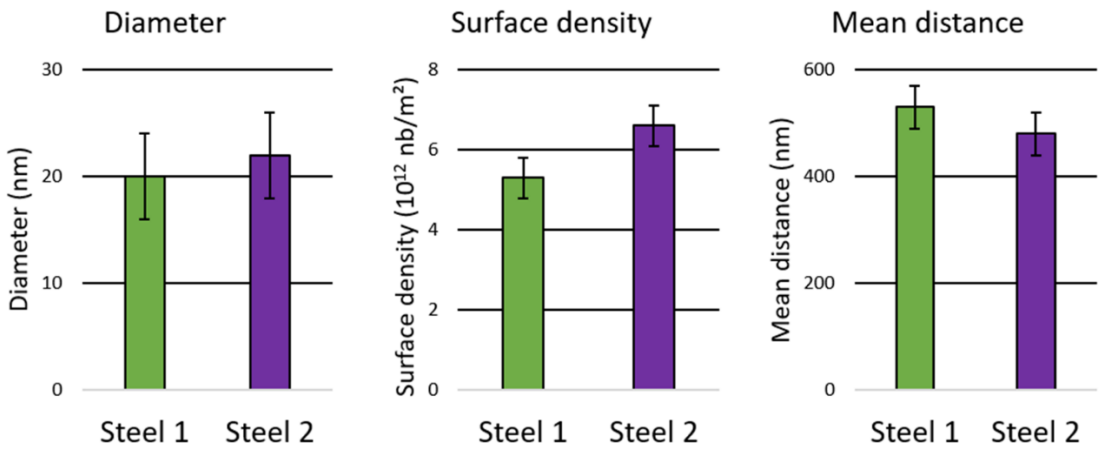

Figure IV-11: Comparison of the oxide population between the as-built Steel 1 and as-built Steel 2 from SEM observations.

IV.3.3 Summary

After a **stress relief heat treatment at 600°C for 1h**, the microstructure remains nearly unchanged in comparison with the as-built conditions: no change in grain size, microsegregation, arrangement of dislocations, and oxide population was evidenced. We just expect a decrease in the residual stresses arising from the processing conditions.

After a **homogenization heat treatment (SR + 900°C/1h)**, no change in grain size was detected. Microsegregation disappears and there is a net decrease in dislocation density. Oxide coalescence was revealed by a reduction of approximately 50% in the number density of oxides. Oxides continue to be preferentially distributed in the former interdendritic regions.

After a **recrystallization heat treatment (SR + 1200°C/1h)** for Steel 1 and 2h for Steel 2, there is nearly full recrystallization of the microstructure. Grains are equiaxed, with a mean grain size of around 20 µm. The texture is modified only in the case of Steel 1, with a decrease in texture intensity, while it is not modified in the case of Steel 2. Oxides undergo an important coalescence, with a decrease in surface density by a factor of nearly 100. Oxides are preferentially located at grain boundaries. The resulting microstructure after this heat treatment at 1200°C is similar to the one achieved in a recrystallized cold-worked product. Distinctions between the recrystallized cold-work product and the recrystallized Steel 2 are characterized by a crystallographic texture (<110>//BD, intensity of 2) and the presence of large oxides with a low surface density.

In the next sections, heat treatments will be called by their effect (stress relief, homogenization, recrystallization) and no longer by their temperature. Table IV-3 gives a summary of the microstructure evolution with heat treatment.

Table IV-3:Summary of the microstructure evolution with heat treatment.

Conditions	Grain morphology and size	Texture	Microsegregation	Arrangement of dislocations	Oxides
As-built	Steel 1: columnar 20 µm	Steel 1: <110>//BD (intensity of 5.1)	Enriched in Cr and Mo in the interdendritic regions	High density of dislocations superimposed to the solidification cells	Preferentially located in solidification cell. Mean diameter = 20 nm
	Steel 2: columnar 6 µm	Steel 2: <110>//BD (intensity of 2.3)			
600°C/1h (stress relief)	Steel 1: columnar 20 µm	Steel 1: <110>//BD (intensity of 5.1)	Enriched in Cr and Mo in the interdendritic regions	High density of dislocations superimposed to the solidification cells	Preferentially located in solidification cell. Mean diameter = 20 nm
	Steel 2: columnar 6 µm	Steel 2: <110>//BD (intensity of 2.3)			
SR+900°C 1/h (Homogenization)	Steel 1: columnar 20 µm	Steel 1: <110>//BD (intensity of 5.1)	None	Decrease of dislocation density. Preferentially located to the former solidification cell.	Preferentially located in former solidification cell. Mean diameter = 30 nm
	Steel 2: columnar 6 µm	Steel 2: <110>//BD (intensity of 2.3)			
SR + 1200°C/1h or 2h (Recrystallization)	Steel 1: equiaxed 25 µm	Steel 1: <110>//BD (intensity of 4.1)	None	Low dislocation density with no arrangement	Preferentially located in grain boundaries. Mean diameter = 200 nm
	Steel 2: equiaxed 23 µm	Steel 2: <110>//BD (intensity of 2.1)			

IV.4 Tensile properties in the as-built condition

IV.4.1 Steel 2

The engineering stress-strain curves for Steel 2 in the as-built conditions as a function of the loading direction are given in Figure IV-12 (a). The sample tested in the horizontal direction shows a slightly higher yield stress than the sample loaded in the vertical direction. This goes along with an increase in the ultimate tensile stress (UTS) but a decrease in total elongation. The horizontal and vertical direction meets the RCC-M standard, i.e. YS =175 MPa, UTS = 490 MPa, A% = 45%.

The true stress-strain curve is shown in Figure IV-12 (b). The horizontal direction exhibits a lower uniform elongation. The work hardening rate as a function of the true stress is given in Figure IV-12 (c). The work hardening can be divided into two stages, stage II with a large decrease in work hardening, and stage III which shows a lower decrease in work hardening. The horizontal direction shows an initial work hardening higher than the vertical direction. The decrease in work hardening for the stage III is linear for the horizontal direction, but is not for the vertical direction, suggesting the occurrence of another deformation mechanism in addition to dislocation glide.

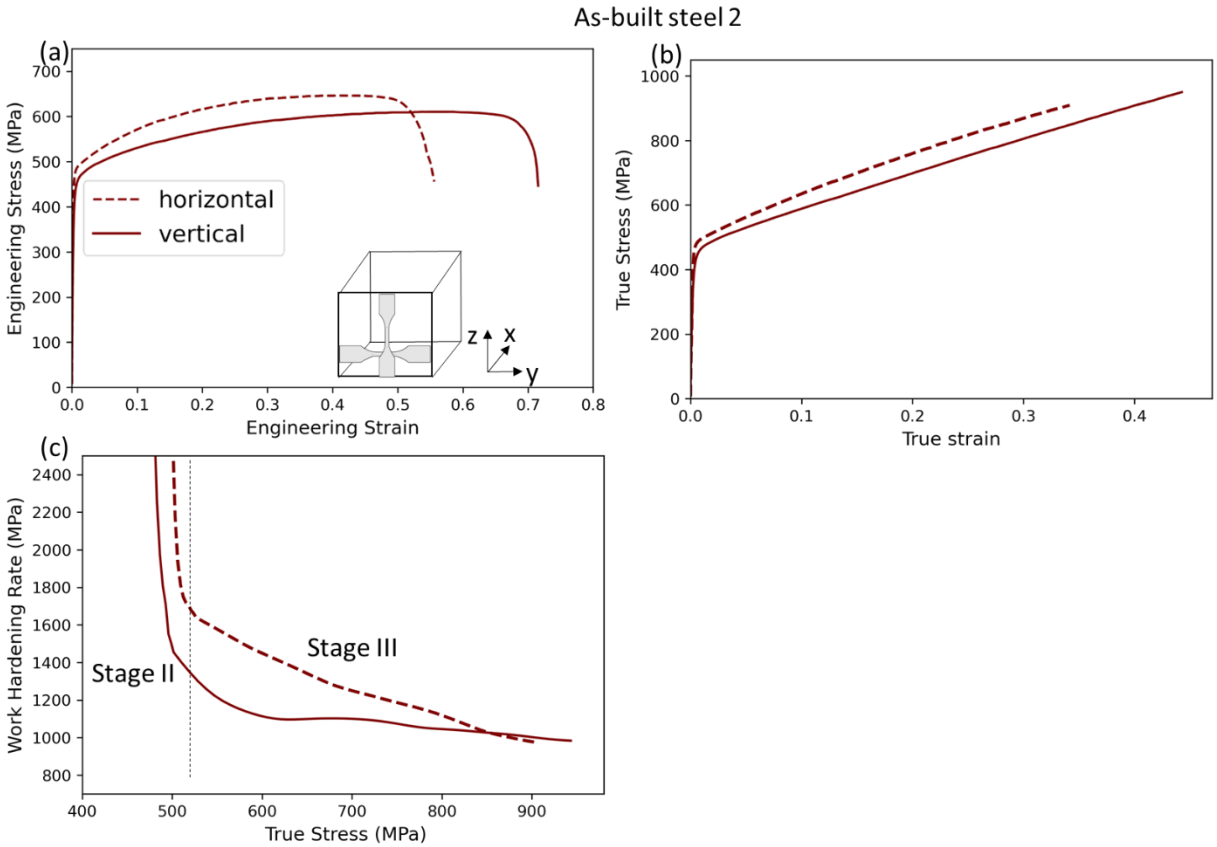

Figure IV-12: Tensile properties of the as-built Steel 2 loaded in the horizontal and vertical direction. Three tensile tests were conducted for each condition. Tensile tests are reproducible and for the sake of clarity only one is shown. (a) Engineering stress-strain curves. (b) True stress-strain curves. (c) Work hardening rate as a function of true stress.

IV.4.2 Steel 1

Engineering stress-strain curves for the as-built Steel 1 are given in Figure IV-13. Three loading directions are tested here because it was shown that the X and Y directions were not equivalent, see section IV.3.2. The X-direction has a slightly lower yield stress than the Y-direction and a lower total elongation. For the sake of clarity, in the subsequent analysis, **only the Y-direction is shown and is considered the horizontal direction** (direction exhibiting the lowest total elongation).

The Z-direction has a lower yield stress than the Y-direction, but a larger total elongation (0.7 vs. 0.43). This difference between the horizontal and vertical loading direction is larger than the one observed in Steel 2 (0.72 vs. 0.57). The as-built Y-direction does not respect the RCC-M standard for the total elongation (0.43 vs. 0.45).

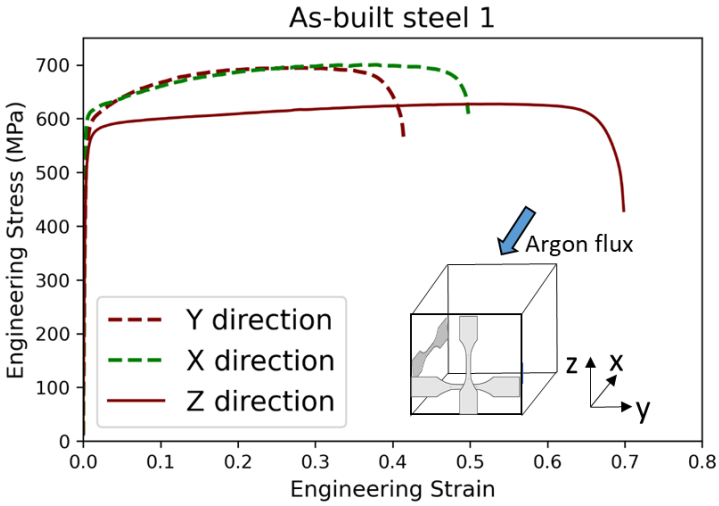

Figure IV-13: Engineering stress-strain curves for the as-built Steel 1 loaded along different directions. Three tensile tests were conducted for each condition. Only one per condition is displayed here.

Figure IV-14 (a) compares the engineering stress-strain curve for the as-built Steel 1 and Steel 2 for the vertical loading direction. Steel 1 is harder than Steel 2, but its work hardening rate becomes quickly lower than that of Steel 2. In Figure IV-14 (b), the uniform elongation is similar between both steels. Figure IV-14 (c) shows that Steel 1, after a quick drop in work hardening rate, has a positive slope more pronounced than the one detected in Steel 2, suggesting once again the occurrence of another deformation mechanism in addition to dislocation glide.

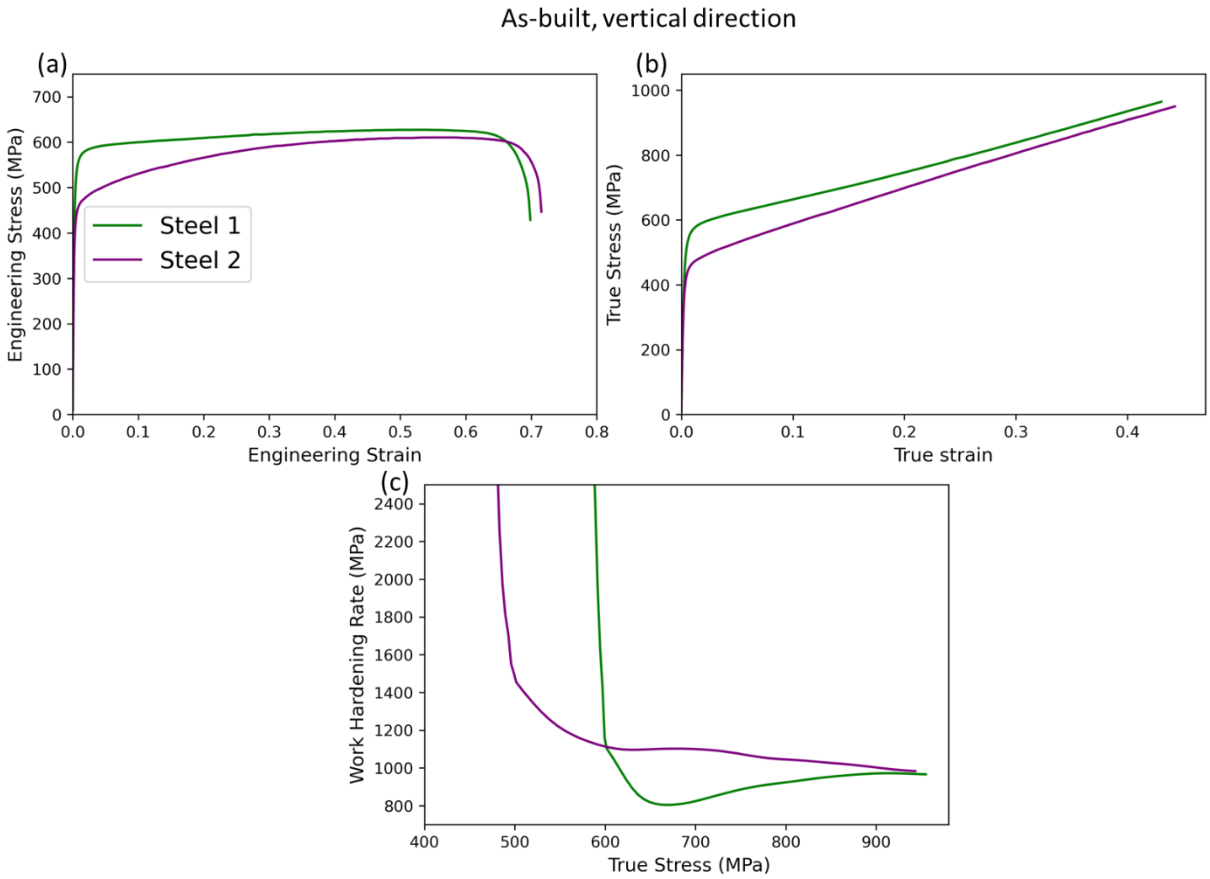

Figure IV-14: Tensile curves comparing the as-built vertical direction for Steel 1 and Steel 2. (a) Engineering stress-strain curves. (b) True stress-strain curves. (c) Work hardening rate as a function of true stress. Three tensile tests were conducted for each condition. Only one is displayed per condition here.

IV.5 Evolution of the tensile properties with heat treatments

The objective of this section is to present the evolution of tensile properties with heat treatment (yield stress, ultimate tensile stress (UTS), uniform elongation, and total elongation). The evolution of the tensile properties is similar between the horizontal and vertical directions, and also between Steel 1 and Steel 2. As a result, we describe the evolution of the mechanical properties with the different heat treatments only for Steel 2 loaded in the vertical direction. All the tensile curves for the other conditions, as well of a table with tensile properties can be found in Appendix G. A summary of the tensile properties for the different conditions is given at the end of this section.

IV.5.1 Steel 2 loaded in the vertical direction

The evolution of the engineering stress-strain curves with heat treatments for Steel 2 loaded in the vertical direction is shown in Figure IV-15 (a). The yield stress and UTS decreases with heat treatment. The total elongation (A%) is similar between the as-built conditions, after a SR heat treatment, and after a homogenization heat treatment, but increases after recrystallization. Regardless of the conditions

shown in Figure IV-15 (a), the RCC-M standard is respected (YS=175 MPa, UTS = 490 MPa, A% = 45%).

The true stress-strain curves are given in Figure IV-15 (b). The uniform elongation shows the same trend as the total elongation. The work hardening rate as a function of the true stress is given in Figure IV-15 (c). The two stages of the work hardening are indicated for the recrystallized condition. The stage III of the work hardening is not linear, as observed for other FCC materials such as copper [41]. Stage III of the work hardening of the as-built, SR, and homogenized conditions are relatively similar. This is an interesting observation, that has not been reported yet in the literature. For stage III, the work hardening of the recrystallized condition is initially lower than in the SR condition but becomes closer at stresses larger than 600 MPa.

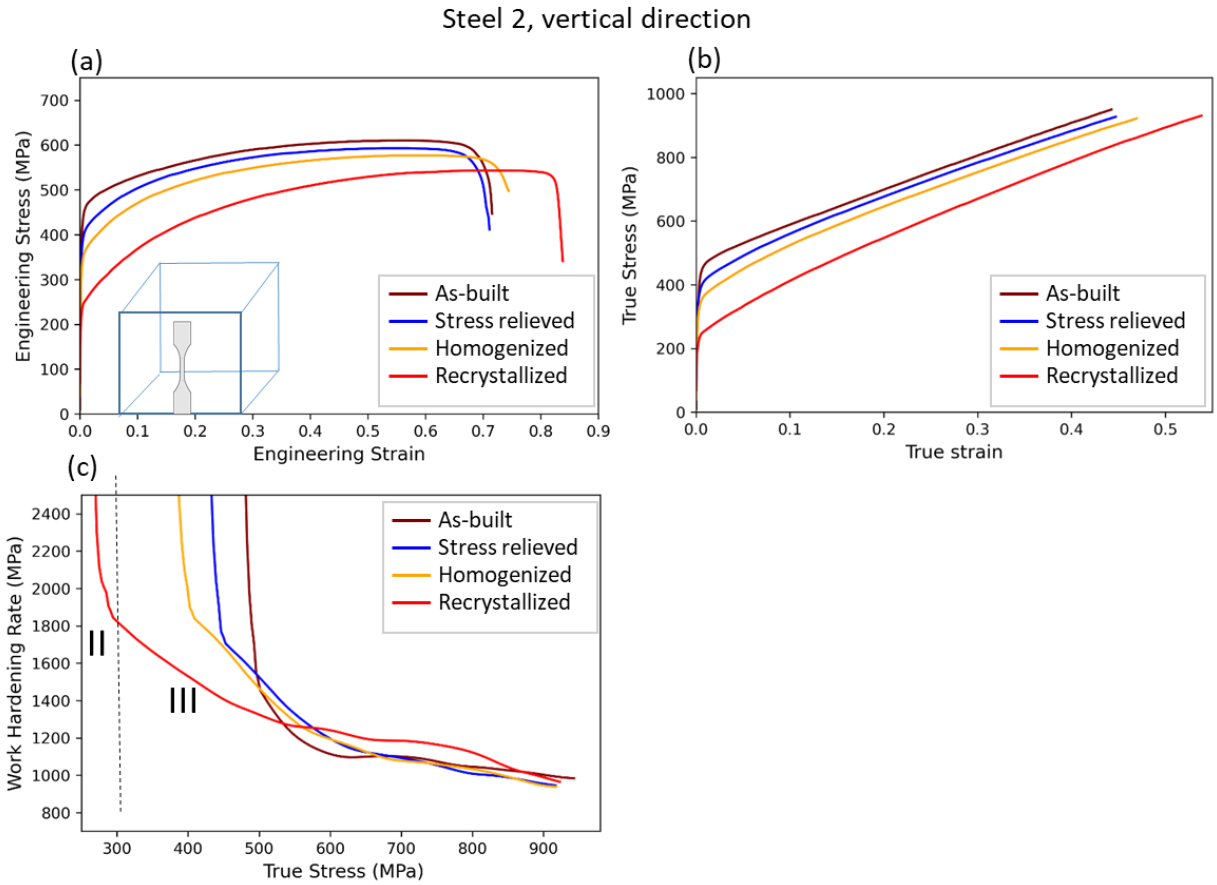

Figure IV-15: Tensile properties of Steel 2 deformed in the vertical direction and heat-treated at different temperatures. (a) Engineering stress-strain curves. (b) True stress-strain curves. (c) Work hardening rate as a function of true stress.

IV.5.2 Summary

The tensile properties as a function of the annealing temperature are summarized in Figure IV-16.

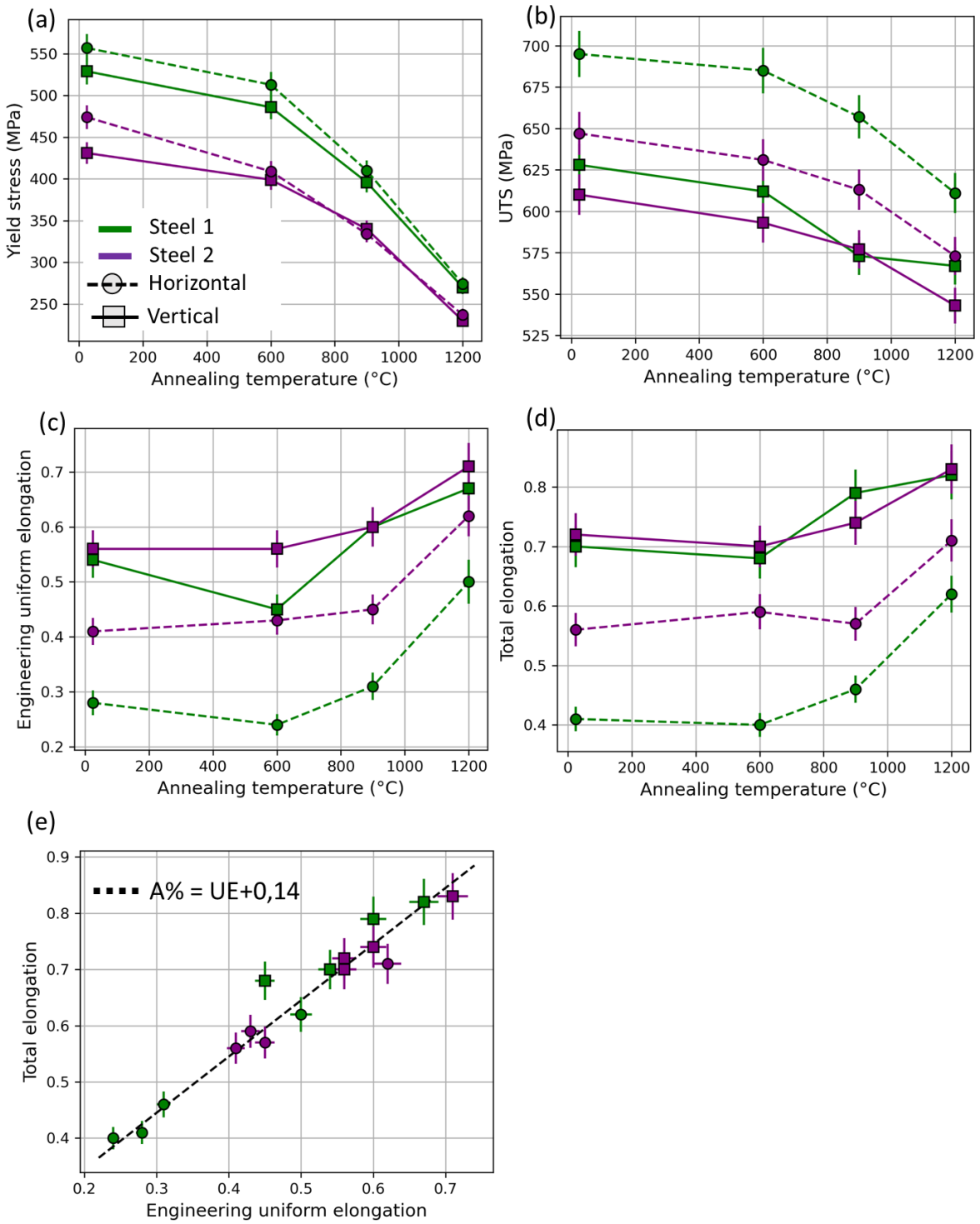

Figure IV-16: (a)-(e) Tensile properties as a function of the annealing temperature for both steels in both loading directions. (a) Yield stress, (b) UTS, (c) Engineering uniform elongation, (d) Total elongation. (e) Total elongation vs. uniform elongation.

IV.6 Observations of the plastic deformation mechanisms

The previous section highlights the influence of post-fabrication heat treatments on the tensile properties. Heat treatment tends to soften the material and increase its total elongation. In order to identify deformation mechanisms and correlate them with microstructural changes, we conducted observations of plastically deformed specimens. These observations are then related to changes in tensile properties. The goal is to conduct a comparative analysis across various heat treatments. This analysis is focused on Steel 2. The characterizations have mostly been carried out in the TEM, as this is the suitable instrument to observe the plastic deformation mechanisms, in particular dislocations.

IV.6.1 Dislocation glide

Dislocation glide is certainly the major plastic deformation mechanism in the 316L steel. However, the initial arrangement of dislocations in elongated cells observed in the as-built conditions may have an impact on this plastic mechanism. The dislocation network in the as-built condition is characterized and compared with the one observed in the heat-treated conditions.

IV.6.1.1 Dislocation network in the as-built condition

Figure IV-17 shows STEM images of the as-built microstructure after different increments of true plastic strain. At 0.0 of plastic strain, there is the presence of tubular dislocations structures with the intracellular regions relatively free of dislocations. After 0.12 of plastic strain, the intracellular regions still appear relatively free of dislocations, but cell walls are thicker. After 0.25 of plastic strain, the intracellular regions are no longer free of dislocations. Cell walls are thicker and additional equiaxed cells are now observed within the initial tubular dislocation structures. Some intracellular regions are not decorated with dislocations while others show a high dislocation density.

Those observations suggest that dislocations are at least partially blocked at the dislocation walls, but at large plastic strain, dislocations can also be found in the intracellular regions.

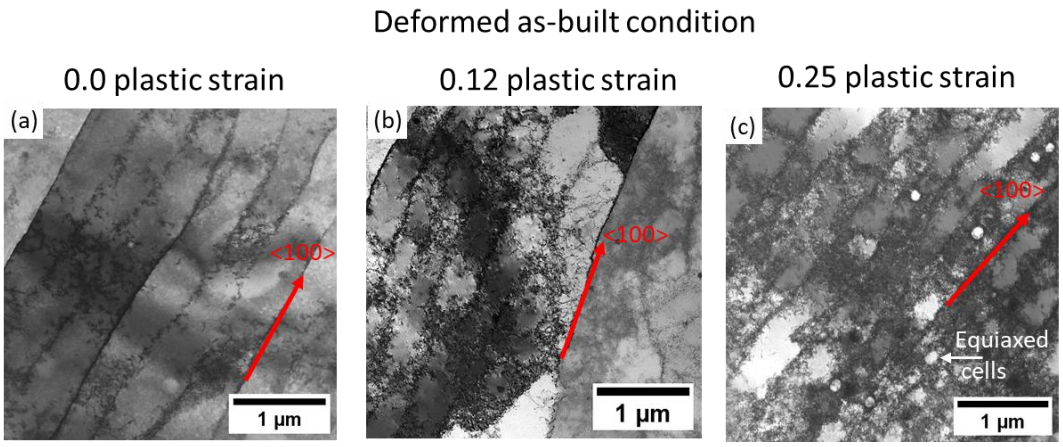

Figure IV-17: STEM bright field images of the as-built microstructure after different increments of plastic strain. (a) As-built condition (0.0 plastic strain), (b) after 0.12 plastic strain, and (c) after 0.25 plastic strain.

It is frequently observed that dislocations can arrange themselves into cells when the material is subjected to plastic deformation, and that these cells are misoriented relative to one another. In the 316L steel processed by LPBF, dislocations arranged in tubular structures are observed in the as-built microstructure although the material was not subjected to plastic deformation by the application of an external load. One hypothesis could be that the cells become misoriented relative to each other during plastic deformation. To characterize the misorientation between cells, ACOM-TEM is used. A misorientation profile across cells in the as-built microstructure (after 0) and 0.25 plastic strain is plotted in Figure IV-18 (a-d). Prior to plastic deformation, the misorientation across cells shows a noise of around 0.3° and the cumulative misorientation does not exceed 0.7° (Figure IV-18(c)). After 0.25 plastic strain, the cumulative misorientation in the grain is higher (2.5°), see Figure IV-18(g). However, the misorientation between cells does not seem to have increased and the point-to-point misorientation remains low. A continuous gradient in misorientation across the cells is evidenced in Figure IV-18(g). The misorientation is not accumulated at the cell boundaries.

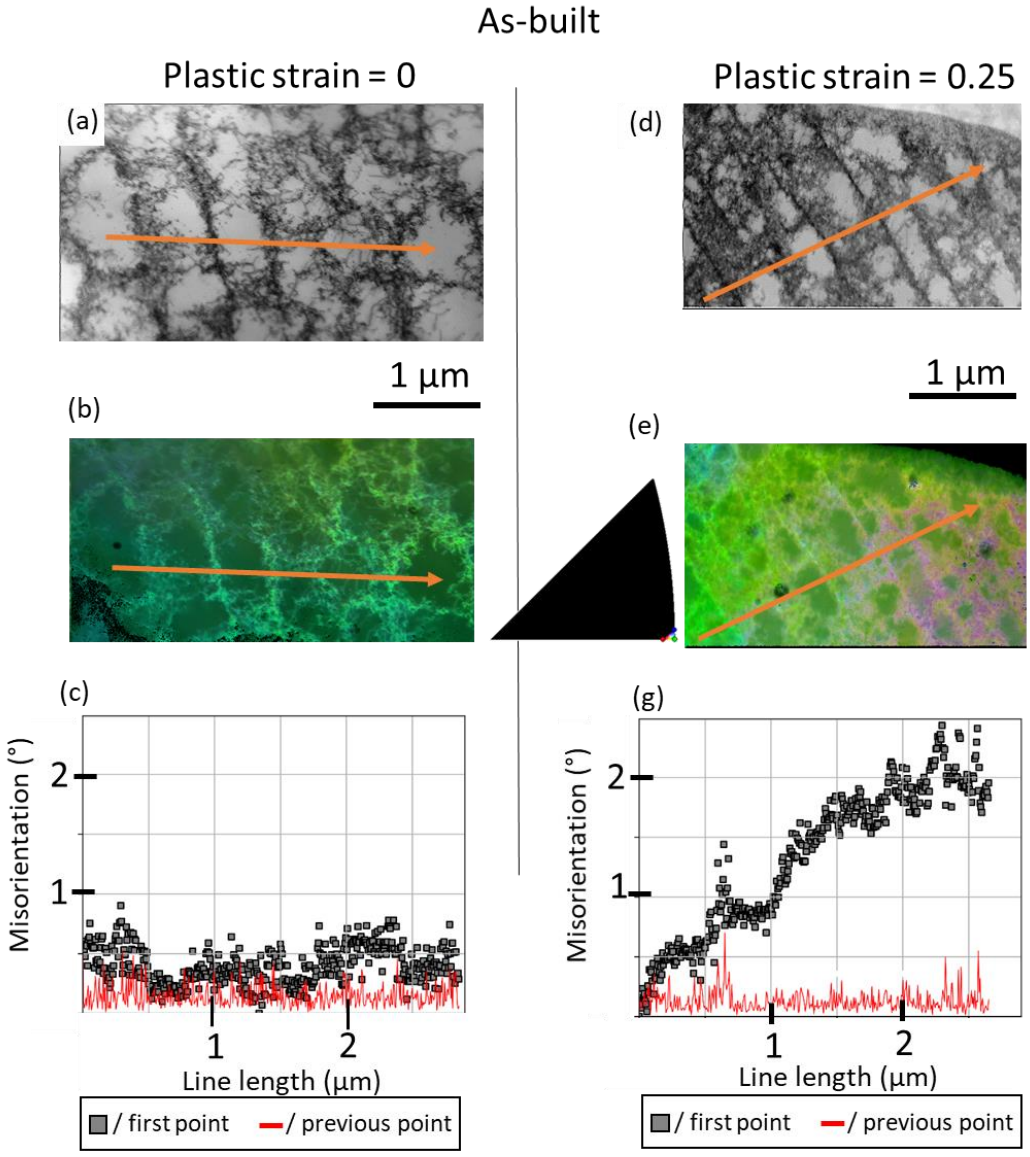

Figure IV-18: (a) Virtual bright field obtained by ACOM close to <110> zone axis. (b) The IPF map superimposes with the index map. (c) The misorientation along the orange arrows. (a)-(c) For the as-built condition after 0.0 plastic strain. (d)-(g) Same than (a)-(c) but for the as-built condition after 0.25 plastic strain.

IV.6.1.2 Comparison between the different conditions

The evolution of the dislocation network with plastic deformation is evaluated for three different conditions (as-built, after homogenization, and after recrystallization). Observations were conducted for a tensile deformation that gives a true stress of 600 MPa. The reason to compare the various microstructures at a given stress rather than at a given plastic strain comes from the observation of the work hardening rate. From a stress of 600 MPa, the work hardening rate is similar regardless of the conditions. Therefore, comparing microstructures at a given stress makes sense. Moreover, comparing materials at a given plastic strain would lead to comparing microstructures with large differences in dislocation density because the as-built condition has an initially high dislocation density. However, assuming that the increase in flow stress results mainly from dislocation hardening, comparing materials at a given stress is equivalent to comparing materials with approximately the same dislocation density. A schematic of the methodology deployed is given in Figure IV-19.

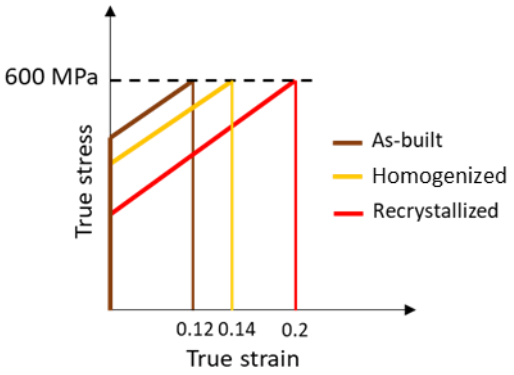

Figure IV-19: Schematic of the methodology used to compare the different conditions.

Figure IV-20 shows STEM images of the different conditions investigated. After homogenization and plastic deformation, the dislocation network is similar to the one observed in the as-built microstructure, although a lot of dislocations were removed during the homogenization heat treatment. This means that during plastic deformation of the homogenized sample, dislocation cells develop and look like these observed in the as-built microstructure. The underlying reason for this cannot be attributed to the microsegregation, it is rather thought that it is induced by the remaining dislocations or oxides decorating the former dislocation cells present in the as-built condition. This is in agreement with the results reported by Riabov et al. [66].

After recrystallization, the dislocation structure is different in comparison with the one observed in the as-built microstructure or after homogenization. The typical size of the dislocation cells is more irregular with some cells around 1 µm and others with a size around 200 nm. For a wrought 316L, the dislocations arrange themselves into cells with deformation. These arrangements have been deeply investigated by Feaugas et al., see e.g. [155]. With plastic deformation, dislocations arrange themselves first as tangles, then walls and finally as cells. In this study [157], it was shown that for plastic strains larger than 0.2, grains can have a dislocation cellular substructure with an average cell size about 180 nm.

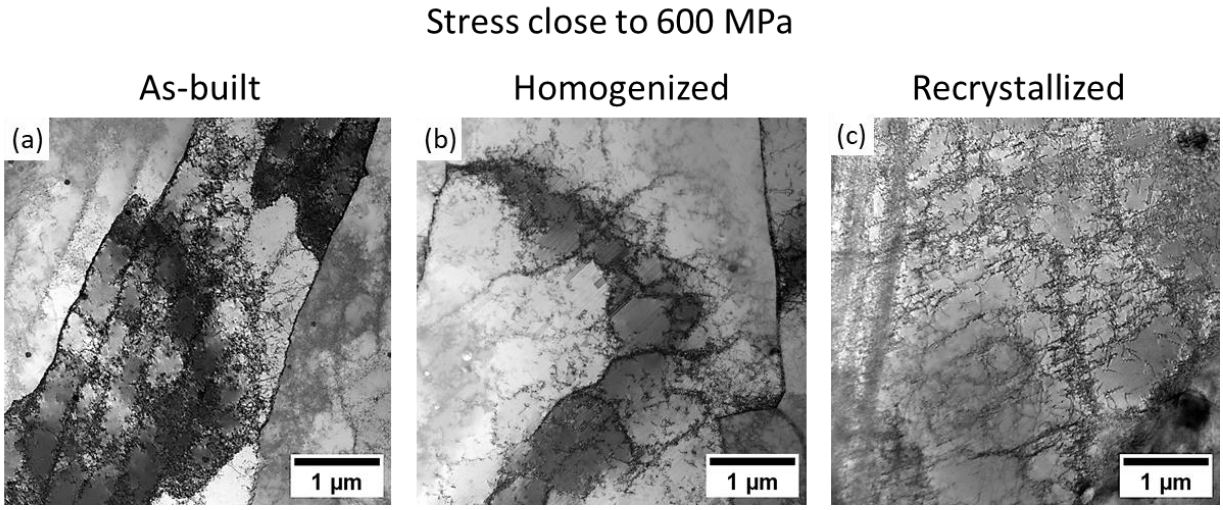

Figure IV-20: STEM bright field images of Steel 2 loaded in the horizontal direction after a tensile deformation such that the true tensile stress is close to 600 MPa. (a) As-built condition after 0.12 true plastic strain (true stress of 630 MPa), (b) After homogenization and after 0.14 true plastic strain (true stress of 600 MPa), (c) Recrystallized condition after 0.20 plastic true strain (true stress of 600 MPa).

IV.6.2 Twinning

Twins are observed in all conditions after the application of sufficient plastic deformation (~0.05), see Figure IV-21. In the as-built conditions, twins cross the dislocation cells. No nucleation of twins is observed at cell boundaries and twins rather nucleate at grain boundaries. No twin stopping at a dislocation wall is observed. As a result, dislocation walls do not seem to be a strong obstacle to twin propagation. Similar observations are made after homogenization. In the recrystallized condition, dislocations are accumulated at twin boundaries. Twin boundaries act as boundaries for dislocation motion. Twins nucleate at grain boundaries. For the different conditions, twins are thin (~20 nm).

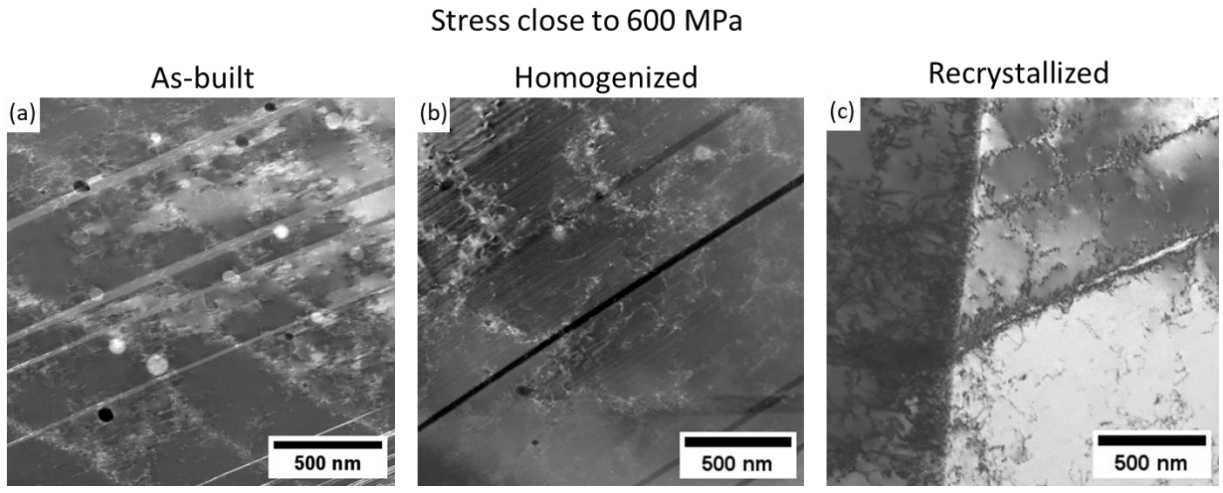

Figure IV-21: STEM images of Steel 2 loaded in the horizontal direction after a tensile deformation such as the true tensile stress is close to 600 MPa. (a) As-built condition after 0.12 true plastic strain (true stress of 630 MPa), STEM dark field, (b) After homogenization and after 0.14 true plastic strain (true stress of 600 MPa), STEM dark field, (c) Recrystallized condition after 0.20 true plastic strain (true stress of 600 MPa), STEM bright field.

Twins can also be observed by EBSD in plastically deformed specimens. Figure IV-22 shows the IPF EBSD map of the as-built condition after different true plastic strains. The loading direction (LD) is horizontal. After a plastic strain of 0.06, the surface fraction of twins is very low, but some twins are detected. After a plastic strain of 0.2, more twins are detected, but the surface fraction is still low. After a plastic strain of 0.32, there is a higher number of twins that can be large (~1 µm). After a true strain of 0.43, most of the grains contain twins, except the one oriented <100>//LD (red in the IPF). This was expected, because TWIP is favored in grains oriented close to <111>//LD, as see in 1.2.2.2, but disfavor in grains oriented <100>//LD. This explains why twin appears preferentially in grains displayed in blue in the IPF map displayed in Figure IV-22. At this plastic strain, the surface fraction of twins is important. The behavior for homogenized and recrystallized condition is identical.

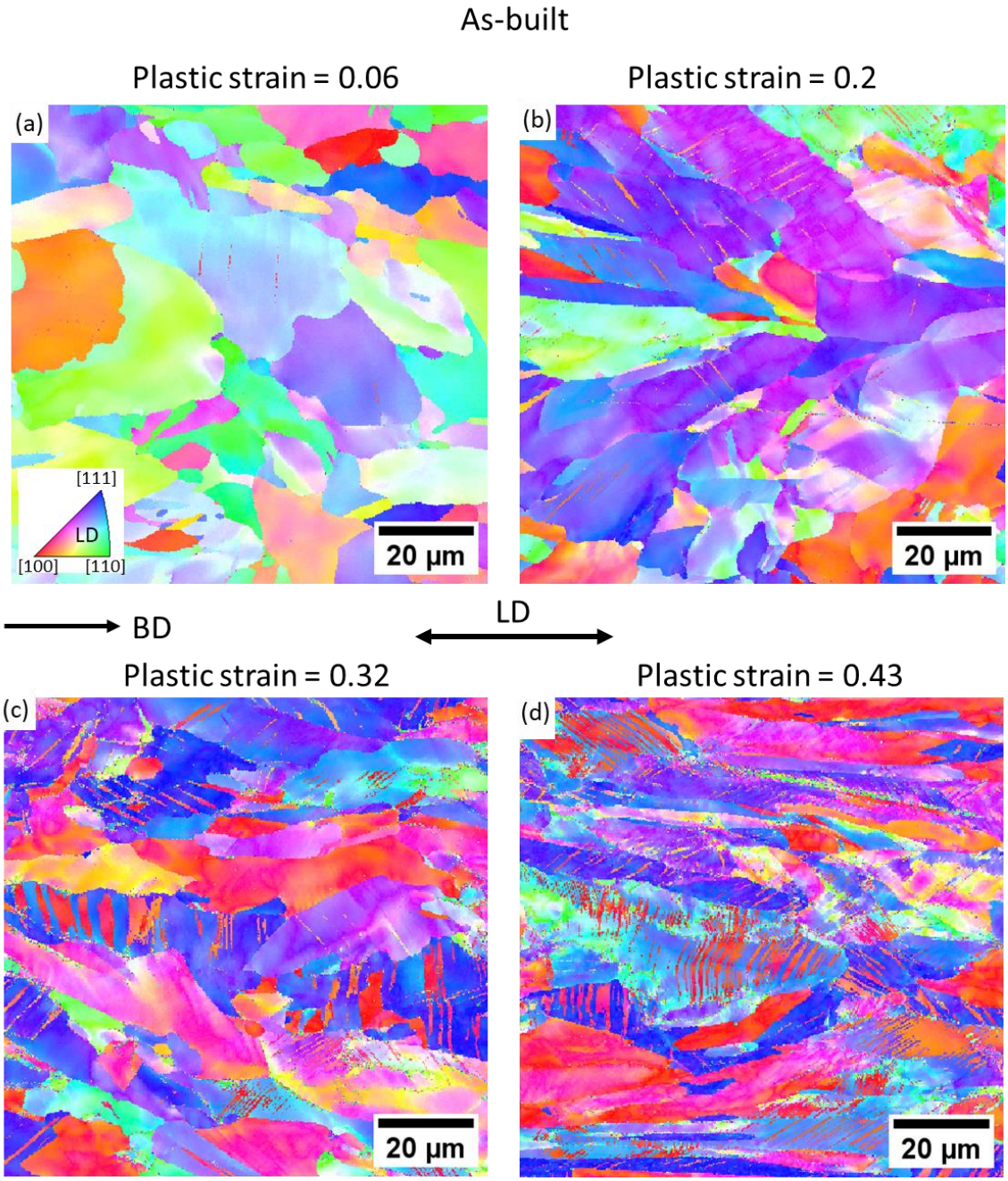

Figure IV-22: IPF EBSD maps taken in the as-built condition after different true plastic strain (loading direction parallel to the build direction). (a) After 0.06, (b) after 0.20, (c) after 0.32, and (d) after 0.43 true plastic strain. Loading direction (LD) is horizontal.

The twin area fraction is measured using EBSD in the as-built microstructure, after homogenization, and after recrystallization in Steel 2 deformed in the vertical direction after different increments of plastic strain. Details of the method employed are given in section II.6. The evolution of the area fraction of twins as a function of plastic strain is given in Figure IV-23 (a). One can see that for a given plastic strain, the area fraction of twin is close regardless of the conditions of interest. The evolution of the twin fraction as a function of flow stress is shown in Figure IV-23 (b). In this case, for a given stress, there is an important difference in twin fraction between the as-built and recrystallized conditions. For the three tested conditions, the twin fraction can be estimated by the same sigmoid function (see equation (IV-1)) that depends only on the level of plastic deformation, see in Figure IV-23 (a).

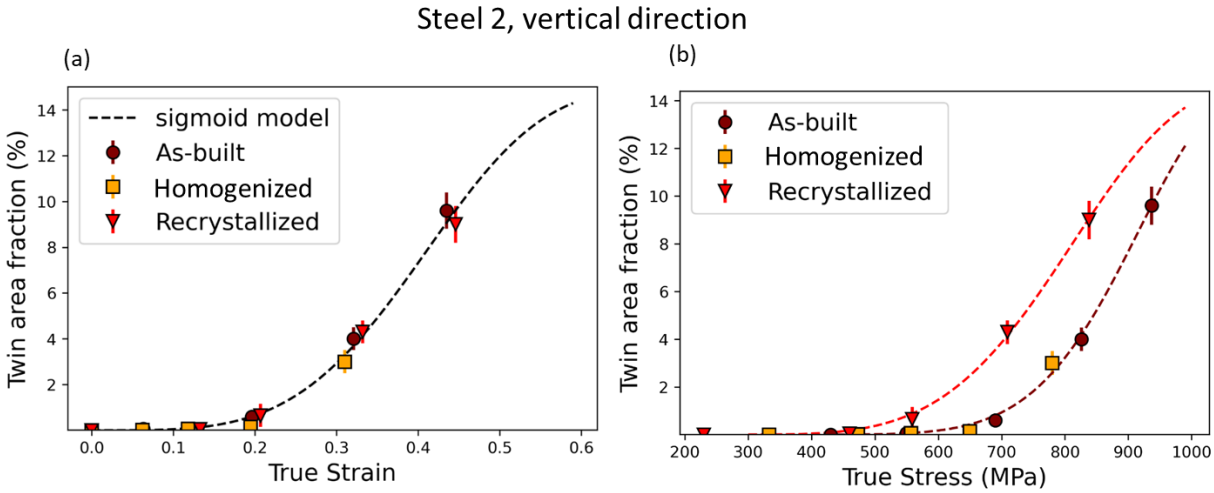

Figure IV-23: Twin area fraction for Steel 2 loaded in the vertical direction for different microstructures along with the sigmoid fitting the experimental results. (a) Twin fraction as a function of function of plastic strain, and (b) as a function of true stress.

$$F = 0.15 * \left(1 - e^{-\left(\frac{\epsilon}{0.44}\right)^{3.9}}\right) \quad \text{(IV-1)}$$

It is remarkable that the evolution of the twin fraction with plastic deformation is similar regardless of the conditions for a given loading direction. At a first sight, this outcome appears surprising, especially considering the difference in microstructures: differences in dislocation density (varying by approximately two orders of magnitude), differences in grain size (increase from 6 to 20 µm between the as-built and recrystallized microstructure). This observation cannot be explained by variations in texture, because it is nearly the same between the three conditions. This result suggests that twin nucleation and growth is not affected by changes in microstructure.

However, for the same level of stress, the twin fraction is quite different between the as-built and the recrystallized condition. For example, at a stress of 700 MPa, the twin fraction is about 0.6% in the as-built microstructure, but increases to 4.6% after recrystallization. This is in contradiction with previous research [50] that established that the TWIP effect is triggered at the same stress regardless of the microstructure. This result from the literature suggests that the critical stress to have a TWIP effect is not affected by microstructural changes. Our results rather suggest that the TWIP effect starts at a given plastic strain and a different critical stress regardless of the microstructure. This is also in contradiction with the expected impact of grain size on twinning. It has been shown in TWIP steels that microstructures with smaller grain sizes should result in a smaller twin fraction for a given plastic strain [47], [158]. The twin fraction was reduced by a factor 2 when the grain size was reduced from 50 to

3 µm in [47] for a plastic deformation of 0.30. Here, the grain size changes from 6 µm in the as-built to 20 µm after recrystallization, but the twin area fraction evolution with plastic strain is similar.

The twin thickness follows a similar evolution with the strain for the different conditions. For small deformation (<0.2), the twin thickness is small ~20-70 µm, see STEM images in Figure IV-21. At larger deformations, twins become larger. Figure IV-24 shows a BSE image of Steel 2 after a true plastic strain of 0.32 for the as-built and recrystallized microstructure. The numbers displayed in the figures indicate the twin thicknesses. In both conditions, the distribution of twin thickness is large. There is the coexistence of small twins ~50 nm and large twins (>1µm) in the same grain. It is likely that there is in parallel during the deformation, growth of twins and nucleation of new twins.

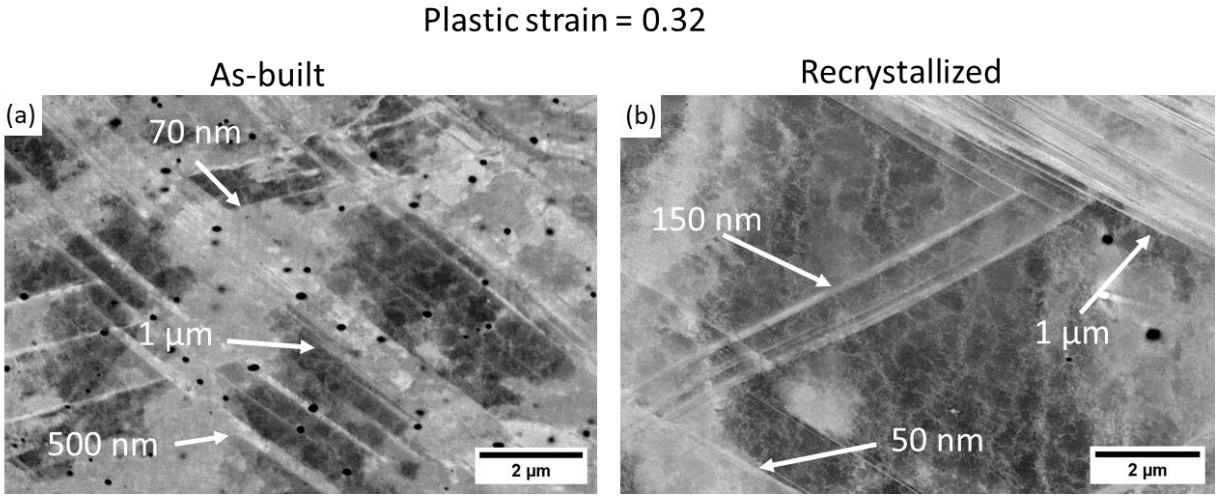

Figure IV-24: SEM-BSE image of Steel 2 after a true plastic strain of 0.32. Values indicated in the images are the thickness of the twins. (a) As-built condition. (b) Recrystallized condition.

IV.7 Discussion

IV.7.1 Strengthening mechanisms: estimation of the different sources of hardening

Several authors attempted to estimate the different contributions to yield stress [13], [50], [57], [72], [88]. However, in the literature, this kind of model was not applied to different microstructures resulting from various post-fabrication heat treatments. Microstructure obtained after different heat treatments is helpful in discriminating the effect of the different sources of strengthening.

For the general case, the yield stress can be estimated using equation (IV-2):

$$\sigma_y = \sigma_0 + \sigma_{ss} + \sigma_{GB} + \sqrt{\sigma_p^2 + \sigma_{df}^2} \qquad \text{(IV-2)}$$

where σ_0 is the Peierls stress, σ_{ss} is the contribution from the solid solution, σ_{GB} is the contribution from the grain boundaries, σ_p is the contribution of particles, and σ_{df} is the contribution from forest dislocations. The Peierls stress can be calculated with common formula [40] and its value is estimated

to be about 2 MPa. This is a small value, and will thus be neglected. The contribution of the solid solution to the yield strength is estimated using the empirical relationship found in [33]:

$$\sigma_{ss} = 68 + 354(\%C) + 493(\%N) + 20(\%Si) + 3.7(\%Cr) + 14.5(\%Mo) \qquad \text{(IV-3)}$$

This is an empirical relationship determined for austenitic stainless steels [33] where the % are given in %.wt. One could argue that particles can modify the solid solution because they capture the Si. However, even by assuming that all the oxygen is captured by the oxides, with a stoichiometry SiO_2, this would only decrease the Si content in the matrix by 0.05%, which would decrease the yield stress by about 1 MPa. This variation is negligible. Microsegregation in the as-built and SR conditions is present, but not after homogenization and recrystallization. Therefore, the contribution of the solid solution to the yield stress may change as a function the microstructure considered. From the literature, the interdendritic regions are about 1%wt richer in Cr and Mo than the dendrite cores in that material [49]. Even assuming that all the material would have the composition of the interdendritic regions, the increase in yield stress would only be 18 MPa (based on equation IV-3). This variation is limited in comparison with the yield stress (>400 MPa for the as-built and SR microstructure), and will thus be neglected. Therefore, in the hardening model, the contribution from the solid solution is taken constant regardless of the heat treatment.

The contribution of grain boundaries to the yield strength follows the Hall-Petch law. In austenitic stainless steels, this law is written as follows [33]:

$$\sigma_{GB} = \frac{225}{\sqrt{D}} \qquad \text{(IV-4)}$$

with σ_{GB} in MPa and D the grain size in µm. It will be assumed that this relation is still valid for 316L elaborated by LPBF.

Hardening induced by particles can be then estimated with the Orowan law as reformulated by Bacon [33]:

$$\sigma_p = M \left(\frac{\ln\left(\frac{2\underline{D}}{b}\right)}{\ln\left(\frac{l}{b}\right)} \right)^{\frac{3}{2}} * \frac{\mu b}{2\pi l} * \ln\left(\frac{l}{b}\right). \qquad \text{(IV-5)}$$

In this equation, *M* is the Taylor factor, *l* is the mean distance between particles, $\underline{D}$ is the harmonic mean between the diameter of particles and the distance *l*, *b* is the Burger vector (0.255 nm in austenitic stainless steels [7]) and μ the shear modulus (78 GPa [155]). The mean distance and mean diameter are respectively evaluated with the Delaunay distance and the diameter given in Figure IV-8. The same values for Steel 1 and Steel 2 are taken, because values of diameter and distance were found to be similar in both steels. The Taylor factor is estimated using the VPSC code [32]. It gives close values for Steel 1 and Steel 2, respectively 2.63 and 2.65.

Hardening induced by dislocations is estimated using the forest dislocation equation [30]:

$$\sigma_{df} = \alpha M \mu b \sqrt{\rho}. \quad \text{(IV-6)}$$

α is taken equal to 0.3 [7]. Such a value is supposed to be valid even if dislocations are organized in cells because hardening induced by dislocations holds with little regard to the arrangement of dislocations [37]. In the recrystallized condition, the dislocation density is estimated to be about $1x10^{12}$ m^{-2}, a typical value for a recrystallized 316L [7]. In the as-built condition, some values have been reported in the literature and are given in Table IV-4. These values are in the range $1x10^{14}$ m^{-2} to $6x10^{14}$ m^{-2}. Such variations result in large differences in the contribution of dislocation hardening, from 160 MPa to 390 MPa, i.e. a difference of nearly 230 MPa. Therefore, the main source of variability when estimating the yield strength from the different sources of strengthening comes from the value of the dislocation density.

In the as-built condition, the average value reported in the literature will be taken ($3.7x10^{14}$ m^{-2}). In the SR condition, the value of the dislocation density will be taken equal to $1x10^{14}$ m^{-2} and $1x10^{13}$ m^{-2} after homogenization.

Table IV-4: Estimated dislocation density in the as-built condition, values found in the literature.

	Tekumalla [122]	Gao [76]	Bertsch [67]	Bahl [13]	Roirand [72]	Average
Dislocation density (10^{14} m^{-2})	1.1	1.5	4	6	6	3.7

Table IV-5 summarizes the different contributions of solid solution, grain size, oxides and dislocations to the yield stress. Oxides and dislocations follow a quadratic addition. This means that the oxides contribution (Oc) is only partially σ_p, and this value depends on the dislocation density. It can be expressed as $((\sigma_{df}^2 + \sigma_p^2)^{0.5} - \sigma_{df})$. The oxides contribution represents the difference in hardening with and without oxides for a given specific dislocation density. This contribution is relatively small in comparison with the yield stress. It is found that oxides bring a low contribution to the yield stress.

Table IV-5: Values for dislocation density and additions of dislocations and oxides for Steel 2.

Condition	σ_{ss}	σ_{GB}	ρ (10^{13} m^{-2})	σ_{df} (MPa)	σ_p (MPa)	$(\sigma_{df}^2 + \sigma_p^2)^{0.5}$	O_c (MPa)	σ_y mod (MPa)	σ_y exp (MPa)
Recrystallized	170	50	0.1	15	10	20	5	240	230
Homogenized	170	90	1	50	60	80	30	340	340
Stress relieved	170	90	10	158	70	170	20	430	400
As-built	170	90	37	300	70	310	10	570	427

Results for the different contributions are summarized in Figure IV-25 and compared to the experimental yield stress. One of the objectives of the hardening model is to weigh the various contributions. In the recrystallized state, the predictions of yield stress are in very good agreement with the experimental values. This means that the model gives a relatively good idea of the respective weights of the solid solution and grain size. In the recrystallized condition, the major contribution to hardening is the solid solution, found to be 210 and 170 MPa respectively for Steel 1 and Steel 2. The grain size only

contributes to about 50 MPa in the two steels. After homogenization, the contribution from grain size, dislocations, and oxides are similar, but the major contribution is still the solid solution. In the SR condition, the contribution from forest dislocation and oxides becomes bigger (170 MPa) in comparison with the one from grain size (respectively 50 and 90 MPa for Steel 1 and Steel 2), and is around the same value as the solid solution (respectively 210 and 170 MPa for Steel 1 and Steel 2). In the as-built state, the contribution from dislocations and oxides (310 MPa) becomes more important than the one from the solid solution (respectively 210 and 170 MPa for Steel 1 and Steel 2).

In the as-built, SR, and homogenized conditions, the predicted yield stress is identical for the two steels, because the contribution from solid solution strengthening in Steel 1 is compensated by a smaller grain size in Steel 2. However, experimentally, Steel 1 is harder than Steel 2, from about 50-100 MPa. This could be due to a difference in dislocation density between Steel 1 and Steel 2, because the variability of the estimations of the other contributions (σ_{ss}, σ_p, σ_{GB}) are too small to explain these differences. In addition, LAGBs are not considered as grain boundaries but as stacking of GNDs, and there are more LAGBs in Steel 1 than in Steel 2, see Figure III-2 in section III.2.1. The solidification of Steel 2 is suspected to be different from the one of Steel 1, with a possible phase transformation. The phase transformation might also impact dislocations, by decreasing their density.

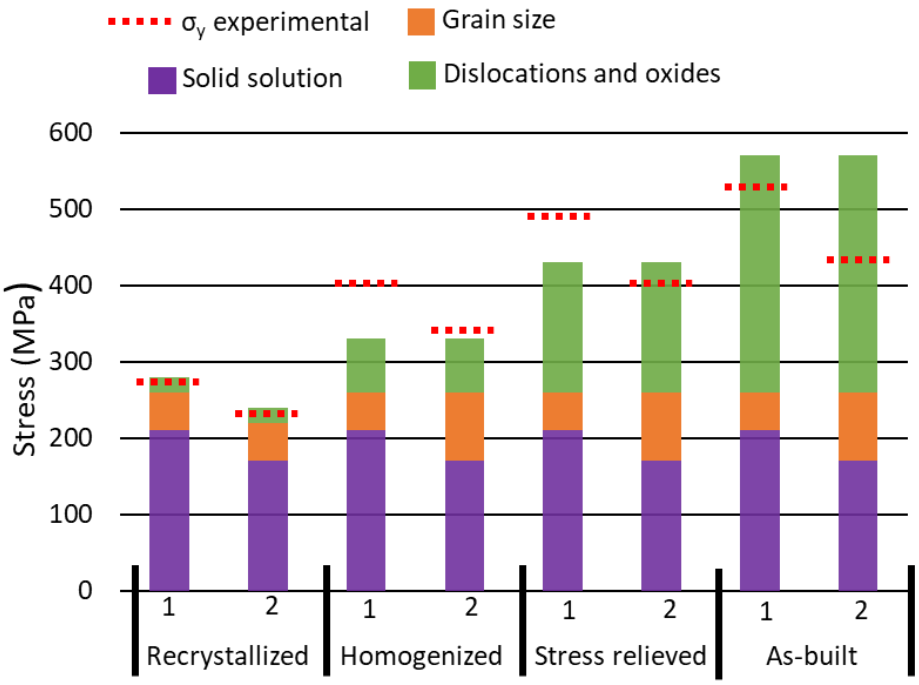

Figure IV-25: Comparison between the experimental (dashed red line) and the estimated yield stress. The different strengthening contributions are represented using different colors. The number along the X-axis stands for the steel: 1 or 2.

IV.7.2 Anisotropy in ductility

Differences in total elongation between the X and Y directions were observed in Steel 1, 0.53 ± 0.02 in the X direction and 0.45 ± 0.03 in the Y direction, where X is parallel to the direction of the argon flux. This cannot be the result of defects, because only spherical gas pores were detected and their morphologies are identical in specimens extracted along the X and Y directions. The difference is then attributed to the difference in texture. Indeed, the pole figure displayed in Figure IV-10 shows that

Steel 1 has preferentially its <100> directions orthogonal to the argon flux (the argon flux is along the X direction). Figure IV-26 displays the inverse pole figure (IPF) of the three loading directions for the as-built Steel 1 and Steel 2. Notably for Steel 1, a preferred <100> orientation can be observed along the Y direction, while the X direction demonstrates a preferred <111> orientation. There is no difference in X and Y for Steel 2. The lower total elongation along the Y direction compared to the X direction can be linked to the variations of crystallographic orientations with respect to the loading direction. The decrease in elongation to fracture along the Y direction can be discussed in the light of the recent findings of Wang [89]. Wang et al. produced a nearly monocrystalline microstructure of 316L by LPBF and demonstrated that a sample with a prominent <100> direction aligned with the loading direction exhibited the lowest total elongation, see Figure I-26 in Chapter I.6.1.2B. Other works tend to agree with these ideas: samples having a strong <100> texture along the tensile direction exhibit a low elongation to fracture [56], [58]. Here, while the preferred orientations are notably less pronounced than those studied by Wang (23 mrd vs. 3 mrd), it seems that even a slight <100> preferential orientation can have a non-negligible influence on the total elongation.

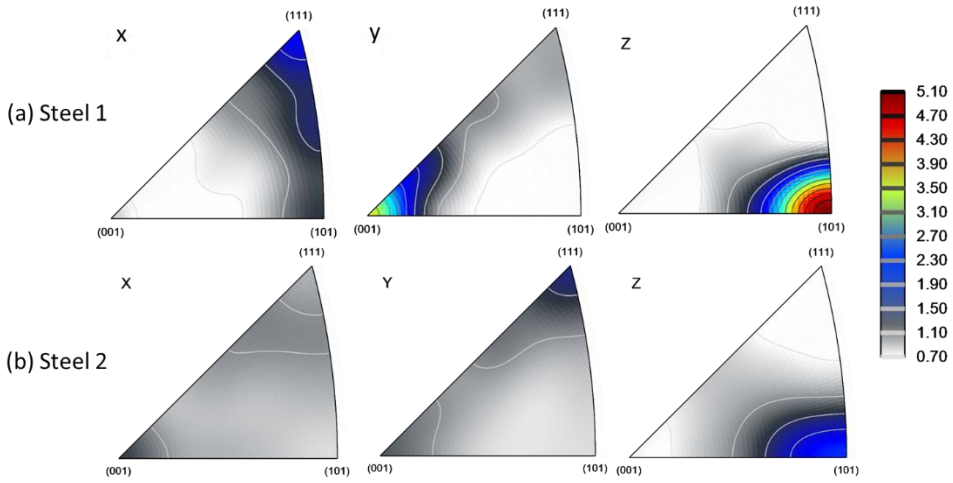

Figure IV-26: IPF for the as-built condition for: (a) Steel 1 and (b) Steel 2.

The origin of the difference in texture between Steel 1 and Steel 2 is attributed to the process parameter limitation window, which imposes restrictions on the laser scan to prevent excessive parallelism of the laser scanning direction with the argon flux as explained in Chapter II.2.1, and recalled in Figure IV-27. The impact of the process parameter limitation window is generally ignored in other studies even though it may have a significant impact on the ductility.

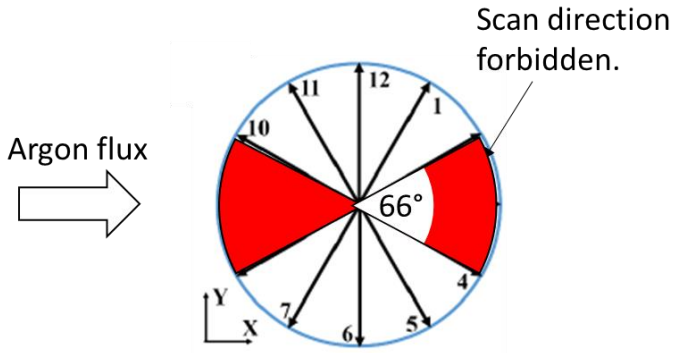

Figure IV-27: Schematic of the limitation window parameter for the scanning direction. Adapted from [1].

IV.7.3 Strain hardening mechanisms

The four microstructures investigated (as-built, SR, homogenized, and recrystallized) have the same work hardening rate for stresses larger than 600 MPa. This observation is similar to the one we would make if a given microstructure was subjected to different plastic pre-strains. To illustrate this concept, loading-unloading-reloading experiments are carried out on Steel 2 in the four conditions. Unloading occurs when the stress reaches 600 MPa. The curves resulting from the reloading are then set at the origin. This is illustrated in Figure IV-28 (a). A comparison of the second loading stage is shown in Figure IV-28 (b). The curves from the second load have the same yield stress. This was expected, since the unloading was carried out at the same stress for the different conditions. However, in addition to having the same yield stress, the curves overlap in the plastic regime. This superimposition of the stress-strain curves shows that the different conditions have the same work-hardening behavior from 600 MPa. The four microstructures of interest show the same work-hardening rate for stresses larger than 600 MPa. One could thus hypothesize that by loading the recrystallized state to increase the dislocation density to approach that of the as-built state, the same work-hardening rate would be observed. This is schematically illustrated in Figure IV-29.

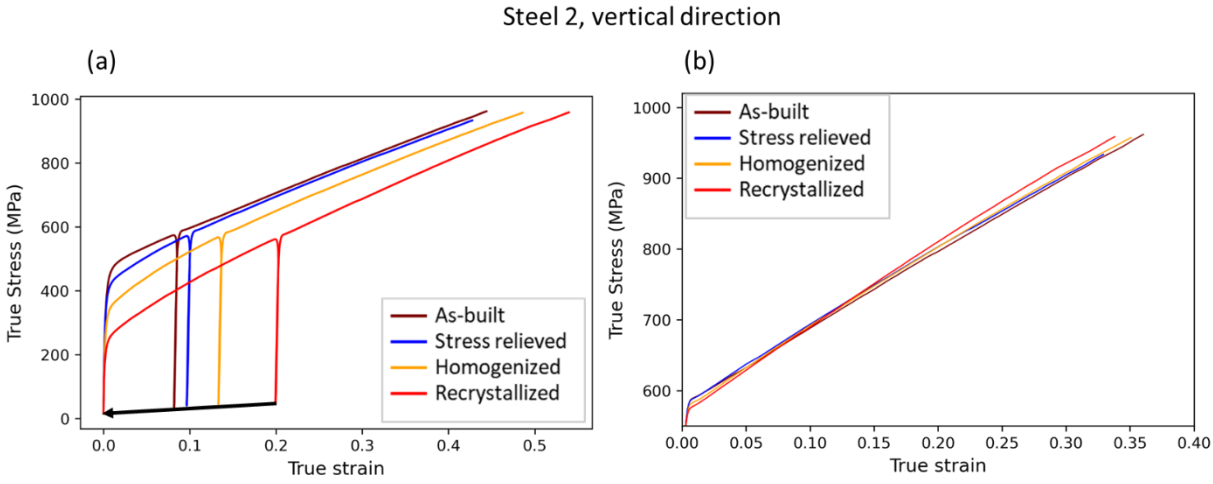

Figure IV-28: (a) True stress strain curves of Steel 2 loaded in the vertical direction, with a loading-unloading cycle at 600 MPa. (b) True stress-strain curves. The curve comes from the loading-unloading experiment, but the second loading is shifted toward the origin.

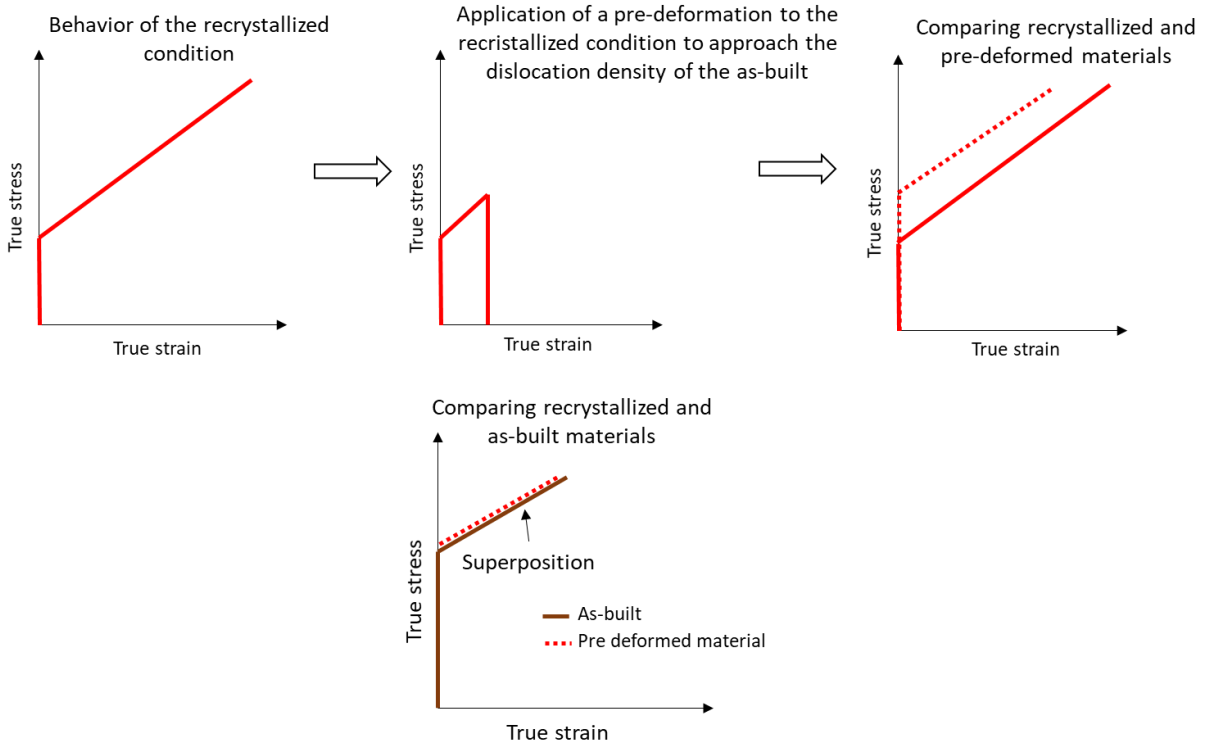

Figure IV-29: Schematic of the mechanical behavior of the 316L LPBF. After a pre-deformation, the recrystallized and the as-built condition are superimposed.

Between the as-built and homogenized conditions, microsegregation vanishes, there is also a slight coalescence of oxides but still preferentially located in cell walls, and a decrease in dislocation density in cell walls. Although the former dislocation structures appear to be regenerated after plastic deformation (Figure IV-20), the crucial observation is that the differences in microstructure do not appear to significantly impact the resulting work hardening behavior. This strengthens the idea that the dislocation density primarily governs the work hardening under these conditions. A noteworthy observation is the limited prevalence of work hardening rate plots depending on the heat treatments in the literature dedicated to the 316L steel produced by LPBF. Such plots can be found in the work of Voisin [50], albeit without the discernible superposition that has been observed in this Ph.D. The underlying reason for the difference between the results from Voisin and the present results remains unclear.

Between the as-built and the recrystallized condition, the work hardening behavior is similar after 600 MPa. However, the arrangement of dislocations at 600 MPa is different between these conditions. It will probably be different throughout plastic deformation. This suggests that the arrangement of dislocations does not seem to have a strong impact on the work hardening. However, in this discussion, so far only dislocation plasticity was discussed. Twinning is known to impact the strain hardening by a dynamic Hall-Petch mechanism [159]. It has been shown that a non-negligible part of the material is twinned at large plastic deformations, 10% after 0.4 true plastic strain. Twinning is likely responsible for the non-linear decrease in work hardening observed for the different vertical directions, and for the local increase in work-hardening rate observed in the as-built Steel 1.

The different microstructures investigated have also a different grain size. One could expect that a difference in grain size would induce a difference in work hardening behavior. It was shown in copper

that grain size does have an impact on the work-hardening but only during the early stages of plastic deformation [160]. This could be a reason why it does not seem to impact the work hardening behavior at high stresses. In [160], the grain size effect on the work hardening is attributed to the back-stress, i.e. to a kinematic contribution to the work hardening.

To weigh the different contributions of grain size, twinning and dislocation glide, a more formal analysis has to be made. To perform this, a model will be developed in Chapter V.

IV.8 Conclusions

The evolution of the microstructure and mechanical properties have been investigated in both Steel 1 and Steel 2. It has been shown that:

- The SR treatment at 600°C/1h does not alter the microstructure (no change in grain size, texture, dislocation density, and oxide population).
- The homogenization treatment at SR + 900°C/1h removes the microsegregation, decreases the dislocation density and induces a slight oxide coalescence. After plastic deformation, the cellular dislocation structure observed in the as-built microstructure is reformed.
- The treatment at SR + 1200°C/1h for Steel 1 and 2h for Steel 2 induces the recrystallization of the material. Grains become equiaxed with a low dislocation density. The texture is not strongly modified after recrystallization. Oxides coalesce strongly. After deformation, a dislocation arrangement is created. This one is different compared to the one evidenced in the as-built microstructure. Cells size are much more irregular than is the as-built condition.
- Following these microstructural evolutions, the yield stress tends to decrease with the temperature of heat treatment while the ductility increases. A summary of the main results is given in Figure IV-30.
- The decrease of the yield stress is most likely caused by the decrease of the dislocation density with the heat treatment temperature.
- The work hardening of the different materials resulting from the different heat treatments is compared. From 600 MPa, the work hardening is identical regardless of the microstructures of interest.
- The twin fraction evolves similarly as a function of strain regardless of the heat treatment.
- The process parameter limitation window breaks the cylindrical symmetry around the building direction that one would have expected with a rotation of 67°. The ductility of

the specimen with the tensile direction aligned with the argon flux is 7% higher than that of the specimen with the tensile direction orthogonal to the argon flux.

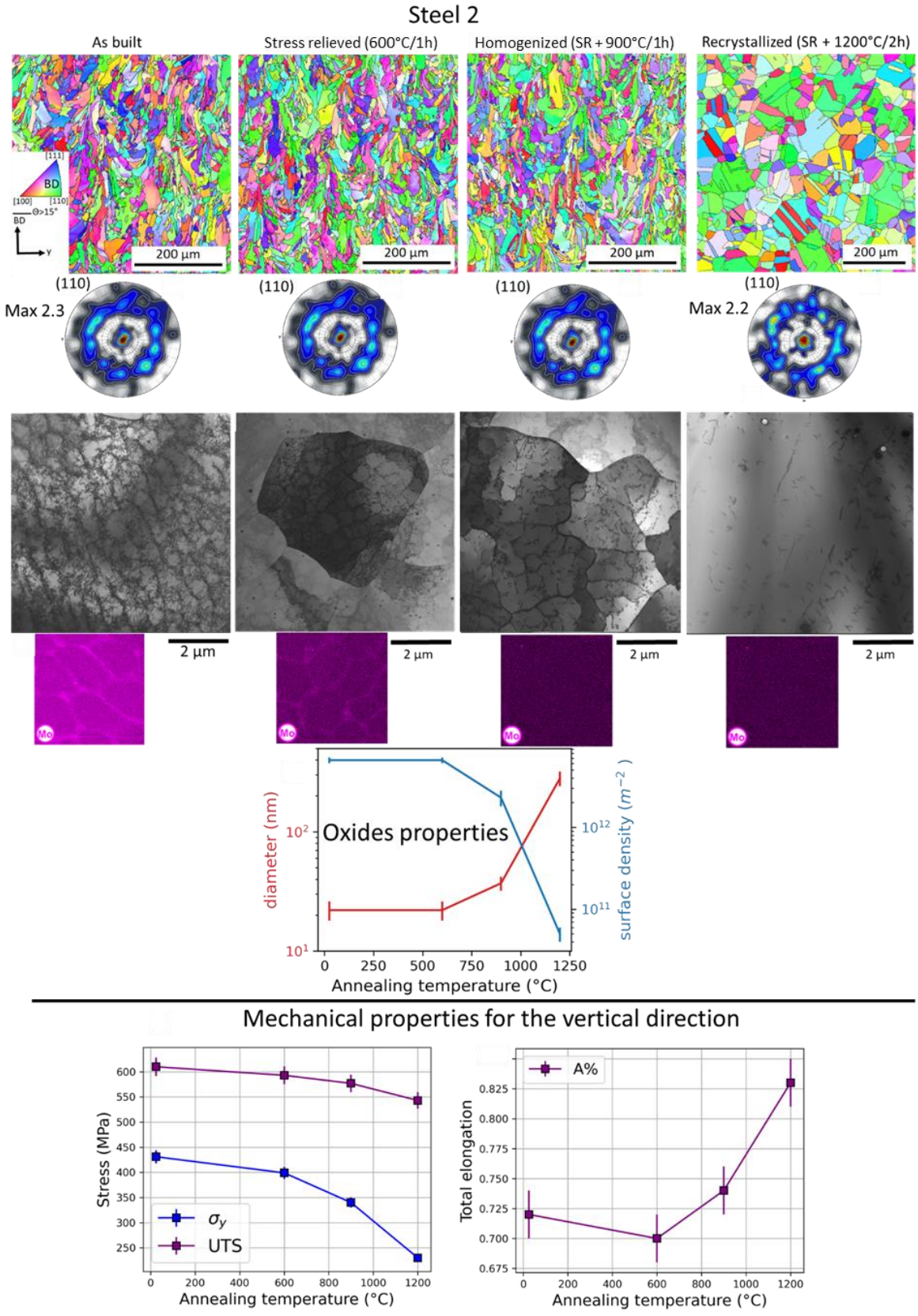

Figure IV-30: Graphical abstract of Chapter IV.

Chapter V. Modeling the tensile response of the 316L produced by LPBF

V.1 Introduction

The aim of this Chapter is to build a framework to model the tensile response of the LPBF 316L alloy subjected to various heat treatments. This should help to weight what are the key factors affecting the plastic mechanical response of the material depending on its microstructure. We deliberately selected a physically-based model that can account for different microstructural features and mechanisms of plastic deformation (dislocation glide and twinning), including factors such as grain size, dislocation density… Previous attempts to model the plasticity of 316L processed using LPBF have been made. However, these models were based on empirical constitutive laws such as Hollomon [161] or Voce law [99] fitted to the experimental results. Such models were not applied to compare different heat treatment conditions [13]. In this context, the Kocks-Mecking model [37] appears to be well-suited and is employed in this Chapter. The model will incorporate considerations regarding the initial grain size and twinning effects, with contributions from both isotropic and kinematic hardening.

However, the present model will not account for the presence of oxides or the arrangement of dislocations. This choice is motivated by our experimental observations: oxides do not bring a significant strengthening contribution as discussed in Chapter IV.7.1. Furthermore, the strain hardening behavior of stress-relieved (600°C/1h) and homogenized (SR+900°C/1h) samples exhibits similarities despite significant differences in the initial dislocation density and arrangement. The objective is to determine if this model can adequately describe the experimental data. If the model is in line with the experimental results, there may be no need to incorporate a higher degree of complexity by taking into account the arrangement of dislocations. However, if the model fails to provide a good description of the mechanical response, adjustments could be made.

This chapter starts by introducing the historical Kocks-Mecking model and the possible modifications that have been proposed over the years to take into account additional mechanisms. A more detailed description of the model employed in this study is given. The strategy deployed to apply the model to our microstructures is described. The model will be first applied on Steel 2 loaded in the vertical direction for the various microstructures investigated (as-built and heat-treated). Then, applied to Steel 1 also in the vertical direction. The subsequent discussion focuses on the influence of different microstructural features that can be inferred from the model. The key outcomes and their consequences are finally summarized.

V.2 Kocks-Mecking based models

V.2.1 The historical Kocks-Mecking model

The pioneering Kocks-Meckings model [37] is a physically-based model allowing the modeling of the work-hardening of polycrystals. The model uses the dislocation density as an internal state variable [162]. In its simplest form, it is described by the two following equations:

$$\sigma_f = \sigma_{ss} + M\alpha\mu b\sqrt{\rho} \quad \text{(V-1)}$$

$$\frac{d\rho}{d\epsilon} = M\left(\frac{1}{b\Lambda} - k_2\rho\right). \quad \text{(V-2)}$$

The first equation expresses the flow stress (σ_f) as a function of the dislocation density (ρ). This equation is the forest hardening equation. In this equation, σ_{ss} is the contribution of the solid solution and including the Peierls stress (2 MPa [40]), M is the Taylor factor, α is the mean interaction strength between dislocations, μ is the shear modulus, and b is the Burger vector. The second equation enables the prediction of the evolution of the dislocation density with plastic deformation (ε). The first part of this equation represents the production of dislocations, which is inversely proportional to the mean free path of dislocations (Λ). The mean free path of dislocations is inversely proportional to the square root of the dislocation density, with a coefficient k_1, which represents the fact that dislocations are not systematically stopped when meeting a forest dislocation. The equation can be then written as:

$$\frac{d\rho}{d\epsilon} = M\left(\frac{k_1}{b}\sqrt{\rho} - k_2\rho\right). \quad \text{(V-3)}$$

The second part represents the annihilation, or dynamic recovery. It is proportional to the dislocation density with a coefficient k_2. This coefficient depends on the strain rate, temperature, and stacking fault energy [37]. Quoting the authors [37] '*this model provides a reasonable fit over a significant range*' of tensile test experiments. By deriving equation V-1, and inserting equation V-2, one can write:

$$\frac{d\sigma_f}{d\epsilon} = M^2\alpha\mu\frac{k_1}{2} + \frac{M\sigma_{ss}}{2}k_2 - \frac{Mk_2}{2}\sigma_f\,. \quad \text{(V-4)}$$

In this equation, one can see that the strain hardening is expressed by a decreasing slope as a function of the flow stress σ_f. Representing the strain hardening as a function of flow stress is called a Kocks-Mecking plot. A Kocks-Mecking plot of a copper polycrystal is shown as an example in Figure V-1. One can see that stage III, which represents the major part of plastic deformation, is effectively well described by a slope.

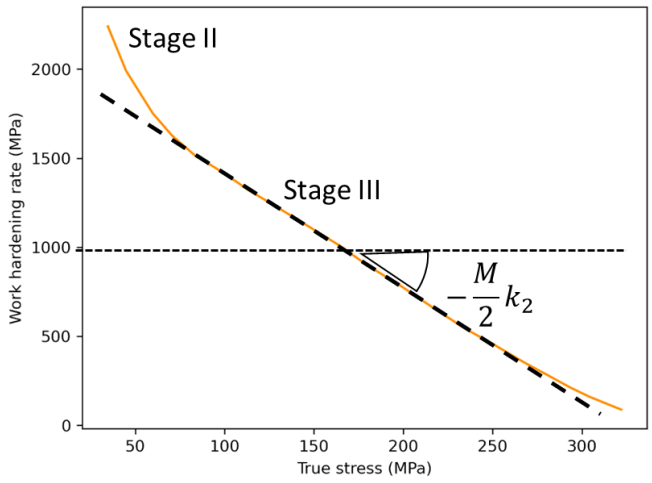

Figure V-1: Kocks-Mecking plot of a copper polycrystal deformed under compression at a strain rate of $1s^{-1}$. From [37].

V.2.2 Modified Kocks-Mecking model including a grain size effect

The Kocks-Mecking model is physically-based and can be modified to take into account additional effects. For instance, it was modified in order to take into account the effect of grain size. Grain size can influence both isotropic and kinematic hardening. From a macroscopic point of view, an isotropic hardening is related to an isotropic growth of the yield surface, while a kinematic hardening is related to a displacement in a certain direction of the yield surface. For uniaxial testing, it is generally in the same direction as the test. From a microscopic point of view, isotropic hardening is related to the accumulation of dislocations in the material, and kinematic hardening is related to the stacking of dislocations in impenetrable obstacles (grain boundaries or non-shearable precipitates) that creates a long-range stress in the inverse direction of the tensile direction.

For isotropic hardening, the stress is still only related to the dislocation density as modeled by equation (V-1). It has been shown that the accumulation of dislocations in the material is expressed based on the mean free path of dislocations. Grain boundaries are considered contributing to the mean free path of dislocations. In this case, grain boundaries are supposed to bring a contribution to the overall strain hardening via an additional storage rate as follows [37]:

$$\frac{d\rho}{d\epsilon} = M\left(\frac{1}{bD} + \frac{k_1}{b}\sqrt{\rho} - k_2\rho\right) \tag{V-5}$$

with D the grain size. This modification of the equation describing the evolution of the dislocation density upon straining leads to an upgrade of strain hardening with the grain size. The grain size is expected to have a strong effect on strain hardening during the total plastic deformation.

For the kinematic hardening, grain boundaries are considered as obstacles to dislocation motion. Dislocations will be piled up at the grain boundaries. This will induce a back stress, opposed to the shear stress which will impede the progress of similar dislocations. This is schematically described in Figure V-2 (a) and has been observed experimentally, see Figure V-2 (b).

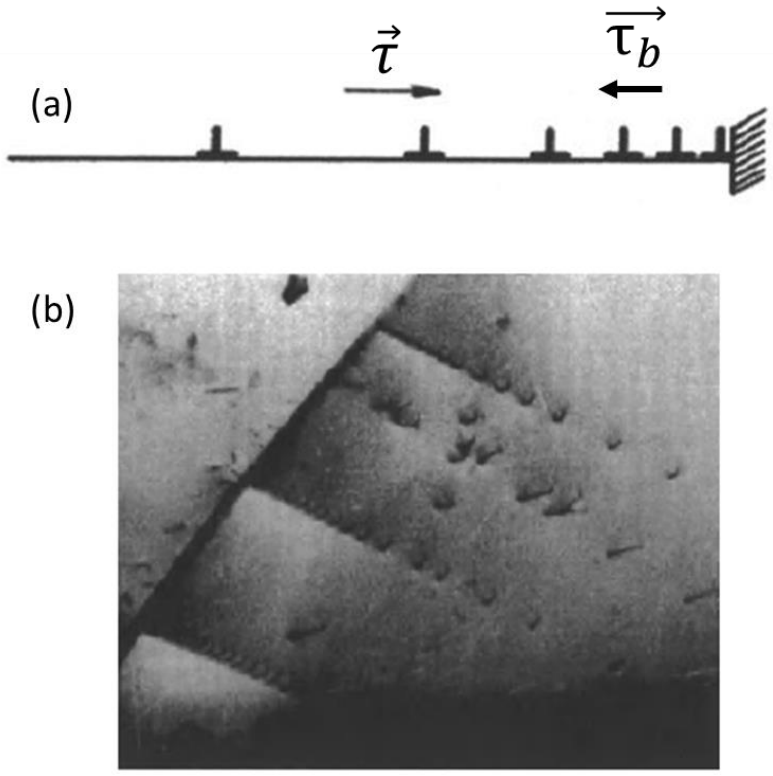

Figure V-2: Dislocation pile-up at grain boundaries: (a) Schematic representation; (b) experimental observation in an austenitic stainless steel. From [30].

The total flow stress can be thus written:

$$\sigma_f = \sigma_{ss} + \sigma_{df} + \sigma_b \tag{V-6}$$

$$\text{with } \sigma_{df} = M\alpha\mu b\sqrt{\rho} \tag{V-7}$$

where σ_{ss} is the solid solution strengthening contribution, σ_{df} is the isotropic hardening induced by dislocation forest, and σ_b is the back stress. Models combining isotropic and kinematic hardening were developed in the past, see e.g. the one developed by Sinclair [160] to describe the mechanical behavior of fine-grained copper and silver. It was shown that the grain size affects the strain hardening at low plastic strain (<5%) but has no impact at larger plastic strains [160]. The model used hereafter is derived from this model. In its simplest expression, the back stress induced by grain boundaries is written as follows:

$$\sigma_b = M\mu\frac{b}{D}n \tag{V-8}$$

where n is the number of dislocations that have been stopped at the boundary on a given slip band. This corresponds to the stress required to bend a dislocation in a semicircle of size D [163]. This equation is valid for an isolated grain. To take into account that grains are not isolated, equation (V-8) was modified as follows:

$$\sigma_b = M\mu\frac{b}{D}n\left(1 - \frac{n}{n_0}\right) \tag{V-9}$$

with n_0 the maximum number of dislocation loops on a given slip band. A law is needed to describe the evolution of the number of dislocations stored at grain boundaries. This law was written as follows:

$$\frac{dn}{d\epsilon} = \frac{\lambda}{b}\left(1 - \frac{n}{n_0}\right) \leftrightarrow n(\epsilon) = n_0\left(1 - e^{-\frac{\lambda * \epsilon}{b * n_0}}\right) \quad \text{(V-10)}$$

where λ is the mean spacing slip line at the grain boundaries. To take into account the contribution of grain size to forest hardening, equation (V-5) was also modified to take into account the number of slip bands close to the boundaries:

$$\frac{d\rho}{d\epsilon} = M\left(\frac{k_3}{bD}\left(1 - \frac{n}{n_0}\right) + \frac{k_1}{b}\sqrt{\rho} - k_2\rho\right) \quad \text{(V-11)}$$

with k_3 accounting for the efficiency of dislocation storage at the grain boundary with respect to forest hardening. With this model, the authors of [160] successfully accounted for the grain size effect, with only three fitting parameters (k_3, λ, n_0).

V.2.3 Modified Kocks-Mecking model including a TWIP effect

The Kocks-Mecking model was modified to include a TWIP effect. Twins contribute to the overall plastic deformation and are often considered as interfaces acting as grain boundaries [159], [164]–[167]. Twinning affects the strain hardening through the so-called dynamic Hall Petch effect. Therefore, if the twin boundary density increases with plastic deformation, the grain size decreases with plastic deformation resulting in a dynamic Hall-Petch effect. Considering that twins contribute to the shear deformation, the following law of mixture was often used [159], [164], [165]:

$$d\gamma = (1 - F)d\gamma_g + \gamma_t dF \quad \text{(V-12)}$$

where $d\gamma$ is the increment in shear strain, γ_g is the shear strain induced by dislocation glide, γ_t is the twinning shear strain equal to $1/\sqrt{2}$ and F is the volume fraction of twin. This law of mixture supposes that there is no dislocation slip within twins, which is most likely true at low plastic strains but becomes questionable at larger plastic strains [168]. The equivalent grain size, which decreases with twinning is obtained by a geometric addition as follows:

$$\frac{1}{D_{eq}} = \frac{1}{D_{gb}} + \frac{1}{d_t} \quad \text{(V-13)}$$

where D_{eq} is the equivalent grain size, and d_t is the mean twin spacing which depends on plastic deformation. The mean twin spacing is difficult to measure experimentally because twins can be very thin with a large dispersion in size and with a heterogeneous spatial distribution. To overcome this issue, Bouaziz used the stereological analysis of Fullman [169] to link the mean twin distance with the twin volume fraction F and the mean twin thickness e using equation (V-14):

$$\frac{1}{d_t} = \frac{F}{2e(1 - F)} \, . \quad \text{(V-14)}$$

It is supposed that all grains show a TWIP effect and that each twin has the same thickness with a constant mean distance between twins. A schematic illustration of the various microstructural objects is shown in Figure V-3. This relation was used in many other studies to model the TWIP effect [7], [165], [167], [170]. In those studies, the twin thickness was fixed constant regardless the level of plastic deformation. The evolution of the twin fraction is described by a set of 1 to 4 parameters that are determined through the best fit of the stress-strain curves. The evolution of the twin fraction depends on the level of plastic strain [159], [165] or on the macroscopic tensile stress [7], [164].

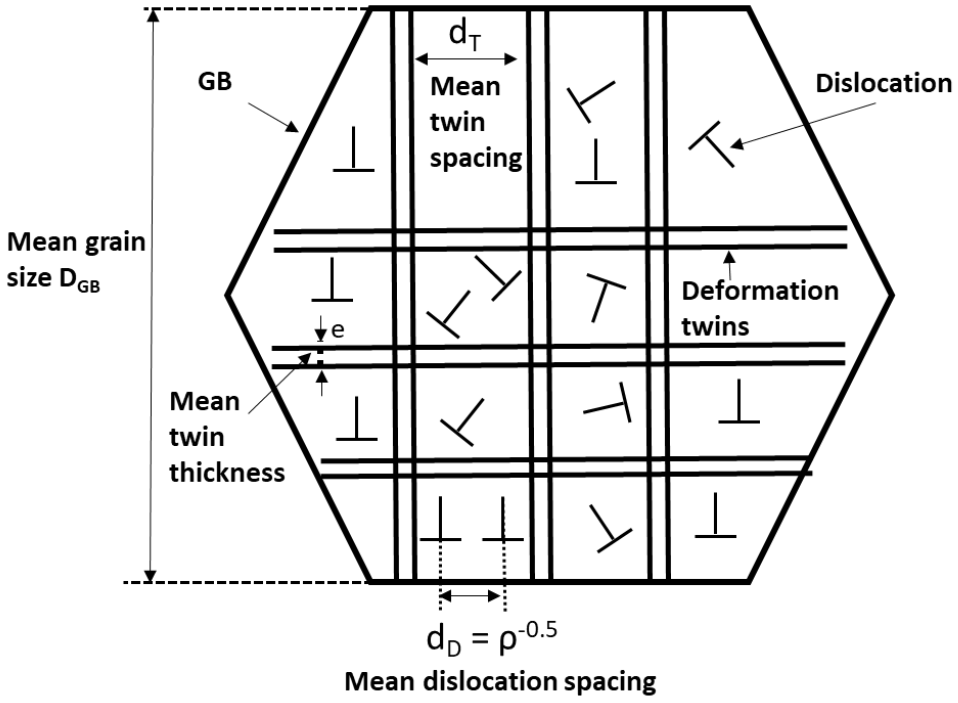

Figure V-3: Schematic illustration of the different microstructural length scales used in the constitutive model. Adapted from [7].

Twin boundaries can have an impact, as grain boundaries, on both isotropic and kinematic hardening. Models that consider only the isotropic hardening use equation (V-5), but with the equivalent grain size that decrease with deformation [7], [159], [164]. Bouaziz [165] proposed a model that consider both isotropic and kinematic hardening. This model is used hereafter and is described in the next section.

V.2.4 Description of the model employed in this work

From the literature, the 316L alloy is expected to show a TWIP effect that strongly affects its strain hardening behavior. In addition, since the grain size is varied when the samples are subjected to heat treatments, we need a model that successfully accounts for the TWIP effect and that is capable of capturing the influence of grain size. After a literature review, the selected model is the one developed by Bouaziz et al. [165] for TWIP steels (Fe-22Mn-0.6C). This model is a modified Kocks-Mecking model that takes into account twinning and grain size, with a combination of isotropic and kinematic contribution to the strain hardening. This model is inspired by the model of Sinclair [160] described above. In [165], the effect of different initial grain sizes is successfully captured and the TWIP effect is

taken into account. The total flow stress is obtained by the addition of the contribution of the solid solution (including the Peirels stress), the hardening from forest dislocation, and the back stress:

$$\sigma_f = \sigma_{ss} + M\alpha\mu b\sqrt{\rho} + M\mu\frac{b}{D_{eq}}n\,. \tag{V-15}$$

In equation (V-15), the back stress is written in its simplest form as in equation (V-8), with *n* the number of dislocations stored at the boundaries. This parameter follows the same evolution with deformation as in the model of Sinclair, see equation (V-10). The evolution of the dislocation density with deformation is thus very similar to the one proposed by Sinclair in [160]:

$$\frac{d\rho}{d\epsilon_g} = M\left(\frac{1}{bD}\left(1-\frac{n}{n_0}\right)+\frac{k_1}{b}\sqrt{\rho}-k_2\rho\right) \tag{V-16}$$

where ε_g is the deformation resulting from dislocation glide. By using equation (V-12), equation (V-16) can be written as a function of the total deformation:

$$\frac{d\rho}{d\epsilon} = \frac{1-\frac{\gamma_t}{M}\left(\frac{dF}{d\epsilon}\right)}{1-F}\,M\left(\frac{1}{bD_{eq}}\left(1-\frac{n}{n_0}\right)+\frac{k_1}{b}\sqrt{\rho}-k_2\rho\right). \tag{V-17}$$

The contribution of twinning to deformation, and the calculation of the equivalent grain size are respectively given in equations (V-12), (V-13), (V-14). In the paper of Bouaziz [165], the twin thickness is fixed and the twin volume fraction is supposed to evolve as a sigmoid described with four parameters: one depending on the grain size and the three other parameters independent from each other. These parameters are determined when the best fit between the experimental and modeling curves is found. To describe plastic deformation for different samples showing five different grain sizes as well as the Bauschinger effect in the sample showing a grain size of 3 µm, the authors had to determine 12 parameters to describe all the conditions of interest [165].

V.3 Methodology employed in the present work to adjust the model

We would like to recall here that the model will be first applied for Steel 2 loaded in the vertical direction for the different microstructures investigated (as-built and heat-treated). The model is also used to describe the tensile response of Steel 1. The following sections describe the methodology employed in this work to adjust the model applied to Steel 2.

V.3.1 Inputs of the model

The model of Bouaziz [165] involves numerous parameters that need to be determined by finding the best fit of the experimental stress-strain response. The model will be considered robust if it is capable of reproducing the mechanical responses of various microstructures. To the best of our knowledge, the model has been used only to describe a 'wrought product'. Throughout this work, a wrought product is

defined as a recrystallized microstructure with equiaxed grains in the range of 1-100 µm in size with a low initial dislocation density. In our specific case, we aimed to assess the model's applicability in describing the plasticity of LPBF microstructures (as-built and heat treated). To do so, we intended to calibrate the modeling parameters using wrought products and subsequently evaluate whether these parameters can be effectively used to describe the mechanical response of LPBF microstructures. However, since we did not conduct experiments on wrought products with varying grain sizes, we relied on values available in the literature for some of the parameters (b, μ, α, λ, n_0) or by estimating them experimentally (grain size, twinning fraction parameters) or with models (Taylor factor, solid solution contribution). These were considered as fixed parameters. The specific values of these fixed parameters are summarized in Table V-2.

V.3.1.1 Parameters from the literature

Some parameters are usual for this type of model and can be easily found in literature of 316L, typically α, b, and μ). This is not the case for the parameters n_0 and λ. These two parameters describe the kinetics of the evolution of the back stress arising from the pile-up of dislocations at grain or twin boundaries. These parameters were found for Copper in [160] and TWIP steels in [165]. A summary of the values of these parameters in previous studies is given in Table V-1. One can see that between Copper and TWIP steel, there is not much variation between these two parameters. With the objective of having the minimum parameters to adjust, we supposed that these two parameters are identical between a high Mn TWIP steel and a 316L steel. Thus, the values from the paper of Bouaziz [165] were used.

With the given values of n_0 and λ, the parameter n approaches saturation rapidly, reaching 0.99*n_0 at a plastic deformation of 3%. This implies that beyond this deformation, grain and twin boundaries do not contribute to the production of dislocation ($1 - n/n_0 \approx 0$ for $\varepsilon > 3\%$ in equation (V-17)). Prior to this deformation, twinning effects are negligible, and thus do not contribute to the production of dislocation. As a result, in the model, in the plastic deformation regime, twinning has no discernible impact on production of dislocation, i.e. isotropic hardening.

Table V-1: Modeling parameters determined in previous studies.

Material and associated reference	λ (nm)	n_0
Copper, Sinclair et al. [160]	413	6.7
High Mn TWIP steel, Bouaziz et al. [165]	325	7.5

V.3.1.2 Parameters determined experimentally

The evolution of the twin fraction was determined using the sigmoid function which describes the experimental data for Steel 2 when loaded along the vertical direction, see Figure V-4. This twin fraction will be considered constant regardless of the conditions.

Experimentally, it was observed that twin thickness increases with plastic deformation, and that the thickness from one twin to the other can be significant. This makes measurement of twin thickness

difficult. In order to minimize the parameters to be adjusted, the twin thickness *e* is assumed constant throughout plastic deformation and is a fitting parameter.

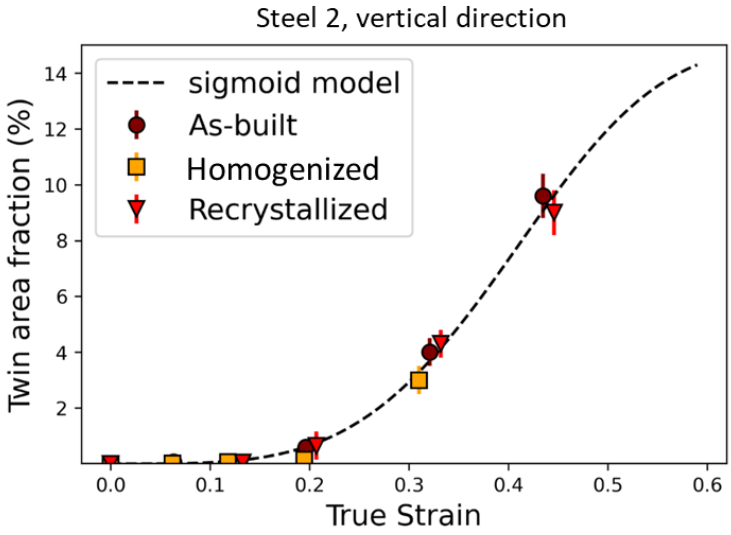

Figure V-4: Experimental evolution of the twin fraction with plastic deformation in Steel 2 for the vertical direction for different conditions (heat treatments).

V.3.1.3 Parameters determined with model

It exists different models to determine the Taylor factor, see Chapter I.3.1.1B. In this Chapter, we will use a crystal plasticity model, namely the Visco-Plastic Self Consistent model (VPSC) [32]. This crystal plasticity allow to estimate this value [39]. For a random texture, its value is equal to 2.65. This is the value found for Steel 2 for the vertical direction. The contribution of solid solution will be estimated from empirical formula given in Chapter IV.7.1, which were found to provide a good prediction of the yield stress of recrystallized microstructures. This contribution of the solid solution will be kept constant regardless of the conditions.

Table V-2: Parameters used for the simulated curves.

Parameters	Physical meaning	Value	Determination
μ	Shear modulus	78 GPa	Ref [7]
b	Burgers vector	0.255	Ref [7]
α	Mean dislocation strength	0.3	Ref [7]
λ	Distance between slip bands	325 nm	Ref [165]
$n0$	Maximum number of loops	7.5	Ref [165]
M	Taylor factor	2.65	Estimated (VPSC) Ref [32]
$\sigma_{ss\text{-}2}$	Solid solution for Steel 2	170 MPa	Estimated (Chap. IV.6)
$D_{r\text{-}2}$	Grain size for recrystallized state for Steel 2	23 µm	Measured (intercept length)
$D_{LPBF\text{-}2}$	Grain size for LPBF state Steel 2	6 µm	Measured (intercept length)

V.3.2 The fitting algorithm

Only four parameters remain to be determined: k_1 and k_2 parameters from the Kocks-Mecking model, the initial dislocation density (ρ_{ini}), and the mean twin thickness (e). To determine the best set of parameters that reproduce closely the experimental true stress-strain curves, an algorithm was developed and implemented in Python.

Only the plastic deformation regime of the experimental true stress-strain curves was selected to exclude the elastic regime. Maximum and minimum value for each variable were set. The minimization algorithm described latter choose several (60) initial set of parameters to test. The dislocation density was estimated for each experimental deformation using equation (V-16). To resolve this differential equation, the *Solve_ivp* function from the *Scipy integrate* library was employed. An explicit Runge-Kutta method of 8th order was used. The step size was calculated to achieve a relative error of 10^{-3}. Knowing the dislocation density for each deformation step, the stress was computed using equation (V-15). Subsequently, the error between the calculated and experimental stress was determined through the least square method. The parameters that minimize this error were identified using the differential evolution minimization algorithm from the *Scipy optimize* library. This algorithm, although typically slower than conventional gradient-based techniques, explores large ranges in the parameter space without requiring an initial solution, but only bounds for each parameter. It was observed that the final solution was independent of the bounds selected initially. To enhance visualization, the first point of the calculated stress was set to zero. Figure V-5(a) illustrates an example of the calculated stress-strain response along with the Kocks-Meckings plot in Figure V-5(b) where the impact of each parameter is illustrated. The initial dislocation density correlates with the yield stress. k_2 is related to the initial slope of the work hardening, k_1 corresponds to the intercept at the origin of the initial work hardening line, and $1/e$ influences the height of the hump induced by twinning.

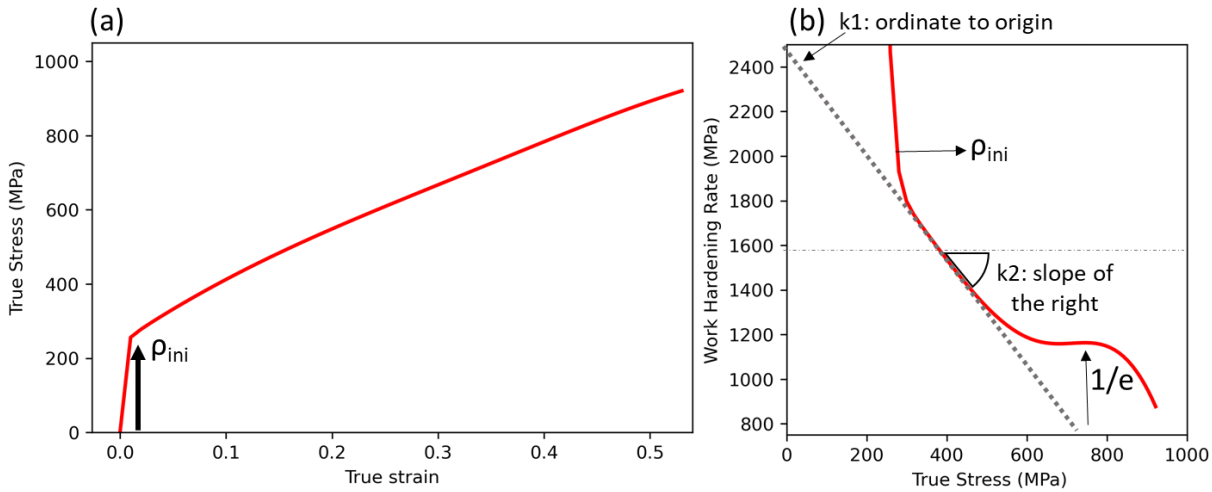

Figure V-5: Example of a calculated (a) true stress-strain curve, and (b) Kocks-Mecking plot (strain hardening rate) where the impact of each parameter is illustrated.

To fit these four parameters, two strategies can be used:

(i) Determining first ρ_{ini}, k_1 and k_2 over the early stage of plastic deformation, typically for plastic strains <20%, a regime in which twinning is expected to have nearly no impact. After

adjusting these three parameters, the mean twin thickness e can be subsequently adjusted to find the best fit of the experimental curve.

(ii) Determining the four parameters (ρ_{ini}, k_1, k_2 and e) giving the best fit over the whole tensile response.

Both methods were attempted. A comparison of the two methods for the recrystallized Steel 2 is given in Figure V-6. One can see that both methods give satisfying results and similar values for the adjusted parameters. Hereafter, the second strategy will be systematically used.

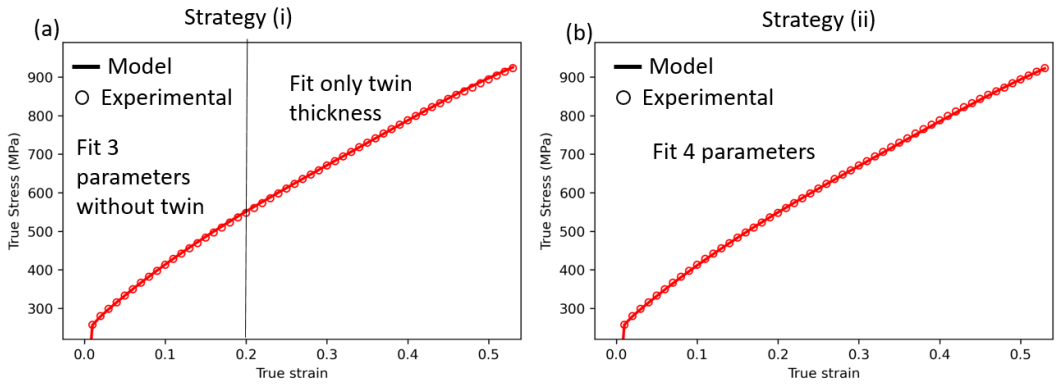

ρ_{ini} (10^{12} m^{-2})	k_1	k_2	e (nm)
9.13	0.0261	1.85	251

ρ_{ini} (10^{12} m^{-2})	k_1	k_2	e (nm)
9.10	0.0264	1.88	245

Figure V-6: Comparison of the two strategies of fitting. (a)-(b) Flow curve comparing the model and experimental for respectively the strategy (i) and (ii). Obtained values are given in the table below.

V.4 Results

Each curve can be characterized by four parameters: the k_1 and k_2 parameters of the Kocks-Mecking model, the initial dislocation density (ρ_{ini}), and the mean twin thickness (e). It is assumed that the evolution of the twin fraction remains constant regardless of the conditions studied. The primary aim of the model is to determine if the parameters obtained from a wrought condition can effectively describe the tensile response of microstructure inherited from LPBF and further heat treated. To achieve this, we will calibrate the model for the recrystallized microstructure of Steel 2 loaded in the vertical direction and then constrain some of the parameters to describe other microstructural conditions. The model is then applied to Steel 1.

V.4.1 Recrystallized microstructure (reference)

The four parameters **(ρ_{ini}, k_1, k_2, e)** will be first determined by fitting the tensile response of Steel 2 loaded along the vertical direction and subjected to SR+1200°C/2h (recrystallized condition). This microstructural condition is close to the one where the model was applied in the literature (equiaxed grains and low dislocation density).

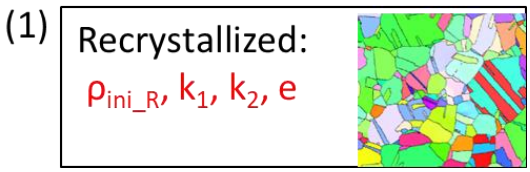

Figure V-7: Schematic of the methodology employed to determine the parameters of the model for the recrystallized microstructure. The parameters are determined through the fit of the experimental curve and are written in red.

The comparison between the experiment and the model is shown in Figure V-8 (a-b). For plastic strains < 0.2 (flow stress < 500 MPa) the fit is excellent. However, for larger plastic strains, the fit is not as good, but still acceptable. This plastic strain of 0.2 corresponds to the critical strain at which the twinning activity becomes significant. This is not surprising because while twinning was included in the model, some assumptions were made and those might be too strong. For example, it was assumed that twinning occurs in all grains and that the twin thickness is constant throughout plastic deformation. However, it was shown experimentally using EBSD that twins preferentially nucleate in specific orientations and that the twins grow during plastic deformation.

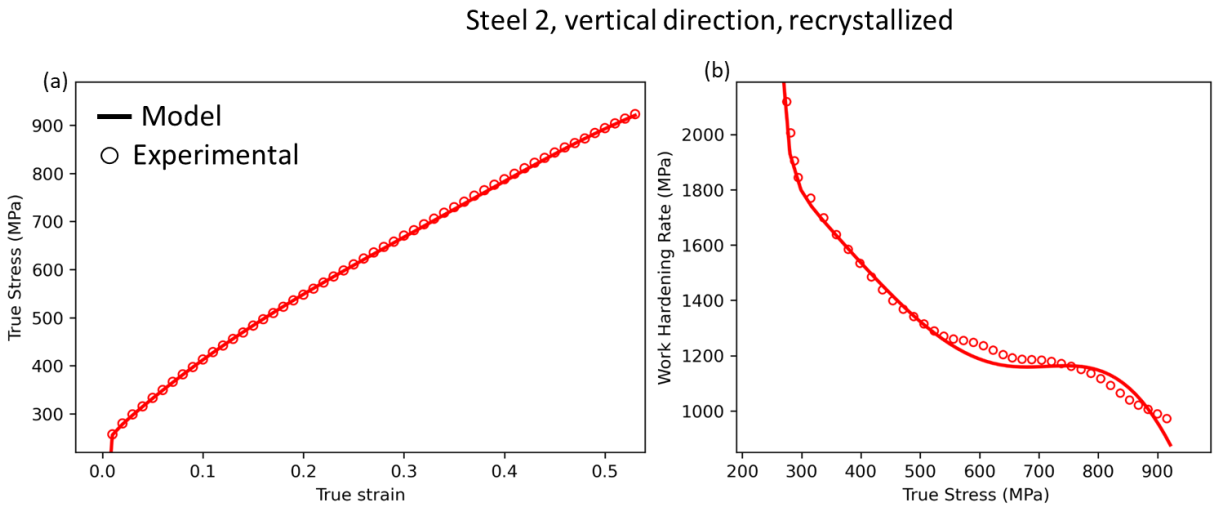

Figure V-8: Comparison between the experiment and the model for the recrystallized Steel 2 loaded along the vertical direction. (a) True stress-strain curve. (b) Kocks-Mecking plot.

The fitting parameters are given in Table V-3. The obtained value for the initial dislocation density for the recrystallized state is 9 x 10^{12} m^{-2}, which gives σ_{df} = 47 MPa. This value of initial dislocation density is higher than the one estimated from the hardening model (1.10^{12} m^{-2}) in IV.7.1, which gave σ_{df} = 16 MPa. This discrepancy is not surprising. First, a value of initial dislocation density of 9 x 10^{12} m^{-2} appears reasonable for a recrystallized state. For example, Monnet et al. [156] found a value close to 5 x 10^{13} m^{-2} for a recrystallized microstructure of 316L. Second, the hardening model was used to estimate the value of the yield stress, while here, the parameters were deduced from the fitting procedure. Besides, the initial dislocation density is sensitive to the value of σ_{ss}. An increase of 10 MPa of this contribution leads to a decrease in initial dislocation density from 9 x 10^{12} m^{-2} to 5 x 10^{12} m^{-2}. To conclude, the value of the initial dislocation density for a recrystallized state does not appear unreasonable and is sensitive to other parameters such as σ_{ss}.

The obtained value for k_1 is 0.026. This value is consistent with the other values found in the literature for the same parameter: 0.032 for copper [160], 0.03 for TWIP steel [164], 0.025 for Ni20Cr [171], and 0.020 for a 316L steel [7]. The obtained value for the k_2 parameter is found equal to 1.88. This value is also consistent with values from the literature: 4.1 for copper [160], 2 for TWIP steel [164], 1.7 for Ni20Cr [171], and 3.9 for a 316L steel [7]. The small difference between values from the literature and the one found here can result from the difference in material, the values of some input parameters (α or M), or ultimately from the model (purely isotropic strain hardening, consideration of grain boundaries, etc).

After the optimization of the model, the mean twin thickness is found to be e = 245 nm. This value is consistent with the experimental observations, see e.g. Figure V-9. Indeed, based on the micrographs, the twin thickness was found to vary between 50 and 700 nm. Moreover, it has been observed (Chapter IV.6.2) that the twin thickness increases during deformation, from several dozens of nanometers to several micrometers at very high deformation (>0.43). The twin thickness derived from the model can be considered as an average value of the twin thickness observed experimentally in plastically deformed specimens.

Table V-3: Fitting parameters for the recrystallized Steel 2 loaded along the vertical direction. Parameters that have been fitted on the actual condition are written in red.

	ρ_{ini} (10^{13} m^{-2})	k_1	k_2	e (nm)
Steel 2, recrystallized	0.9	0.026	1.88	245

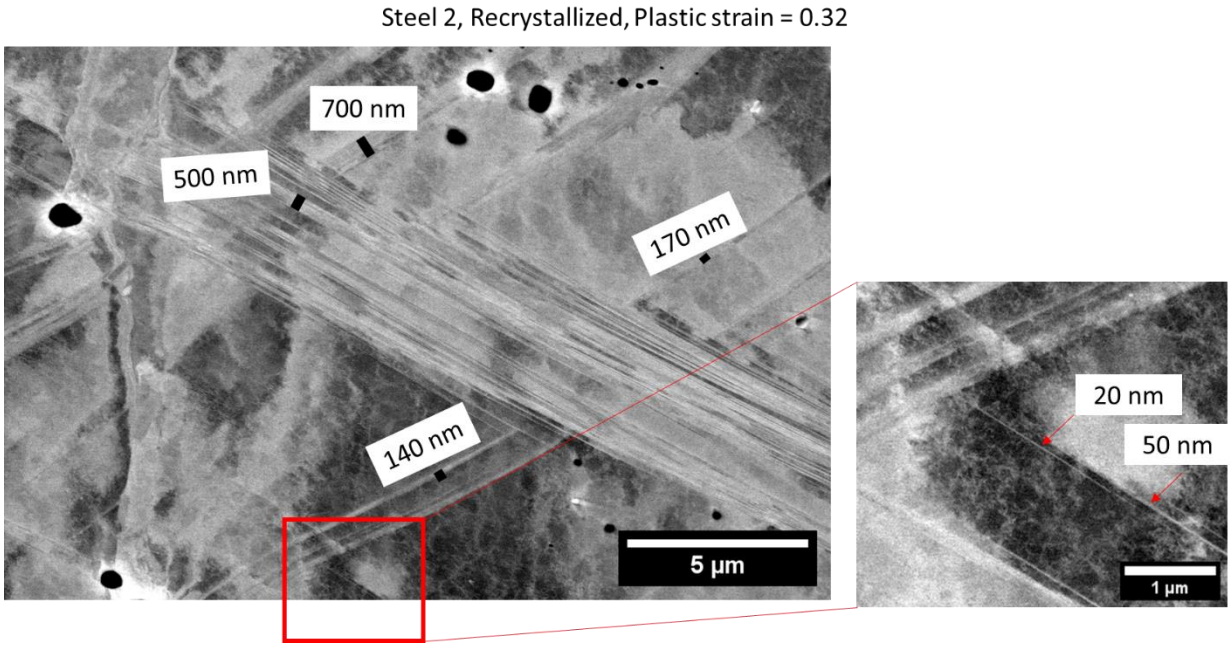

Figure V-9: SEM-BSE images of Steel 2 in the recrystallized condition. Thickness of some of deformation twins are noted.

V.4.2 Other microstructural conditions

In order to adjust the model for different microstructures showing the same texture and loaded along the same direction, the initial dislocation density (ρ_{ini}) was the sole parameter to be adjusted. The other parameters, namely k_1, k_2 and e, are fixed to the values found for the recrystallized condition. This is a strong hypothesis because it supposes that k_2 is independent of the grain size or of the arrangement of dislocations. Experimentally, no significant differences in twin thickness was observed regardless of the condition. This explains why, it was decided to keep the twin thickness e constant for the different conditions examined. The grain size will be adjusted depending on the heat treatment considered using our experimental measurements. The texture is identical between the different microstructural conditions (M is unchanged). With this procedure, the goal is to evaluate if the parameters used to describe the tensile behavior of a recrystallized microstructure (equiaxed grains and low dislocation density) can be used to describe the tensile behavior of microstructures inherited from LPBF. This hypothesis is not straightforward because the organization of dislocations in the microstructure inherited from LPBF, in particular in the as-built and stress-relieved conditions, may have an impact on the Kocks-Mecking parameters k_1 or k_2. It is worth mentioning that there is no consideration on oxides nor on the dislocation arrangement in the model employed here. The strengthening contribution of the solid solution will be kept constant for a given steel composition, i.e. we suppose that our material is chemically homogeneous.

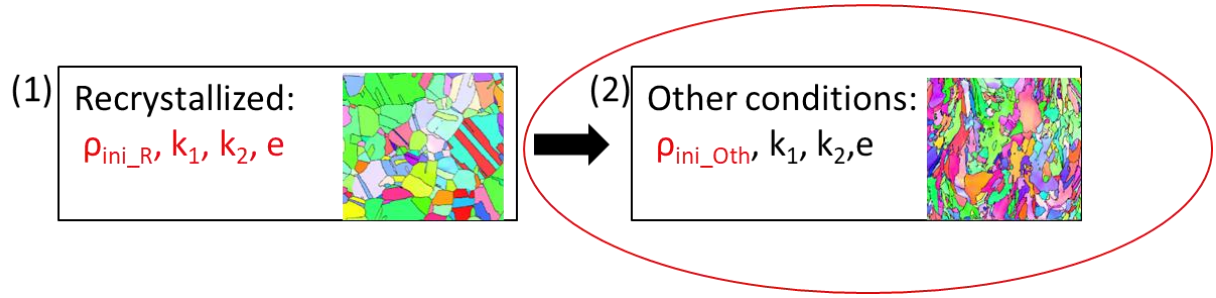

Figure V-10: Schematic of the methodology deployed to determine the parameters of the model for the other conditions when the material is loaded in the vertical direction. The parameters which are determined through the fit of the experimental curves are written in red.

The comparison between the experiments and the model for the SR (600°C/1h) and recrystallized condition is shown in Figure V-11 (a). The comparison of these two conditions is of interest to discuss the role of the arrangement of dislocations because in the SR condition the dislocation network is similar to the one found in an as-built LPBF microstructure but with an expected negligible residual stresses. One can see that the model describes well the SR condition. However, the fit is better in the regime where the twinning activity is not significant. This could be due to the simplify approach used to take into account the twinning contribution in the model. The comparison in work hardening rate is shown in Figure V-11 (b). The model successfully describes the trend observed experimentally between these two conditions. The initial work hardening is higher for the stress relieved condition, but becomes lower while approaching a true stress of 600 MPa. However, in the SR condition, the model's initial work hardening (between 450 and 600 MPa) is slightly lower compared to the values measured experimentally.

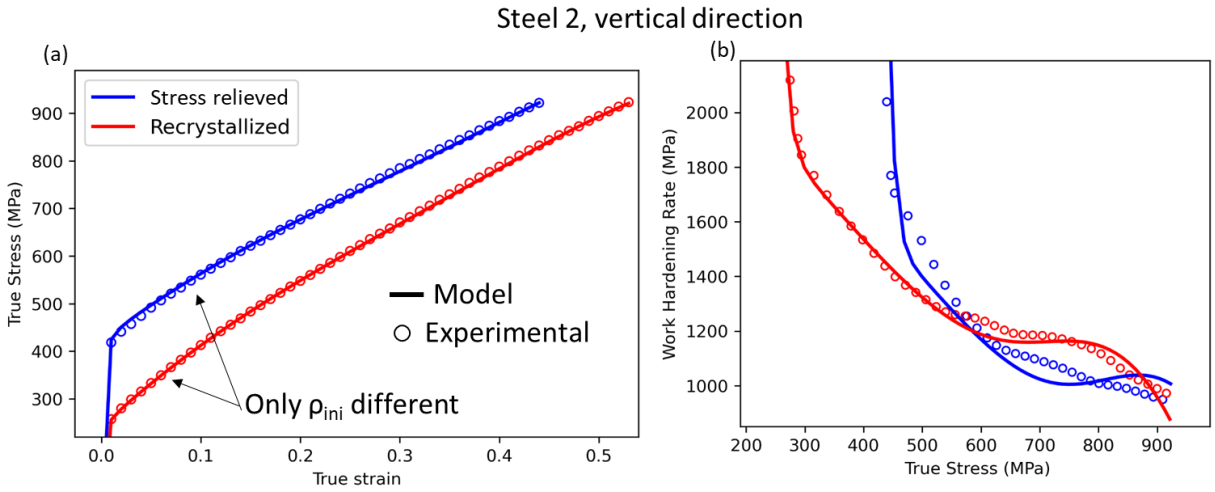

Figure V-11: Comparison between the experiments and the model for Steel 2 loaded along the vertical direction. (a) True stress-strain curve for the SR and recrystallized conditions. (b) Kocks-Mecking plot for the same conditions as shown in (a).

The model can also describe the other conditions. The comparison between the experiments and the model for the as-built and homogenized (SR+900°C/1h) conditions is shown in Figure V-12 (a) for the stress-strain response. One can see that the model describes well these conditions. The comparison in work hardening is shown in Figure V-12 (b). In this case, it fits well the homogenized condition but the fit is less good for the as-built condition.

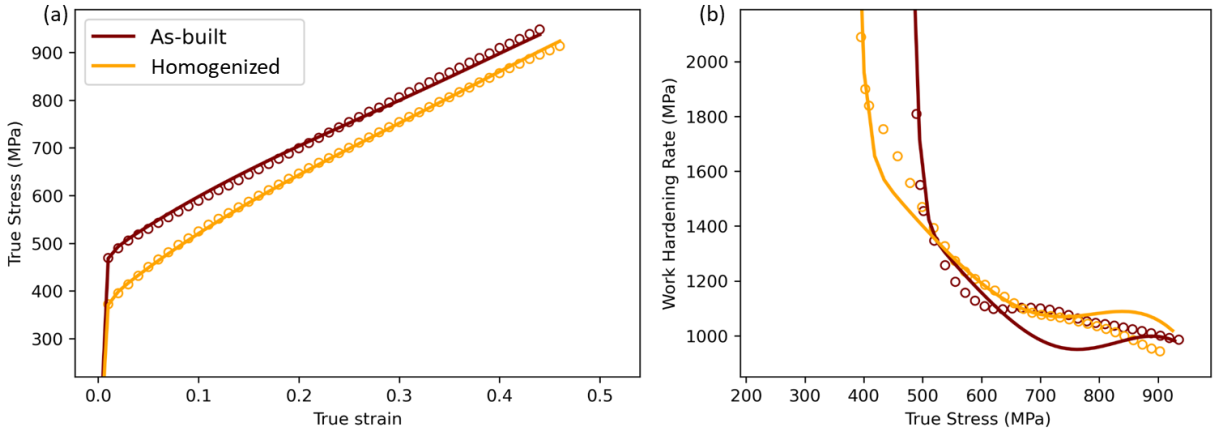

Figure V-12: Comparison between the experiments and the model for Steel 2 loaded along the vertical direction. (a) True stress-strain curve for the as-built and homogenized conditions. (b) Kocks-Mecking plot for the same conditions than (c).

The fitting parameters are summarized in Table V-4. We recall here that the only fitting parameter here was the initial dislocation density. Here, by reducing the number of fitting parameters to the sole dislocation density, the model captures rather well the experimental trends. The initial dislocation densities determined while fitting the experimental data are in good agreement with the values estimated from the strengthening model used in Chapter IV.7.1. In the as-built condition, the dislocation density is found 2.2 x 10^{14} m^{-2} (from the fit) vs 3.7 x 10^{14} m^{-2} (estimation for the strengthening model). For the SR sample, it is found 1.4 x 10^{14} m^{-2} vs 1 x 10^{14} m^{-2}, and for the homogenized condition, it is found 6.5 x 10^{13} m^{-2} vs 1 x 10^{13} m^{-2}.

Table V-4: Fitting parameters for Steel 2 loaded along the vertical direction for the different microstructure studied. Parameters that have been fitted on the actual conditions are written in red and those that have been fitted based on another condition are written in black.

Steel 2 vertical direction	ρ_{ini} (10^{13} m^{-2})	k_1	k_2	e (nm)
Recrystallized (SR+1200°C/2h)	0.9	0.026	1.88	245
Homogenized (SR+900°C/1h)	6.5	0.026	1.88	245
Stress relieved (600°C/1h)	14	0.026	1.88	245
As-built	22	0.026	1.88	245

V.4.3 Application to Steel 1

The objective here is to evaluate if the parameters describing the strain hardening of Steel 2 can be used to describe the one of Steel 1. This will only be done for the vertical orientation. There are three main differences between Steel 2 and Steel 1: the nominal composition, the texture intensity, and the grain size. The chemical composition will induce a different contribution of the solid solution. This will be estimated using the empirical formula detailed in Chapter IV.7.1. It is estimated at 170 MPa for Steel 2 and at 210 MPa for Steel 1. The texture intensity between Steel 1 and Steel 2 is different, from 2.0 in the recrystallized Steel 2, to 4.0 for the recrystallized Steel 1, and 5.1 for the as-built Steel 1. The Taylor factor is then estimated to be 2.63 for the recrystallized and as-built Steel 1.

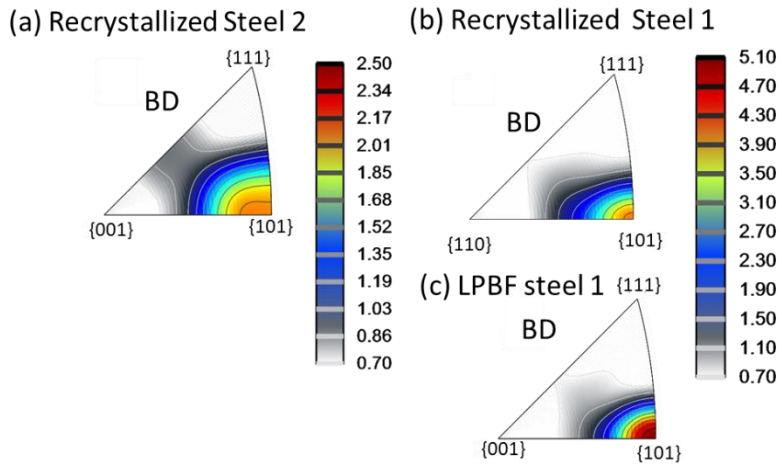

Figure V-13: IPF in the vertical direction for (a) the recrystallized Steel 1 (SR+1200°C/1h), (b) the recrystallized Steel 2 (SR+1200°C/2h), and (c) the as-built microstructure of Steel 1.

It will be assumed that the twinning behavior, ρ_{ini}, k_1, k_2, and e will be identical between Steel 1 and Steel 2 in the vertical direction. The initial dislocation density can be roughly identical between Steel 1 and Steel 2 because these two steels are processed with the same processing parameters. The k_2 parameter is linked with the stacking fault energy (SFE) (possibility of dislocations to be dissociated and that cannot cross slip, see Chapter I.3.2.1). It is reasonable to believe that the difference in composition between the two steels does not result in a large difference in SFE: 26 mJ/m² for Steel 1 vs. 28 mJ/m² for Steel 2, see Chapter III.3.2. Given that the SFE is similar between the two steels, it can reasonably be hypothesized that the difference in chemical composition will not affect the twinning behavior.

Figure V-15 shows the comparison between the experimental tensile curves and the modeled ones in the SR and recrystallized condition. One can see that the model describes well the recrystallized condition, but not the SR. Specifically, the yield stress of the SR condition appears to be too low (~100 MPa) in comparison with the experimental results.

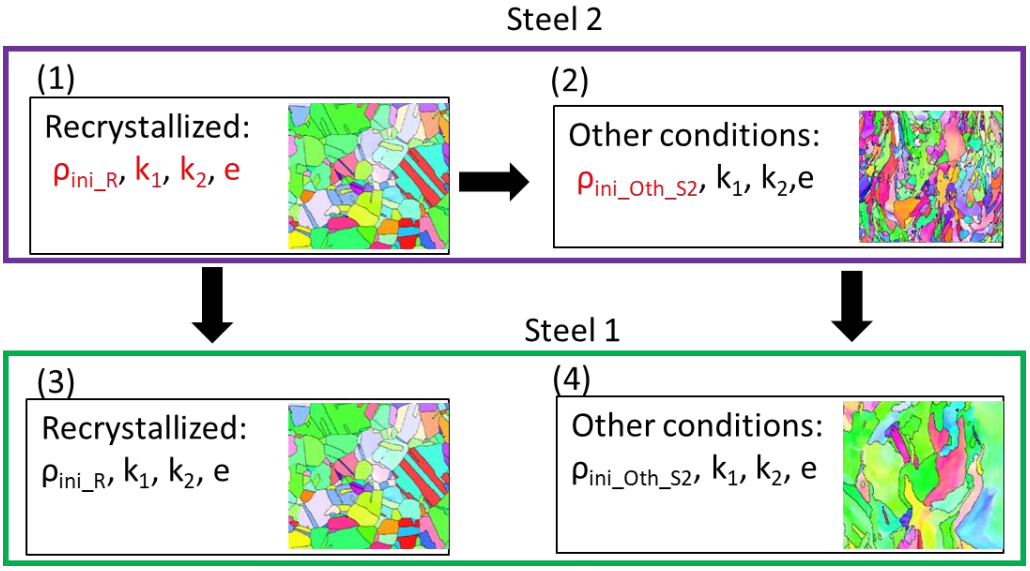

Figure V-14: Schematic of the methodology deployed to determine the parameters of the model for Steel 1. The parameters are determined through the fit of the experimental curve and are written in red.

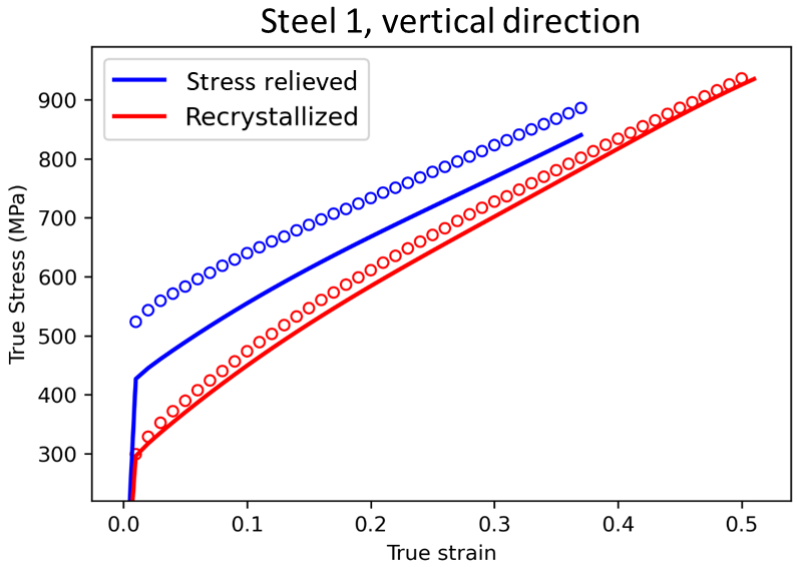

Figure V-15: Comparison in flow curve between the experiments and the model for the recrystallized and SR Steel 1 loaded along the vertical direction.

To account for the difference between the experimental and modeling results for Steel 1, a parameter must change. The only physical parameter that can impact the hardness and might be different between Steel 1 and Steel 2 is the dislocation density. This could be induced by the difference in LAGBs density, that we consider here as stacking of dislocations, or from the difference in solidification between the two steels, discussed in Chapter III.3.4. From now, the dislocation density (***ρ_{ini}***) for the homogenized, SR and as-built condition will be considered as a fitting parameter.

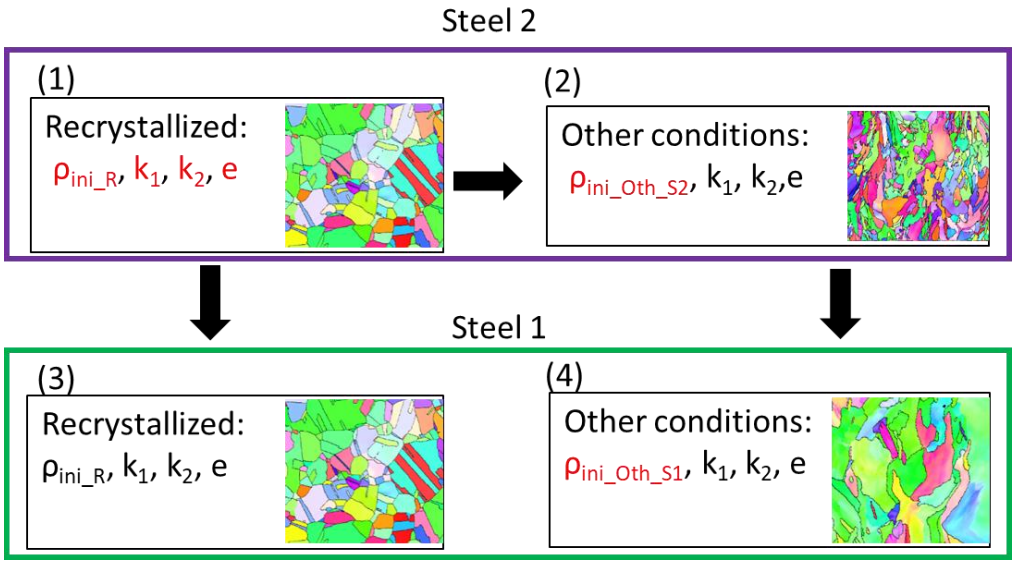

Figure V-16: Schematic of the methodology deployed to determine the parameters of the model for Steel 1 considering the initial dislocation density as a fitting parameter. The parameters are determined through the fit of the experimental curves and are written in red.

Figure V-17 (a) shows the comparison between the experimental tensile curves and the modeled ones in the SR and recrystallized conditions. It describes well these two conditions. Figure V-17 (b) compares the work hardening behavior. One can see that it successfully describes the experiment, with a lower work hardening rate for the SR condition compared to the recrystallized one. The inflection point observed experimentally for the stress relieved is well described, at the good stress level.

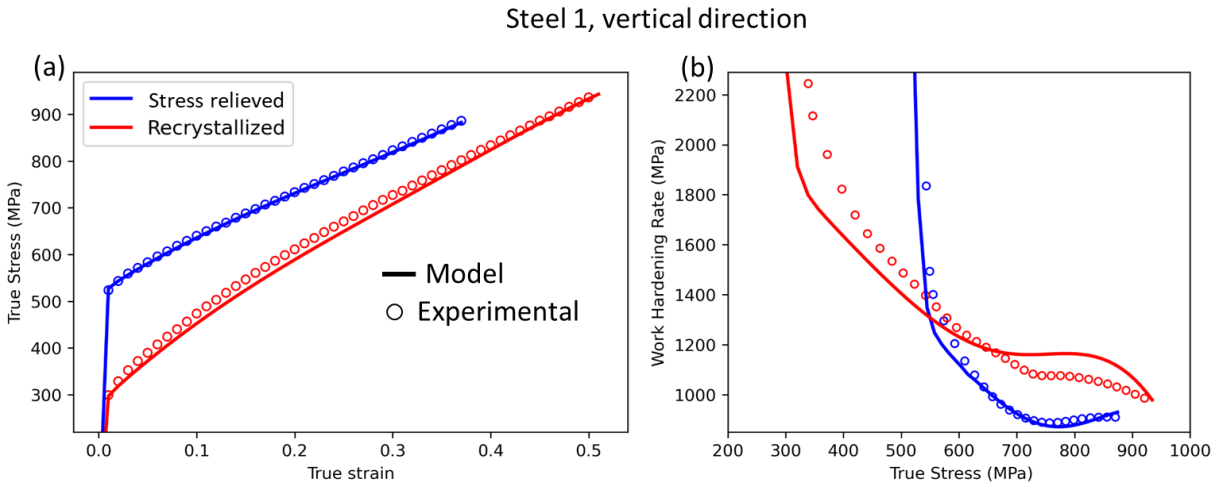

Figure V-17: Comparison between the experimental and modeled data. (a) True stress-strain plot for the recrystallized and stress relieved sample. (b) Kocks-Mecking plot for the same condition as shown in (a).

Figure V-18 (b) shows the comparison between the experimental and modeled tensile curves of the as-built and homogenized conditions. It also describes well these two conditions. Figure V-18 (b) compares the work hardening behavior. One can see that it successfully describes the lower work hardening rate for the as-built condition compared to the homogenized. However, the model struggles to accurately describe the strain hardening of the as-built conditions, with an inflection point occurring at a higher stress level than observed in the experimental data.

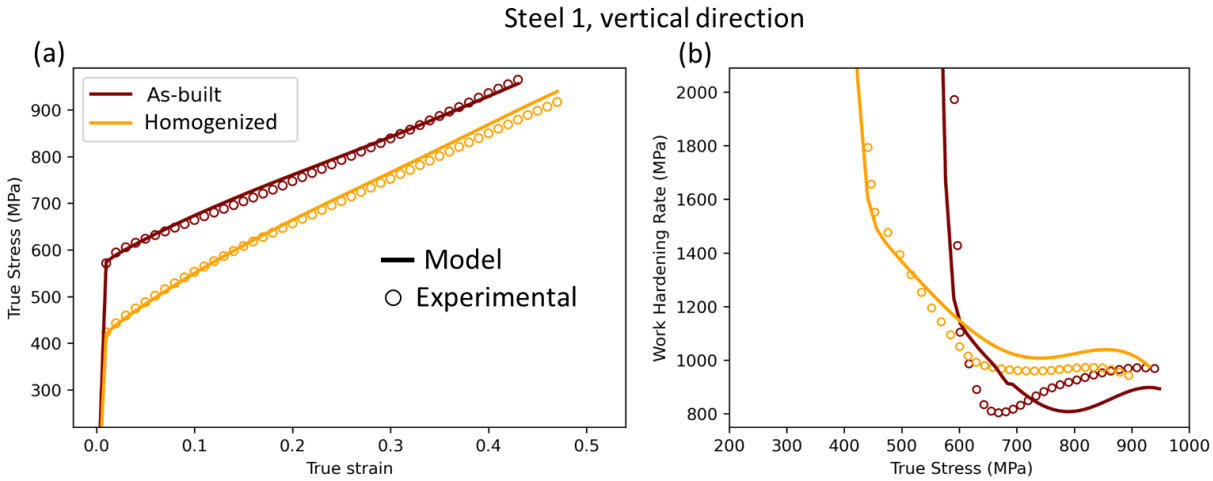

Figure V-18: Comparison between the experimental and modeled data. (a) True stress-strain plot for the homogenized and as-built sample. (b) Kocks-Mecking plot for the same condition as shown in (a).

The values of the fitting parameters are summarized in Table V-5. Notably, the initial dislocation density determined through fitting are approximately twice as high in Steel 1 compared to Steel 2, regardless of the conditions except in the recrystallized state. In the as-built condition, it is respectively found in Steel 1 and Steel 2, 4.8 x10^{14} m^{-2} vs. 2.2 x 10^{14} m^{-2}; 3.5 x 10^{14} m^{-2} vs. 1.4 x 10^{14} m^{-2} in the SR condition; and 13 x 10^{13} m^{-2} vs. 6.5 x 10^{13} m^{-2} in the homogenized condition.

Table V-5: Fitting parameters of Steel 1 loaded vertically for all microstructural conditions. Parameters that have been fitted on the actual condition are written in red and those that have been fitted on another condition are written in black.

Steel 1 vertical direction	ρ_{ini} (10^{13} m^{-2})	k_1	k_2	e (nm)
Recrystallized	0.9	0.026	1.88	245
Homogenized	13	0.026	1.88	245
Stress relieved	35	0.026	1.88	245
As-built	48	0.026	1.88	245

In summary, the model provides an excellent description of the SR, homogenized, and recrystallized conditions but is less accurate when applied to the as-built conditions. At this stage, it can be concluded that the parameters derived from recrystallized conditions can successfully characterize the tensile response of a 316L material manufactured by LPBF.

V.5 Discussion

Now that the model has been found to provide a good description of different microstructures loaded in different directions, one can discuss about the effect of the different microstructural features with the help of the model developed and applied.

V.5.1 Effect of grain size

We aimed to evaluate the effect of grain size on the true stress-strain response of Steel 2 in the SR condition focusing on the vertical orientation. In this condition, there is a high initial dislocation density, organized into cells. One can wonder if the grain size would have an effect in this condition. To try to address this, we simulate a curve with a grain size of 6 µm (measured grain size) and 100 µm (a fictive and very large grain size). The comparison between the model and the experiment is shown in Figure V-19 (a). One can see that the curve starts with a yield stress too low. However, it was expected that setting a larger grain size would give a yield stress too low because the initial dislocation density is adjusted to give the yield stress corresponding to the measured grain size (this was the only adjusted parameter). To address the question about grain size, a second simulation has been done with a grain size of 100 µm, but by adjusting the initial dislocation density to approach the experimental yield stress. The comparison between the model and the experiment is now shown in Figure V-19 (b). With the grain size set to 100 µm, it describes less well the experimental tensile response.

These results suggest that the grain size does have an impact on the work hardening of additively manufactured 316L. This effect was not obvious. Indeed, the as-built microstructure has a high initial dislocation density (~10^{14} m^{-2}) organized in cells. The mean free path of dislocations could have been driven by the cell size, making the effect of grain boundaries negligible in comparison with the cell size. However, the present results suggest that grain boundaries do have an effect on the plastic response of the material.

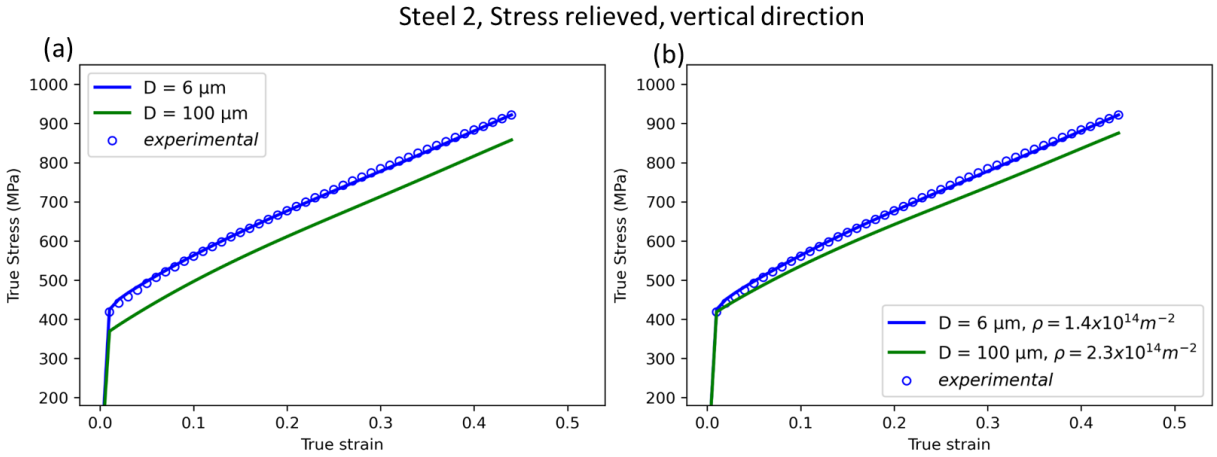

Figure V-19: Evaluation of the effect of grain size in the SR conditions. (a) True stress strain curves for two different grain sizes, 6 and 100 µm respectively. (b) True stress strain curves for two different grain sizes but with the dislocation density adjusted to obtain the experimentally measured yield stress.

V.5.2 Effect of twinning

With the model and the measured twin fraction, one can attempt to estimate the contribution of twinning to the overall plastic deformation. The increment in shear strain with twinning is written in equation (V-12). In this equation, $(1-F)d\gamma_g$ is the contribution of dislocation slip for an increment of shear strain, while $\gamma_t dF$ is the contribution of twinning for an increment of shear strain. By multiplying by the Taylor factor, one can write:

$$d\epsilon = d\epsilon_g + d\epsilon_t\,. \tag{V-18}$$

By integrating: $\epsilon = \epsilon_g + \epsilon_t$, where $\epsilon_t = \frac{F}{M\sqrt{2}}$. The contribution of twinning to the overall tensile deformation can be written $f_{\epsilon t} = \frac{\epsilon_t}{\epsilon}$, while the contribution of twinning for an increment of tensile deformation can be written $df_{\epsilon t} = \frac{dF}{d\epsilon} * \frac{1}{M\sqrt{2}}$. Figure V-20 (a) shows the contribution of twinning and dislocation glide to the overall plastic deformation. At large plastic strains, twinning contributes to less than 10% to the overall plastic deformation. Figure V-20 (b) shows the contribution of twinning for an increment of tensile deformation. The maximum twinning activity is around 35% strain and contributes to a maximum of 20% of the instantaneous plastic strain. This indicates that regardless of the level of plastic deformation, dislocation slip is the main deformation mode, and twinning brings a limited contribution to the plastic deformation.

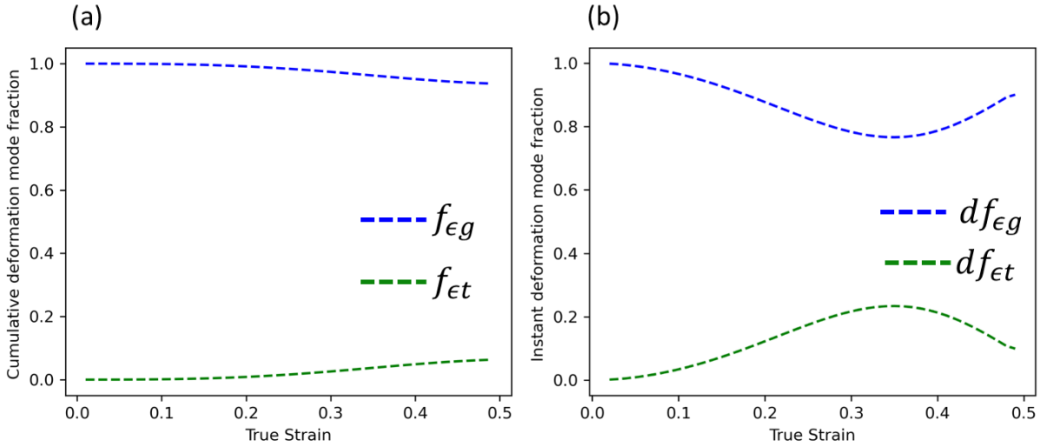

Figure V-20: Contribution of twinning and dislocation slip to the overall plastic deformation, for Steel 2 in the vertical directions. (a) Cumulative contributions. (b) Instantaneous contributions.

The effect of twinning on the true stress-strain curve is evaluated in Steel 2 in the SR and recrystallized conditions for the vertical orientation. To do so, the tensile response is simulated but without accounting for twinning in the model. The resulting true stress-strain curves are shown in Figure V-21 (a), and the corresponding Kocks-Meckings plots in Figure V-21 (b). One can see that until 0.2 plastic strain, twinning plays a minor role and becomes important from 0.2 plastic deformation. On the Kocks-Mecking plots, one can see that the model without twinning does not predict the higher work-hardening rate of the recrystallized condition for plastic deformation exceeding 0.2.

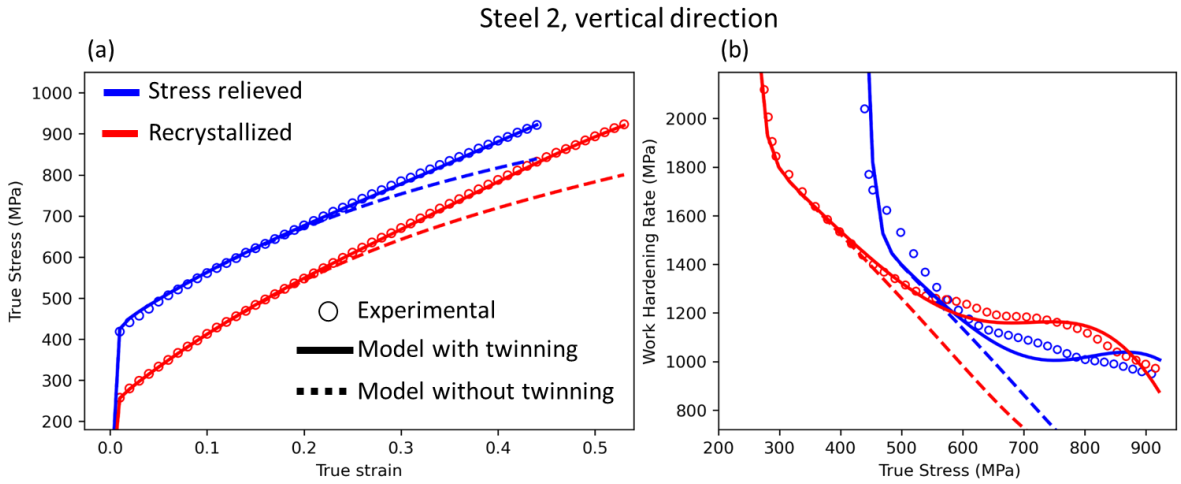

Figure V-21: Contribution of twinning to the tensile behavior. (a) True stress-strain curve simulated with and without accounting for twinning. (b) Resulting Kocks-Mecking plots.

V.5.3 Effect of the dislocation (density and arrangement), and oxides

It has been shown that it was possible to provide a satisfactory description of the tensile behavior of the different microstructures, only by adjusting the dislocation density and modifying the grain size based on the one measured experimentally. The other parameters are calibrated based on the recrystallized conditions. The discrepancy between the model and the experiments regardless of the microstructure considered is rather limited. Moreover, parameters adjusted on a recrystallized sample can be used to describe the tensile behavior of another steel composition and microstructure, considering that the texture is closed.

In the recrystallized conditions, oxides are unlikely to impact the tensile behavior. In the other microstructural states, oxides may impact the tensile behavior. These oxides are not taken into account in the model. However, the model still fits well the experiments. This suggests that these oxides have a minor impact on the plasticity of the material.

Similarly, no dislocation cell is present in the recrystallized condition. Even after plastic deformation, the dislocations do not arrange themselves in the same way as in the SR condition, they are much less distinct, see Figure IV-20. These differences in the arrangement of the dislocation network are not taken into account in the model, but it still provides a good description of the SR condition. This is obtained by only changing the dislocation density between the SR and the recrystallized condition. This result is also true for Steel 1. This suggests that the organization of dislocations into cells has only a limited impact on the tensile response. The microstructural characteristic that controls the tensile response seems to be the initial dislocation density.

V.5.4 Effect of the back stress (kinematic hardening)

The model gives the evolution of the back stress with the deformation. It is predicted that the back stress contributes to around 15% of the total strain hardening. The back stress for Steel 2 in the recrystallized and stress relieved condition is plotted in Figure V-22 (a) as a function plastic strain. The

back stress starts with a plateau at a value depending on the grain size, and then increases drastically due to twinning. The back stress in the SR condition is higher than in the recrystallized condition because of the lower grain size.

To evaluate if the model provides a good estimate of the back stress, uniaxial tension-compression Bauschinger tests should be performed. However, no Bauschinger test was performed in the present work. As a result, we relied on the results of Bauschinger tests from the literature. We found a Bauschinger test conducted on a rolled and recrystallized 316L at room temperature [46] which gives a back stress at 20 MPa at 6% plastic strain, see Figure V-22 (b). This is close to the value obtained in the recrystallized condition of Steel 2 here (~22 MPa). This suggests that the value of back stress estimated from the model is consistent with the literature, at least in the recrystallized condition.

However, it cannot be excluded that the modeled back stress would be in bad agreement with experimental for the SR condition. Indeed, the initial dislocation arrangement could affect the cyclic behavior. It was shown in Copper [41], [172], and in Aluminum [173] that their organization of dislocation in cells during the deformation increased their Bauschinger effect. The dislocation arrangement of the SR could have a similar impact.

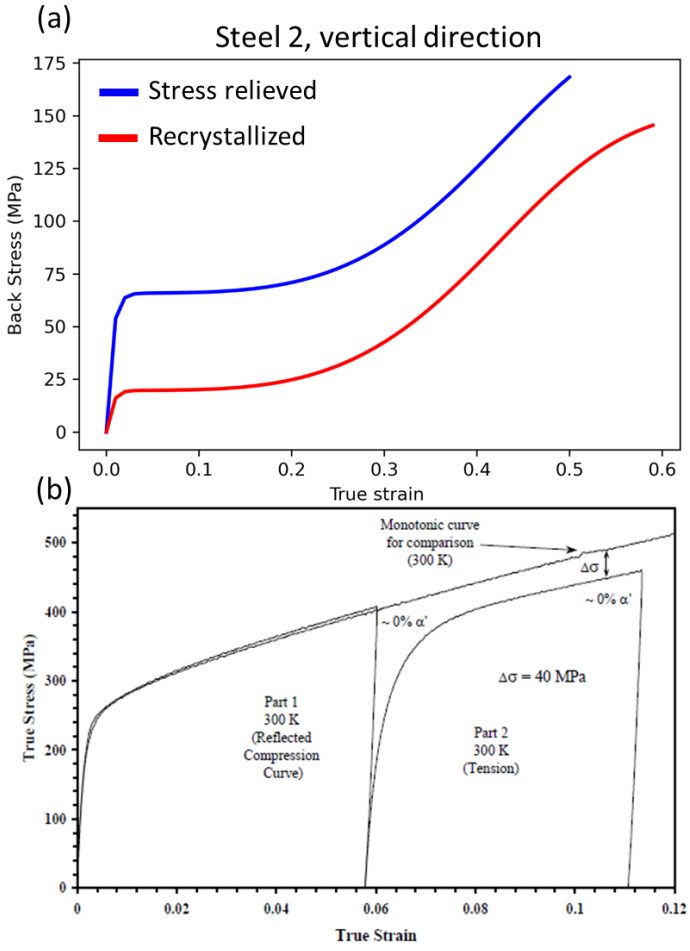

Figure V-22: (a) Estimation of the back stress from the model. (b) Bauschinger test conducted on a rolled and recrystallized 316L from [46].

V.6 Conclusion

A Kocks-Mecking model based on the formulation proposed by Bouaziz in [165] implementing considerations for grain size and twinning effects was employed to analyze the mechanical response of the 316L alloy inherited from LPBF and subjected to different heat treatments. Experimental results regarding the evolution of the twin fraction during plastic deformation are used as inputs to the model. The other parameters are calibrated based on the mechanical response of the recrystallized microstructure. This condition closely approximates the microstructural state in which the model was initially validated, albeit maintaining the same composition and texture as the LPBF material being studied.

While one could expect that the parameters determined from the recrystallized state could not be applicable to LPBF microstructures, it applies relatively well. In the model, only the grain size and the initial dislocation density are different between a recrystallized condition and a LPBF non-recrystallized material. Remarkably, parameters derived from a recrystallized condition can even be extended to describe LPBF non-recrystallized materials with different compositions, provided that their textures are similar.

From these findings, it was possible to evaluate the various microstructural factors influencing the tensile response:

- Dislocation density. The dislocation density is much higher in as-built and stress relieved conditions in comparison with recrystallized samples. This high initial dislocation density increases the yield stress of the material, but decreases its strain hardening.

- Grain size. Grain size contribute to the yield stress in the same way than in wrought material. A smaller grain size increases the work hardening during the early stages of plastic deformation.

- Other microstructural parameters do not appear to significantly affect the strain hardening. These microstructural parameters are microsegregation, the arrangement of dislocations in cells, and the presence of oxides. This conclusion is based on the result that those aspects are not accounted for in the model but it is still able to give a relatively good description of the experimental results. It was already shown in the literature that the arrangement of dislocation does not significantly affect the hardening [37], here we draw the same conclusion for the strain hardening of the 316L. What matters the most is the dislocation density, not really the organization of the dislocation network into cells.

Chapter VI. Microstructure and mechanical properties of 316L processed by WAAM

VI.1 Introduction

This chapter presents a study of the 316L fabricated by wire and arc additive manufacturing (WAAM). It is somewhat separated from the previous chapters since it investigates a different process, however, comparisons with the materials inherited from LPBF will be made. The depth of the analyses reported in this chapter is not at the same level in comparison with what was done for the material processed by LPBF. This is due to the time constraint of the Ph.D.; the materials were fabricated during the second year of the thesis.

The main objective is to characterize the microstructure obtained after fabrication and its evolution with heat treatments. Mechanical properties are also investigated, but only after the stress relief heat treatment. The chapter starts with a literature review of austenitic stainless steels processed by WAAM, then the processing conditions and experimental procedures are described. The next section is dedicated to the characterization of the as-built microstructure and its evolution upon heat treatments. Three different heat treatments were investigated: a stress relief heat treatment, a ferrite regression heat treatment, and a recrystallization heat treatment. The mechanical properties in different tensile directions and after the stress relief heat treatment are summarized. Finally, the results are briefly discussed.

VI.2 Literature review

VI.2.1 The WAAM process

Wire arc additive manufacturing (WAAM) is an additive manufacturing (AM) process that enables the construction of large components [4]. This process is inherited from welding and can potentially be performed using any welding equipment. While there are numerous WAAM techniques available, the MAG type (metal active gas) - as shown in Figure VI-1(a) - is the most commonly employed. This method uses an electric arc to melt a wire to fabricate three-dimensional objects layer-by-layer. The process involves the use of a welding power source, a wire feeder, and a welding torch or manipulator [2]. The molten metal from the wire is then deposited onto the workpiece surface, thus progressively building the part. This molten bead then solidifies and forms a new layer, which is subsequently covered with subsequent layers. To control the temperature of the previously deposited layer, a dwell time can be defined between the deposit of successive layers. Up to date, there are fewer scanning strategies available in comparison with LPBF. The most widely adopted scanning strategy is uniaxial, where the weld beads are laid one on top of the other in the same direction, possibly with the direction reversed.

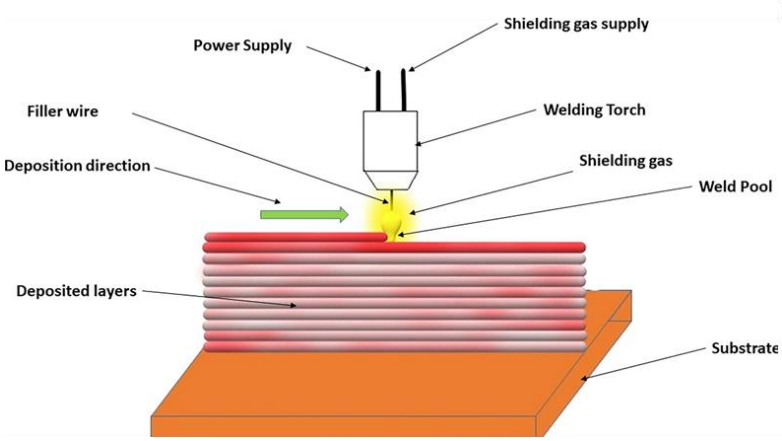

Figure VI-1: Schematic drawing showing layers deposition in WAAM, from [2].

Table VI-1 compares the primary characteristics of the LPBF and WAAM process. Laser Powder Bed Fusion (LPBF) and Wire Arc Additive Manufacturing (WAAM) are complementary to one another. LPBF is primarily utilized for producing relatively small and complex parts with high precision. By contrast, WAAM is well-suited for the fabrication of large components with simple geometries, and requires machining after fabrication. The WAAM process is characterized by much higher deposition rates than LPBF.

Table VI-1: Main characteristics of the LPBF and WAAM processes.

Process	Feed material	Deposition rate ($cm^3.h^{-1}$)	Melt pool depth (µm)	Minimum roughness (Ra µm)
LPBF	Powder (15-45 µm)	10-40 [1]	50-200	10 [1]
WAAM	Wire (diameter ~ 1mm)	200 [15]	4000 [15]	1000 [1]

VI.2.2 Microstructure of the 316L steel made by WAAM

VI.2.2.1 Melt pool and grain structure

In comparison with LPBF, the state-of-the-art on WAAM of 316L is much more limited. However, a few recent works focused on the microstructure and properties obtained by WAAM can be found. For example, Palmeira Belotti et al. [174] have investigated the melt pool shapes and dimensions of the 316L steel inherited from WAAM, see Figure VI-2. This microstructure is obtained with a uniaxial scanning strategy. Melt pools are about 5 mm in width and 2 mm in height. Their center exhibits a concave shape, while their sides exhibit a more convex shape. As a result, the microstructure of parts obtained by WAAM can be divided into two regions. The first region is the melt pool side where grains grow along the building direction, and is called the overlapped region (OR) [174]. The second region is the melt pool center, where grains grow toward the center of the melt pool. This region is called center of fusion zone (CFZ). Figure VI-1 (b) shows an IPF map of a microstructure obtained by WAAM. From the IPF-EBSD map, Palmeira Belotti et al. found that the OR has a fiber texture <100>//BD, while no clear texture is found in the CFZ.

Compared to LPBF, the shape of the melt pool is different. In LPBF, the convex part of the melt pool is very limited. The depth of the melt pool is around 20 times larger in WAAM compared to LPBF, from 100 µm in LPBF to 2 mm in WAAM. The average grain size (between BD and TD) in WAAM is larger in the OR than in the CFZ, but is still much larger than in LPBF (~100 µm vs. 20 µm).

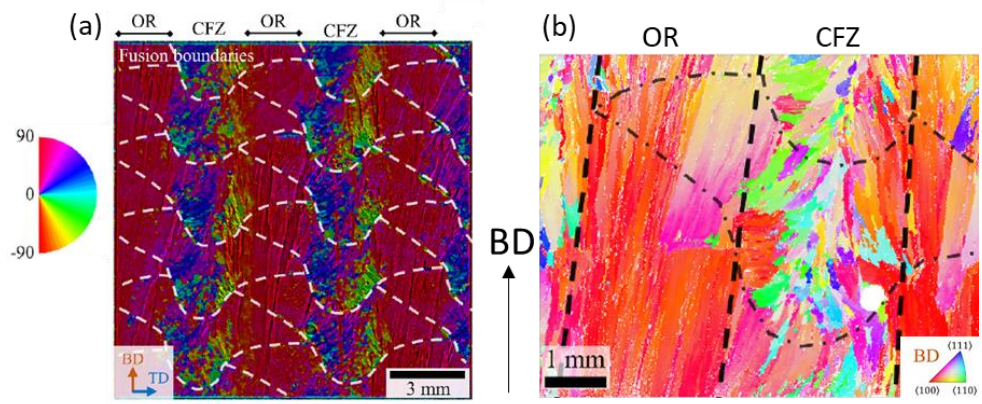

Figure VI-2: (a) Map of the local angular information in the TD-BD plane emphasizing the dependency of the grain growth direction on the curvature of the fusion boundary. The colors represent the local grain growth direction relative to the TD in degrees. Adapted from [175] (b) Map of the austenite crystal orientations normal to the BD, represented by different colors. The approximated fusion zone contour and corresponding OR and CFZ are marked in black. Adapted from [175].

VI.2.2.2 Phases in presence

At a finer scale, the austenite grains are found to contain ferrite, see Figure VI-3 (a). This is attributed to a solidification mode F/A, which is desired in WAAM process to avoid hot cracking (better solubility of S and P in ferrite than in austenite [19]). The ferrite is found to exhibit two different morphologies: vermicular or lathy [174], see Figure VI-3 (a). Vermicular ferrite, also called skeletal ferrite, is characterized by a continuous network of ferrite that is found to be located at the former core of primary dendrite and secondary arms. Lathy ferrite is characterized by interlaced ferrite networks located in primary ferrite dendrites and surrounded by austenite. These two morphologies result from the F/A solidification mode and can exist in the same region [174]. The ferrite morphology is known to depend on the growth direction of ferrite during solidification relative to the direction of the thermal gradient [176]. The residual ferrite fraction is known to depend on the composition [19] and is around 5-10% [174], [177].

In the work of Chen et al. [11], the σ phase was also identified in the as-built microstructure. However, the presence of σ phase does not seem to be systematic [174], [177], [178].

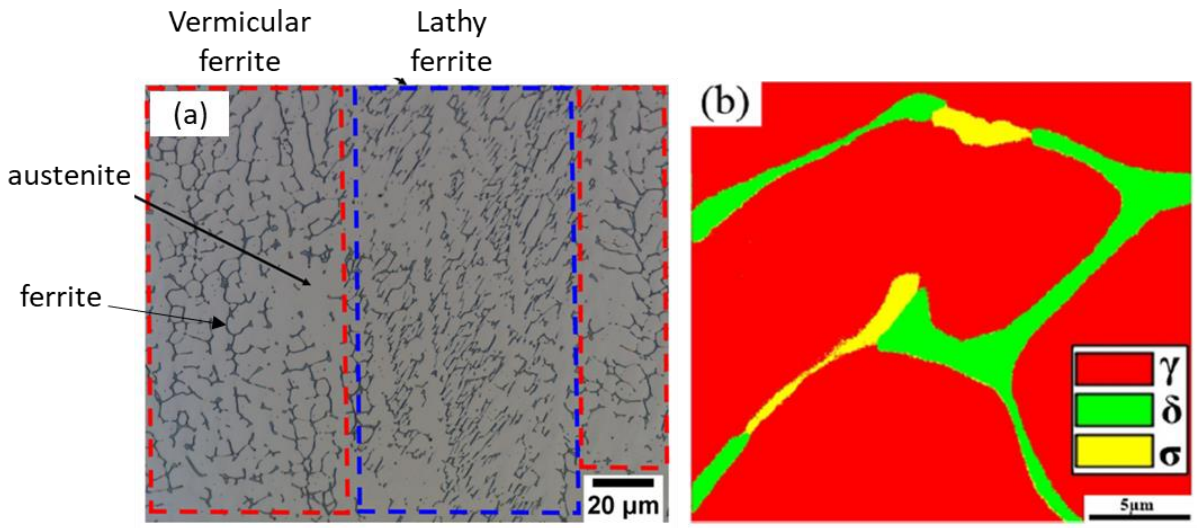

Figure VI-3: Optical image after electro-etching in an aqueous NaOH solution. From [174]. EBSD phase map of a 316L WAAM. From [11].

VI.2.2.3 Particles

Particles are often found in the microstructure inherited from WAAM. An example is shown in Figure VI-4. These particles are rather large (>200 nm) and are identified as oxides rich in Mn and Si [174], [177]. It is still unclear if these particles are already present in the feeding wire or on its surface, or if these form during the process by a reaction of the molten metal with the atmosphere. These particles are distributed homogeneously within the microstructure.

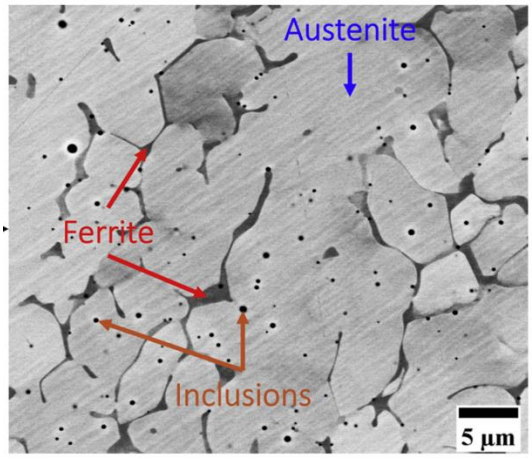

Figure VI-4: SEM image of a 316L fabricated by WAAM. From [174].

VI.2.2.4 Evolution with heat treatments

The evolution of the microstructure during heat treatments has been investigated by Wang et al. [178]. Figure VI-5 (a) shows an IPF-EBSD map of the microstructure, with the OR and CFZ regions highlighted. Figure VI-5 (b)-(d) show the exact same region as in (a) but after different heat treatments. No grain growth or recrystallization is reported after 1000°C for 1h, as shown in Figure VI-5 (b). Recrystallization occurs after 1h at 1100°C, see Figure VI-5 (c). It is found that recrystallization

preferentially starts below the melt pool boundary in the CFZ, see Figure VI-5 (c) and (d). After 1200°C/1h, the material is recrystallized except above the melt pool boundary.

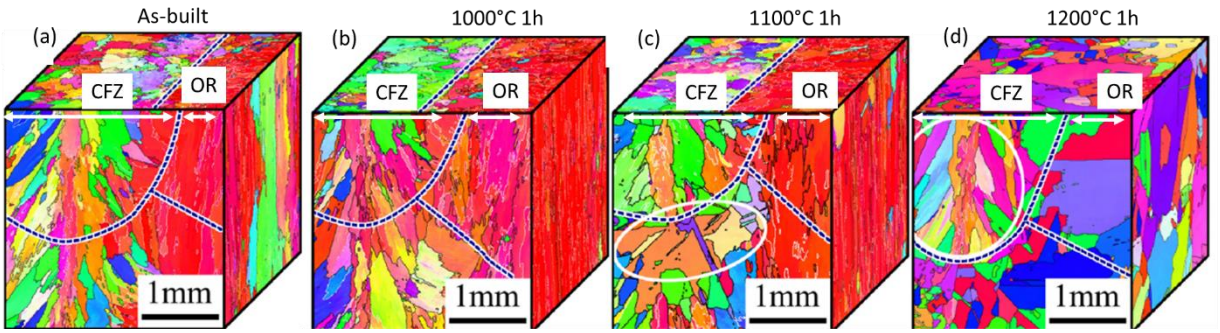

Figure VI-5: IPF-EBSD maps after different heat treatments. (a) As-built, (b) after 1000°C/1h, (c) after 1100°C/1h, and (d) after 1200°C/1h.

The morphology and fraction of the phases are also found to evolve with heat treatments. Figure VI-6 (a), taken from the as-built state, shows vermicular ferrite. After 1h at 650°C, the ferrite morphology has not changed. After 1h at 1100°C, the fraction of ferrite decreases, and the residual ferrite becomes globular, see Figure VI-6 (d).

Figure VI-6 (b) also shows that white particles appear in the ferrite after 1h at 650°C. The authors reported that those white particles are associated with the σ phase. After 1000°C for 1h, all the ferrite is transformed into σ, which was identified by EBSD. This is consistent with the fact that the σ phase usually forms by the decomposition of ferrite at temperatures between 700 and 1000°C [19]. After 1100°C/1h, no sigma phase is found, but small ferrite islands are still there.

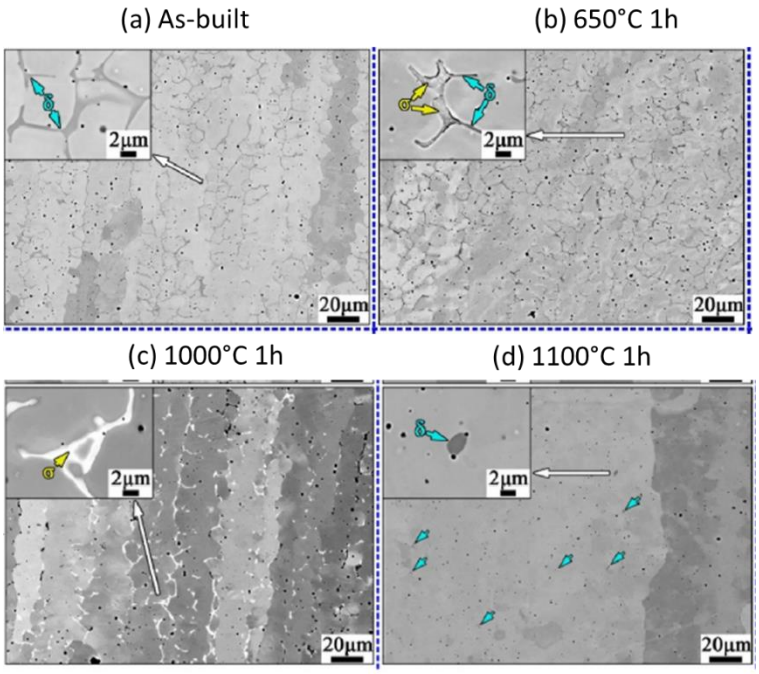

Figure VI-6: SEM-BSE images of the 316L fabricated by WAAM after different heat treatments. (a) As-built, (b) after 650°C/1h, (c) after 1000°C/1h, and (d) after 1100°C/1h. From [178]

VI.2.3 Tensile properties

Two articles reported the tensile properties of the 316L steel inherited from WAAM [175], [177]. The tensile properties in the two studies are similar. A comparison between the typical stress-strain curve of a WAAM 316L and a wrought 316L is shown in Figure VI-7 (a). According to Wang et al. [177], the 316L elaborated by WAAM is stronger but less ductile than its wrought counterpart. However, as shown by Belotti et al. [174], tensile properties are in fact strongly dependent on the loading direction, see Figure VI-7 (b). The yield stress is higher in the transverse direction than in the diagonal direction, but the elongation to fracture is much lower in the transverse direction.

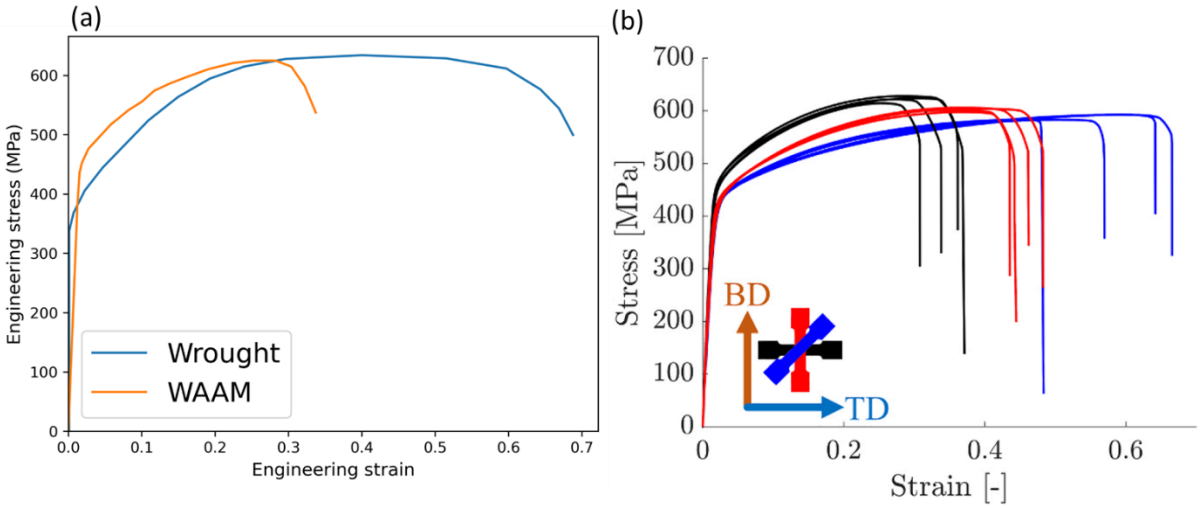

Figure VI-7: Engineering stress-strain curves. (a) Comparison between a wrought recrystallized 316L [12] and a 316L elaborated by WAAM [175]. (b) Effect of the loading direction on the tensile properties of the 316L steel fabricated by WAAM. From [175].

The number of studies dedicated to the characterization of the microstructure of the 316L steel inherited from WAAM is limited. Therefore, the first objective was to compare our results with the ones found in the literature. Moreover, one characteristic feature of parts obtained by WAAM is that they contain ferrite. By contrast, wrought products contain less than 1% of ferrite. Thus, in order for the 316L processed by WAAM to have similar properties as its wrought counterpart, ferrite must be dissolved. Heat treatments to dissolve ferrite in WAAM parts have been poorly investigated in the literature.

VI.3 Materials and methods

VI.3.1 Sample fabrication

Samples were fabricated by EDF at their Lab in Chatou and received 16 months after the starting of this Ph.D. work. The feeding wire was made of 316L Si with a diameter of 1 mm. The substrate was a 316L stainless steel plate with the following dimensions: 160 × 150 × 20 mm^3. The machine was a CMT Fronius TPSi500 and the cold metal transfer (CMT) mode was adopted. The deposition parameters are summarized as follows: arc current 150 A, arc voltage 14.5 V, wire feeding rate 9 m/min, scanning speed 4.6 mm/s, and hatching distance 6 mm. The angle between the wire and the normal to the

substrate plane was set to 0°. Ar-2% CO_2 was used as shielding gas at a flow rate of 18 L/min. The scanning strategy is an inverted raster, schematically represented in Figure VI-8 (a). Each layer consisted of 16 straight and parallel weld beads deposited with the same scanning/printing direction, and stacked along the transverse direction (TD). A similar stacking of weld beads is used for consecutive layers, but the scanning direction is rotated by 180°. In total, 32 layers are stacked on top of each other along the building direction (BD). This results in a block (L x l x H= 14 x 9 x 14 cm^3) shown in Figure VI-8 (b). In order to prevent the formation of the σ phase in the resulting microstructure, the inter-pass temperature (measured with a pyrometer) was set at 150°C.

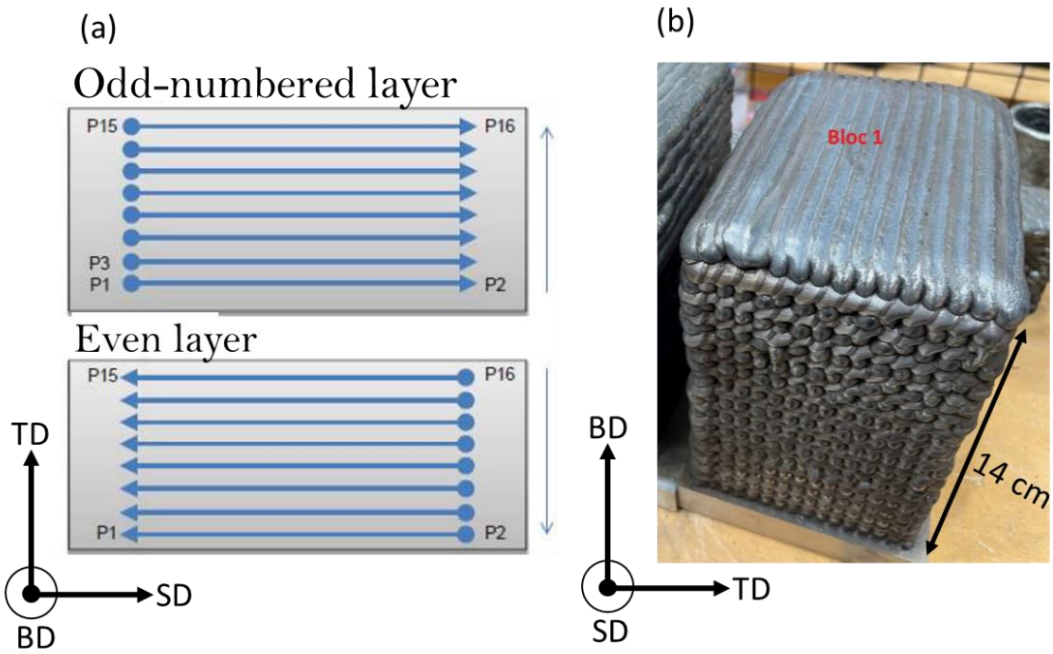

Figure VI-8: (a) Schematic of the scanning strategy. (b) Picture of the fabricated block.

The nominal composition of the wire and the fabricated samples was measured by inductively coupled plasma atomic emission spectroscopy (ICP-AES) for major elements and by combustion analysis for trace elements (O, N, C…). Compositions are given in Table VI-2. These compositions are compared to the standard composition for the wrought 316L alloy. The composition of the wire is within the bounds of the RCC-M standard. However, after fabrication, the carbon content (410 ppm) is slightly higher than the standard (300 ppm). This probably results from contamination of the metal by the protective gas, which contains 2% of CO_2.

Table VI-2: Nominal composition of the wire and fabricated block.

	Weight %					Weight ppm				
Element	Cr	Ni	Mn	Mo	Si	O	N	C	P	S
Wire	18.41	11.13	1.83	2.57	0.78	240	1000	280	190	150
Part	17.91	10.71	1.72	2.48	0.63	500	1000	410	150	60
RCC-M	16-19	10-14	<2	2-2.5	<1	-	-	<300	<300	<150

VI.3.2 Heat treatments

After fabrication, samples extracted from the block were subjected to three different heat treatments. Those heat treatments are described in Figure VI-9. The first heat treatment is a stress relief heat treatment for 1h at 600°C. The role of this heat treatment is to reduce the residual stresses inherited from the fabrication. This treatment was applied to a 10 x 9 x 14 cm^3 block. To ensure that the heat treatment was homogeneous in the block, a temperature ramp for heating and cooling was set at 5°C/min.

The second heat treatment is a ferrite regression treatment. It consists of a stress relief heat treatment, followed by a treatment at 1050°C for 1h. This heat treatment was followed by water quenching. The role of this heat treatment is to decrease the ferrite fraction without inducing recrystallization. This is also a common heat treatment for as-cast 316L showing a similar microstructure (mixture of ferrite and austenite) [179]. This heat treatment was performed on a sample with the following dimensions: 1 x 9 x 9 cm^3. The sample was introduced in the hot furnace.

The third heat treatment is a recrystallization heat treatment. It consists first of a stress relief heat treatment, followed by an annealing at 1200°C for 30 min and a final quench in water. The time and temperature were suggested by Edouard De Sonis in his Ph.D. This heat treatment was performed on a sample of dimensions 1 x 5 x 5 cm^3. The sample was introduced in the hot furnace.

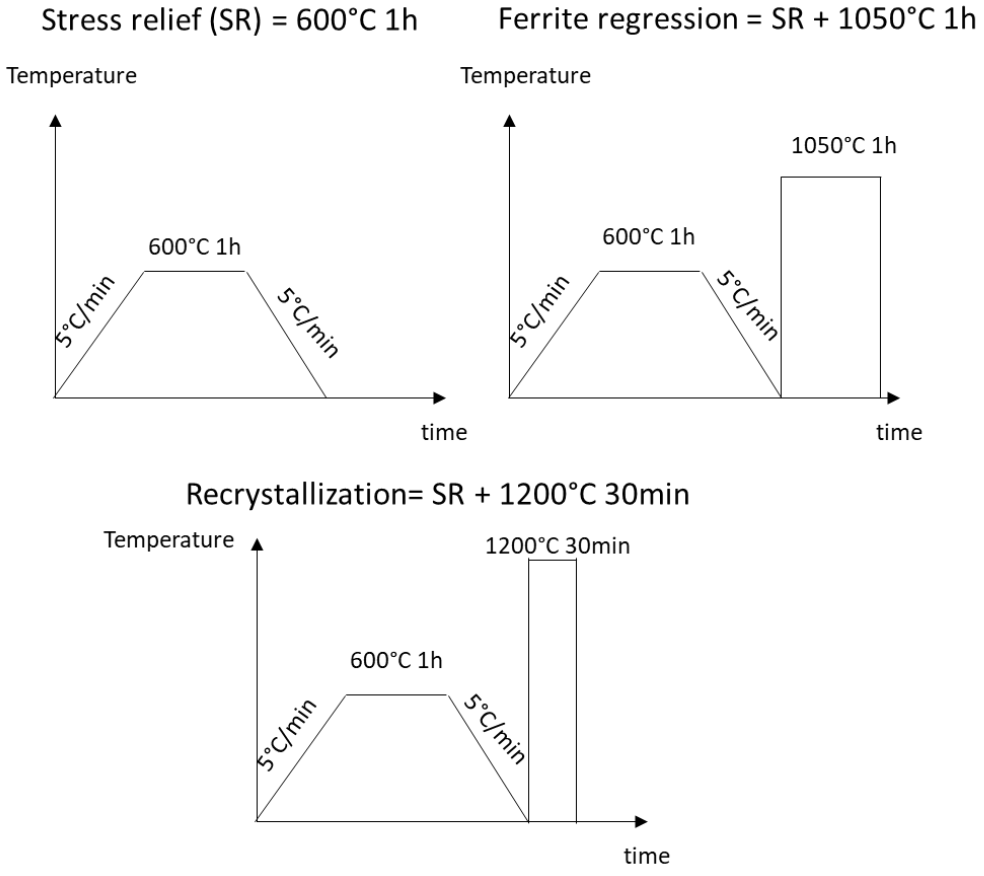

Figure VI-9: Summary of the various heat treatments studied.

VI.3.3 Microstructural characterization

The microstructural characterization which is similar between LPBF and WAAM has been described in Chapter I. This part only describes the characterizations specific to WAAM.

To measure the ferrite fraction, samples were electro-etched in an aqueous NaOH solution (40% of NaOH in distilled water) with a tension of 5V. Then, samples were imaged in an optical microscope. Images were treated using the Image-J software [100]. Colors were split and only the intensity of the green color was kept, which was the color that gives the best contrast. The background was subtracted with a rolling ball, followed by a threshold using the IsoData algorithm.

Because of the scale of the microstructure, large EBSD maps were performed with a CamScan X500-FE CrystalProbe SEM-EBSD equipped with the Oxford NordlysNano EBSD detector at the Geosciences lab in Montpellier by Fabrice Barou. This microscope allows for very large fields of view to be acquired. Operating conditions were an acceleration voltage of 15 kV and a working distance of 24–25 mm, with a step size of 7 µm. EBSD patterns were indexed using the AZtecHKL software of Oxford Instruments.

VI.3.4 Mechanical testing

VI.3.4.1 Hardness

Micro hardness was performed using a Tukon 1102 hardness machine with a load of 1Kg, which gives an indent size around 100 µm. Average hardness was measured by a matrix of 5x4 indents spaced by 700 µm. No difference in hardness is measured between the top and the bottom of the build (respectively 212 ± 7 HV1 and 208 ± 7 HV1). The local hardness of specific regions (below and above the melt pool boundary) is measured by the average of 8 indents in each zone.

VI.3.4.2 Tensile test

Cylindrical tensile test specimens were extracted from the as-built block that was stress relieved before. This condition was chosen because it was the reference condition for the fracture study conducted by Edouard De Sonis. Tensile samples were machined in three different directions, the transverse direction (TD), the scanning direction (SD), and the diagonal direction (Diag). This is illustrated in Figure VI-10 (a). The dimensions of the tensile specimens are given in Figure VI-10 (b), and follow the ASTM standard E8. The diameter of the specimens is chosen as large as possible, since the grain size is known to be very large in WAAM samples. Tensile tests were performed in the same conditions as for LPBF specimens. A more complete description can be found in Chapter II.5.2

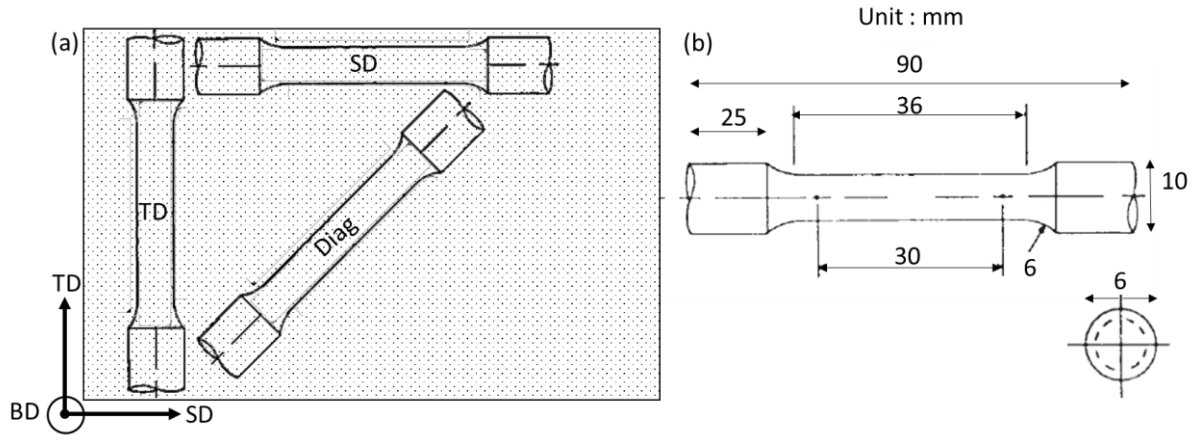

Figure VI-10: (a) Schematic diagram illustrating the position of the different cylindrical tensile. (b) Dimensions of the tensile specimens used for mechanical characterization.

VI.3.5 X-ray tomography

Prior to tensile straining, 3 tensile specimens were inspected using X-ray tomography. An Easytom-XL lab tomograph from RX-solutions® was used (X-ray source Hamamatsu L10711 transmission tube, LaB_6 filament, and a 1 µm thick tungsten target). Scans were acquired at an accelerating voltage of 150 kV with 4500 projections. The detector is a flat panel Varex 2520, with 1920 × 1536 square pixels of 127 µm. The voxel size was 8 µm. In this case, all pores with a diameter larger than 20 µm are detected. The volumes were reconstructed using the X-Act software by filtering the back-projection and applying a beam hardening correction. Fiji® was employed to process the 3D images. Volumes were filtered with a 3D median filter with a radius of 2 voxels. To discriminate the pores from the bulk material, an automatic threshold was applied using the IsoData algorithm.

VI.4 Experimental Results

VI.4.1 As-built microstructure

VI.4.1.1 Defects and grain structure

The density of the sample was measured to be 99.5% by image analysis, yet, large pores can be observed by eye, see Figure VI-11. The largest pore has an equivalent diameter of 250 µm. Many pores are aligned with the building direction. The presence of pores is not systematically reported in the literature [174], [177], [178]. That means that it is possible to achieve a fully dense material with optimized processing parameters.

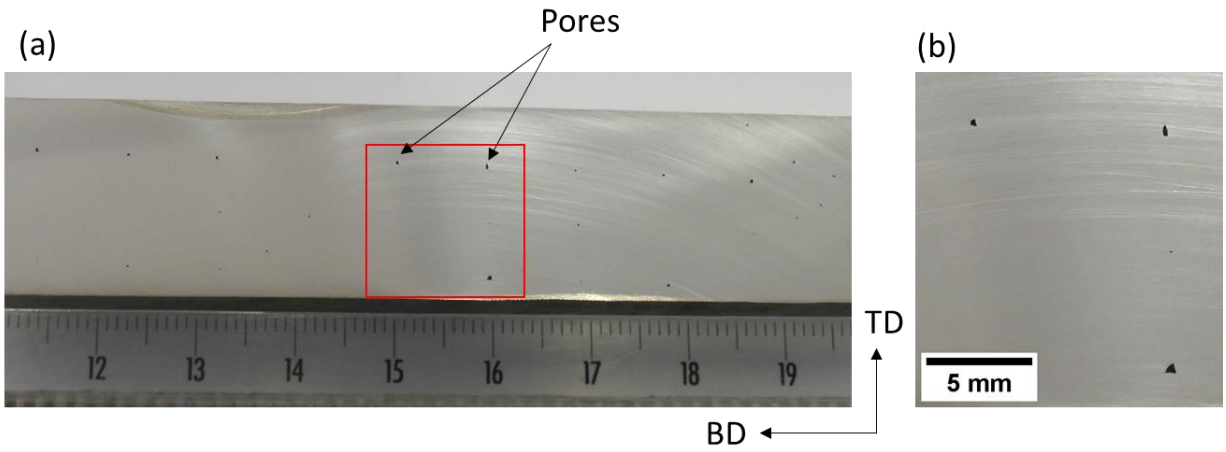

Figure VI-11: (a) Image of the block sample. (b) Magnified view of the red square highlighted in (a).

Figure VI-12 shows an optical image of the sample after etching. The melt pool boundaries (MPB) are drawn in white, while some pores are circled in black. All pores are located at triple junctions of MPB. This explains the alignment of pores observed in Figure VI-11.

The melt pool depth is around 2 mm. This value is close to the observations of Wang et al. and Belotti et al. [174], [177]. However, the melt pools are not totally symmetrical along the building direction. They are slightly oriented toward the right for odd-numbered layers and to the left for even-numbered layers. This is due to the scanning direction that rotates by 180° between each layer. The asymmetry of the melt pool is caused by the local boundary conditions. Indeed, when the wire is deposited, on one side there is an adjacent solidified track, while on the other side there is no adjacent track. This means that the heat is released preferentially on the side where there is an adjacent track. This asymmetry of the melt pool is not reported in the literature, but can be observed [175]. Orange arrows indicate the deposition direction of tracks for these specific layers.

Figure VI-12 (b) shows a large map acquired by EBSD. The microstructure can be seen as a composite, with the presence of two zones already identified in the literature [174], [177], overlapped region (OR) and center of fusion zone (CFZ). The OR is characterized by large columnar grains with a strong <100>//BD texture (red in the IPF map), propagating over several millimeters. The CFZ is characterized by smaller columnar grains that grow toward the center of the melt pool. The grain size is measured to

be 130 µm by the average intercept method between TD, SD and BD. Grains are finer in the CFZ, with an intercept length of 70 µm. These grains are preferentially oriented such that their <110>//BD (grains displayed in green with the IPF color code), although other orientations may exist.

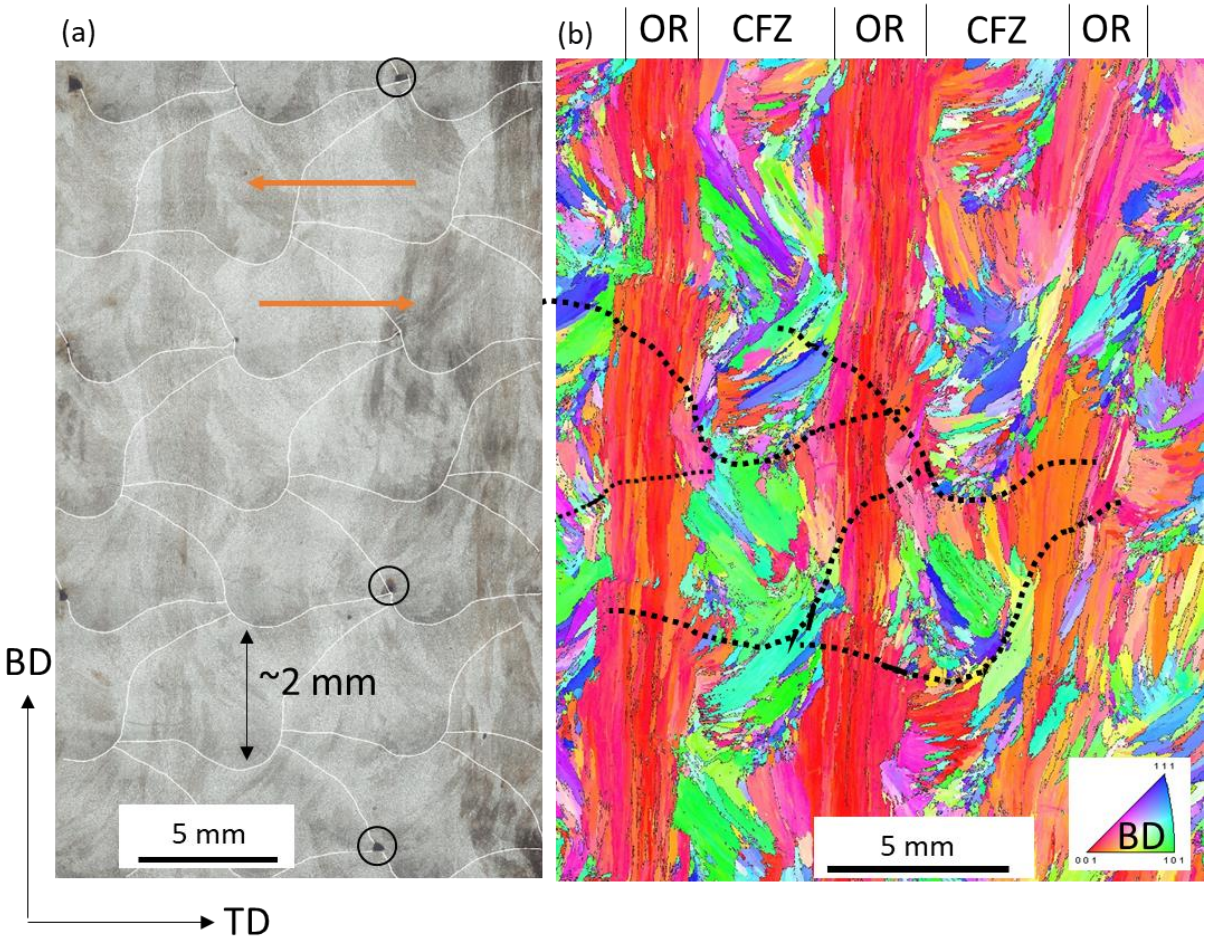

Figure VI-12: (a) Optical image of the sample after etching using the V2a solution. Melt pool boundaries are drawn in white. Some pores are circled in black. Orange arrows indicate the deposition direction of this specific layer. (b) Large scale IPF-EBSD map collected using a step size of 7 µm.

The (100) and (110) pole figures extracted from Figure VI-12 (b) are shown in Figure VI-13. The texture is composed of two main orientations: an orientation having (<100>//BD and <100>//SD), highlighted using red circles in the pole figures; and an orientation having (<110>//BD and <100>//SD), highlighted using green circles in the pole figures. These two main orientations are directly related to the two different zones. The (100) and (110) pole figures of the two different zones are respectively shown in Figure VI-13 (b) and (c). The OR shows as a main orientation (<100>//BD and <100>//SD), while the CFZ shows as a main orientation (<110>//BD and <100>//SD).

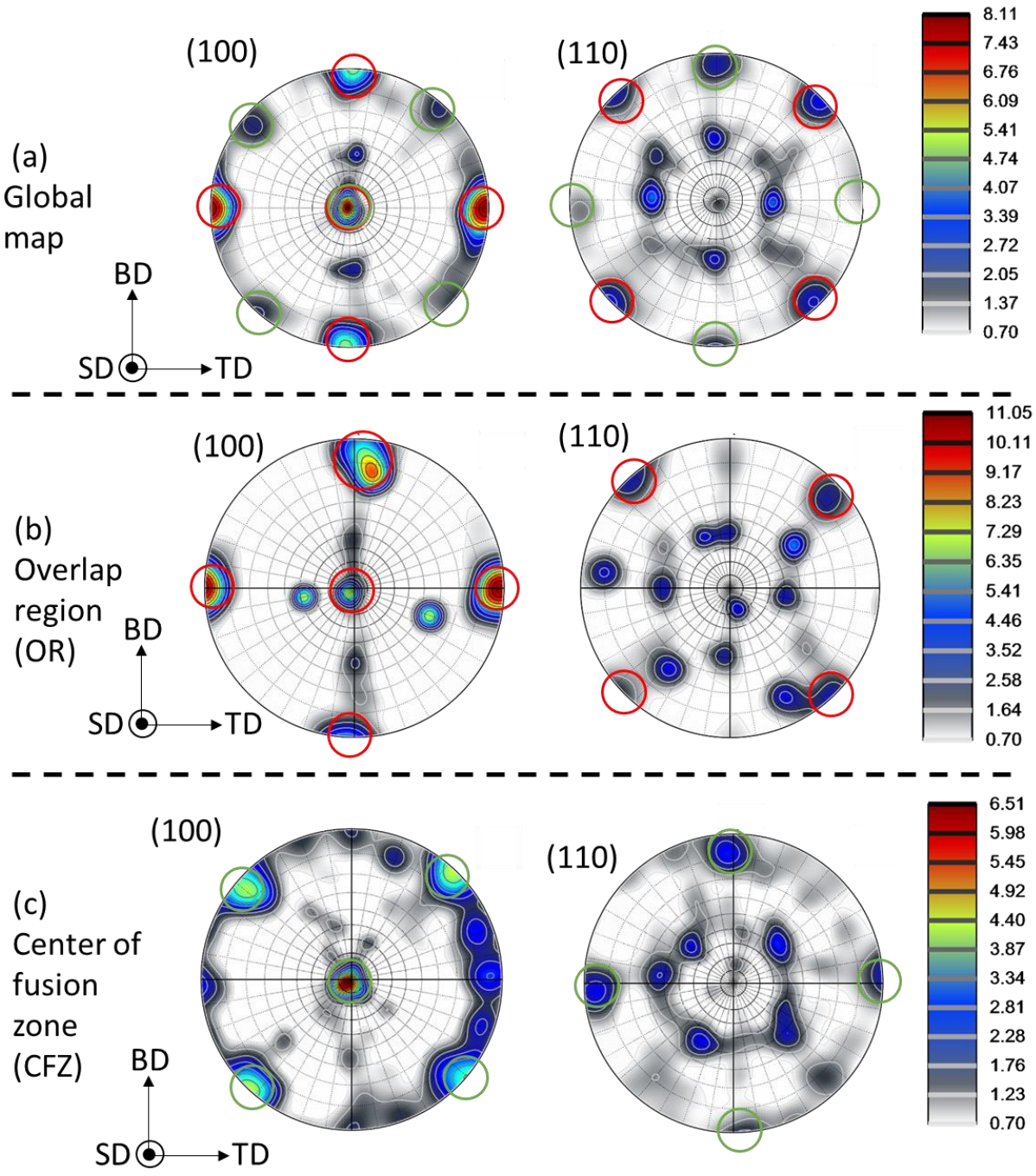

Figure VI-13: (100) and (110) pole figures, calculated from Figure VI-12 (b). (a) For the overall map, (b) for the overlapped region (OR), and (c) for the Center of fusion zone (CFZ). Red circles represent the orientation 1 found in the OR and green circles the orientation 2 found in the CFZ.

VI.4.1.2 Identification and characterization of the different phases

Figure VI-14 (a) shows an EBSD phase map of the sample taken at higher magnification. Small islands of ferrite are found in the austenite. No σ phase is detected. Figure VI-14 (b) shows a BSE image at a similar magnification. No thin white precipitates are found in the ferrite confirming the absence of σ phase in the as-built sample. The small dark particles are associated with oxides as reported in the literature [11], [174], [177].

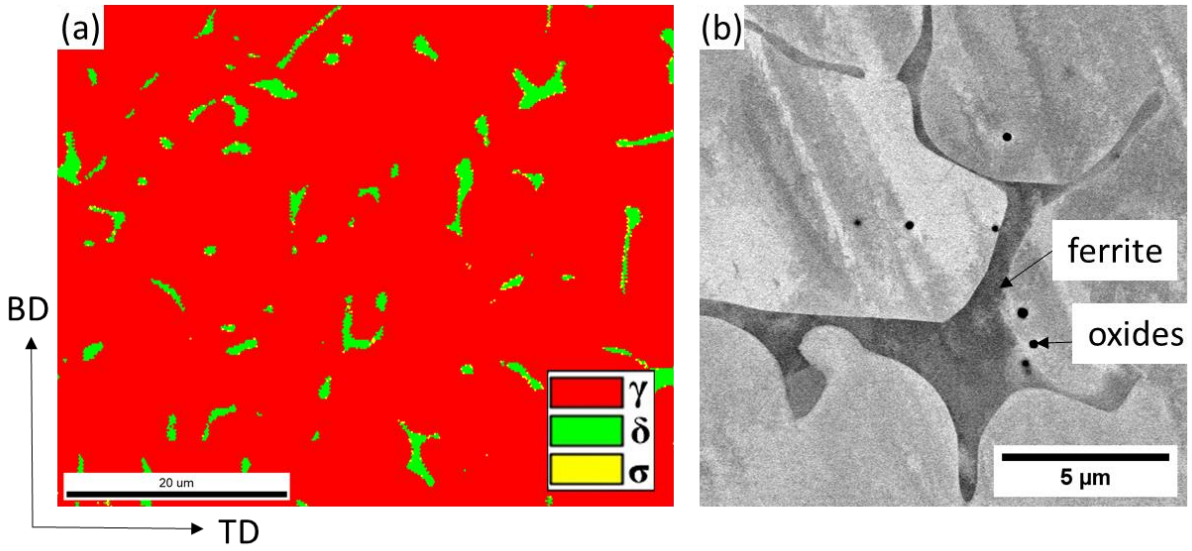

Figure VI-14: (a) EBSD phase map (step size = 200 nm). (b) SEM-BSE image.

The ferrite morphology and area fraction were characterized at two different locations: below and above the concave melt pool boundary (MPB). These two different locations are shown in Figure VI-15 (a). The image taken above the MPB for ferrite quantification is shown in Figure VI-15 (b) and the one taken below the MPB is shown in Figure VI-15 (e). Above the MPB, the ferrite morphology is a mixture of lathy and vermicular ferrite, see Figure VI-15 (c) and (d). Below the MPB, the ferrite is mostly vermicular. These ferrite morphologies are typical of a F/A solidification [19]. The measured ferrite area fraction is identical between the two locations: 8 ± 1%.

The primary ferrite dendrite arm spacing is measured to be about 8 µm (green arrow in Figure VI-15 (d) and (f)). From the empirical formula given in [29], this corresponds to a cooling rate of 10^3 °C/s. This is 1000 times less than the cooling rates encountered in LPBF. No difference in hardness is found between the area above and below the MPB (respectively 210 ± 7 HV1 and 214 ± 7 HV1).

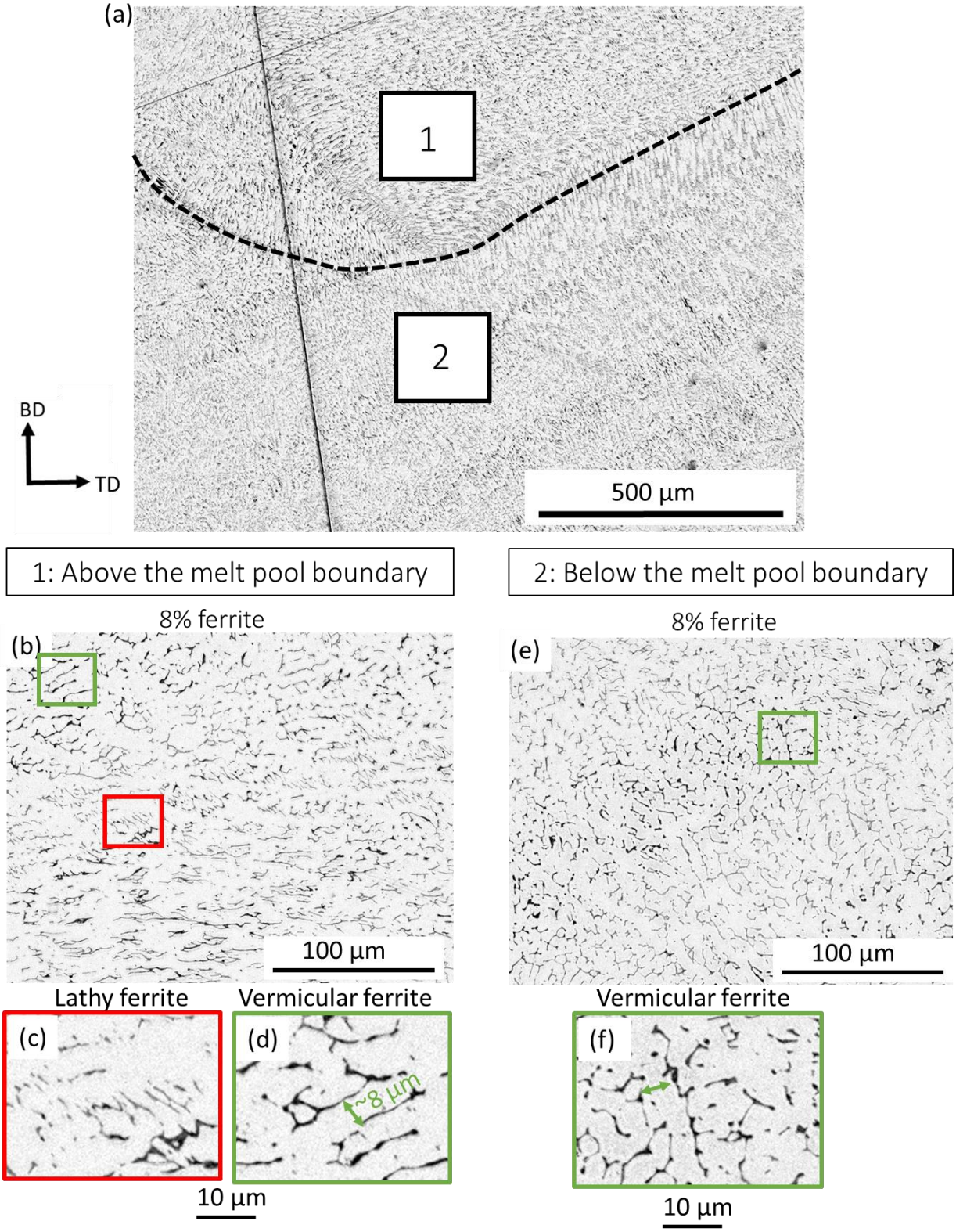

Figure VI-15: Optical image after electro-etching in a NaOH aqueous solution. (a) Pictures of the melt pool. (b) Magnification of area noted 1 from (a). (c)-(d) Magnification of respectively red and green squares shown in (b). (e) Magnification of area noted 2 in (a). (f) Magnification of green square shown in (e).

VI.4.1.3 Particles

Figure VI-16 (a) shows an optical image after polishing. Particles can be observed in the microstructure, see the black dots randomly distributed in the sample. The area fraction of these particles is estimated to be about 0.27%. Figure VI-16 (b) shows an enlarged view of such particles (SEM-BSE image). Particles appear in black and their size is ranging between 200 nm and several micrometers. The composition of the large particle shown in (b) measured by EDS is given in Figure VI-16 (c). The particle is rich in O, Si, Mn, Ca, Mg, Al, and Ti. Compositions of other particles have been measured and similar enrichments were found. It was surprising to see enriched particles in Ca and Mg, because this was not reported in the literature. The Ca content of the global sample is measured at 70 ppm. This contamination might come from the lubricant used during the fabrication of the wire. The composition of Mg was too low to be measured (<30 ppm).

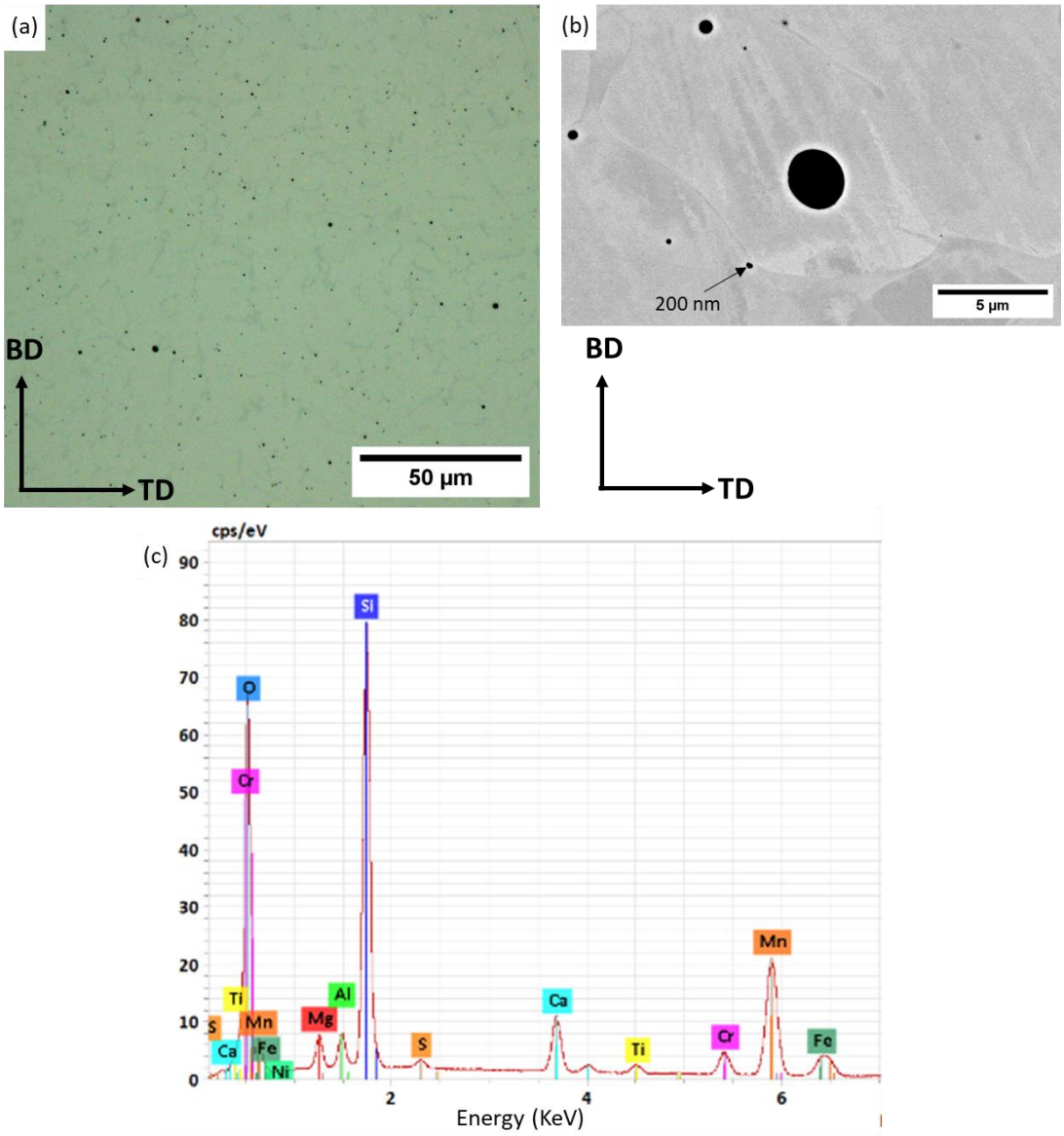

Figure VI-16: (a) Optical image prior to etching revealing the spatial distribution of the oxides. (b) SEM-BSE image prior to etching showing a few oxide particles. (c) EDS spectrum of the large particle shown in (b).

VI.4.2 Evolution of the microstructure with heat treatments

VI.4.2.1 After a stress relief heat treatment (600°C/1h)

After 600°C/1h heat treatment, it is not expected to see any modification of the grain structure. Wang et al. [178] observed modification of grains from 1100°C/1h. Figure VI-17 compares optical micrographs of the as-built and stress relieved states. The stress relief (SR) heat treatment does not seem to induce a change in the fraction and morphology of the ferrite. This confirms the observations of Wang et al. [178].

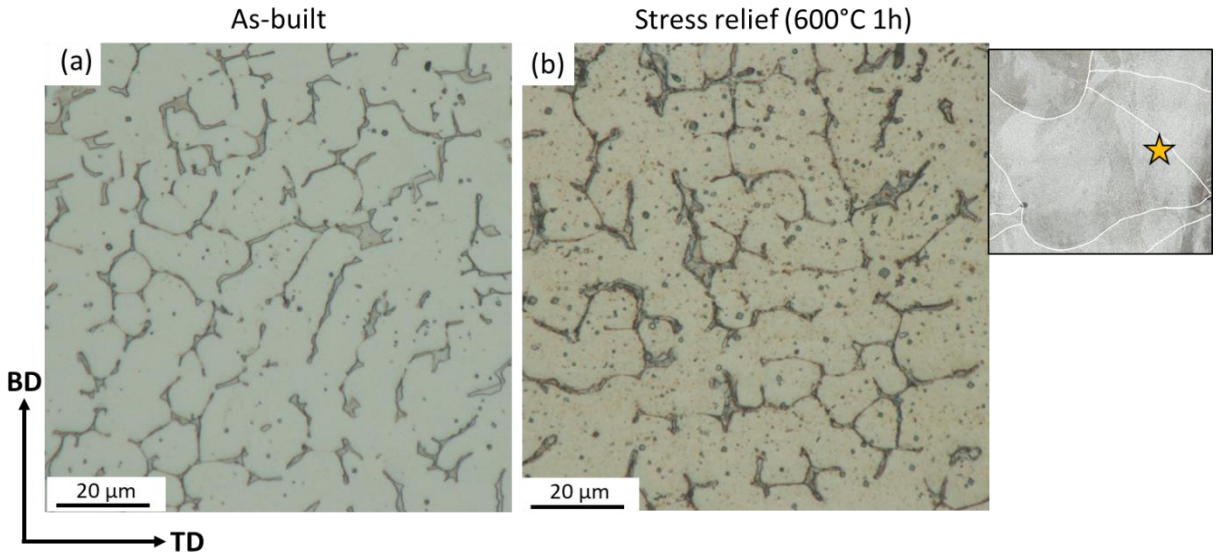

Figure VI-17: Optical images after etching with the V2a solution. (a) As-built condition and (b) after stress relief (600°C/1h).

Figure VI-18 shows a SEM-BSE image after a SR heat treatment. The precipitation of a second phase appearing in bright is observed in the ferrite. This second phase is mainly observed in large ferrite islands.

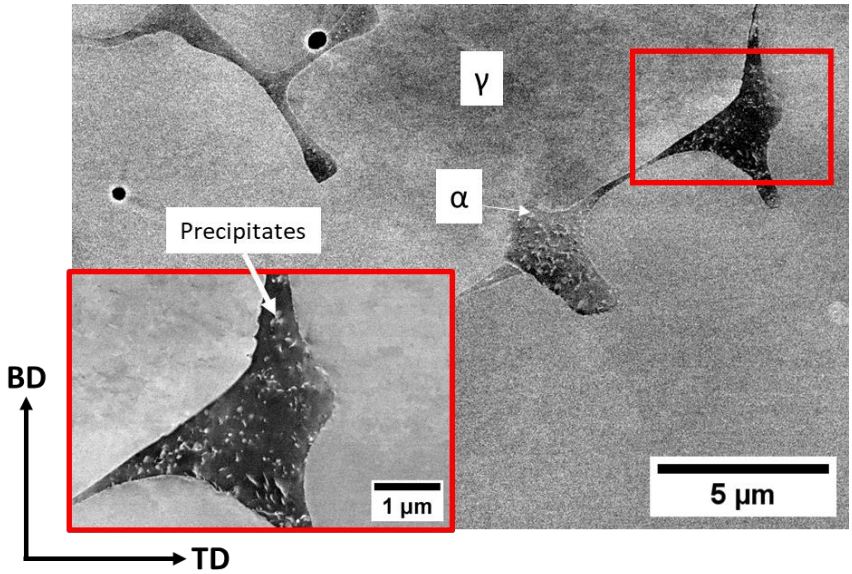

Figure VI-18: SEM-BSE image of the microstructure after a SR heat treatment and revealing the presence of bright precipitates in ferrite islands.

To identify the nature of the precipitates, TEM observations were carried out. Figure VI-19 (a) shows a STEM image of the sample after SR. One can see a ferrite island in the austenite matrix. Precipitates appear in black in the ferrite. Figure VI-19 (b) shows a magnification of (a). The size of precipitates is around 50 nm. Precipitates show a faceted morphology. Figure VI-19 (c) compares the EDS spectrum of the ferrite with that of a precipitate. The precipitate is richer in Si, Mo and Cr. Such enrichments are consistent with intermetallic Fe-Cr-Mo phases such as the σ or χ phase [33]. The crystallography of the observed phase could not be determined, since the precipitates were too thick to give a strong diffraction signal. However, as both σ and χ phases are known to be detrimental to the mechanical properties [33], this kind of heat treatment does not seem to be appropriate for 316L made by WAAM. The hardness is about 188 ± 7 HV1.

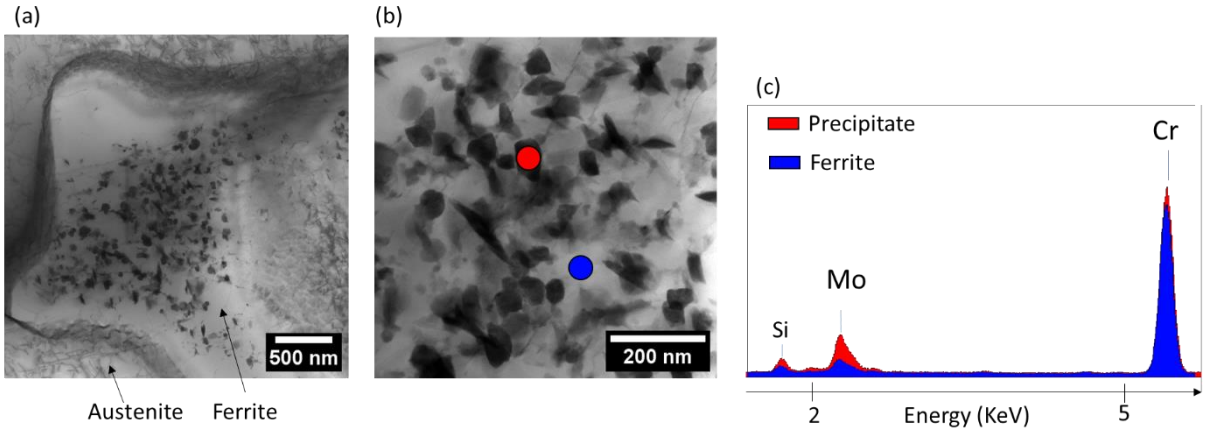

Figure VI-19: (a)-(b) STEM-BF images of the bottom of the build for the stress relief condition. (b) is a magnified view of (a). (c) EDS spectrum comparing the composition of the precipitates and that of the ferrite, the blue and red circles indicate the position where the EDS spectra were acquired in (b).

Figure VI-20 shows STEM bright field images of dislocations after the stress relief heat treatment. A high density of dislocations can be observed in the microstructure. Dislocations cells can be distinguished but their size is not regular and a high dislocation density can be observed inside the cells.

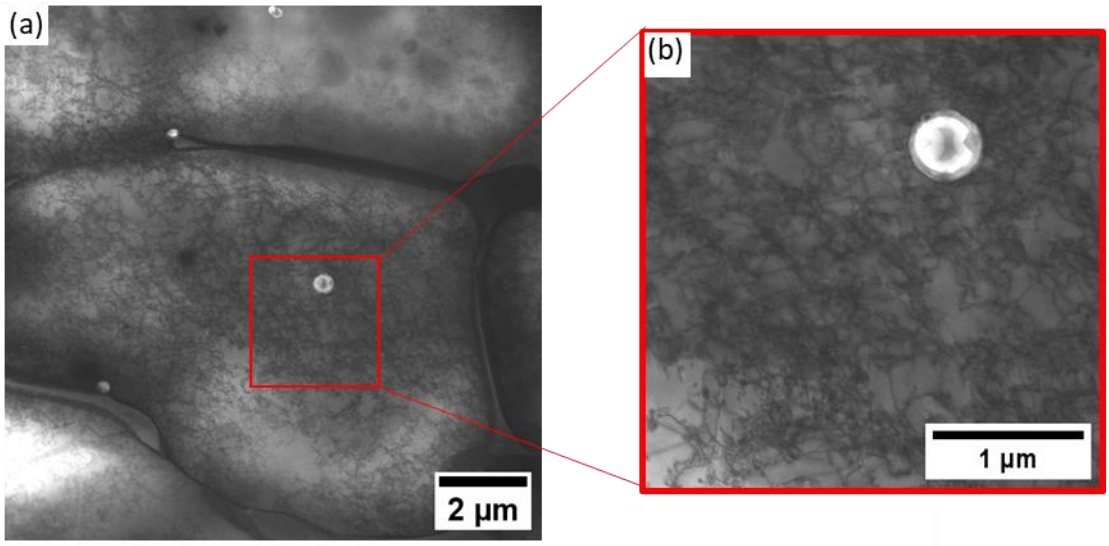

Figure VI-20: (a)-(b) STEM bright field images of dislocations after the stress relief heat treatment. (b) Magnified view of the red square shown in (a).

VI.4.2.2 After a ferrite regression heat treatment (SR + 1050°C/1h)

Figure VI-21 shows an IPF-EBSD map after the ferrite regression heat treatment. The OR and CFZ are still visible, as well as the melt pool boundary (MPB). There is no evidence of recrystallization after this heat treatment.

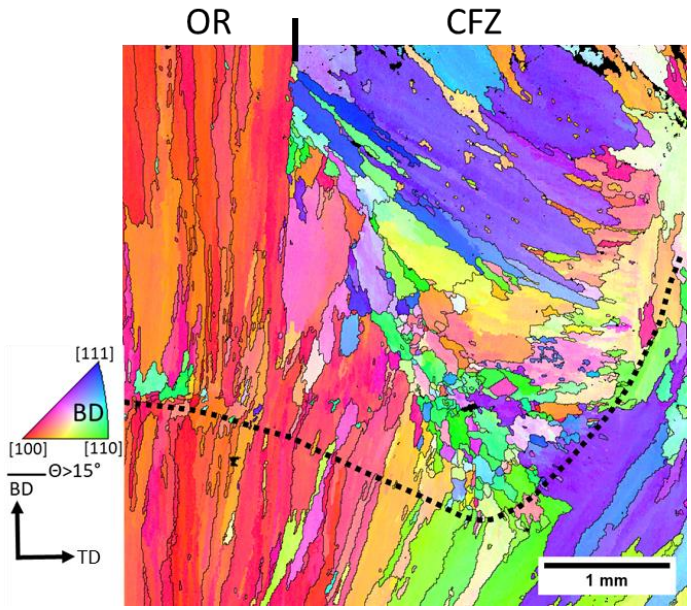

Figure VI-21: IPF-EBSD map after the ferrite regression heat treatment (SR + 1050°C/1h).

Figure VI-22 (a) shows an optical image after the ferrite regression heat treatment. The melt pool boundaries can still be distinguished. The area above the MPB seems to have much less ferrite than the one below the MPB. Figure VI-22 (b) and (c) show optical images respectively above and below the MPB. In both locations, ferrite is globular, but with a different average diameter: it is about 1 µm above and 4 µm below. Below, there is still some trace of vermicular ferrite, indicating that globularisation is not completed. The fraction of ferrite is different between these two locations, 0.8% above the MPB and 4.5% below. No difference in hardness was found above and below the MPB (respectively 168 ± 8 Hv1 and 172 ± 7 Hv1). The difference in dissolution kinetics of the ferrite as a function of the region of interest (above or below the MPB) was, to the best of our knowledge, not reported yet in the literature.

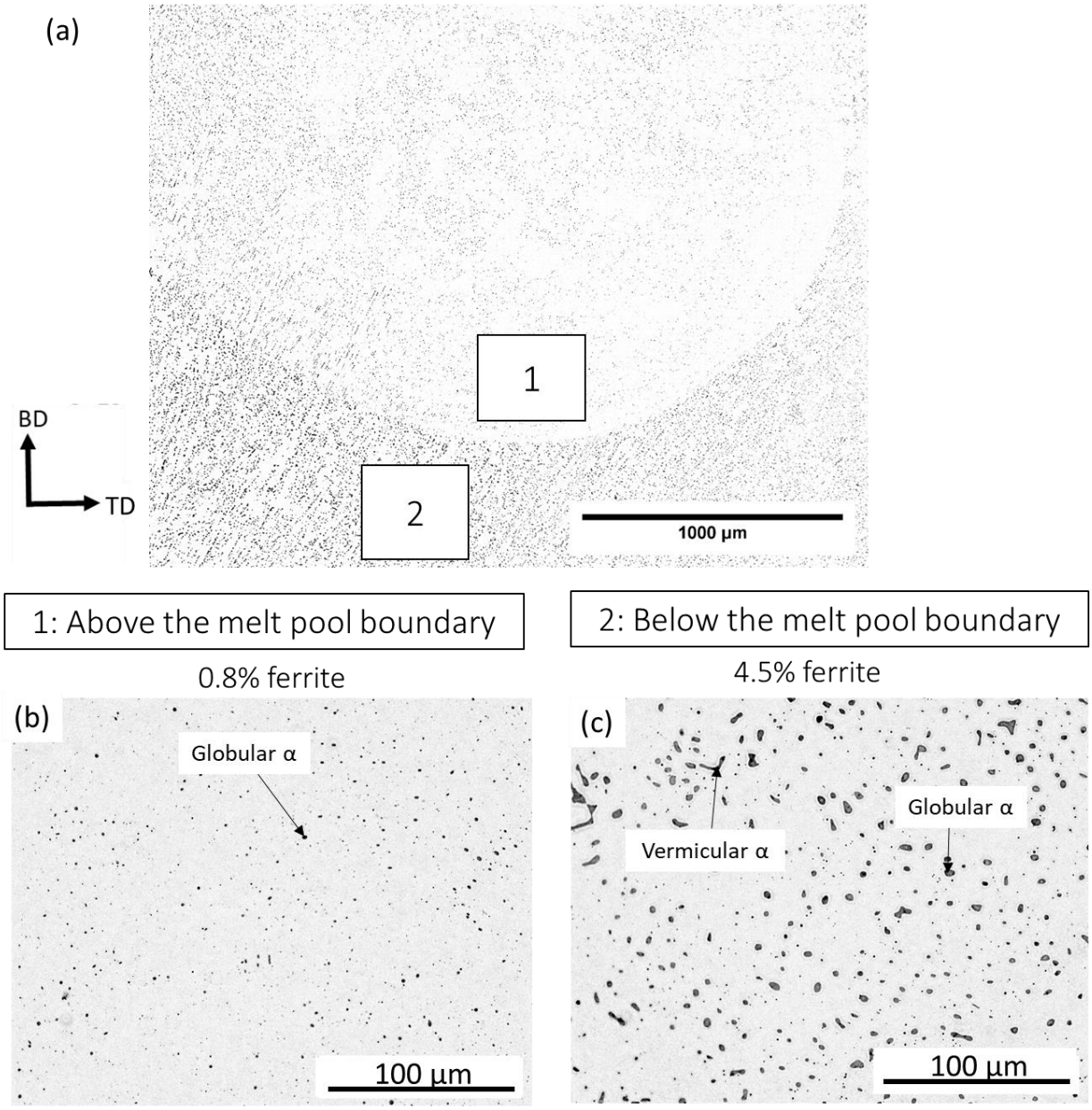

Figure VI-22: Optical image after the ferrite regression heat treatment and after electro-etching in a NaOH aqueous solution. (a) Low-magnification image where MPB can be seen. (b) Magnification of area 1 highlighted in (a). (c) Magnification of area 2 highlighted in (a).

VI.4.2.3 After a recrystallization heat treatment (SR + 1200°C 30 min)

Figure VI-23 shows the IPF-EBSD map after the recrystallization heat treatment. After this heat treatment, the recrystallized area fraction is 93%. It shows equiaxed grains with an average size of 140 µm. The width of the map is large enough to cover both the OR and CFZ, and also large enough to cover the area below and above the MPB. All these regions are recrystallized. This is different from the result of Wang et al. [178] which does not obtain recrystallization above the MPB after 1200°C/1h. The grains contain annealing twins, the latter appear as white interfaces in the EBSD map shown in Figure VI-23.

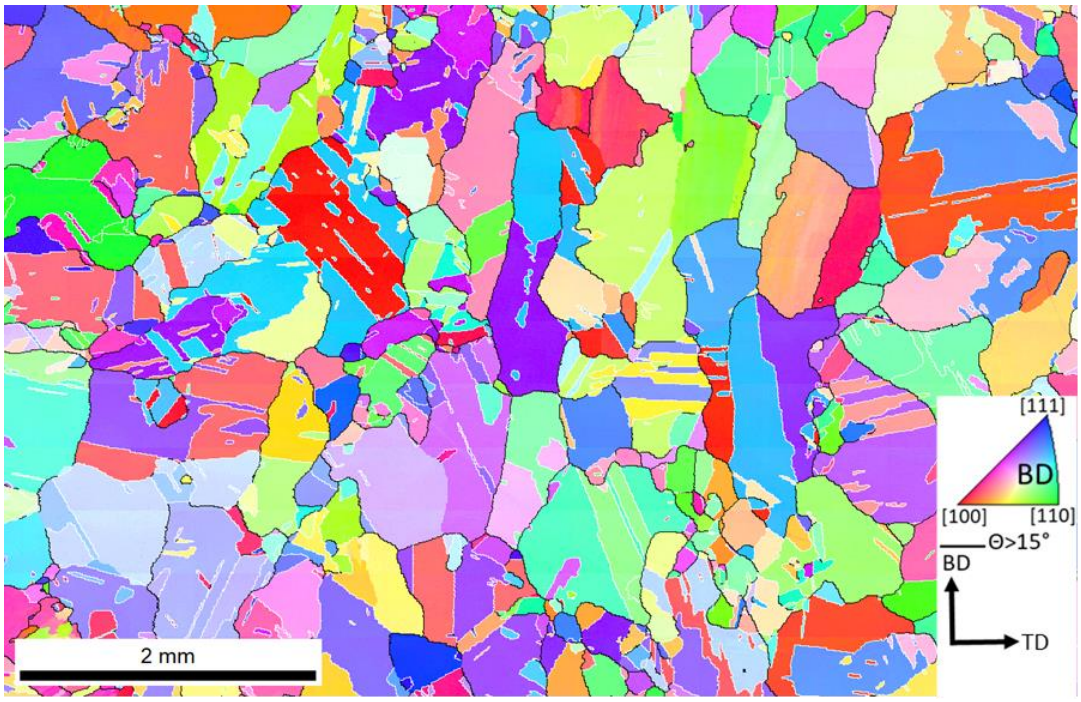

Figure VI-23: IPF-EBSD map after the recrystallization heat treatment.

Figure VI-24 shows the (100) and (110) pole figures after the recrystallization heat treatment. The texture is calculated based on two maps of the same dimensions as those shown in Figure VI-23, and contains more than 3000 grains. With a maximum intensity of 2.03 mrd, the texture is randomized in comparison with the as-built condition (it was 8 mrd in the as-built).

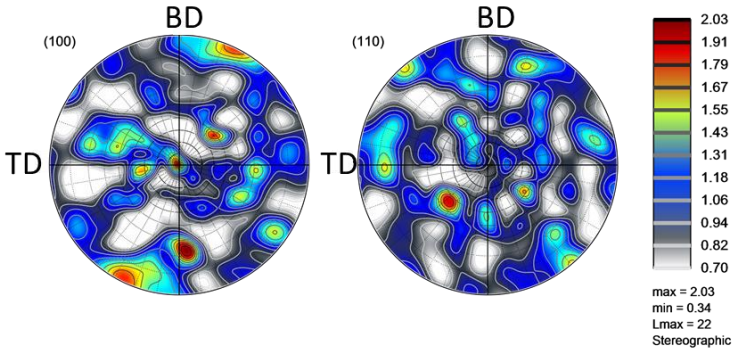

Figure VI-24: (100) and (110) pole figures after the recrystallization heat treatment.

Figure VI-25 shows an optical image after the recrystallization heat treatment. The former position of the MPB is visible because of a sharp change in the ferrite fraction. The area above the MPB has a lower ferrite fraction than the area below the MPB. Figure VI-25 (b) and (c) show optical images respectively above and below the MPB. No ferrite is found above the MPB (black dots are oxides), while a small fraction of ferrite is still found below the MPB (2.3%). In this specific location, there is no more trace of vermicular ferrite and the ferrite fraction is lower than after the ferrite regression heat treatment. The dissolution of the ferrite is faster at 1200°C compared to 1050°C, in agreement with the literature [33], [179], [180]. No difference in hardness was detected between the area above and below the MPB (respectively 150 ± 6 Hv1 and 154 ± 6 Hv1).

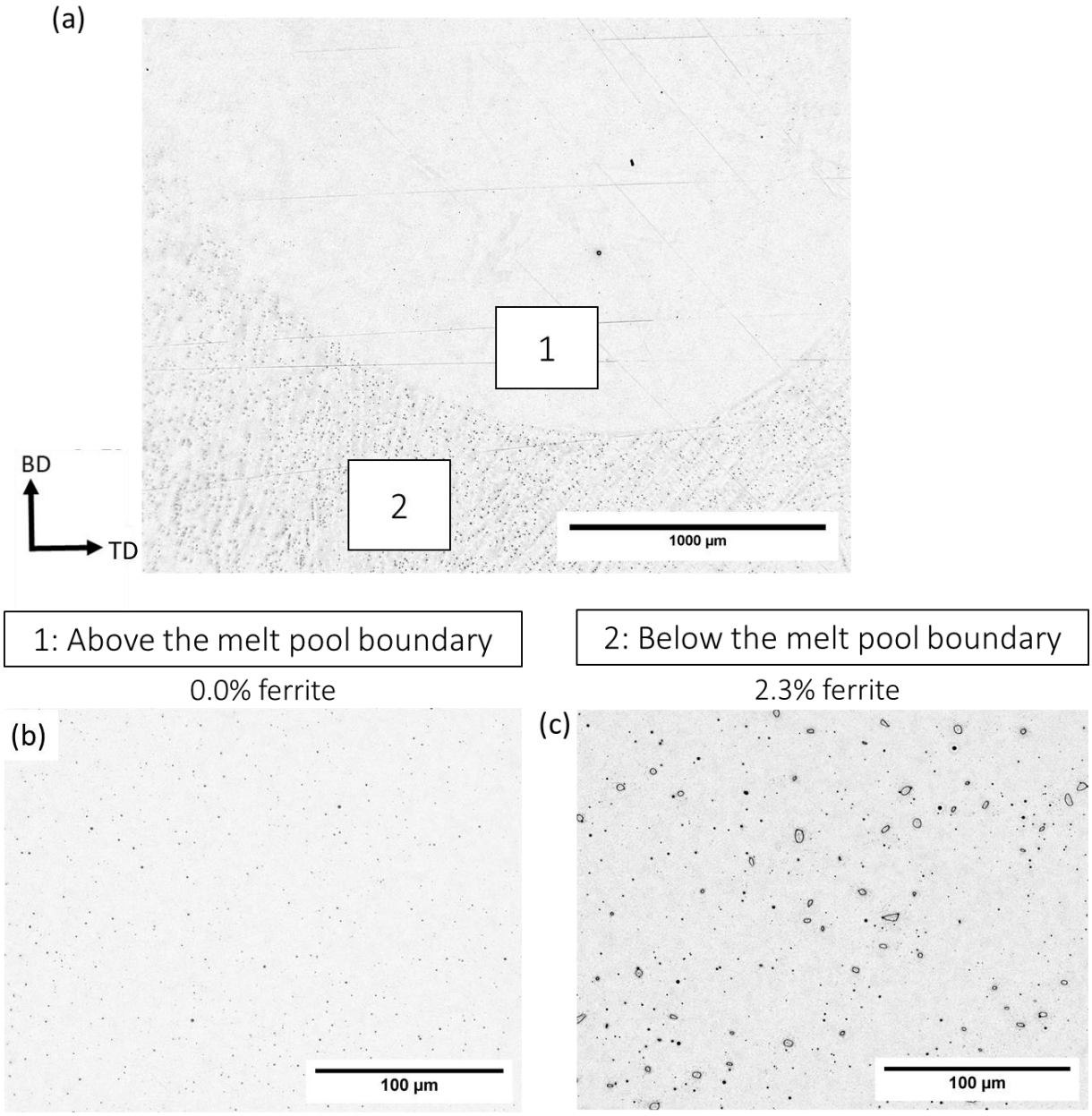

Figure VI-25: Optical image after the recrystallization heat treatment and after electro-etching in a NaOH aqueous solution. (a) Image showing a MPB. (b) Magnified view of area 1 highlighted in (a). (c) Magnified view of area 2 highlighted in (a).

VI.4.3 Tensile properties after the stress relief heat treatment

Tensile properties are determined only in the SR condition. Figure VI-26 shows the engineering stress-strain curves of different tensile samples after the SR heat treatment. For all tensile specimens, the yield stress and the UTS are above the RCC-M standard for wrought products (>175 MPa and >490 MPa respectively). However, for all tensile samples, the standard for the total elongation is not respected (>45%). When the loading direction is parallel to SD, tensile tests are relatively well reproducible, with no major change in yield stress or in total elongation. For the loading direction along TD, the tensile properties are reproducible until 15% of plastic deformation but variations in total elongation are observed.

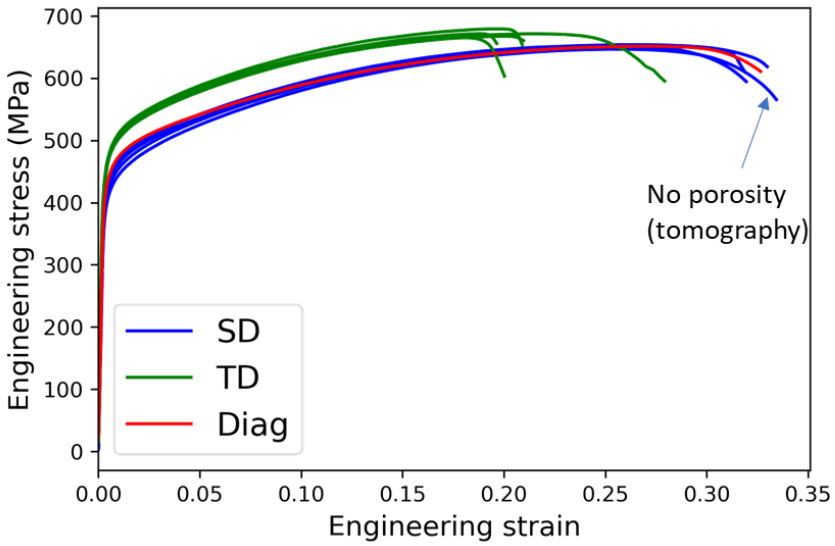

Figure VI-26: Tensile properties measured for loading different directions in the SR condition.

The width of the melt pool is 6 mm. This is about the same order of magnitude as the diameter of the tensile specimens. This means that the gauge length of the tensile specimen cannot be considered as a representative volume element (VER). This could explain the variability in the mechanical property between samples loaded in the same direction.

Differences in porosity could also be expected between samples. To have an idea of the impact of pores on the mechanical properties, X-Ray tomography was performed prior to straining in three different tensile specimens (1 extracted at 45° with respect to SD (Diag orientation) and 2 extracted such that the loading direction is aligned with SD). The 3D reconstructed images of the gauge length of the three tensile specimens inspected using X-ray tomography are shown in Figure VI-27. In some samples, a few but large pores can be observed. The pores can be approximated by a cylinder, because they follow the triple joint of the MPB, and so they are oriented along SD. For the Diag orientation, pores have a volume equivalent to a cylinder of 2 mm in length and 350 µm in diameter. In the SD1 specimen, the pore is a cylinder of a diameter of roughly 400 µm in diameter oriented in the loading direction and is as long as the gauge length of the tensile sample. Based on X-Ray tomography, the density of the SD1 specimen is 99.4%. However, in sample SD2, no pore is detected, at least with the resolution employed (voxel size = 8 µm).

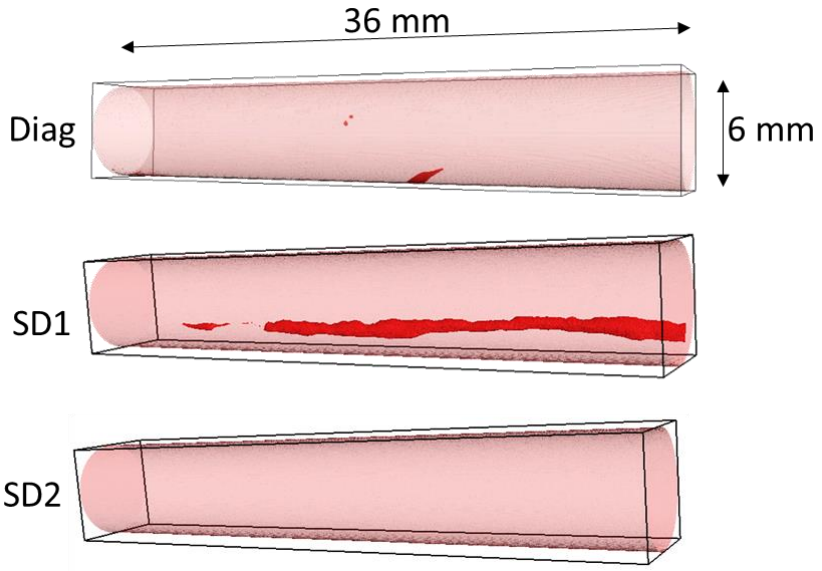

Figure VI-27: 3D images of the gauge length of the 3 tensile specimens characterized using X-ray tomography prior to testing. Pores are displayed in dark red.

In the sample SD1, there is a large pore, while the sample SD2 is free of pore. However, the total elongation is similar between these two samples. This observation suggests that the large pore in the sample SD1 does not have a big impact on the tensile behavior. This can be because the pore is not connected to the surface and is aligned with the tensile direction (not favorable for crack opening). Moreover, the density of the sample SD1 is still acceptable (99.4%).

In the Diag orientation, there is the presence of a large pore that is connected to the surface and oriented such that a crack opening is possible. However, the total elongation of this specimen is the same as in the SD2 sample (without pores). This could suggest that pores do not impact significantly the total elongation. However, one should keep in mind that texture can have an impact on the ductility as discussed in Chapter IV.7.2. Figure VI-28 shows the IPF along the tensile direction for the SD and Diag samples respectively. The IPF in the Diag and SD sample is different. SD samples have a high proportion of grains with their <100> direction parallel to the loading direction, while the Diag sample has a strong proportion of grains such that their <110> or <111> directions are parallel to the loading direction. As a result, such differences in IPF could also impact the ductility as it was shown in LPBF. For LPBF, samples having a strong proportion of grains with their <100> direction aligned with the loading direction exhibit a lower elongation to fracture compared to the one obtained for other textures [56], [58]. It was then expected that the Diag sample would have a higher total elongation than SD sample because of the texture, but this might be not observed because of the presence of pores.

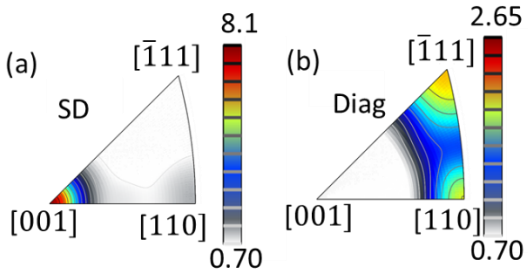

Figure VI-28: IPF along the tensile direction for (a) the SD sample, (b) the Diag sample.

It was shown that the Diag and SD samples have a similar yield stress (430 vs. 420 MPa), but the TD sample shows a slightly higher yield stress (463 MPa). A hypothesis to explain this anisotropy in yield stress would be the austenite texture. However, this hypothesis seems to not be consistent with the measured texture. Indeed, the Taylor factor between the SD and TD direction is identical (2.58). This yield stress anisotropy might be induced because tensile specimens cannot be considered as representative of the overall microstructure (too small with respect to the VER). The diameter of the tensile sample could be not large enough compared to the VER.

VI.5 Discussion

VI.5.1 Difference in ferrite dissolution kinetics above and below the melt pool boundary

It was observed that the ferrite fraction was different above and below the MPB after a ferrite regression heat treatment and after a recrystallization heat treatment. In the as-built condition, there was no clear difference in ferrite fraction between above and below the MPB. However, after the heat treatment, a difference was revealed. This suggests that the kinetics of ferrite dissolution vary between these two areas. The first hypothesis that could explain the difference in ferrite dissolution kinetics is the difference in ferrite morphology. Previous research demonstrated that lathy ferrite dissolves more rapidly than vermicular ferrite [181]. It appears that the area above the MPB contains a higher fraction of lathy ferrite. Therefore, this could explain why the ferrite located above the MPB dissolves faster. However, above the MPB, the ferrite morphology is a mix of lathy and vermicular ferrite. If the difference in dissolution kinetics were solely related to the difference in morphology, one could expect the vermicular ferrite present above the MPB to be of the same size as that observed below the MPB. There would be ferrite globules of 4 µm in diameter above the MPB. This is not observed experimentally. Therefore, the difference in ferrite morphology can only partially explain the difference in ferrite dissolution kinetic.

A second hypothesis to explain this difference in dissolution kinetics is that the ferrite composition varies from below to above the MPB. It cannot be excluded that the composition of the ferrite differs between these two areas. This could be induced by a difference in local thermal history (cooling rate, growth rate, thermal cycling…). Since the kinetics of dissolution are primarily driven by the composition of the ferrite [181], the eventual difference in composition between below and above the MPB could affect the

kinetics of dissolution. This hypothesis has to be verified by measuring the composition of the ferrite at different locations in the as-built state using electron probe microanalysis (EPMA).

VI.5.2 WAAM vs. LPBF

This section compares the microstructure and the tensile properties of the 316L processed by WAAM and LPBF. Tensile properties are measured after the stress relief heat treatment, so the microstructure is also compared after this heat treatment. The two microstructures after a stress relief heat treatment differ on many points. These differences are summarized in Figure VI-29, which compares some of the characteristics of the microstructures at the same scale. The differences can be summarized as follows:

- The melt pool of the WAAM steel is 50 times larger than the one from LPBF.
- The grain size of the WAAM steel is much coarser than the one from the LPBF steel, from 20 to 130 µm.
- The WAAM steel shows a stronger texture than the LPBF steel. The LPBF steel has a texture that can mainly be described as <110>//BD and <100>//Y, while the WAAM steel shows a texture that can mainly be described as <100>//BD and <100>//SD.
- The LPBF steel has a fully austenitic microstructure, with microsegregated regions separated by of 450 nm (intercellular spacing). The WAAM steel has 8% ferrite, with an interdendritic spacing around 8 µm. In the ferrite, the WAAM steel has intermetallic that precipitated during the stress-relief heat treatment.
- The LPBF steel has oxides with an average diameter of 20 nm, preferentially located in the interdendritic areas. The WAAM steel has oxides with an average diameter larger than 200 nm.
- Both materials have a high density of dislocations. However, the arrangement of dislocations differs. Dislocations in the LPBF steel are arranged in elongated cells, with a low dislocation density inside the cells, while the WAAM steel has a more random arrangement of dislocations.

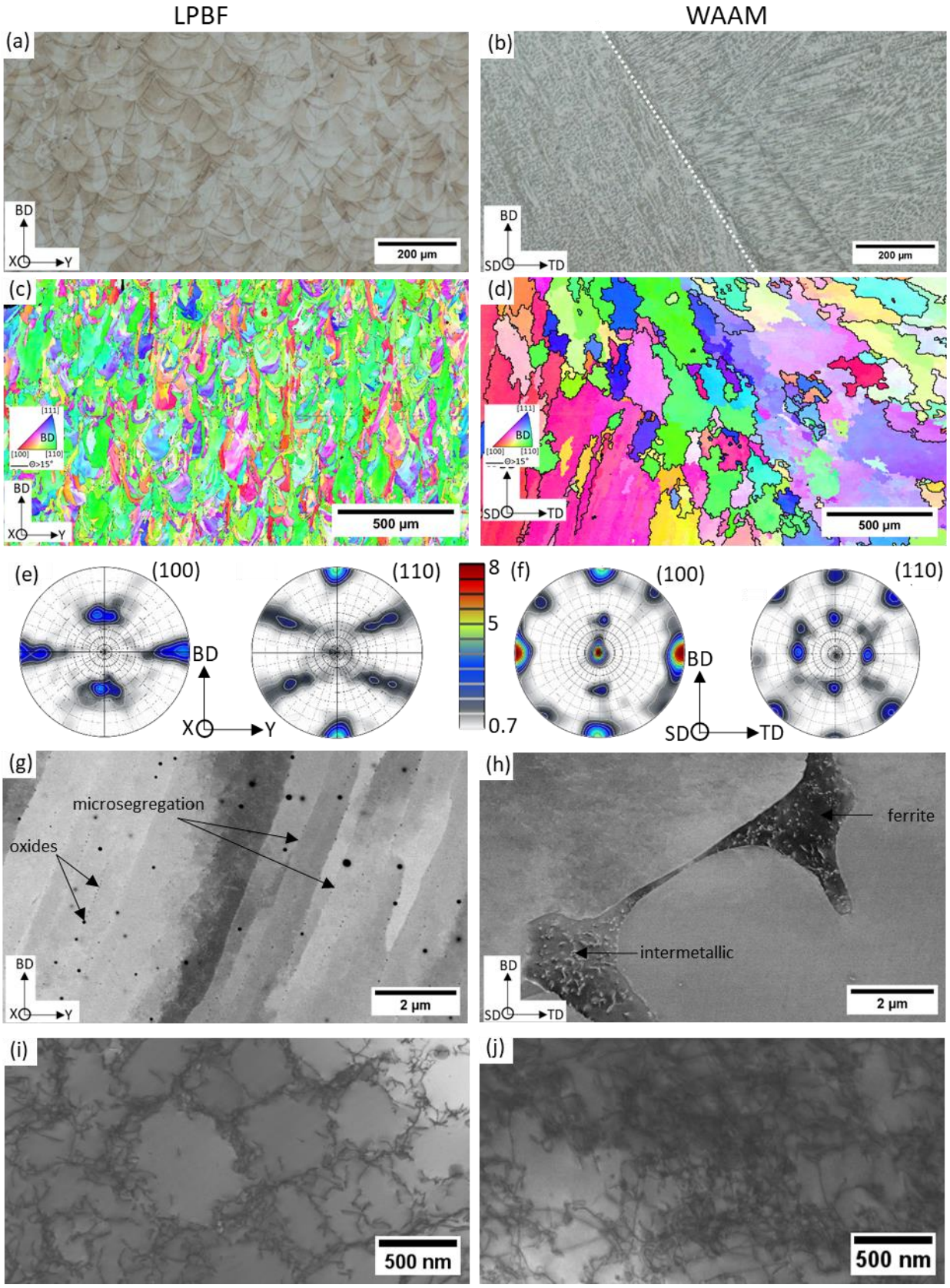

Figure VI-29: Comparison of the microstructure obtained by LPBF and WAAM after a stress relief heat treatment 600°C/1h at the same scale. Left images for the LPBF microstructure and right images for the WAAM microstructure. (a)-(b) Optical images after V2a etching. The white line draws the melt pool boundaries. (c)-(d) IPF-EBSD maps. (e)-(f) (100) and (110) pole figures. (g)-(h) SEM-BSE images. (i)-(j) STEM bright field images.

To compare the mechanical properties of the 316L processed by WAAM and LPBF, similar conditions must be chosen. The sample of WAAM to compare is the one loaded in the scanning direction, where no pore was detected. To compare both processing routes, the best is to compare materials that have the same nominal composition. The composition of the WAAM steel has a high N content (1000 ppm). Therefore, it will be compared to Steel 1 which has also a high N content. In WAAM, the main grain direction along SD is <100>. In Steel 1, the y direction is the one which also has as main orientation the <100> direction. Finally, both conditions must be compared after the same heat treatment i.e. stress relief.

Figure VI-30 shows the true stress-strain curve comparing the tensile properties of the WAAM and of the LPBF Steel 1 in the y direction after the stress relief heat treatment. The LPBF steel is harder (yield stress = 520 MPa in the LPBF steel vs. 410 MPa in the WAAM steel) than the WAAM steel but has a slightly lower true uniform elongation (0.22 for LPBF vs. 0.23 for WAAM steel).

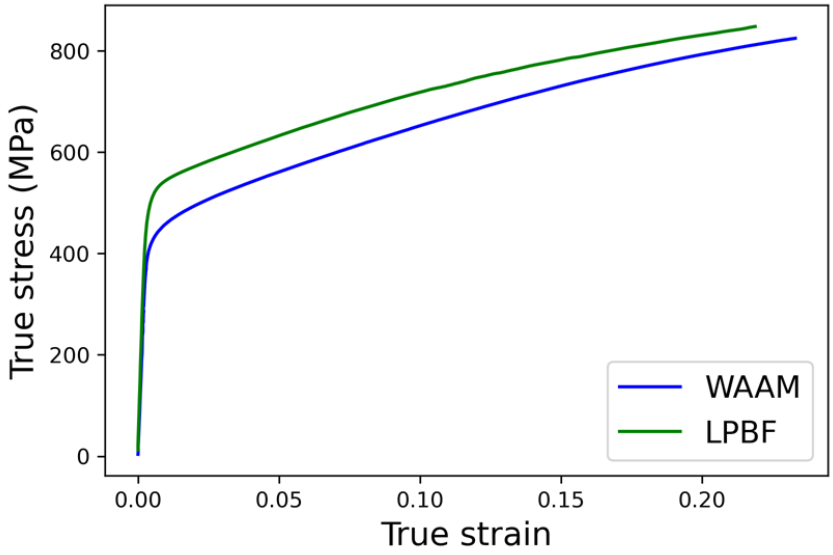

Figure VI-30: True stress-strain curve of the LPBF Steel 1 loaded in the y direction, and of the WAAM loaded in the scanning direction. No pore is found in this WAAM tensile specimen (based on X-ray tomography). Both conditions are tested after a similar SR heat treatment (600°C/1h).

The contribution of the solid solution to the yield stress is the following [33]:

$$\sigma_{ss} = 68 + 354(\%C) + 493(\%N) + 20(\%Si) + 3.7(\%Cr) + 14.5(\%Mo) \qquad \text{(VI-1)}$$

With σ_{ss} the yield stress in MPa, and the concentration of elements in weight percent. The contribution of solid solution is similar in both materials (210 MPa for SLM and 230 MPa for WAAM). Therefore, the composition of the material cannot be held responsible for the 110 MPa difference in yield stress.

Several other contributions could explain this difference in yield stress: the ferrite might be enriched in alloying element, decreasing the contribution of the solid solution in austenite; the grain size is much larger in WAAM compared to LPBF which might give a softer microstructure; oxides might contribute to harden the LPBF material; the dislocation density might be higher in LPBF compared to WAAM.

VI.6 Conclusion

The objective of this chapter was to investigate the microstructure and properties of the 316L steel processed by WAAM. After fabrication, the microstructure is relatively coarse and consists of two regions: the overlapping region (OR) and the center of fusion zones (CFZ). The overlapping region shows long columnar grains, and has as a main orientation (<100>//BD, <100>//SD), while the CFZ shows more refined grains and have as a main orientation (<110>//BD, <100>//SD). The average grain size is 130 µm. At the intragranular scale, a mixture of ferrite and austenite is observed, with about 8% of ferrite. Inclusions >200 nm identified as silicates are also found in the microstructure.

The evolution of the microstructure with heat treatment was also investigated. Those evolutions can be summarized as follows:

- After a stress relief heat treatment (600°C/1h), no change in ferrite morphology is observed. However, a phase enriched in Cr and Mo precipitates in the ferrite. This phase has not been formally identified, but it seems that it is an intermetallic phase that could be the σ phase.

- After a ferrite regression heat treatment (SR + 1050°C/1h), the ferrite becomes globular. The fraction of ferrite depends on the region of interest. Above the melt pool boundary, the ferrite fraction is lower than below the melt pool boundary (4% vs. 0.8%). The reason for this difference in dissolution kinetics might result from the difference in morphology or composition of the ferrite.

- After a recrystallization heat treatment (SR + 1200°C/30min), the microstructure shows large equiaxed grains of 140 µm in size. The texture is found more random than in the as-built condition. A small fraction of ferrite (2%) is still found below the melt pool boundary, but ferrite is totally dissolved above.

Tensile tests were also performed in the SR condition in three different directions. Anisotropy in yield stress is found between these directions. The yield stress is higher when the loading direction is parallel to the transverse direction, compared to when it is parallel to the scanning direction. The reason for this difference is not clear yet, but might be due to the size of the tensile specimens that may not be representative of the overall microstructure (VER larger than the specimen diameter). In comparison with a wrought 316L steel, WAAM produces harder material, but with a much lower total elongation. Compared to LPBF, the WAAM produces a softer material, with a similar uniform elongation. The reasons for this difference in yield stress are not yet perfectly understood.

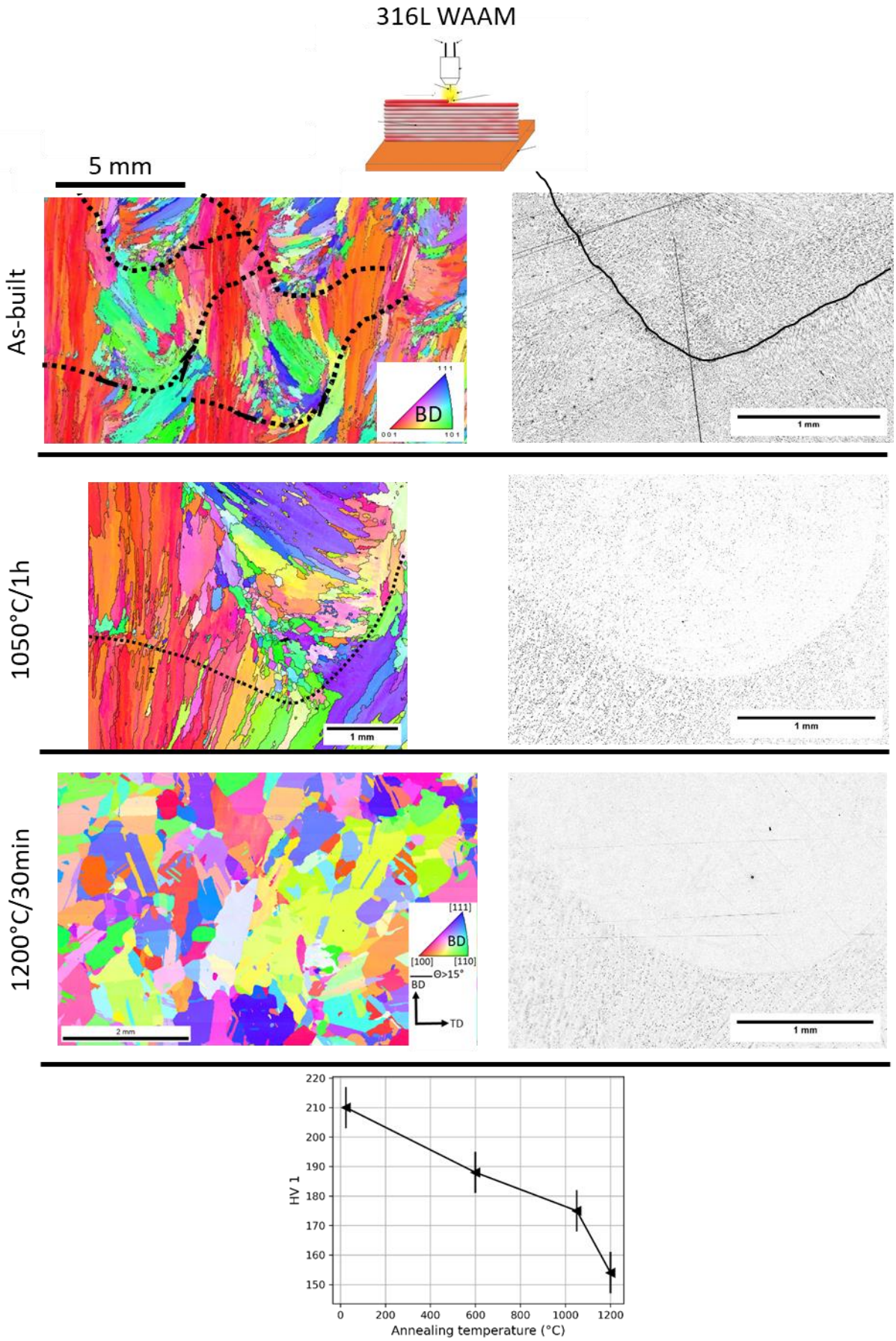

Figure VI-31: Graphical abstract of Chapter 5.

Chapter VII. Conclusions and perspectives

VII.1 Concluding remarks

This thesis aimed to provide better control of the mechanical properties of austenitic stainless steels (316L grade) produced by additive manufacturing (LPBF and WAAM). This is mandatory to establish microstructure standards that meet property requirements. This is also required to obtain constitutive laws adapted to the microstructure inherited from additive manufacturing. The control of properties requires, on the one hand, an understanding of the microstructure resulting from AM; and, on the other hand, the dissociation of the effect of the different microstructural characteristics on the mechanical properties.

- The first objective of this Ph.D. thesis was to understand the origin of a difference in microstructure between two steel compositions produced by LPBF. To this end, two 316L steels were produced by LPBF from two different powder batches under the same manufacturing conditions. Steel 1 shows a microstructure often reported in the literature, with a fully austenitic microstructure consisting of columnar grains growing along the build direction, a <110>//BD fiber texture, an absence of twins, and a cellular solidification structure with microsegregation (elemental partitioning of Cr and Mo) observed everywhere in the material. Steel 2 also shows a fully austenitic microstructure but with finer grains exhibiting a nearly equiaxed morphology, a nearly random texture, the presence of a high fraction of twin boundary, and a cellular solidification structure with microsegregation (elemental partitioning in Cr and Mo) observed in only 50% of the microstructure. No microsegregation was found in the other 50% rest of the microstructure. This difference in microstructure between Steel 1 and Steel 2 is attributed to a difference in solidification path. Steel 1 solidifies following an A mode (full austenitic solidification), while Steel 2 is supposed to solidify following a mixed solidification mode, with primary austenite or ferrite depending on the location within the melt pool. In Steel 2, ferrite is thought to transform into austenite via a massive phase transformation, leading to grain refinement and the presence of a high density of twin boundaries (most likely forming via the so-called growth accident mechanism during the migration of the α/γ interface occurring during the massive phase transformation). However, another hypothesis turns to be also in agreement with our observations and is based on the liquid structure (ISRO effect) which would affect the solidification (nucleation via ISRO mediated nucleation and growth via ISRO induced stacking fault). This hypothesis is less likely, but cannot be excluded.

- The second objective of the thesis was to discriminate the different microstructural contributions to the tensile properties. To this end, both steels were subjected to various heat treatments designed so as to alter only some microstructural features (residual stresses, microsegregation, grain shape and size, dislocation density). Then, the tensile properties of the as-built and heat-treated microstructures were tested for different build orientations. The plastic deformation mechanisms were also investigated. It was shown that the dislocation cells already present in

the as-built condition do not accumulate misorientation with plastic deformation. The fraction of deformation twins depends, in first order, on the deformation of the material, and was not sensitive to the microstructure, (grain size and morphology). A modified Kocks-Meckings model taking into account the effect of grain size and twinning was used. This model makes it possible to compare the work-hardening of a recrystallized steel, a microstructure mimicking the one of a product obtained via the more traditional forging processing route with the one of materials inherited from LPBF. One advantage of such an approach is that both materials have the same composition and texture. It is shown that the parameters describing the plasticity of a recrystallized microstructure can be used to model the plasticity of a material fabricated by LPBF. Based on this result, it was concluded that the dislocation density is a key parameter to describe the plasticity of the 316L steel processed by LPBF, but that the organization of these dislocations into tubular cells does not appear to be of first importance.

- The third objective was to study the 316L steel fabricated by WAAM. A particular attention was paid to establish the links between the process, the microstructure and its evolution with heat treatments. Due to time constraints, it was only possible to conduct a few characterizations. The presence of large pores in the as-built material made more difficult the measurement of the tensile mechanical properties. However, pores can be suppressed and fully dense samples can be produced with optimized processing parameters. The microstructure resulting from WAAM is much coarser than the one inherited from LPBF and was strongly textured. It consists of a mixture of ferrite in large austenitic grains. The microstructure was found to react heterogeneously during post-fabrication heat treatments. After 1h at 600°C, an intermetallic phase precipitates in the ferrite. After 1h at 1050°C, the ferrite shows a more globular morphology and is present in smaller fractions above the melt pool boundary compared to above. A similar result is reported after 30min at 1200°C, even if the fraction of ferrite is lower than after 1050°C for 1h. This heterogeneous evolution of the ferrite fraction and morphology was attributed to a difference in morphology or/and composition between these two areas.

Guidelines and recommendations

An equiaxed microstructure can be considered as an advantage when using the 316L steel produced by AM because (i) it shows a more isotropic mechanical behaviour in comparison with a columnar microstructure with a strong texture; (ii) isotropic constitutive laws are easier to implement in simulation codes; and (iii) a random texture makes easier the use of non-destructive testing using ultrasonic waves. To achieve such a microstructure using LPBF, it is certainly necessary to impose a tight control of the steel composition, with a sufficient amount of elements promoting ferrite in comparison with elements promoting austenite. However, the upper bound for the content of α stabilizer is imposed by the presence of residual ferrite that is undesirable.

The mechanical properties required by the nuclear industry for the 316L produced by AM are those of the products fabricated using more traditional processing route such as forging (relatively low yield stress > 170 MPa but high total elongation > 45%). When produced by LPBF, the material is stronger (YS>400 MPa), mainly because of the high dislocation density observed in the as-built conditions.

However, it can show in some loading directions, a reduction in total elongation (A%<45%). This is mainly attributed to the combination of a high dislocation density and a relatively strong texture. To achieve a total elongation that meets the standard required, one strategy is to perform a heat treatment to reduce the dislocation density. A recrystallization heat treatment can be suitable to this purpose. However, this heat treatment is not currently considered in the future, as it leads to a drop in toughness as demonstrated by Edouard De SONIS in his Ph.D. thesis. A suitable heat treatment is one that leads to a reduction of the dislocation density while avoiding recrystallization. Thus a heat treatment at 900°C for 1h turns out to be a good option.

When modeling the yield stress of the material, it is important to take into account both dislocation density and grain size. To model the plasticity of the material, it is important to take into account the dislocation density, the grain size as well as the texture.

In the case of the material produced by WAAM, data are still lacking to establish the appropriate heat treatment. However, a single residual stress-relief heat treatment should be avoided because it leads to the precipitation of an intermetallic phase that is likely to cause embrittlement. A recrystallization heat treatment leads to the formation of large grains (~150 µm) and may result in a material that is too soft depending on the composition. A heat treatment at 1050°C for 1h, inspired from what is done for cast 316L, can be adapted to remove residual stresses, and improve the total elongation without risking the nucleation of brittle phases or the initiation of recrystallization.

VII.2 Future work

Microstructure variability

In order to specify a steel composition that induces fine and equiaxed grains, it is necessary to impose a tight control of the nominal composition. In this work, we attempted to identify the compositional range giving the targeted microstructure based on literature data. However, this approach suffers from several limitations. In particular, process parameters differ from a study to another, which makes impossible to compare the impact of composition for the same processing parameters. Moreover, the criterion for determining the type of microstructure, fine grains vs columnar grains, is based on the visualization of the IPF EBSD map, that makes possible interpretation error. To establish this composition range, we propose a new idea. The first step would be to build steels from different powder compositions, using constant processing parameters, and then characterize the microstructure (optical observations for the detection of solidification cells and EBSD to get information regarding the grain size and morphology, the presence of twin boundaries, and the possible presence of residual ferrite). From these data, a mapping derived from the WRC-92 diagram could be produced. However, this first step requires large quantities of powder to make a build, and switching from one powder batch to another in the LPBF machine is time-consuming. A proposal for an alternative methodology was developed as part of a 3-month M1 internship (Sylvain Trouvé, student from PHELMA). The idea was to sinter powder pellets and then expose those pellets to a laser beam in the LPBF machine. These laser tracks were then characterized. The advantage of this approach is that it requires very few powders for each characterization (~4g), and there is no need to load powder into the machine. To mimic the stacking of layers during LPBF, several laser expositions can be made using a 67° rotation at different powers.

After adjusting these parameters, given in Appendix H, it is possible to identify a composition that solidifies purely in primary austenite or likely with a mixed solidification mode, see Figure VII-1. These differences in solidification can be identified by the absence of solidification cells in some regions of the microstructure in the optical micrographs, and by the presence of fine grains with a high density of twin boundaries in the EBSD maps.

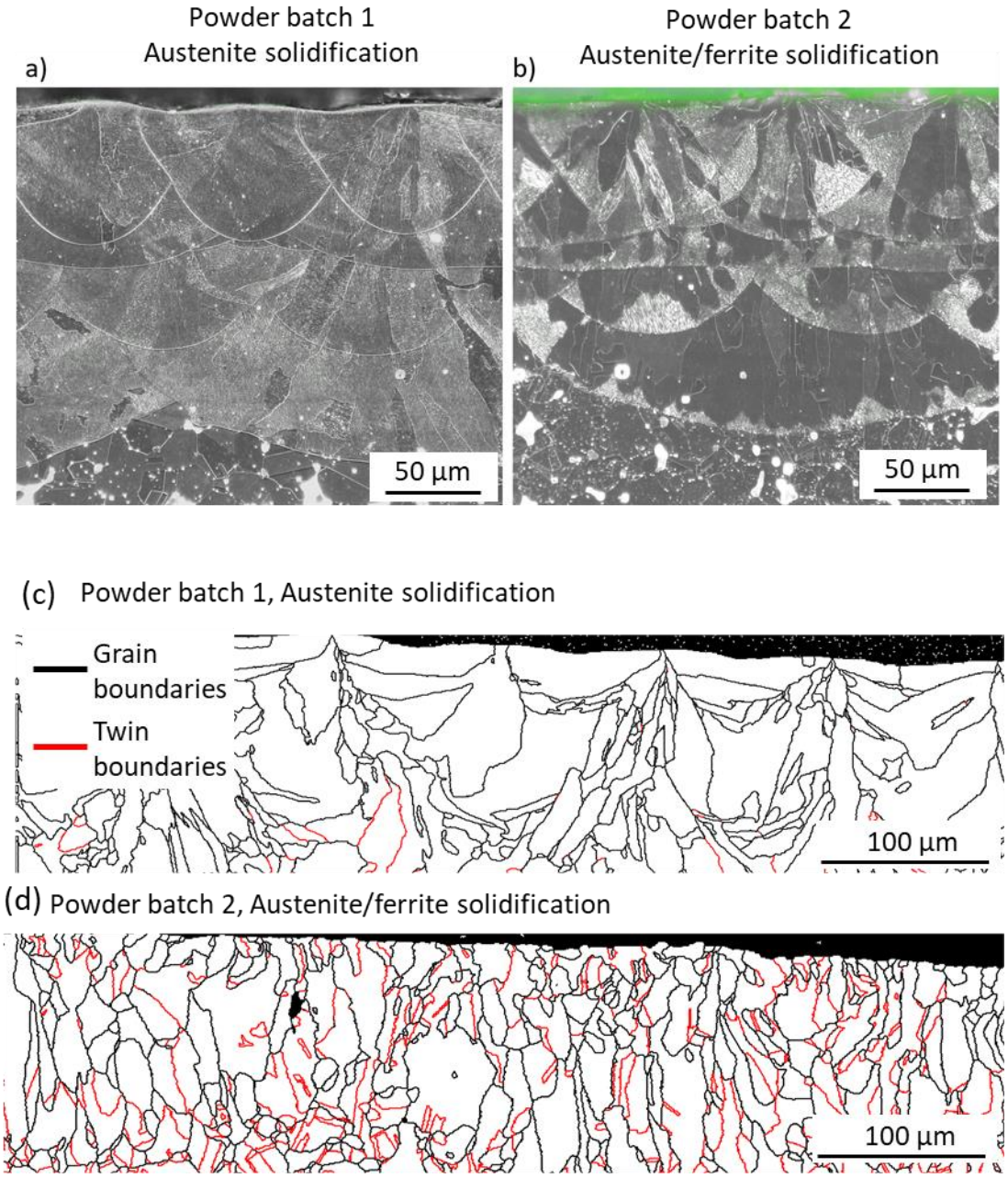

Figure VII-1: (a)-(b) Optical micrographs (polarized contrast) taken after etching using oxalic acid of the microstructure obtained after having exposed respectively the pellet made from powder batch 1 and powder batch 2 to the laser. Cells appear in bright. (a) The entire microstructure is composed of solidification cells, and (b) The microstructure consists of regions were solidification cells are easily observed and other regions where they are hardly visible. (c)-(d) Grain maps collected in the samples made respectively from powder batch 1 and powder batch 2. Grain boundaries are shown in black and twin boundaries in red.

The impact of solidification conditions on the primary phase should be further investigated. In particular, it is not yet fully understood why, for the same nominal composition, there are regions solidifying in

ferrite and others in austenite. Is this induced by differences in growth kinetics between ferrite and austenite? Or by the presence or absence of ferrite seeds? To investigate this, solidification simulations taking into account the dendrite tip temperature seem to be a suitable tool. To investigate the impact of ferrite seeds on the solidification microstructure, one could do an experiment. This would consist by first select a composition that shows a mix solidification mode (e.g.: the composition of powder batch 2). The material could be a sintered pellet or a metal sheet. Then, a part of the material could be melt by TIG, which would result in a mix microstructure of ferrite and austenite, and the other part would remain fully austenitic. Then, both part could be exposed to a laser beam in LPBF machine. During solidification, the part of material which has been melt by TIG has ferrite seed, while the other part has not. Microstructure between both parts could be compared, regarding the impact of ferrite seeds on the resulting microstructure.

In addition, there is a lack of experimental data on interface velocities during the massive phase transformation. This seem difficult to obtain but turns out to be necessary to achieve a complete understanding of the underlying mechanism. Finally, the consequences of this massive phase transformation on the arrangement and density of dislocations remain unknown. It would thus be interesting to study more deeply this aspect.

Measurement and role of the kinematic contribution to the work-hardening

The model used to study the material work-hardening takes into account the back stress (kinematic contribution to the work-hardening). However, this back-stress was not evaluated experimentally in this work. To measure this back stress, uniaxial tension-compression Bauschinger tests should be carried out for different forward plastic strains. This would enable the results to be compared with the model's predictions, and eventually adapt the model consequently. These Bauschinger tests could be carried out in the recrystallized and stress-relieved conditions to investigate the possible role of the arrangement of dislocation into tubular cells.

WAAM

Important work remains to be done to control the mechanical properties of the material inherited from WAAM. On the one hand, the microstructure needs to be controlled via the process and possibly via optimized post-fabrication heat treatments. To control the microstructure with heat treatments, it would be necessary to measure the ferrite composition by microprobe analysis at different regions in the melt pool. This measurement could be combined with a precipitation or phase transformation model to be able to predict its ageing or its dissolution kinetics. To establish the link between microstructure and mechanical properties, the methodology applied to the materials fabricated by LPBF can be applied to WAAM. To study the effect of the residual ferrite content on the mechanical properties, various ferrite contents could be obtained using appropriate heat treatments to dissolve part or the overall ferrite content without modifying the grain shape or crystallographic texture.

Bibliography

[1] O. Andreau, « Nocivité en fatigue et contrôle de défauts produits par fabrication additive », ENSAM Université, 2019.

[2] R. Warsi, K. H. Kazmi, et M. Chandra, « Mechanical properties of wire and arc additive manufactured component deposited by a CNC controlled GMAW », *Materials Today: Proceedings*, vol. 56, p. 2818-2825, 2022, doi: 10.1016/j.matpr.2021.10.114.

[3] « Nucobam ». Consulté le: 16 mai 2023. [En ligne]. Disponible sur: https://nucobam.eu/additive-manufacturing/

[4] « Première pièce produite en fabrication additive pour les centrales EDF Hydro. », 14 juin 2022. Consulté le: 19 mai 2023. [En ligne]. Disponible sur: https://www.vallourec.com/fr/toutes-les-actualites/groupe-2022-waam-EDF-Hydro

[5] *Prévention de l'endommagement des matériels mécaniques. Introduction aux règles de conception, de réalisation et d'analyse au RCC-M.* in RCC-M Criteria, no. 2. AFCEN, 2014.

[6] L. Lemarquis, P. F. Giroux, H. Maskrot, B. Barkia, O. Hercher, et P. Castany, « Cold-rolling effects on the microstructure properties of 316L stainless steel parts produced by Laser Powder Bed Fusion (LPBF) », *Journal of Materials Research and Technology*, vol. 15, p. 4725-4736, nov. 2021, doi: 10.1016/j.jmrt.2021.10.077.

[7] H. Pommier, « Stress relaxation cracking in AISI 316L-type austenitic stainless steels », Ecole nationale supérieure des Mines de Paris, 2015.

[8] S. Chen, G. Ma, G. Wu, A. Godfrey, T. Huang, et X. Huang, « Strengthening mechanisms in selective laser melted 316L stainless steel », *Materials Science and Engineering: A*, vol. 832, p. 142434, janv. 2022, doi: 10.1016/j.msea.2021.142434.

[9] A. Chniouel, « Etude de l'élaboration de l'acier inoxydable 316L par fusion laser sélective sur lit de poudre : influence des paramètres du procédé, des caractéristiques de la poudre, et des traitements thermiques sur la microstructure et les propriétés mécaniques. », Université Paris-Saclay, Paris, 2019.

[10] L. Palmeira Belotti, T. F. W. van Nuland, M. G. D. Geers, J. P. M. Hoefnagels, et J. A. W. van Dommelen, « On the anisotropy of thick-walled wire arc additively manufactured stainless steel parts », *Materials Science and Engineering: A*, vol. 863, p. 144538, janv. 2023, doi: 10.1016/j.msea.2022.144538.

[11] X. Chen, J. Li, X. Cheng, B. He, H. Wang, et Z. Huang, « Microstructure and mechanical properties of the austenitic stainless steel 316L fabricated by gas metal arc additive manufacturing », *Materials Science and Engineering: A*, vol. 703, p. 567-577, août 2017, doi: 10.1016/j.msea.2017.05.024.

[12] M. Godec, S. Zaefferer, B. Podgornik, M. Šinko, et E. Tchernychova, « Quantitative multiscale correlative microstructure analysis of additive manufacturing of stainless steel 316L processed by selective laser melting », *Materials Characterization*, vol. 160, p. 110074, févr. 2020, doi: 10.1016/j.matchar.2019.110074.

[13] S. Bahl, S. Mishra, K. U. Yazar, I. R. Kola, K. Chatterjee, et S. Suwas, « Non-equilibrium microstructure, crystallographic texture and morphological texture synergistically result in unusual mechanical properties of 3D printed 316L stainless steel », *Additive Manufacturing*, vol. 28, p. 65-77, août 2019, doi: 10.1016/j.addma.2019.04.016.

[14] J. Cunat, « Aciers inoxydables - Critères de choix et structure ». Techniques de l'ingénieur, 10 mars 2000.

[15] « Acier inoxydable », Wikipedia. [En ligne]. Disponible sur: https://fr.wikipedia.org/wiki/Acier_inoxydable

[16] « Pieces forgées ou estampées en acier inoxydable austenitiques de niveau 1,2 et 3. », in *RCCM*, in Tome II, no. M 3000. , 2020, p. M3000 107.

[17] A. J. Cooper, W. J. Brayshaw, et A. H. Sherry, « Tensile Fracture Behavior of 316L Austenitic Stainless Steel Manufactured by Hot Isostatic Pressing », *Metall Mater Trans A*, vol. 49, nº 5, p. 1579-1591, mai 2018, doi: 10.1007/s11661-018-4518-2.

[18] D. J. Kotecki et T. A. Siewert, « WRC-1992 constitution diagram for stainless steel weld metals: a modification of the WRC-1988 diagram », *Welding Journal*, vol. 71, nº 5, p. 171-178, 1992.

[19] J. Lippold et D. Kotecki, *Welding metallurgy and weldability of austenitic stainless steels*. 2005.

[20] E. Folkhard, *Welding metallurgy of stainless steel*. Springer Science & business media, 2012.

[21] J.-C. lippold, « Solidification behavior and cracking susceptibility of pulsed-laser welds in austenitic stainless steels », *Welding Journal Including Welding Research Supplement*, vol. 73, nº 6, p. 129-139, 1994.

[22] A. R. Pavan, N. Chandrasekar, B. Arivazhagan, S. Kumar, et M. Vasudevan, « Study of arc characteristics using varying shielding gas and optimization of activated-tig welding technique for thick AISI 316L(N) plates », *CIRP Journal of Manufacturing Science and Technology*, vol. 35, p. 675-690, nov. 2021, doi: 10.1016/j.cirpj.2021.08.013.

[23] M. Bobadilla, J. Lacaze, et G. Lesoult, « Influence des conditions de solidification sur le déroulement de la solidification des aciers inoxydables austénitiques », *Journal of Crystal Growth*, vol. 89, nº 4, p. 531-544, juill. 1988, doi: 10.1016/0022-0248(88)90216-3.

[24] M. Hillert, « Thermodynamics of the massive transformation », *Metall Trans A*, vol. 15, nº 3, p. 411-419, mars 1984, doi: 10.1007/BF02644964.

[25] Y. Bréchet, Éd., *Solid-solid phase transformations in inorganic materials*. in Solid state phenomena, no. v. 172-174. Durnten-Zuerich ; Enfield, NH: Trans Tech Publications, 2011.

[26] B. Chehab, « Transformations microstructurales et endommagement à chaud des aciers inoxydables biphasés », Institut national polytechnique de grenoble, Grenoble, 2007.
[27] J. Singh, G. R. Purdy, et G. C. Weatherly, « Microstructural and microchemical aspects of the solid-state decomposition of delta ferrite in austenitic stainless steels », *Metall Trans A*, vol. 16, nº 8, p. 1363-1369, août 1985, doi: 10.1007/BF02658669.
[28] J. W. Elmer, « The influence of cooling rate on the microstructure of stainless steel alloys », MASSACHUSETTS INSTITUTE OF TECHNOLOGY, 1988.
[29] J. W. Elmer, S. M. Allen, et T. W. Eagar, « Microstructural development during solidification of stainless steel alloys », *MTA*, vol. 20, nº 10, p. 2117-2131, oct. 1989, doi: 10.1007/BF02650298.
[30] G. Gottstein, *Physical Foundations of Materials Science*. Berlin, Heidelberg: Springer Berlin Heidelberg, 2004. doi: 10.1007/978-3-662-09291-0.
[31] M. A. Lakhdari, « Relation entre la microstructure et les propriétés d'acier superduplex inoxydable : influence de la topologie et de la fraction de phases », Université Grenoble Alpes, 2020.
[32] R. A. Lebensohn et C. N. Tomé, « A self-consistent anisotropic approach for the simulation of plastic deformation and texture development of polycrystals: Application to zirconium alloys », *Acta Metallurgica et Materialia*, vol. 41, nº 9, p. 2611-2624, sept. 1993, doi: 10.1016/0956-7151(93)90130-K.
[33] P. Lacombe, B. Baroux, et G. Beranger, *Stainless steels*. Les éditions de physique, 1990.
[34] J. Schwartz, « Approche non locale en plasticité cristalline : application à l'étude du comportement mécanique de l'acier AISI 316LN en fatigue oligocyclique », Centrale Paris, 2011.
[35] B. P. Kashyap et K. Tangri, « On the Hall-Petch relationship and substructural evolution in type 316L stainless steel », *Acta Metallurgica et Materialia*, vol. 43, nº 11, p. 3971-3981, nov. 1995, doi: 10.1016/0956-7151(95)00110-H.
[36] X. Feaugas et H. Haddou, « Grain-size effects on tensile behavior of nickel and AISI 316L stainless steel », *Metall and Mat Trans A*, vol. 34, nº 10, p. 2329-2340, oct. 2003, doi: 10.1007/s11661-003-0296-5.
[37] U. F. Kocks et H. Mecking, « Physics and phenomenology of strain hardening: the FCC case », *Progress in Materials Science*, vol. 48, nº 3, p. 171-273, janv. 2003, doi: 10.1016/S0079-6425(02)00003-8.
[38] U. F. Kocks, A. S. Argon, et M. F. Ashby, « Models for macroscopic slip », *Progress in Materials Science*, vol. 19, p. 171-229, 1975.
[39] W. J. Poole, J. D. Embury, et D. J. Lloyd, « Work hardening in aluminium alloys », in *Fundamentals of Aluminium Metallurgy*, Elsevier, 2011, p. 307-344. doi: 10.1533/9780857090256.2.307.
[40] M. Dadé *et al.*, « Influence of microstructural parameters on the mechanical properties of oxide dispersion strengthened Fe-14Cr steels », *Acta Materialia*, vol. 127, p. 165-177, avr. 2017, doi: 10.1016/j.actamat.2017.01.026.
[41] N. Christodoulou, O. T. Woo, et S. R. MacEwen, « Effect of stress reversals on the work hardening behaviour of polycrystalline copper », *Acta Metallurgica*, vol. 34, nº 8, p. 1553-1562, août 1986, doi: 10.1016/0001-6160(86)90100-8.
[42] M. Whelan, P. Hirsch, R. Horne, et W. Bollman, « Dislocations and stacking faults in stainless steel », *Proc. R. Soc. Lond. A*, vol. 240, nº 1223, p. 524-538, juill. 1957, doi: 10.1098/rspa.1957.0105.
[43] G. Meric de Bellefon et J. C. van Duysen, « Tailoring plasticity of austenitic stainless steels for nuclear applications: Review of mechanisms controlling plasticity of austenitic steels below 400 °C », *Journal of Nuclear Materials*, vol. 475, p. 168-191, juill. 2016, doi: 10.1016/j.jnucmat.2016.04.015.
[44] G. Meric de Bellefon, J. C. van Duysen, et K. Sridharan, « Composition-dependence of stacking fault energy in austenitic stainless steels through linear regression with random intercepts », *Journal of Nuclear Materials*, vol. 492, p. 227-230, août 2017, doi: 10.1016/j.jnucmat.2017.05.037.
[45] F. B. Pickering, *Stainless Steels '84 : proceedings of the conference ; held at Chalmers University of Technology, Göteborg, on 3 - 4 September 1984*. London: Institute of metals, 1985.
[46] K. Spencer, « The work hardening of austenitic stainless steel, applied to the fabrication of high strength conductors. », McMaster University, 2004.
[47] I. Gutierrez-Urrutia, S. Zaefferer, et D. Raabe, « The effect of grain size and grain orientation on deformation twinning in a Fe–22wt.% Mn–0.6wt.% C TWIP steel », *Materials Science and Engineering: A*, vol. 527, nº 15, p. 3552-3560, juin 2010, doi: 10.1016/j.msea.2010.02.041.
[48] M. Ma, Z. Wang, et X. Zeng, « A comparison on metallurgical behaviors of 316L stainless steel by selective laser melting and laser cladding deposition », *Materials Science and Engineering: A*, vol. 685, p. 265-273, févr. 2017, doi: 10.1016/j.msea.2016.12.112.
[49] S. Dépinoy, « Influence of solidification conditions on chemical heterogeneities and dislocations patterning in additively manufactured 316L stainless steel », *Materialia*, vol. 24, p. 101472, août 2022, doi: 10.1016/j.mtla.2022.101472.
[50] T. Voisin *et al.*, « New insights on cellular structures strengthening mechanisms and thermal stability of an austenitic stainless steel fabricated by laser powder-bed-fusion », *Acta Materialia*, vol. 203, p. 116476, janv. 2021, doi: 10.1016/j.actamat.2020.11.018.

[51] A. Chniouel *et al.*, « Influence of substrate temperature on microstructural and mechanical properties of 316L stainless steel consolidated by laser powder bed fusion », *Int J Adv Manuf Technol*, vol. 111, nº 11-12, p. 3489-3503, déc. 2020, doi: 10.1007/s00170-020-06316-4.

[52] M. S. Pham, B. Dovgyy, et P. A. Hooper, « Twinning induced plasticity in austenitic stainless steel 316L made by additive manufacturing », *Materials Science and Engineering: A*, vol. 704, p. 102-111, sept. 2017, doi: 10.1016/j.msea.2017.07.082.

[53] Q. Chao, S. Thomas, N. Birbilis, P. Cizek, P. D. Hodgson, et D. Fabijanic, « The effect of post-processing heat treatment on the microstructure, residual stress and mechanical properties of selective laser melted 316L stainless steel », *Materials Science and Engineering: A*, vol. 821, p. 141611, juill. 2021, doi: 10.1016/j.msea.2021.141611.

[54] J. A. Dantzig et M. Rappaz, *Solidification*, 1st ed. in Engineering sciences Materials. Lausanne: EPFL Press, 2009.

[55] S.-H. Sun, T. Ishimoto, K. Hagihara, Y. Tsutsumi, T. Hanawa, et T. Nakano, « Excellent mechanical and corrosion properties of austenitic stainless steel with a unique crystallographic lamellar microstructure via selective laser melting », *Scripta Materialia*, vol. 159, p. 89-93, janv. 2019, doi: 10.1016/j.scriptamat.2018.09.017.

[56] J. J. Marattukalam *et al.*, « The effect of laser scanning strategies on texture, mechanical properties, and site-specific grain orientation in selective laser melted 316L SS », *Materials & Design*, vol. 193, p. 108852, août 2020, doi: 10.1016/j.matdes.2020.108852.

[57] Y. M. Wang *et al.*, « Additively manufactured hierarchical stainless steels with high strength and ductility », *Nature Mater*, vol. 17, nº 1, p. 63-71, janv. 2018, doi: 10.1038/nmat5021.

[58] Z. Sun, X. Tan, S. B. Tor, et C. K. Chua, « Simultaneously enhanced strength and ductility for 3D-printed stainless steel 316L by selective laser melting », *NPG Asia Mater*, vol. 10, nº 4, p. 127-136, avr. 2018, doi: 10.1038/s41427-018-0018-5.

[59] A. Baumard, D. Ayrault, O. Fandeur, C. Bordreuil, et F. Deschaux-Beaume, « Numerical prediction of grain structure formation during laser powder bed fusion of 316 L stainless steel », *Materials & Design*, vol. 199, p. 109434, févr. 2021, doi: 10.1016/j.matdes.2020.109434.

[60] M.-S. Pham, B. Dovgyy, P. A. Hooper, C. M. Gourlay, et A. Piglione, « The role of side-branching in microstructure development in laser powder-bed fusion », *Nat Commun*, vol. 11, nº 1, p. 749, déc. 2020, doi: 10.1038/s41467-020-14453-3.

[61] Th. Camus, D. Maisonnette, O. Baulin, O. Senninger, G. Guillemot, et Ch.-A. Gandin, « Three-dimensional modeling of solidification grain structures generated by laser powder bed fusion », *Materialia*, vol. 30, p. 101804, août 2023, doi: 10.1016/j.mtla.2023.101804.

[62] U. Scipioni Bertoli, B. E. MacDonald, et J. M. Schoenung, « Stability of cellular microstructure in laser powder bed fusion of 316L stainless steel », *Materials Science and Engineering: A*, vol. 739, p. 109-117, janv. 2019, doi: 10.1016/j.msea.2018.10.051.

[63] S. Ziri, « Combined effect of powder properties and process parameters on the mechanical properties of stainless steel 316L elaborated by Laser Powder Bed Fusion », Université de Toulouse, Toulouse, 2022.

[64] P. Peyre et É. Charkaluk, *La fabrication additive des alliages métalliques*. in Collection Science des matériaux. London: ISTE éditions, 2022.

[65] L. Cui, S. Jiang, J. Xu, R. L. Peng, R. T. Mousavian, et J. Moverare, « Revealing relationships between microstructure and hardening nature of additively manufactured 316L stainless steel », *Materials & Design*, vol. 198, p. 109385, janv. 2021, doi: 10.1016/j.matdes.2020.109385.

[66] D. Riabov, A. Leicht, J. Ahlström, et E. Hryha, « Investigation of the strengthening mechanism in 316L stainless steel produced with laser powder bed fusion », *Materials Science and Engineering: A*, vol. 822, p. 141699, août 2021, doi: 10.1016/j.msea.2021.141699.

[67] K. M. Bertsch, G. Meric de Bellefon, B. Kuehl, et D. J. Thoma, « Origin of dislocation structures in an additively manufactured austenitic stainless steel 316L », *Acta Materialia*, vol. 199, p. 19-33, oct. 2020, doi: 10.1016/j.actamat.2020.07.063.

[68] S. Gaudez *et al.*, « High-resolution reciprocal space mapping reveals dislocation structure evolution during 3D printing », *Additive Manufacturing*, p. 103602, mai 2023, doi: 10.1016/j.addma.2023.103602.

[69] P. Deng, M. Karadge, R. B. Rebak, V. K. Gupta, B. C. Prorok, et X. Lou, « The origin and formation of oxygen inclusions in austenitic stainless steels manufactured by laser powder bed fusion », *Additive Manufacturing*, vol. 35, p. 101334, oct. 2020, doi: 10.1016/j.addma.2020.101334.

[70] Z. Li *et al.*, « Tensile properties, strain rate sensitivity, and activation volume of additively manufactured 316L stainless steels », *International Journal of Plasticity*, vol. 120, p. 395-410, sept. 2019, doi: 10.1016/j.ijplas.2019.05.009.

[71] X. Wang, O. Sanchez-Mata, S. E. Atabay, J. A. Muñiz-Lerma, M. Attarian Shandiz, et M. Brochu, « Crystallographic orientation dependence of Charpy impact behaviours in stainless steel 316L fabricated by laser powder bed fusion », *Additive Manufacturing*, vol. 46, p. 102104, oct. 2021, doi: 10.1016/j.addma.2021.102104.

[72] H. Roirand, « Apport de la fabrication additive pour la compréhension de la compétition défauts/microstructure sur le comportement en fatigue de l'acier inoxydable 316L », Hesam Université, Bordeaux, 2023.

[73] D. Riabov, M. Rashidi, E. Hryha, et S. Bengtsson, « Effect of the powder feedstock on the oxide dispersion strengthening of 316L stainless steel produced by laser powder bed fusion », *Materials Characterization*, vol. 169, p. 110582, nov. 2020, doi: 10.1016/j.matchar.2020.110582.

[74] F. Yan, W. Xiong, E. Faierson, et G. B. Olson, « Characterization of nano-scale oxides in austenitic stainless steel processed by powder bed fusion », *Scripta Materialia*, vol. 155, p. 104-108, oct. 2018, doi: 10.1016/j.scriptamat.2018.06.011.

[75] S. Relave, « Caractérisation et prédiction de la microstructure obtenue par fabrication additive. Application aux aciers inoxydables. », Ecole des mines de saint etienne, Saint-etienne, 2020.

[76] S. Gao *et al.*, « Recrystallization-based grain boundary engineering of 316L stainless steel produced via selective laser melting », *Acta Materialia*, vol. 200, p. 366-377, nov. 2020, doi: 10.1016/j.actamat.2020.09.015.

[77] L. S. Aota *et al.*, « Recrystallization kinetics, mechanisms, and topology in alloys processed by laser powder-bed fusion: AISI 316L stainless steel as example », *Materialia*, p. 101236, sept. 2021, doi: 10.1016/j.mtla.2021.101236.

[78] Y. Hong, C. Zhou, Y. Zheng, L. Zhang, et J. Zheng, « The cellular boundary with high density of dislocations governed the strengthening mechanism in selective laser melted 316L stainless steel », *Materials Science and Engineering: A*, vol. 799, p. 140279, janv. 2021, doi: 10.1016/j.msea.2020.140279.

[79] P. Krakhmalev *et al.*, « Microstructure, Solidification Texture, and Thermal Stability of 316 L Stainless Steel Manufactured by Laser Powder Bed Fusion », *Metals*, vol. 8, nº 8, p. 643, août 2018, doi: 10.3390/met8080643.

[80] C. Herrera, R. L. Plaut, et A. F. Padilha, « Microstructural Refinement during Annealing of Plastically Deformed Austenitic Stainless Steels », *MSF*, vol. 550, p. 423-428, juill. 2007, doi: 10.4028/www.scientific.net/MSF.550.423.

[81] P. Deng *et al.*, « On the thermal coarsening and transformation of nanoscale oxide inclusions in 316L stainless steel manufactured by laser powder bed fusion and its influence on impact toughness », *Materials Science and Engineering: A*, vol. 835, p. 142690, févr. 2022, doi: 10.1016/j.msea.2022.142690.

[82] D. Kong *et al.*, « Mechanical properties and corrosion behavior of selective laser melted 316L stainless steel after different heat treatment processes », *Journal of Materials Science & Technology*, vol. 35, nº 7, p. 1499-1507, juill. 2019, doi: 10.1016/j.jmst.2019.03.003.

[83] S. Dryepondt, P. Nandwana, P. Fernandez-Zelaia, et F. List, « Microstructure and high temperature tensile properties of 316L fabricated by laser powder-bed fusion », *Additive Manufacturing*, vol. 37, p. 101723, janv. 2021, doi: 10.1016/j.addma.2020.101723.

[84] T. S. Byun *et al.*, « Mechanical behavior of additively manufactured and wrought 316L stainless steels before and after neutron irradiation », *Journal of Nuclear Materials*, vol. 548, p. 152849, mai 2021, doi: 10.1016/j.jnucmat.2021.152849.

[85] A. Charmi *et al.*, « Mechanical anisotropy of additively manufactured stainless steel 316L: An experimental and numerical study », *Materials Science and Engineering: A*, vol. 799, p. 140154, janv. 2021, doi: 10.1016/j.msea.2020.140154.

[86] Y. Hong *et al.*, « Formation of strain-induced martensite in selective laser melting austenitic stainless steel », *Materials Science and Engineering: A*, vol. 740-741, p. 420-426, janv. 2019, doi: 10.1016/j.msea.2018.10.121.

[87] T. Kurzynowski, K. Gruber, W. Stopyra, B. Kuźnicka, et E. Chlebus, « Correlation between process parameters, microstructure and properties of 316 L stainless steel processed by selective laser melting », *Materials Science and Engineering: A*, vol. 718, p. 64-73, mars 2018, doi: 10.1016/j.msea.2018.01.103.

[88] Md. Shamsujjoha, S. R. Agnew, J. M. Fitz-Gerald, W. R. Moore, et T. A. Newman, « High Strength and Ductility of Additively Manufactured 316L Stainless Steel Explained », *Metall and Mat Trans A*, vol. 49, nº 7, p. 3011-3027, juill. 2018, doi: 10.1007/s11661-018-4607-2.

[89] X. Wang, J. A. Muñiz-Lerma, M. Attarian Shandiz, O. Sanchez-Mata, et M. Brochu, « Crystallographic-orientation-dependent tensile behaviours of stainless steel 316L fabricated by laser powder bed fusion », *Materials Science and Engineering: A*, vol. 766, p. 138395, oct. 2019, doi: 10.1016/j.msea.2019.138395.

[90] Z. Li, B. He, et Q. Guo, « Strengthening and hardening mechanisms of additively manufactured stainless steels: The role of cell sizes », *Scripta Materialia*, vol. 177, p. 17-21, mars 2020, doi: 10.1016/j.scriptamat.2019.10.005.

[91] D. Kong, C. Dong, X. Ni, L. Zhang, et X. Li, « Cellular size dependence on the strength of additively manufactured austenitic stainless steel », *Materials Letters*, vol. 279, p. 128524, nov. 2020, doi: 10.1016/j.matlet.2020.128524.

[92] C. Bean *et al.*, « Heterogeneous slip localization in an additively manufactured 316L stainless steel », *International Journal of Plasticity*, vol. 159, p. 103436, déc. 2022, doi: 10.1016/j.ijplas.2022.103436.

[93] W. Chen *et al.*, « Microscale residual stresses in additively manufactured stainless steel », *Nat Commun*, vol. 10, nº 1, p. 4338, déc. 2019, doi: 10.1038/s41467-019-12265-8.

[94] L. Liu *et al.*, « Dislocation network in additive manufactured steel breaks strength–ductility trade-off », *Materials Today*, vol. 21, nº 4, p. 354-361, mai 2018, doi: 10.1016/j.mattod.2017.11.004.

[95] F. He *et al.*, « Deformation faulting and dislocation-cell refinement in a selective laser melted 316L stainless steel », *International Journal of Plasticity*, vol. 156, p. 103346, sept. 2022, doi: 10.1016/j.ijplas.2022.103346.

[96] O. O. Salman, C. Gammer, A. K. Chaubey, J. Eckert, et S. Scudino, « Effect of heat treatment on microstructure and mechanical properties of 316L steel synthesized by selective laser melting », *Materials Science and Engineering: A*, vol. 748, p. 205-212, mars 2019, doi: 10.1016/j.msea.2019.01.110.

[97] F. He *et al.*, « Deformation faulting and dislocation-cell refinement in a selective laser melted 316L stainless steel », *International Journal of Plasticity*, vol. 156, p. 103346, sept. 2022, doi: 10.1016/j.ijplas.2022.103346.

[98] T. Voisin, Guss, J. Mckeown, et M. J. Matthews, « Microstructural characterization of L-PBF stainless steel 316L as-built and in situ during plastic deformation. » Lawrence livermore national laboratory, 30 décembre 2019.

[99] X. Yang *et al.*, « Understanding orientation-dependent plasticity in laser beam powder bed fusion stainless steel through crystal plasticity modelling », *Materials Science and Engineering: A*, vol. 852, p. 143682, sept. 2022, doi: 10.1016/j.msea.2022.143682.

[100] J. Schindelin *et al.*, « Fiji: an open-source platform for biological-image analysis », *Nat Methods*, vol. 9, nº 7, p. 676-682, juill. 2012, doi: 10.1038/nmeth.2019.

[101] D. G. Brandon, « The structure of high-angle grain boundaries », *Acta Metallurgica*, vol. 14, nº 11, p. 1479-1484, nov. 1966, doi: 10.1016/0001-6160(66)90168-4.

[102] N. Bozzolo et M. Bernacki, « Viewpoint on the Formation and Evolution of Annealing Twins During Thermomechanical Processing of FCC Metals and Alloys », *Metall Mater Trans A*, vol. 51, nº 6, p. 2665-2684, juin 2020, doi: 10.1007/s11661-020-05772-7.

[103] J. K. Mackenzie, « Second Paper on Statistics Associated with the Random Disorientation of Cubes », *Biometrika*, vol. 45, nº 1/2, p. 229, juin 1958, doi: 10.2307/2333059.

[104] B. Beausir et J.-J. Fundenberger, « Analysis Tools for Electron and X-ray diffraction », *ATEX - software*, Université de Lorraine - Metz 2017.

[105] E. F. Rauch et M. Véron, « Automated crystal orientation and phase mapping in TEM », *Materials Characterization*, vol. 98, p. 1-9, déc. 2014, doi: 10.1016/j.matchar.2014.08.010.

[106] D. Mainprice, R. Hielscher, et H. Schaeben, « Calculating anisotropic physical properties from texture data using the MTEX open-source package », *Geological Society, London, Special Publications*, vol. 360, nº 1, p. 175-192, 2011, doi: 10.1144/SP360.10.

[107] L. Malerba *et al.*, « Advances on GenIV structural and fuel materials and cross-cutting activities between fission and fusion », *EPJ Nuclear Sci. Technol.*, vol. 6, p. 32, 2020, doi: 10.1051/epjn/2019021.

[108] B. Barkia *et al.*, « On the origin of the high tensile strength and ductility of additively manufactured 316L stainless steel: Multiscale investigation », *Journal of Materials Science & Technology*, vol. 41, p. 209-218, mars 2020, doi: 10.1016/j.jmst.2019.09.017.

[109] O. Andreau *et al.*, « Texture control of 316L parts by modulation of the melt pool morphology in selective laser melting », *Journal of Materials Processing Technology*, vol. 264, p. 21-31, févr. 2019, doi: 10.1016/j.jmatprotec.2018.08.049.

[110] A.-H. Puichaud *et al.*, « Microstructure and mechanical properties relationship of additively manufactured 316L stainless steel by selective laser melting », *EPJ Nuclear Sci. Technol.*, vol. 5, p. 23, 2019, doi: 10.1051/epjn/2019051.

[111] M. Laleh, A. E. Hughes, M. Y. Tan, G. S. Rohrer, S. Primig, et N. Haghdadi, « Grain boundary character distribution in an additively manufactured austenitic stainless steel », *Scripta Materialia*, vol. 192, p. 115-119, févr. 2021, doi: 10.1016/j.scriptamat.2020.10.018.

[112] J. Hou, W. Chen, Z. Chen, K. Zhang, et A. Huang, « Microstructure, tensile properties and mechanical anisotropy of selective laser melted 304L stainless steel », *Journal of Materials Science & Technology*, vol. 48, p. 63-71, juill. 2020, doi: 10.1016/j.jmst.2020.01.011.

[113] Z. Zhu *et al.*, « Enhanced strength–ductility synergy and transformation-induced plasticity of the selective laser melting fabricated 304L stainless steel », *Additive Manufacturing*, vol. 35, p. 101300, oct. 2020, doi: 10.1016/j.addma.2020.101300.

[114] I. Cazic, J. Zollinger, S. Mathieu, M. El Kandaoui, P. Plapper, et B. Appolaire, « New insights into the origin of fine equiaxed microstructures in additively manufactured Inconel 718 », *Scripta Materialia*, vol. 195, p. 113740, avr. 2021, doi: 10.1016/j.scriptamat.2021.113740.

[115] I. Cazic *et al.*, « Nucleation burst in additively manufactured Inconel 718: 3D characterization of ISRO-induced equiaxed microstructure », *Additive Manufacturing*, vol. 66, p. 103458, mars 2023, doi: 10.1016/j.addma.2023.103458.

[116] C. Galera-Rueda, M. L. Montero-Sistiaga, K. Vanmeensel, M. Godino-Martínez, J. Llorca, et M. T. Pérez-Prado, « Icosahedral quasicrystal-enhanced nucleation in Al alloys fabricated by selective laser melting », *Additive Manufacturing*, vol. 44, p. 102053, août 2021, doi: 10.1016/j.addma.2021.102053.

[117] M. Buttard *et al.*, « Towards an alloy design strategy by tuning liquid local ordering: What solidification of an Al-alloy designed for laser powder bed fusion teaches us », *Additive Manufacturing*, vol. 61, p. 103313, janv. 2023, doi: 10.1016/j.addma.2022.103313.

[118] C. Galera-Rueda, X. Jin, J. LLorca, et M. T. Pérez-Prado, « Icosahedral quasicrystal enhanced nucleation in commercially pure Ni processed by selective laser melting », *Scripta Materialia*, vol. 211, p. 114512, avr. 2022, doi: 10.1016/j.scriptamat.2022.114512.

[119] M. Rappaz, Ph. Jarry, G. Kurtuldu, et J. Zollinger, « Solidification of Metallic Alloys: Does the Structure of the Liquid Matter? », *Metall Mater Trans A*, vol. 51, nº 6, p. 2651-2664, juin 2020, doi: 10.1007/s11661-020-05770-9.

[120] S. Patel et M. Vlasea, « Melting modes in laser powder bed fusion », *Materialia*, vol. 9, p. 100591, mars 2020, doi: 10.1016/j.mtla.2020.100591.
[121] S. Katayama et A. Matsunawa, « Solidification microstructure of laser welded stainless steels », in *International Congress on Applications of Lasers & Electro-Optics*, Boston, Massachusetts, USA: Laser Institute of America, 1984, p. 60-67. doi: 10.2351/1.5057623.
[122] S. Tekumalla, B. Selvarajou, S. Raman, S. Gao, et M. Seita, « The role of the solidification structure on orientation-dependent hardness in stainless steel 316L produced by laser powder bed fusion », *Materials Science and Engineering: A*, vol. 833, p. 142493, janv. 2022, doi: 10.1016/j.msea.2021.142493.
[123] A. Bhowmik, W. Zhai, W. Zhou, et S. M. L. Nai, « Characterization of carbide particle-reinforced 316L stainless steel fabricated by selective laser melting », *Materials Characterization*, vol. 179, p. 111360, sept. 2021, doi: 10.1016/j.matchar.2021.111360.
[124] S. Zhang *et al.*, « Refinement mechanism of cerium addition on solidification structure and sigma phase of super austenitic stainless steel S32654 », *Journal of Materials Science & Technology*, vol. 102, p. 105-114, mars 2022, doi: 10.1016/j.jmst.2021.06.033.
[125] H. Ikehata, D. Mayweg, et E. Jägle, « Grain refinement of Fe--Ti alloys fabricated by laser powder bed fusion », *Materials & Design*, vol. 204, p. 109665, juin 2021, doi: 10.1016/j.matdes.2021.109665.
[126] H. Ding *et al.*, « Effect of in-situ TiB2 particles on microstructure and mechanical properties of Al–Fe–Ni manufactured by selective laser melting », *Materials Science and Engineering: A*, p. 143065, mars 2022, doi: 10.1016/j.msea.2022.143065.
[127] S. Tokita, H. Kokawa, Y. S. Sato, et H. T. Fujii, « In situ EBSD observation of grain boundary character distribution evolution during thermomechanical process used for grain boundary engineering of 304 austenitic stainless steel », *Materials Characterization*, vol. 131, p. 31-38, sept. 2017, doi: 10.1016/j.matchar.2017.06.032.
[128] H. E. Sabzi *et al.*, « Grain refinement in laser powder bed fusion: The influence of dynamic recrystallization and recovery », *Materials & Design*, vol. 196, p. 109181, nov. 2020, doi: 10.1016/j.matdes.2020.109181.
[129] D. Turnbull et J. C. Fisher, « Rate of Nucleation in Condensed Systems », *The Journal of Chemical Physics*, vol. 17, nº 1, p. 71-73, janv. 1949, doi: 10.1063/1.1747055.
[130] S. Krishnan et D. L. Price, « X-ray diffraction from levitated liquids », *J. Phys.: Condens. Matter*, vol. 12, nº 12, p. R145-R176, mars 2000, doi: 10.1088/0953-8984/12/12/201.
[131] G. Kurtuldu, P. Jarry, et M. Rappaz, « Influence of Cr on the nucleation of primary Al and formation of twinned dendrites in Al–Zn–Cr alloys: Can icosahedral solid clusters play a role? », *Acta Materialia*, vol. 61, nº 19, p. 7098-7108, nov. 2013, doi: 10.1016/j.actamat.2013.07.056.
[132] F. Frank, « Supercooling of liquids », *Proc. R. Soc. Lond. A*, vol. 215, nº 1120, p. 43-46, nov. 1952, doi: 10.1098/rspa.1952.0194.
[133] T. Schenk, D. Holland-Moritz, V. Simonet, R. Bellissent, et D. M. Herlach, « Icosahedral Short-Range Order in Deeply Undercooled Metallic Melts », *Phys. Rev. Lett.*, vol. 89, nº 7, p. 075507, juill. 2002, doi: 10.1103/PhysRevLett.89.075507.
[134] G. Kurtuldu, A. Sicco, et M. Rappaz, « Icosahedral quasicrystal-enhanced nucleation of the fcc phase in liquid gold alloys », *Acta Materialia*, vol. 70, p. 240-248, mai 2014, doi: 10.1016/j.actamat.2014.02.037.
[135] G. Kurtuldu, P. Jarry, et M. Rappaz, « Influence of icosahedral short range order on diffusion in liquids: A study on Al-Zn-Cr alloys », *Acta Materialia*, vol. 115, p. 423-433, août 2016, doi: 10.1016/j.actamat.2016.05.051.
[136] H. Sidhom et R. Portier, « An icosahedral phase in annealed austenitic stainless steel? », *Philosophical Magazine Letters*, vol. 59, nº 3, p. 131-139, mars 1989, doi: 10.1080/09500838908206334.
[137] Y. J. Oh, W. S. Ryu, C. Sung, I. H. Kuk, et J. H. Hong, « Grain boundary filmlike Fe–Mo–Cr phase in nitrogen-added type 316L stainless steels », *J. Mater. Res.*, vol. 14, nº 2, p. 390-397, févr. 1999, doi: 10.1557/JMR.1999.0057.
[138] F. Bachmann, R. Hielscher, et H. Schaeben, « Texture Analysis with MTEX – Free and Open Source Software Toolbox », *SSP*, vol. 160, p. 63-68, févr. 2010, doi: 10.4028/www.scientific.net/SSP.160.63.
[139] F. Royer, J. Zollinger, B. Rouat, et M. Rappaz, « Influence of Minor Cr Additions on Crystal Growth in Rapidly Solidified Al-20Zn Alloys », *Materials*, vol. 13, nº 2, p. 379, janv. 2020, doi: 10.3390/ma13020379.
[140] J. Zollinger, B. Rouat, J. Guyon, S. K. Pillai, et M. Rappaz, « Influence of Ir Additions and Icosahedral Short Range Order (ISRO) on Nucleation and Growth Kinetics in Au-20.5Wt Pct Cu-4.5Wt PctAg Alloy », *Metall and Mat Trans A*, vol. 50, nº 5, p. 2279-2288, mai 2019, doi: 10.1007/s11661-019-05176-2.
[141] B. Jönsson, « Assessment of the Mobilities of Cr, Fe, and Ni in fcce Cr-Fe-Ni Alloys », *International Journal of Materials Research*, vol. 86, nº 10, p. 686-692, oct. 1995, doi: 10.1515/ijmr-1995-861006.
[142] B. Jönsson, « Assessment of the Mobilities of Cr, Fe and Ni in bcc Cr-Fe-Ni Alloys. », *ISIJ International*, vol. 35, nº 11, p. 1415-1421, 1995, doi: 10.2355/isijinternational.35.1415.
[143] A. J. Godfrey, J. Simpson, D. Leonard, K. Sisco, R. R. Dehoff, et S. S. Babu, « Heterogeneity and Solidification Pathways in Additively Manufactured 316L Stainless Steels », *Metall Mater Trans A*, vol. 53, nº 9, p. 3321-3340, sept. 2022, doi: 10.1007/s11661-022-06747-6.
[144] A. J. Birnbaum, J. C. Steuben, E. J. Barrick, A. P. Iliopoulos, et J. G. Michopoulos, « Intrinsic strain aging, Σ3 boundaries, and origins of cellular substructure in additively manufactured 316L », *Additive Manufacturing*, vol. 29, p. 100784, oct. 2019, doi: 10.1016/j.addma.2019.100784.

[145] S. Fukumoto et W. Kurz, « Prediction of the .DELTA. to .GAMMA. Transition in Austenitic Stainless Steels during Laser Treatment. », *ISIJ International*, vol. 38, nº 1, p. 71-77, 1998, doi: 10.2355/isijinternational.38.71.

[146] M. Hillert et L. Hoglund, « Mobility of α/γ phase interfaces in Fe alloys », *Scripta Materialia*, vol. 54, nº 7, p. 1259-1263, avr. 2006, doi: 10.1016/j.scriptamat.2005.12.023.

[147] T. J. Lienert et J. C. Lippold, « Improved weldability diagram for pulsed laser welded austenitic stainless steels », *Science and Technology of Welding and Joining*, vol. 8, nº 1, p. 1-9, févr. 2003, doi: 10.1179/136217103225008847.

[148] A. Pasturel et N. Jakse, « Influence of Cr on local order and dynamic properties of liquid and undercooled Al–Zn alloys », *The Journal of Chemical Physics*, vol. 146, nº 18, p. 184502, mai 2017, doi: 10.1063/1.4982887.

[149] N. Jakse et A. Pasturel, « Correlation between dynamic slowing down and local icosahedral ordering in undercooled liquid $Al_{80}Ni_{20}$ alloy », *The Journal of Chemical Physics*, vol. 143, nº 8, p. 084508, août 2015, doi: 10.1063/1.4929481.

[150] N. Jakse, O. L. Bacq, et A. Pasturel, « Short-range order of liquid and undercooled metals: Ab initio molecular dynamics study », *Journal of Non-Crystalline Solids*, vol. 353, nº 32-40, p. 3684-3688, oct. 2007, doi: 10.1016/j.jnoncrysol.2007.05.131.

[151] P. Ganesh et M. Widom, « *Ab initio* simulations of geometrical frustration in supercooled liquid Fe and Fe-based metallic glass », *Phys. Rev. B*, vol. 77, nº 1, p. 014205, janv. 2008, doi: 10.1103/PhysRevB.77.014205.

[152] A. Sobolev et A. Mirzoev, « Ab initio studies of the short-range atomic structure of liquid iron–carbon alloys », *Journal of Molecular Liquids*, vol. 179, p. 12-17, mars 2013, doi: 10.1016/j.molliq.2012.11.019.

[153] E. de Sonis *et al.*, « Dependency of recrystallization kinetics on the solidification microstructure of 316L stainless steel processed by laser powder bed fusion (LPBF) », *Materials Characterization*, vol. 194, p. 112370, déc. 2022, doi: 10.1016/j.matchar.2022.112370.

[154] H. Nitta, K. Miura, et Y. Iijima, « Self-diffusion in iron-based Fe–Mo alloys », *Acta Materialia*, vol. 54, nº 10, p. 2833-2847, juin 2006, doi: 10.1016/j.actamat.2006.02.020.

[155] X. Feaugas, « On the origin of the tensile flow stress in the stainless steel AISI 316L at 300 K: back stress and effective stress », *Acta Materialia*, vol. 47, nº 13, p. 3617-3632, oct. 1999, doi: 10.1016/S1359-6454(99)00222-0.

[156] G. Monnet et M. A. Pouchon, « Determination of the critical resolved shear stress and the friction stress in austenitic stainless steels by compression of pillars extracted from single grains », *Materials Letters*, vol. 98, p. 128-130, mai 2013, doi: 10.1016/j.matlet.2013.01.118.

[157] X. Feaugas et H. Haddou, « Effects of grain size on dislocation organization and internal stresses developed under tensile loading in fcc metals », *Philosophical Magazine*, vol. 87, nº 7, p. 989-1018, mars 2007, doi: 10.1080/14786430601019441.

[158] R. Ueji *et al.*, « Tensile properties and twinning behavior of high manganese austenitic steel with fine-grained structure », *Scripta Materialia*, vol. 59, nº 9, p. 963-966, nov. 2008, doi: 10.1016/j.scriptamat.2008.06.050.

[159] O. Bouaziz et N. Guelton, « Modelling of TWIP effect on work-hardening », *Materials Science and Engineering: A*, vol. 319-321, p. 246-249, déc. 2001, doi: 10.1016/S0921-5093(00)02019-0.

[160] C. W. Sinclair, W. J. Poole, et Y. Bréchet, « A model for the grain size dependent work hardening of copper », *Scripta Materialia*, vol. 55, nº 8, p. 739-742, oct. 2006, doi: 10.1016/j.scriptamat.2006.05.018.

[161] A. Taghipour *et al.*, « Strengthening Mechanisms and Strain Hardening Behavior of 316L Stainless Steel Manufactured by Laser-Based Powder Bed Fusion », *Adv Eng Mater*, vol. 25, nº 4, p. 2201230, févr. 2023, doi: 10.1002/adem.202201230.

[162] M. F. Ashby, « Physical modelling of materials problems », *Materials Science and Technology*, vol. 8, nº 2, p. 102-111, févr. 1992, doi: 10.1179/mst.1992.8.2.102.

[163] J. Friedel, N. Kurti, et R. Smoluchowski, *Dislocations*. Elsevier Science.

[164] S. Allain, J.-P. Chateau, et O. Bouaziz, « A physical model of the twinning-induced plasticity effect in a high manganese austenitic steel », *Materials Science and Engineering: A*, vol. 387-389, p. 143-147, déc. 2004, doi: 10.1016/j.msea.2004.01.060.

[165] O. Bouaziz, S. Allain, et C. Scott, « Effect of grain and twin boundaries on the hardening mechanisms of twinning-induced plasticity steels », *Scripta Materialia*, vol. 58, nº 6, p. 484-487, mars 2008, doi: 10.1016/j.scriptamat.2007.10.050.

[166] I. Gutierrez-Urrutia et D. Raabe, « Dislocation and twin substructure evolution during strain hardening of an Fe–22wt.% Mn–0.6wt.% C TWIP steel observed by electron channeling contrast imaging », *Acta Materialia*, vol. 59, nº 16, p. 6449-6462, sept. 2011, doi: 10.1016/j.actamat.2011.07.009.

[167] J. Kim, Y. Estrin, et B. C. De Cooman, « Application of a Dislocation Density-Based Constitutive Model to Al-Alloyed TWIP Steel », *Metall Mater Trans A*, vol. 44, nº 9, p. 4168-4182, sept. 2013, doi: 10.1007/s11661-013-1771-2.

[168] L. Rémy, « The interaction between slip and twinning systems and the influence of twinning on the mechanical behavior of fcc metals and alloys », *Metall Trans A*, vol. 12, nº 3, p. 387-408, mars 1981, doi: 10.1007/BF02648536.

[169] R. L. Fullman, « Measurement of Particle Sizes in Opaque Bodies », *JOM*, vol. 5, nº 3, p. 447-452, mars 1953, doi: 10.1007/BF03398971.

[170] B. C. De Cooman, Y. Estrin, et S. K. Kim, « Twinning-induced plasticity (TWIP) steels », *Acta Materialia*, vol. 142, p. 283-362, janv. 2018, doi: 10.1016/j.actamat.2017.06.046.

[171] S. S. Joshi, C. Keller, L. Mas, W. Lefebvre, E. Hug, et J.-P. Couzinie, « On the origin of the strain hardening mechanisms of Ni20Cr alloy manufactured by laser powder bed fusion », *International Journal of Plasticity*, vol. 165, p. 103610, juin 2023, doi: 10.1016/j.ijplas.2023.103610.

[172] O. B. Pedersen, L. M. Brown, et W. M. Stobbs, « The bauschinger effect in copper », *Acta Metallurgica*, vol. 29, nº 11, p. 1843-1850, nov. 1981, doi: 10.1016/0001-6160(81)90110-3.

[173] J. Chicois, R. Fougeres, G. Guichon, A. Hamel, et A. Vincent, « Mobilite des dislocations lors de la sollicitation cyclique de l'aluminium polycristallin », *Acta Metallurgica*, vol. 34, nº 11, p. 2157-2170, nov. 1986, doi: 10.1016/0001-6160(86)90161-6.

[174] L. Palmeira Belotti, J. A. W. van Dommelen, M. G. D. Geers, C. Goulas, W. Ya, et J. P. M. Hoefnagels, « Microstructural characterisation of thick-walled wire arc additively manufactured stainless steel », *Journal of Materials Processing Technology*, vol. 299, p. 117373, janv. 2022, doi: 10.1016/j.jmatprotec.2021.117373.

[175] L. Palmeira Belotti, T. F. W. van Nuland, M. G. D. Geers, J. P. M. Hoefnagels, et J. A. W. van Dommelen, « On the anisotropy of thick-walled wire arc additively manufactured stainless steel parts », *Materials Science and Engineering: A*, vol. 863, p. 144538, janv. 2023, doi: 10.1016/j.msea.2022.144538.

[176] H. Inoue, T. Koseki, S. Ohkita, et M. Fuji, « Formation mechanism of vermicular and lacy ferrite in austenitic stainless steel weld metals », *Science and Technology of Welding and Joining*, vol. 5, nº 6, p. 385-396, déc. 2000, doi: 10.1179/136217100101538452.

[177] C. Wang, T. G. Liu, P. Zhu, Y. H. Lu, et T. Shoji, « Study on microstructure and tensile properties of 316L stainless steel fabricated by CMT wire and arc additive manufacturing », *Materials Science and Engineering: A*, vol. 796, p. 140006, oct. 2020, doi: 10.1016/j.msea.2020.140006.

[178] C. Wang, P. Zhu, Y. H. Lu, et T. Shoji, « Effect of heat treatment temperature on microstructure and tensile properties of austenitic stainless 316L using wire and arc additive manufacturing », *Materials Science and Engineering: A*, vol. 832, p. 142446, janv. 2022, doi: 10.1016/j.msea.2021.142446.

[179] R. Cohen, « The effects of solidification rate and heat treatment on the microstructure and mechanical properties of ceramic shell investment cast CF3M. », University of Oklahoma, 1990.

[180] K. Saeidi, X. Gao, Y. Zhong, et Z. J. Shen, « Hardened austenite steel with columnar sub-grain structure formed by laser melting », *Materials Science and Engineering: A*, vol. 625, p. 221-229, févr. 2015, doi: 10.1016/j.msea.2014.12.018.

[181] M. Saied, « Experimental and numerical modeling of the dissolution of δ-ferrite in the Fe-Cr-Ni system: Application to austenitic stainless steels », Université Grenoble Alpes, 2016.

[182] Y. Li *et al.*, « Hardening behavior of selective laser melted 304L stainless steel under Xe irradiation », *Vacuum*, vol. 192, p. 110453, oct. 2021, doi: 10.1016/j.vacuum.2021.110453.

[183] J. Zhao *et al.*, « Evaluating impact performance of a selective laser melted 304L stainless steel with weak texture », *Materials Today Communications*, vol. 25, p. 101299, déc. 2020, doi: 10.1016/j.mtcomm.2020.101299.

[184] T. Pan *et al.*, « Effect of processing parameters and build orientation on microstructure and performance of AISI stainless steel 304L made with selective laser melting under different strain rates », *Materials Science and Engineering: A*, vol. 835, p. 142686, févr. 2022, doi: 10.1016/j.msea.2022.142686.

[185] C. Sofras *et al.*, « Tailored deformation behavior of 304L stainless steel through control of the crystallographic texture with laser-powder bed fusion », *Materials & Design*, vol. 219, p. 110789, juill. 2022, doi: 10.1016/j.matdes.2022.110789.

[186] M. Sprengel *et al.*, « Towards the Optimization of Post-Laser Powder Bed Fusion Stress-Relieve Treatments of Stainless Steel 316L », *Metall Mater Trans A*, vol. 52, nº 12, p. 5342-5356, déc. 2021, doi: 10.1007/s11661-021-06472-6.

[187] I. Bressler, B. R. Pauw, et A. F. Thünemann, « *McSAS* : software for the retrieval of model parameter distributions from scattering patterns », *J Appl Crystallogr*, vol. 48, nº 3, p. 962-969, juin 2015, doi: 10.1107/S1600576715007347.

Appendix

Appendix A – Grain clusters with 5-fold symmetry axes

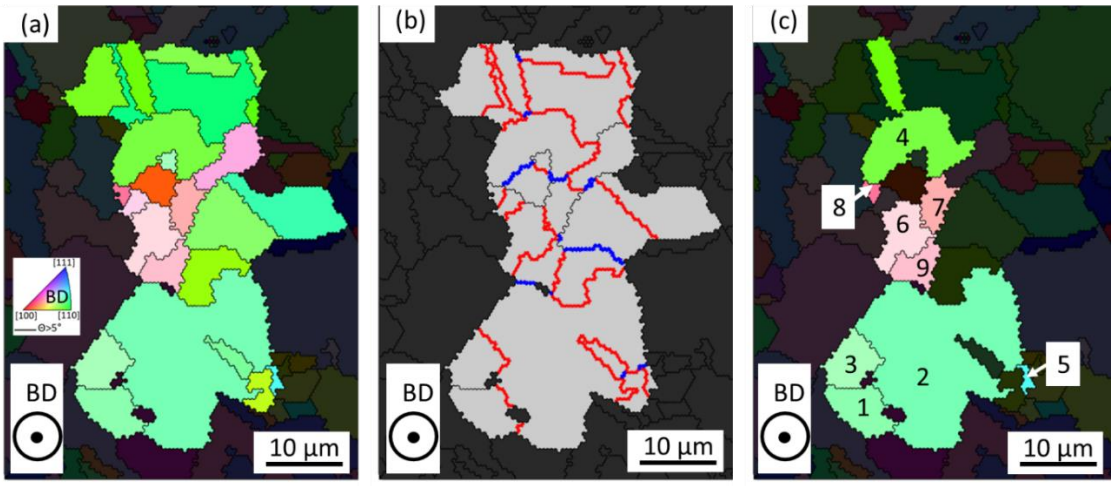

Figure A-1 : (a) EBSD-IPF map where the color code corresponds to the average orientation per grain. Grains belonging to the identified cluster are highlighted. (b) Grain boundary map of this cluster of grains, with Σ3 in red and Σ9 in blue. (c) EBSD-IPF map of the 9 different grain orientations (labeled from 1 to 9) found in this cluster.

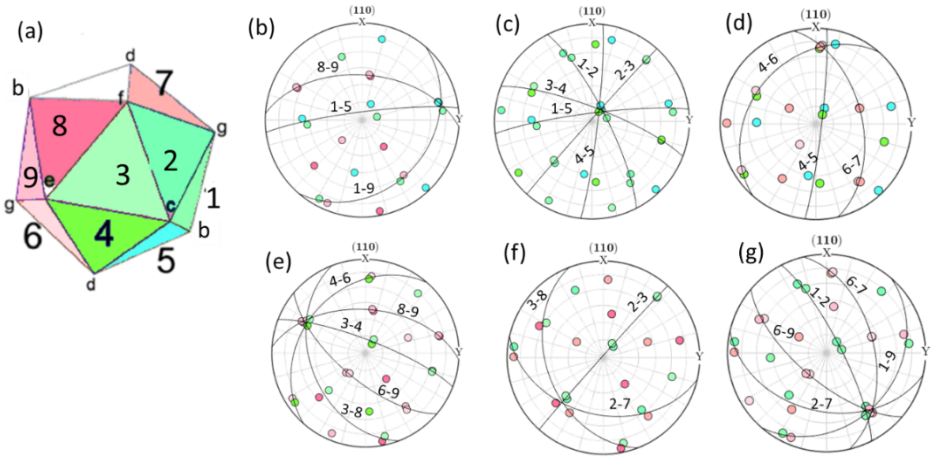

Figure A-2: The <110> pole figures of sets of multiple twin grains from Figure A-1 are shown in (b through g), with the indication of the {111} twin or near-twin planes by arcs of circles. The <110> common pole (fivefold symmetry) is found at the intersection of the twin planes. In (a), an icosahedron has been schematically drawn in a position such that the six 5-fold symmetry axes labeled (b through g) approximately correspond to the common <110> axes of the FCC grains, and with corresponding facets of the same color as grains in Figure A-1. Adapted from ref [134].

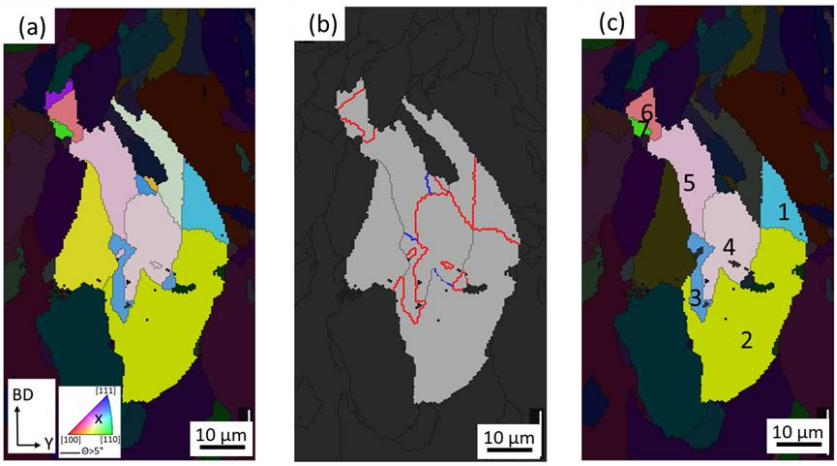

Figure A-3: (a) EBSD-IPF map where the color code corresponds to the average orientation per grain. Grains belonging to the identified cluster are highlighted. (b) Grain boundary map of this cluster of grains, with Σ3 in red and Σ9 in blue. (c) EBSD-IPF map of the 7 different grain orientations (labeled from 1 to 7) found in this cluster.

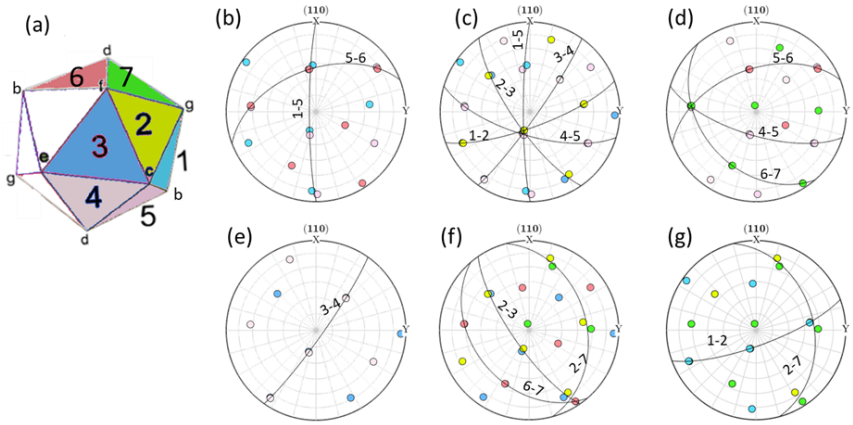

Figure A-4: The <110> pole figures of sets of multiple twin grains from Figure A-3 are shown in (b through g), with the indication of the {111} twin or near-twin planes by arcs of circles. The <110> common pole (fivefold symmetry) is found at the intersection of the twin planes. In (a), an icosahedron has been schematically drawn in a position such that the six 5-fold symmetry axes labeled (b through g) approximately correspond to the common <110> axes of the FCC grains, and with corresponding facets of the same color as grains in Figure A-3. Adapted from ref [134].

Appendix B – Correlation between microstructure and compositions

Table B-1: Used compositions to correlations made in III.4. The equivalent Cr and Ni are computed with the WRC 92 formula. Compositions in red show compositions which gives a Steel 2 microstructure like [9], [72], [75], [83], [84], [113], [182], [183]. Compositions in blue show compositions which give a Steel 1 microstructure [1], [9], [12], [50], [57], [65], [72], [87], [88], [184]–[186].

Reference	Cr	Ni	Mo	Mn	Si	C	N	Cr_{eq}	Ni_{eq}	Cr_{eq}/Ni_{eq}
Byun 2021	17.1	12.1	2.41	1.19	0.46	0.006	0.01	19.51	12.51	1.56
Roirand 2023 (1)	17.7	13.6	2.7	1.5	0	0.005	0.01	20.40	13.98	1.46
Roirand 2023 (2)	17.7	11.9	2.3	1.5	0.2	0.005	0.01	20.00	12.28	1.63
Chniouel 2019 (1)	17.7	12.25	2.17	0.55	0.65	0.013	0.0103	19.87	12.91	1.54
Li 2021	19.07	9.62	0.87	0.054	0.065	0.014	0.013	19.94	10.37	1.92
Steel 2 (This work)	16.94	12.18	2.69	1.21	0.498	0.006	0.013	19.63	12.65	1.55
Zhu 2020	18.45	9.22	0	0.66	0.42	0.008	0.016	18.45	9.82	1.88
Relave 2020 (1)	16.8	10.68	2.26	0.85	0.54	0.02	0.021	19.06	11.80	1.62
Zhao 2020	19.14	9.41	0.9	0.013	0.033	0.014	0.023	20.04	10.36	1.93
Dryepondt 2021	16.9	11.9	2.6	1.1	0.43	0.008	0.03	19.50	12.78	1.53
Shamsujjoha 2018	20	16	2.5	1	0.4	0.006	0.049	22.50	17.19	1.31
Wang 2017 (2)	16.5	10.6	2.06	1.2	0.37	0.011	0.053	18.56	12.05	1.54
Pan 2022	18.4	9.8	0	1.4	0.6	0.018	0.06	18.40	11.63	1.58
Sofras 2022	18.4	9.8	0	1.4	0.6	0.015	0.07	18.40	11.73	1.57
Andreau 2020	17.7	12.7	2.31	0.89	0.61	0.018	0.09	20.01	15.13	1.32
Kurzynowski 2018	17.09	10.61	2.38	1.17	0.59	0.013	0.09	19.47	12.87	1.51
Steel 1 (This work)	17.63	12.42	2.36	0.895	0.68	0.021	0.09	19.99	14.96	1.34
Cui 2021	17.7	12.69	2.32	0.9	0.7	0.023	0.091	20.02	15.32	1.31
Godec 2019	17.7	13.6	2.8	1.6	0.22	0.006	0.092	20.50	15.65	1.31
Wang 2017 (1)	16.9	12.4	2.32	1.22	0.7	0.016	0.094	19.22	14.84	1.30
Sprengel 2021	17.7	12.6	2.35	0.92	0.6	0.017	0.1	20.05	15.20	1.32
Chniouel 2019 (2)	17.5	12.3	2	1	0.6	0.015	0.12	19.50	15.23	1.28
Voisin 2020	16.7	10.8	2.2	1.2	0.54	0.011	0.17	18.90	14.59	1.30

Appendix C – Identification of the σ phase after SR+900°C/1h for Steel 2.

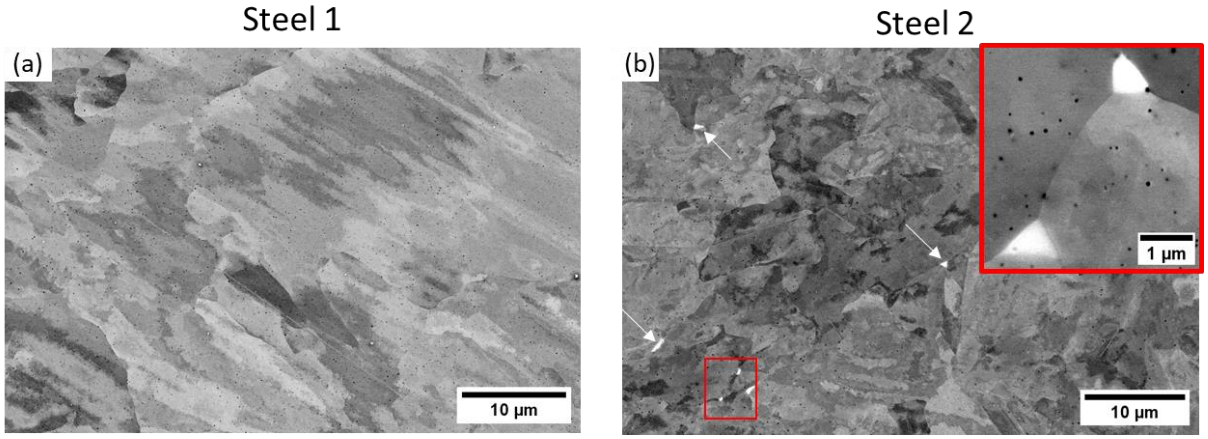

Figure C-1: BSE images after the homogenization heat treatment (SR+900°C/1h). (a) For Steel 1, (b) For Steel 2. Nucleation of white phases is observed for Steel 2 and represents 0.02% surface fraction. It is not observed for Steel 1.

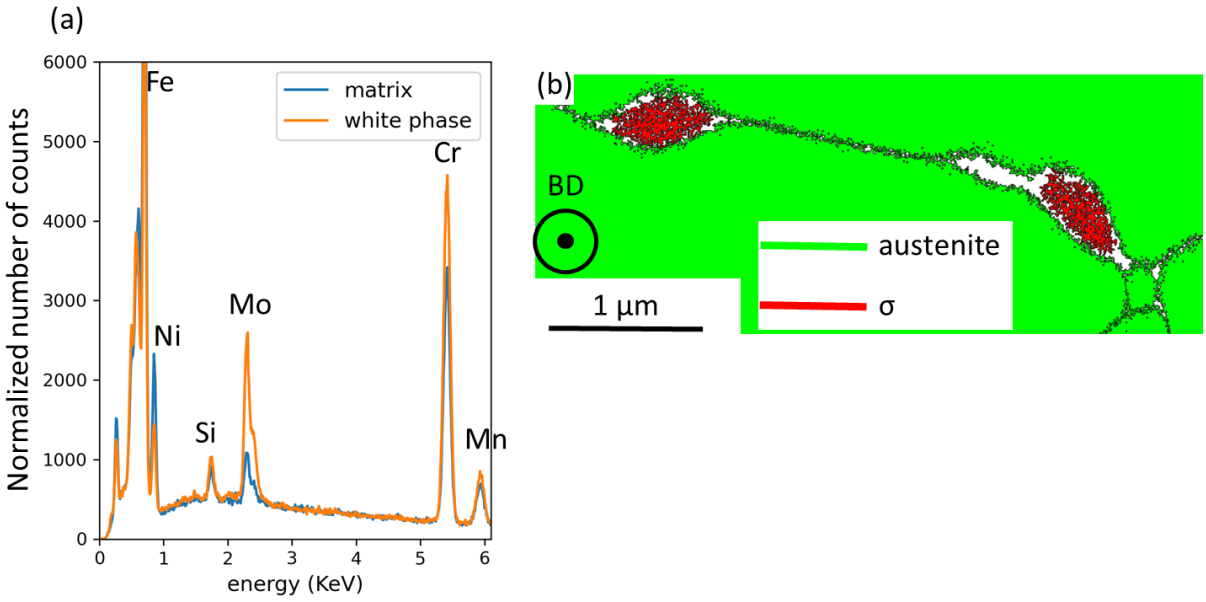

Figure C-2: (a) Superposition of EDX spectrograph between the matrix and the white phase. The withe phase is enriched in Mo and Cr. EBSD phase map of an area with white phase with a step size of 10 nm. White phases saw in SEM are indexed as σ phase. Ferrite was also entered as a possible phase.

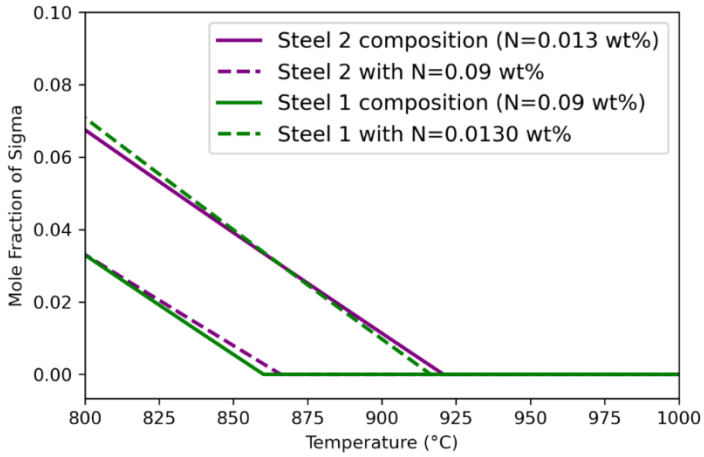

Figure C-3: Thermocalc simulation (TCFE11) of fraction of σ phase at equilibrium, for both steels at different nitrogen content. Nitrogen content has the first order impact on the σ phase fraction at equilibrium. The difference in N content between the two steels explain why there is precipitation in Steel 2 but not in Steel 1.

Appendix D – TEM analysis of the oxides particles

To characterize the crystallography of oxides, the ACOM (Automated Crystallographic Orientation Mapping) tool was used. The results of this analysis on Steel 2 are shown in Figure D-1. It is possible to process the image obtained by considering only the information of a certain zone present on the diffraction pattern of each point. In the case of amorphous oxides, it is interesting to take the information contained in the diffraction circle characteristic of the diffraction of the amorphous phase. The resulting image can be called a virtual annular dark-field image. The area considered on the diffraction pattern to make this image is shown in Figure D-1(b). The resulting image is shown in Figure D-1 (c). It contrasts the particles and dislocations in the material much more visibly than in Figure D-1(a) taken in bright-field STEM mode. Numerous particles of around forty nanometers can be seen, as well as larger ones of up to a hundred nanometers. A strong particle-dislocation interaction can also be seen. This observation is difficult to achieve with other techniques, which often contrast either dislocations or oxides via chemical contrast. Figure D-1 shows that some particles are partially crystallized, while others are amorphous.

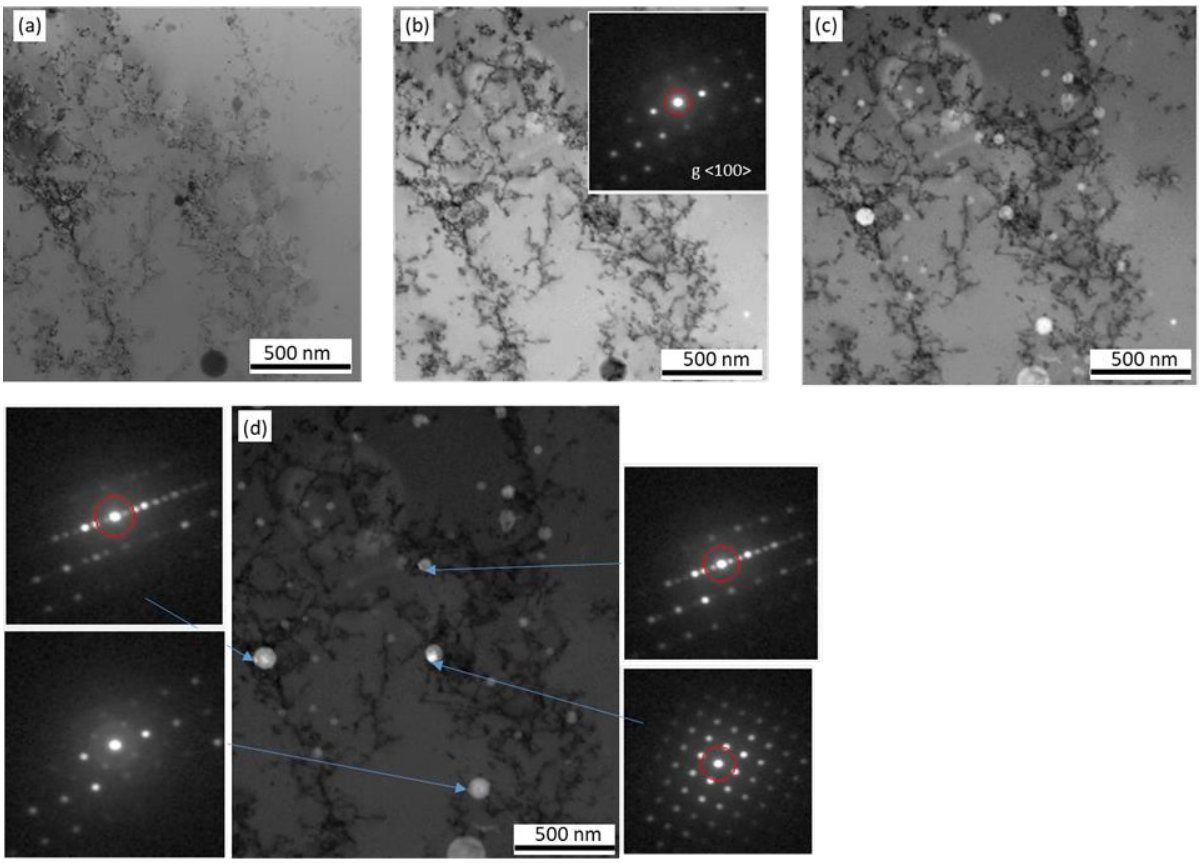

Figure D-1: TEM images of raw Praxair steel. (a) STEM bright field images. (b) ACOM bright field of the same area as (a). The diffraction shows a zone axis <100>. The red circle corresponds to the information used to make image (c); (c) Virtual annular dark field of (b). (d) Virtual dark field and diffraction of certain particle zones.

A partial crystallization form is identified as SiO_2 cristobalite coherent with the austenitic matrix, which is an FCC metastable form of SiO_2, see Figure D-2. A second crystallographic form present in the oxides is visible, but could not be identified. The analysis was also carried out on Steel 1, and the same conclusions were drawn regarding the nature of the precipitates.

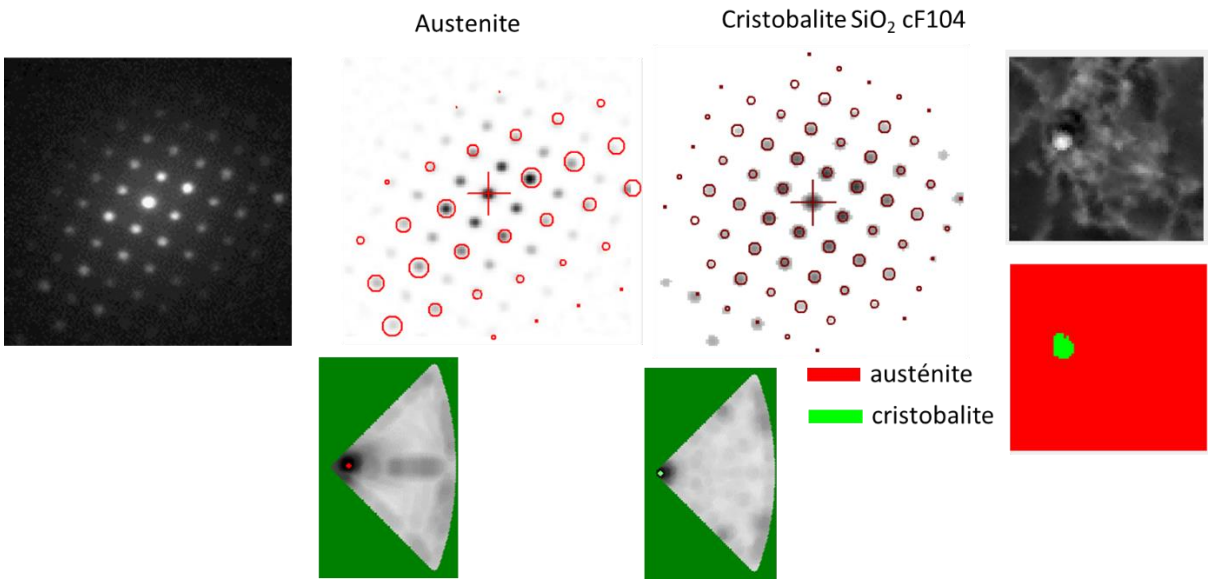

Figure D-2: Identification of a partial crystallization of the oxides as cristobalite SiO_2.

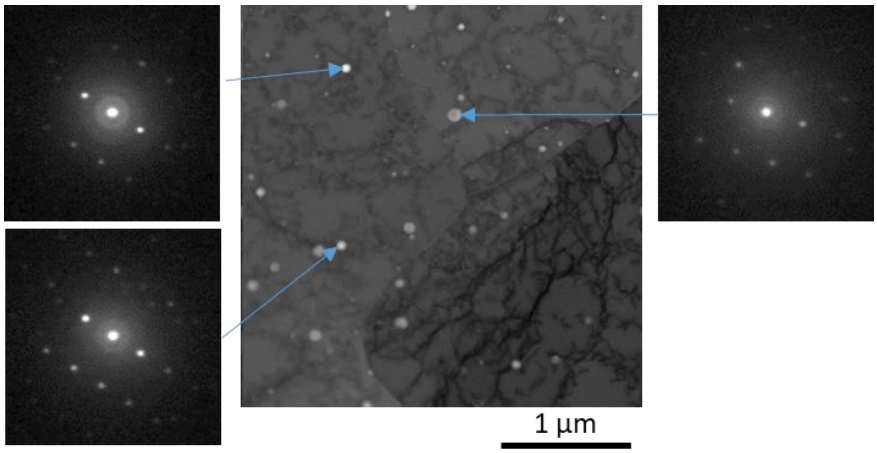

Figure D-3: Crystallography of oxides for Steel 2 after a stress relief heat treatment (600°C/1h). Only amorphous oxides are found.

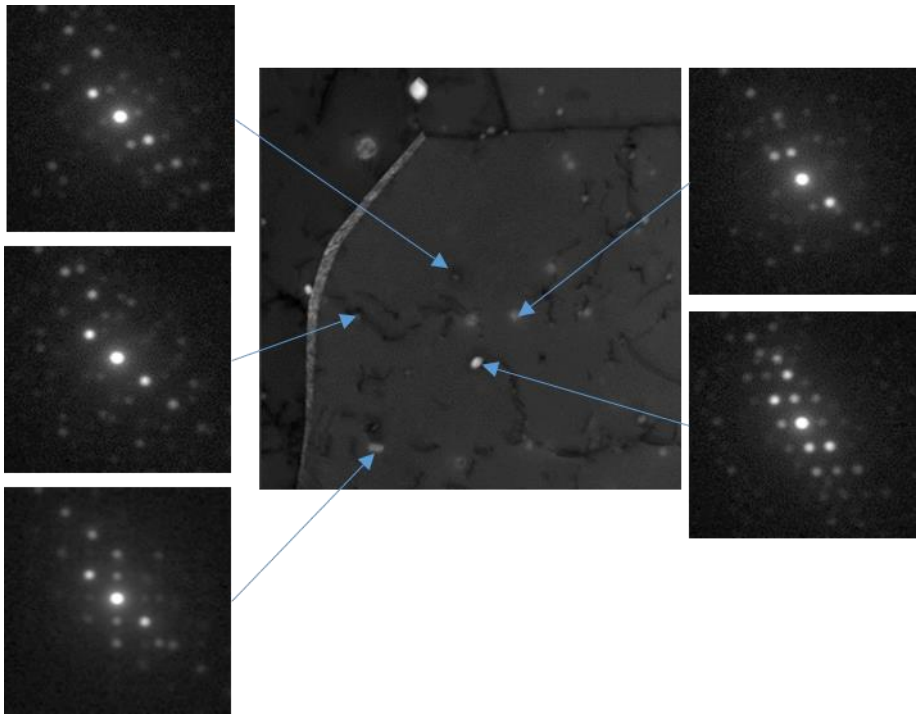

Figure D-4: Crystallography of oxides after homogenization (SR + 900°C/1h). Some oxides are amorphous and a large number are crystallized. The crystallography was not successfully identified.

Appendix E – Evolution of oxides with heat treatment

Table E-1: Evolution of oxides diameter, surface density, and Delaunay distance for Steel 1 and Steel 2 with heat treatment. Values between Steel 1 and Steel 2 are closed for every conditions.

	Diameter (nm)		**Surface density (10^{12} nb/m^2)**		**Delaunay distance (nm)**	
Condition	Steel 1	Steel 2	Steel 1	Steel 2	Steel 1	Steel 2
As built	20 ± 4	22 ± 4	5.3 ± 0.5	6.6 ± 0.5	530 ± 40	480 ± 40
Stress relieved	20 ± 4	22 ± 4	5.3 ± 0.5	6.6 ± 0.5	530 ± 40	480 ± 40
Homogenized	39 ± 5	37 ± 5	3 ± 0.5	2.3 ± 0.5	730 ± 40	740 ± 40
Recrystallized	310 ± 50	280 ± 40	0.04 ± 0.01	0.05 ± 0.01	5000 ± 500	4900 ± 450

Appendix F – Oxides size distribution

The difference in oxide distribution between Steel 1 and Steel 2 is evaluated by small angle X-ray scattering (SAXS). It was done in close collaboration with ENSAM Bordeaux (Lorène Héraud) and CIRIMAT in Toulouse (Benoit Malard) in the framework of the Ph.D. thesis of Hugo Roirand. Data processing was carried out with Frederic de Geuser, from SIMaP. Experiments were carried out at the ID02 beamline of the European Synchrotron Research Facility (ESRF), with a beam energy of 19.5 KeV, with a sample-to-detector lengths of 20 m. A length of 20 m is necessary to obtain information on large particles (>200 nm diameter), and this length is only possible on ESRF. The samples were ground polished to a thickness close to 50 µm with a final polishing using a 3 µm suspension on both faces. A grid of 5x5 measurement points with a displacement of 150 µm was done. The volume fraction and particle size distribution are obtained by fitting a model onto the experimental data. The model requires preliminary assumptions regarding the particles (composition, morphology, and nature of the size distribution). It assumes an abrupt interface between the particles and the matrix. There are different definitions of the normalization of I, but the one chosen here is to divide by the thickness of the sample. The thickness e is calculated as follows (Tr: Transmission, µ absorption coefficient, [I] concentration in wt%):

$$\begin{cases} e = -\dfrac{\ln(Tr)}{\mu_{alloy}} \\ \mu_{alloy} = \rho_{alloy} * \displaystyle\sum_{I} \frac{[I]\mu_I}{\rho_I} \end{cases}$$

The results of each ex-situ sample are the average of the 25 normalized measurements. To obtain the distribution and the volume fraction, the MCSAS software [187] was used. This software does not make any hypothesis on the particle size distribution, and determines this distribution using Monte Carlo simulations. It is assumed that particles have a composition of $MnSiO_3$ (a SiO_2 assumption would give a 13% difference on the volume fraction). The particles were supposed to be spherical, with a diameter range between 8 nm and 100 nm (all of the particles observed in the TEM were in this range of size).

The I(q) values obtained for both as-built Steel 1 and Steel 2 are shown in Figure F-1 (a). I is the normalized signal intensity while q is the scattering vector defined as $q= 4\pi\sin(\theta)/\lambda$. It is noteworthy that the high q curves for the two steel samples coincide, suggesting that the volume fraction of small oxides is the same in both steels. On the other hand, at low q values, the curves do not overlap. The intensity of the low q values is stronger for Steel 2 than Steel 1. This implies a higher fraction of large oxides in Steel 2. The distribution of the volume fraction is presented in Figure F-1 (b). The cumulative area under this distribution represents the total measured volume fraction. It becomes evident that up to a diameter of 30 nm, there is no substantial distinction in volume fraction between the two steel variants. Beyond this point, a discernible difference emerges. Notably, Steel 2 exhibits an elevated presence of particles with diameters exceeding 80 nm. Additionally, the volume distribution of oxides in Steel 2 does not conform to an unimodal pattern; a trough appears around the 50 nm diameter, a feature absent in Steel 1. While the total volume fraction of oxides in Steel 2 surpasses that of Steel 1 (0.3% compared to 0.25%), this disparity is modest in relation to the dissimilarity in oxygen content (increasing from 300 ppm in Steel 1 to 700 ppm in Steel 2). One might intuit that a twofold increase in oxygen content would

correspond to a twofold increase in volume fraction. This point remains unclear and potentially stems from limitations in the experimental representability. The scanning volume of (SAXS) may be insufficient given the material's heterogeneity, or the composition of the analyzed sample's composition may inadequately represent the material's heterogeneity due to its limited size.

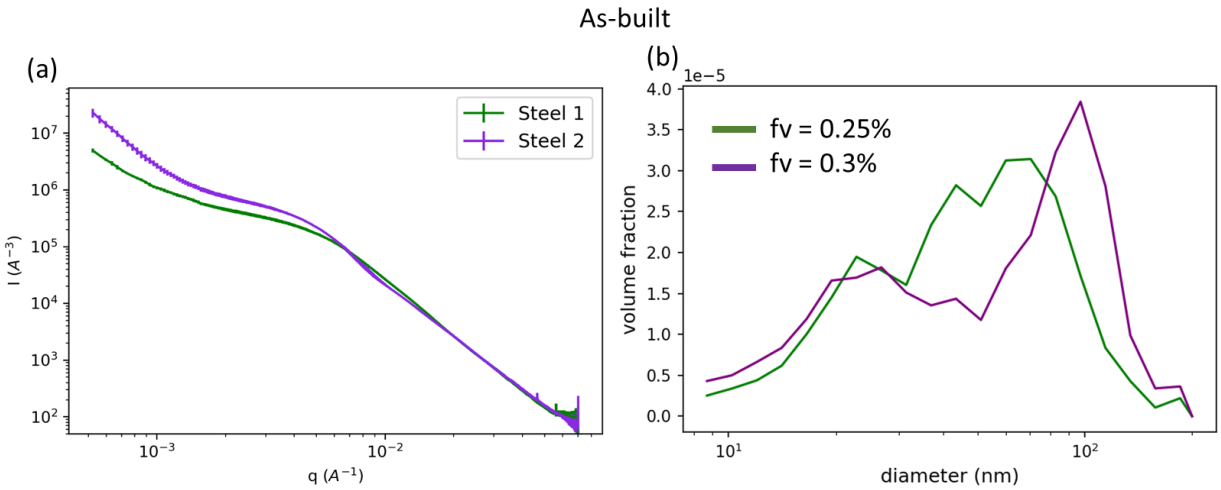

Figure F-1: SAXS result for the as built conditions (a) I(q) curve for both steels. (b) distribution of the volume fraction for both steels.

Appendix G – Summary of the mechanical properties

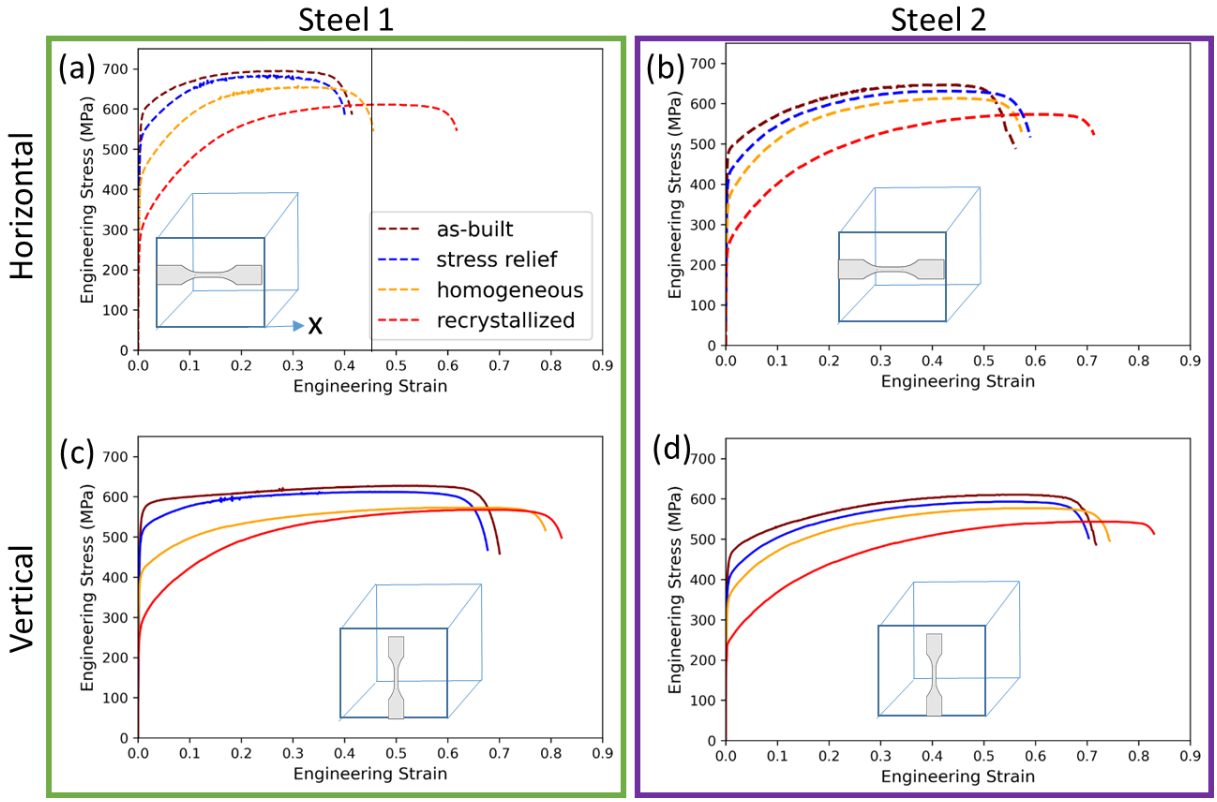

Figure G-1: Engineering stress-strain curve for (a) Steel 1 loaded in the horizontal direction. (b) Steel 2 loaded in the horizontal direction. (c) Steel 1 loaded in the vertical direction. (d) Steel 2 loaded in the vertical direction.

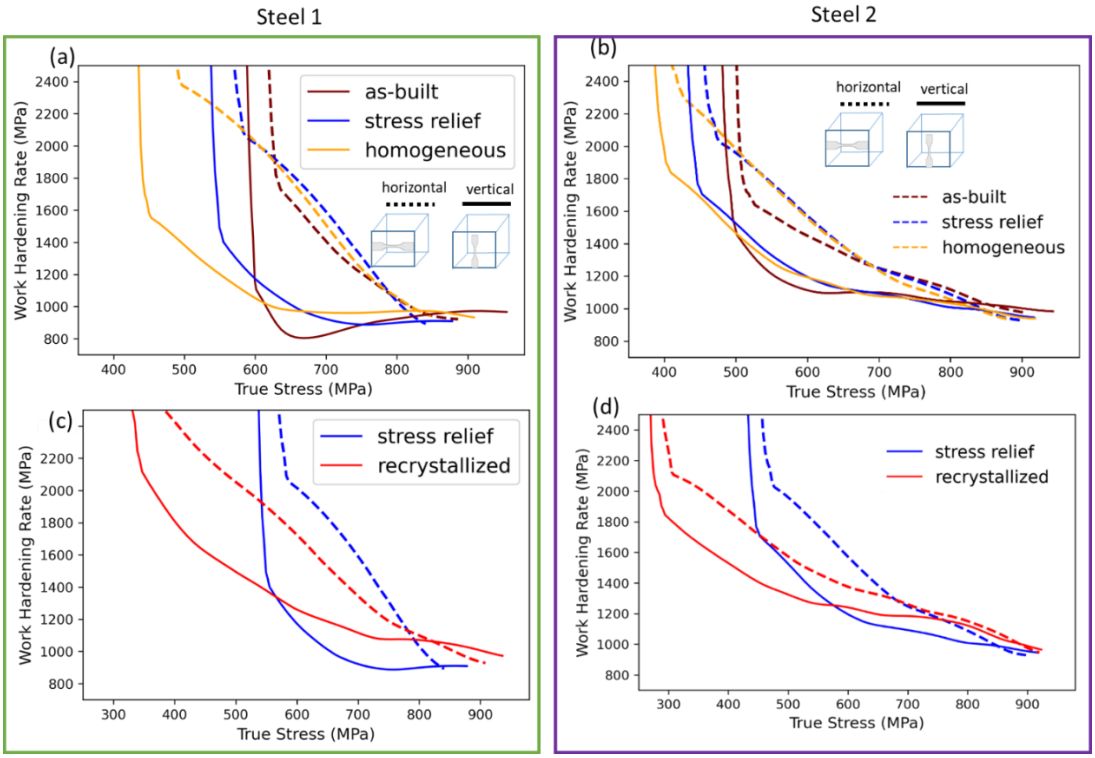

Figure G-2: Work hardening rate as a function of the true stress. (a)-(b) For the as-built. stress relief. and homogeneous condition for two directions for respectively Steel 1 and Steel 2. (c)-(d) For the stress relief and recrystallized condition for respectively Steel 1 and Steel 2.

Table G-1: Tensile properties

Steel	direction	Annealing temperature (°C)	σ_y (MPa)	UTS (MPa)	Engineering uniform elongation	Total elongation
1	Y	25	557	695	0.28	0.41
		600	513	685	0.24	0.4
		900	410	657	0.31	0.46
		1200	274	611	0.5	0.62
	X	25	596	703	0.36	0.5
		600	529	693	0.33	0.46
		900	438	669	0.39	0.47
	Z	25	529	628	0.54	0.7
		600	486	612	0.45	0.68
		900	396	573	0.6	0.79
		1200	270	567	0.67	0.82
2	X	25	474	647	0.41	0.56
		600	409	631	0.43	0.59
		900	334	613	0.45	0.57
		1200	237	573	0.62	0.71
	Z	25	431	610	0.56	0.72
		600	399	593	0.56	0.7
		900	340	577	0.6	0.74
		1200	230	543	0.71	0.83

Appendix H – Laser processing parameters to investigate the solidification mode

Table H-1: Parameters used to determine the solidification mode from lasing a pellet of a sintered powder. Other parameters are: beam diameter = 40 µm, hatching distance = 80 µm, scanning strategy = 67°. The LPBF machine is an Orlas Creator, under argon flow.

	Layer 1	**Layer 2**	**Layer 3 to 7**	**Layer 8**
Power (W)	225	175	125	125
Velocity (mm/s)	700	700	600	600

Abstract

Additive manufacturing of austenitic stainless steels using laser powder bed fusion (LPBF) or wire arc melting (WAAM) processes still presents a number of difficulties in terms of processes, resulting properties, and qualification. In particular, (i) the microstructure obtained shows a variability to slight changes in nominal composition, and (ii) the tensile properties differ strongly in comparison with their wrought counterparts. The magnitude of these differences can be considerable, questioning its use in a large variety of applications such as the nuclear industry and the design of parts based on constitutive laws that do not include those differences. The origin of these changes in properties is attributed to the directional nature of the fabrication as well as from the out-of-equilibrium nature of the microstructure inherited from LPBF due to high cooling rates (in the order of 10^6 °C/s). The first part of this thesis is devoted to understanding the origin of this variability in microstructure to slight changes in nominal composition. To this end, two 316L steels with different microstructures were produced using LPBF, and their microstructures were characterized at different scales. It is likely that this variability is due to a difference in the primary phase during solidification, from austenite solidification to ferrite solidification followed by a massive phase transformation. The second part of the project focuses on the impact of different microstructural characteristics (residual stresses, microsegregation, organization of the dislocation network) on the tensile properties. To this end, heat treatments were designed to help discriminate the role of each of those microstructural characteristics. Those heat treatments were carried out on both steels, and tensile tests in several loading directions were performed. To model the tensile response of the 316L steel inherited from LPBF, a modified Kocks-Mecking model including the effect of grain size and twinning was employed. It is shown that the parameters describing the strain hardening of a recrystallized state can describe the plasticity of the materials fabricated by LPBF, despite significant differences in the microstructure. A third section focuses on the understanding of the microstructure of the 316L steel inherited from WAAM and its evolution with heat treatments. This evolution is heterogeneous within the material. Based on the results of this Ph.D. thesis, industrial recommendations for controlling the microstructure and the corresponding mechanical properties through close control of the nominal composition and optimization of post-fabrication heat treatments are proposed.